UNIVERSITÀ DEGLI STUDI DI MILANO

DEPARTMENT OF PHYSICS

PH.D. SCHOOL IN
PHYSICS, ASTROPHYSICS AND APPLIED PHYSICS
CYCLE XXXVI

Time-Resolved Probing of Magneto-Elastic Excitations in Magnetic Materials

Disciplinary Scientific Sector FIS/03

Ph.D. Thesis of:
Pietro Carrara

Director of the School: Prof. Matteo Paris
Supervisor of the Thesis: Prof. Giorgio Rossi
Co-supervisor of the Thesis: Dr. Riccardo Cucini

A.Y. 2022-2023

Commission of the final examination:

External Referees:
Prof. Renato Torre & Prof. Em. Danilo Pescia

External Members:
Prof. Renato Torre & Prof. Stefano Bonetti

Internal Member:
Prof. Giorgio Rossi

Final examination:

22$^{\text{nd}}$ January 2024

Dipartimento di Fisica, Università degli Studi di Milano, Italy

ὁ δὲ ἀνεξέταστος βίος
οὐ βιωτὸς ἀνθρώπῳ

life without questions
is not livable for man

Plato, *Apology* 38a

Contents

Abstract

This booklet collects the results of my work as a doctoral student of the Ph.D. School in Physics, Astrophysics and Applied Physics at Università degli Studi di Milano, that has been carried out since November 2020 at Istituto Officina dei Materiali of Consiglio Nazionale delle Ricerche (IOM-CNR) and within the framework of Nanoscale Foundries and Fine Analysis (NFFA) consortium.

My experimental activity addressed the coupling of magnetic and acoustic degrees of freedom in transition-metal ferromagnetic systems. Within the NFFA-SPRINT laboratory, hosted in the premises of the facility FERMI@Elettra (Elettra-Sincrotrone Trieste), I developed a setup to perform optical Transient-Grating spectroscopy, and correlative time-resolved optical spectroscopies (time-resolved reflectivity and polarimetry). Via sub-picosecond optical pulses, acoustic and magnetic transients are impulsively generated: their intertwined evolution and decay are monitored via time-resolved optical probing.

In a first experiment, a Ni thin film was investigated via Transient-Grating spectroscopy. Acoustically-driven magnetization precession was observed at the condition of crossing of phononic and magnonic dispersions, at finite wavevector. With the aid of correlative ferromagnetic resonance measurements the boundary of applicability of the proposed experimental approach was established.

In a second experiment, time-resolved magneto-optical polarimetry was employed to investigate magneto-acoustic waves excited in a ferromagnetic nanostructured array. The details of the magnon-phonon mode crossing allowed to identify experimental features which qualify the degree of coherence in the coupling; a Hamiltonian model was proposed to account for the observations.

Introduction

Low-energy excitations in the solid state naturally arise as a consequence of spontaneous symmetry breaking and the onset of ordered phases. In the case of the ferromagnetic transition, the rotational symmetry of a paramagnet is broken upon crossing the Curie temperature: the ferromagnetic phase sets in, characterized by a finite magnetization **M** as order parameter. Excitations of **M** are modulations of the magnetization direction that can propagate in the form of waves: they are called Spin Waves (SWs) or magnons. Their dispersion relation contains information on the fundamental interaction that drives the phase transition, namely the exchange constant in the case of SWs [1]. Similarly, acoustic phonons in solids arise as low-energy excitations in the low-symmetry crystalline phase; the elastic parameters define their dispersion relation [2]. This general observation calls for investigation tools to address the finite wavevector range of low-energy excitations in the solid state.

Moreover, in correlated systems the rich ground-state phase diagram is determined by correlations and interactions that coexist at similar low energy [3]. Their energy competition can be addressed via spectroscopy of excited states, whence light on the phase boundaries can be shed. Purposely enhanced population of low-energy modes can also alter the ground-state equilibrium, driving phase transitions across the boundaries: pump-probe experiments inducing transient order parameters ultimately stem from this concept [4, 5].

To address these systems, it is of great help to conceptually separate a solid into different reservoirs: the electrons, the spin, the orbitals, the lattice. Each of these reservoirs behaves as a closed thermodynamical subsystem, with its own thermal capacity. Inter-subsystem coupling (electron-lattice, spin-lattice...) occurs at specific time and energy scale. With the aid of the reservoirs approximation, it is possible to visualize how energy is injected into the system, where it is dissipated, and which coupling channels are at play [6]. Low-energy excitations are at the very core of thermal equilibrium in materials, as they are the primary channels of inter-subsystems energy exchange.

Time-resolved experiments are an efficient approach, as they allow to visualize the timescale at which phenomena occur, and thus the energies involved, as dictated by the time-energy uncertainty. Ultrafast pulses [optical lasers, Extreme Ultraviolet (EUV) and X-ray Free Electron Lasers (FELs), ultrarelativistic electron bunches] are the typical sources employed: they are the fastest tool ever engineered by mankind, now mature to go routinely in the sub-femtosecond regime. [1]

---

[1] While I am writing this thesis, Pierre Agostini, Ferenc Krausz and Anne L'Huillier are awarded the Nobel

Typically, ultrafast optical lasers are tuned to inject energy into the electron subsystem: then a de-excitation path starts, involving energy redistribution and finally thermal equilibration. This is the case for a striking phenomenon investigated since 1996: magnetization quenching in Ni at the 100 fs timescale, with subsequent recovery in the picosecond timescale [7]. This observation raised a complementary question: as magnetization is intimately linked to angular momentum, a decrease of **M** must be accompanied by a transfer of angular momentum at the same timescale. So, where is angular momentum going in 100 fs? This question prompted intensive research in ultrafast magnetization dynamics (or *femtomagnetism*) during the last thirty years, nicely accounted for in Ref.[8]. In recent experiments [9, 10] concurrently to magnetization quenching the generation of circularly polarized phonons and strain waves was observed: they are suggested as the sought-after sub-picosecond sink of angular momentum.

Complementary approaches have been pursued. If the ultrafast laser is in the Mid Infrared (MIR) or terahertz range, light effectively couples to dipole-active phonons. In the reservoirs model, the energy is injected into the lattice subsystem, whence it spreads to the other reservoirs. Optical phonons have been observed to tickle the magnetization and possibly to drive metastable phases [11]; or THz-driven circularly polarized phonons to generate an effective magnetic field via spin-orbit coupling [12]. These examples suggest the pivotal role of low-energy excitations for the investigation of the details of the interactions responsible for the onset of material phases.

Most of the reported examples involve excitation at zero wavevector: then what about finite-wavevector excitations? Of course, this is a meaningful question only for dispersive excitations: optical phonons, for instance, feature a basically flat dispersion, and there is probably no reason to excite them at finite wavevector. For other excitations, the possibility to drive and exploit the finite-wavevector range opens new possibilities, starting from the quantification of the parameters of the underlying interactions, as stated above. Furthermore, at finite wavevector crossing of different modes can take place. In these configurations, coupling enhancement is expected between the two involved reservoirs: for instance, hybrid magnon-phonon waves could enhance energy (and angular momentum) transfer between the spin and lattice degrees of freedom. At mode crossing, the coupling can take place coherently, with intriguing possibilities for coupling engineering. Finally, finite-wavevector modes often propagate: one could envision *local* driving of a transient order parameter, which is then allowed to propagate as sustained by the excited mode.

This is the general framework in which this thesis is developed. The coupling between lattice and spin subsystems was tackled with time-resolved and finite-wavevector optical techniques, mostly with the aid of an experimental optical setup for Transient-Grating (TG) spectroscopy designed and commissioned during the thesis. Optically-excited acoustic phonons and SWs, and their mutual interaction, were investigated in ferromagnetic $3d$ systems (thin films or periodic nanostructures). The basic observation is that coherent magneto-elastic dynamics is observed in the configuration of mode degeneracy, so at finite wavevector, upon application of suitable boundary conditions (magnetic field strength, angle to anisotropy axis). These features find a natural place in the context of acoustically-driven magnetization dynamics, often investigated for its interesting technological fallouts: for instance, phonon-driven control of magnetization allows to envision fast and energy-efficient next-generation magnetic storage platforms

---

Prize in Physics *for experimental methods that generate attosecond pulses of light for the study of electron dynamics in matter*; https://www.nobelprize.org/prizes/physics/2023/press-release/.

[13]. Framing the reported observations in the context of finite-wavevector excitation of the order parameter opens the door to extension to more complex cases, which only waits to be tackled with this approach.

Thesis overview

The present thesis reports experimental results on the coupling between acoustic and magnetic low-energy excitations in ferromagnetic systems. The systems were tackled mainly via optical spectroscopy, in a time-resolved fashion.

Part I aims at providing the *building bricks*, namely the theoretical and experimental details needed to understand the performed experiments.

Chapter 1 gives a quick overview on elastic and magnetic properties in the solid state: after a general introduction of the relevant terminology, the phenomenology of excitations that can be addressed is presented. The details of magneto-elastic coupling, with emphasis on the cases relevant for the experimental results, is then provided.

In Chapter 2 the experimental approach employed is described. The fundamental aspects of excitation and detection of acoustic and magnetic transients via optical ultrafast pulses are briefly described. Then the working principles of TG spectroscopy are provided: this technique *by-design* allows to address finite-wavevector excitations, and as such can be the tool of choice in the context presented above. The details of the experimental setup built during this thesis are then explained.

Part II (Chapter 3) collects the experimental results obtained on ferromagnetic resonance driven by surface acoustic waves in a Ni thin film. The simplicity of the tackled system allowed to investigate the limit of applicability of the proposed TG approach, also in connection with complementary characterization via photon-driven ferromagnetic resonance.

Part III reports experimental observation of magnon-phonon coupling in a one-dimensional artificial crystal. In this case the sample is on-purpose engineered to enhance interaction of acoustic and spin waves: the periodic modulation of magnetic and elastic properties defines it as a magnonic-phononic crystal, where non-traveling modes are hosted and effectively interact.

In Chapter 4 the sample is described, together with the adopted experimental approach. Discussion of the observed signal proceeds together with supporting measurements and simulations. Some insights into the sample magnetic and acoustic dynamics are then reported.

In Chapter 5 the main analysis on the magnonic-phononic crystal results is reported. The observed details at the crossing of a magnon and phonon modes prompted the development of a Hamiltonian model for the interacting quasi-particles. The model (and the observational details that led to it) are suggested as a phenomenological indicator for general cases of hybridizing particles.

Part I

Building bricks

Elasticity and Magnetism in solid-state: a quick overview

The experimental work reported in this thesis addresses the interplay of acoustic and magnetic low-energy excitations, both impulsively excited via ultrafast optical laser pulses. This calls for an introductory overview on the modeling of acoustic and magnetization waves in solids, to make clear the employed terminology, and to provide a broader view of the context in which this project fits. The focus is on surface modes, as the experiments mostly address excitations at the free surface of solid samples. The approach of this chapter is mainly on the results of the employed models, while few details on their derivation are given: reference literature is suggested for each topic.

This chapter is organized as follows: the basics of acoustic dynamics in bulk solids and surfaces is presented in Sect.1.1; the general framework to describe magnetization dynamics, and the spectrum of low-energy excitations in ferromagnets are discussed in Sect.1.2; the theoretical modeling of magneto-elastic coupling is the content of Sect.1.3.

1.1 Acoustic waves

The focus of this section is on acoustic excitations at the surface of a solid sample, in the form of Surface Acoustic Waves (SAWs). [1] Only acoustic waves with wavelength Λ much longer than the unit cell of the investigated material are considered. This limit is appropriately modeled in the continuum approximation, where the discrete nature of materials at the atomic level is averaged into a continuous elastic system; quantization effects are correspondingly negligible. The concept of *phonon* naturally arises upon quantization of ionic motion, while in the continuum usually one speaks of acoustic waves; this is just a matter of nomenclature, and throughout this thesis I will speak of phonons and of acoustic (or elastic) waves with equal meaning. The continuum approximation is usually valid for $\Lambda > 10^{-8}$ m, which typically means for frequencies $f < 1$ THz [14]. For acoustic waves in the continuum approximation, the dispersion relation is linear, and the phase velocity does not depend on the frequency. Details on the continuum elasticity theory can be found in Ref.[14–16]. The discussion develops with the following steps: (i) how to describe deformations and forces in an elastic continuum, and how propagating acoustic waves arise as solutions of the Newton equation; (ii) special wave-like solutions at the free surface of a solid; (iii) phenomenology of acoustic excitation in thin films, both free-standing and supported.

---

[1]Throughout this thesis, the terms *acoustic* and *elastic* waves are used with the same meaning, as long as no confusion with the category of elastic/inelastic processes is possible. Strictly speaking, acoustics refers to wave-like dynamical processes (sound waves), while elasticity indicates deformations that could be present also without any acoustic wave. As the physical mechanisms at the basis of both are the same, the distinction is not relevant here.
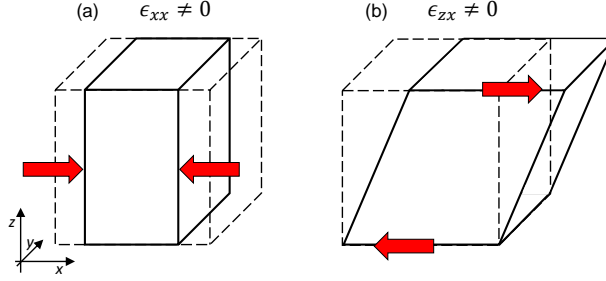
Figure 1.1: Deformation of the infinitesimal volume dV for (a) $\epsilon_{xx} \neq 0$ (longitudinal strain) or (b) $\epsilon_{zx} \neq 0$ (shear strain).

Acoustic waves in bulk solids

The mechanical deformation of an elastic body in the continuum model is encoded in the displacement field. Consider a point located at $\mathbf{r}$ in the relaxed configuration; when the deformation is applied, the point moves to $\mathbf{r}' = \mathbf{r} + \mathbf{u}(\mathbf{r})$. The displacement is $\mathbf{u}(\mathbf{r}) = \hat{x}u_x(\mathbf{r}) + \hat{y}u_y(\mathbf{r}) + \hat{z}u_z(\mathbf{r})$. The movement of each material point, possibly with explicit time dependence, is fully specified by the displacement field $\mathbf{u}(\mathbf{r}, t)$. This quantity is nonzero also for rigid translations and rotations: for this reason, to quantify the deformation it is appropriate to consider the derivatives of $\mathbf{u}(\mathbf{r})$, which are nonzero only for non-uniform displacement. Only six components are independent, and constitute the *strain* tensor ϵ_{ij} (not to be confused with the dielectric constant ε_{ij}):

$$\epsilon_{xx} = \frac{\partial u_x}{\partial x} \qquad \epsilon_{yy} = \frac{\partial u_y}{\partial y} \qquad \epsilon_{zz} = \frac{\partial u_z}{\partial z} \tag{1.1}$$

$$\epsilon_{yz} = \frac{1}{2}\left(\frac{\partial u_y}{\partial z} + \frac{\partial u_z}{\partial y}\right) \quad \epsilon_{zx} = \frac{1}{2}\left(\frac{\partial u_z}{\partial x} + \frac{\partial u_x}{\partial z}\right) \quad \epsilon_{xy} = \frac{1}{2}\left(\frac{\partial u_x}{\partial y} + \frac{\partial u_y}{\partial x}\right) . \tag{1.2}$$

The diagonal components refer to longitudinal deformation (compression or expansion) and result in volume change of the unit cell; the off-diagonal symmetric components refer to transverse deformation (shear) and only result in change of the relative angles of the body, with no volume change (see Fig.1.1).

Now consider an infinitesimal volume dV of the solid, in cubic shape for simplicity. The forces at play in elastic deformation are ultimately due to the electronic bonding in the material, and they are as such short-range forces: the resultant of the external forces acting on dV can be expressed as the sum of forces acting at the surfaces of the cube. This concept is encoded in the *stress* tensor σ_{ij}. It quantifies the force along direction j applied on a unit surface whose external normal is along i, with $i, j = x, y, z$. In analogy with the strain, the diagonal components quantify traction forces, and the off-diagonal components quantify shear forces. Stress always involves equal and opposite forces on opposite surfaces of dV: if instead a force is applied to a single face, the cube accelerates or starts rotating. This also fixes $\sigma_{yz} = \sigma_{zy}$, and similar for the other off-diagonal components.

In the linear elastic regime, stress and strain are in linear relation via the Hooke law:

$$\sigma_{ij} = C_{ijkl}\epsilon_{kl} \qquad\qquad \epsilon_{ij} = S_{ijkl}\sigma_{kl} , \tag{1.3}$$

where C_{ijkl} and S_{ijkl} are the *stiffness* and *compliance* tensors, respectively. [2] Symmetry of the crystals lowers the number of independent components [14]. For cubic crystals and isotropic solids, the stiffness reads

$$
\begin{pmatrix}
C_{11} & C_{12} & C_{12} & 0 & 0 & 0 \\
C_{12} & C_{11} & C_{12} & 0 & 0 & 0 \\
C_{12} & C_{12} & C_{11} & 0 & 0 & 0 \\
0 & 0 & 0 & C_{44} & 0 & 0 \\
0 & 0 & 0 & 0 & C_{44} & 0 \\
0 & 0 & 0 & 0 & 0 & C_{44}
\end{pmatrix} ,
\tag{1.4}
$$

where the Voigt notation has been employed to group indexes in pairs: $xx \to 1$, $yy \to 2$, $zz \to 3$, $yz \to 4$, $zx \to 5$, $xy \to 6$. In the case of an isotropic solid $2C_{44} = C_{11} - C_{12}$: thus only two elastic parameters are required to characterize the isotropic solid. Often, instead of C_{11} and C_{12} the Young modulus E and the Poisson ratio ν are given, as they are more accessible experimentally. Any elastic parameter can be obtained combining two other parameters [17].

The net force acting on dV along x is

$$
F_x = \left(\frac{\partial \sigma_{xx}}{\partial x} + \frac{\partial \sigma_{yx}}{\partial y} + \frac{\partial \sigma_{zx}}{\partial z} \right) dV ;
\tag{1.5}
$$

similar relations hold along y and z. After some manipulation [18], the Newton equation per unit volume reads

$$
\rho \frac{\partial^2 u_i}{\partial t^2} = C_{ijkl} \frac{\partial^2 u_k}{\partial x_j \partial x_l} ,
\tag{1.6}
$$

where ρ is the average density. The displacement **u** propagates in the material in the form of a wave.

Consider a plane-wave propagating along the $(1\,0\,0)$ direction in a cubic solid (the same holds for an isotropic solid at arbitrary propagation direction). Three independent solutions exist, identified by their polarization [19]: a *longitudinal* wave, where only ϵ_{xx} is nonzero, propagates via local compression/expansion with velocity $v_L = \sqrt{C_{11}/\rho}$; two orthogonal *transverse* waves, where either ϵ_{xy} or ϵ_{xz} are nonzero, propagate via shear strains with velocity $v_T = \sqrt{C_{44}/\rho}$. For other propagation directions, as well as for other crystal structures, more complicated combinations of the compliance coefficients determine the velocity; moreover the polarization states can be not well defined, resulting in a mixture of longitudinal and transverse character [14]. Note that the velocity in this derivation does not depend on the wavevector: the dispersion relation is linear.

Acoustic waves in semi-infinite media

At the free surface of a semi-infinite solid half of the short-range restoring forces are missing: the acoustic modes are modified accordingly. Consider the free surface as the (x, y) plane, the propagation direction of the surface wave being along x; the (x, z) plane is dubbed *sagittal* plane. The boundary condition at the free surface is $\sigma_{zz} = \sigma_{zx} = \sigma_{yz} = 0$, namely no stress is applied from the vacuum.

---

[2]For isotropic solids, this linear relation reads $\epsilon = \sigma/E$, where E is the Young modulus, and both stress and strain are referred to the same axis. This means that $1/E = S_{1111}$; however, $E \neq C_{1111}$ as a matrix inversion has to be performed.
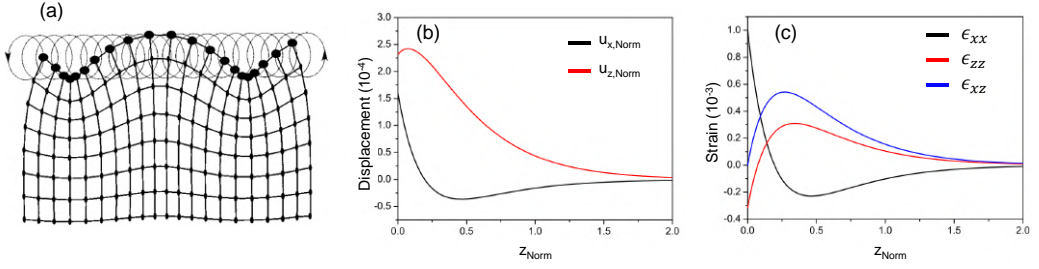
Figure 1.2: (a) Schematic strain and particle displacement for a RSAW. Adapted from [22]. (b-c) Displacement [panel (b)] and strain [panel (c)] associated with a RSAW in soda lime glass as a function of the depth into the bulk; the depth is measured in units of Λ, as well as the displacements $u_{i,\text{Norm}} = u_i/\Lambda$. Typical displacements are in the angstrom range. Adapted from [23].

Plane-wave solutions to Eq.1.6 with this boundary condition result in a new acoustic mode, known as Rayleigh Surface Acoustic Wave (RSAW) [20, 21]; see Fig.1.2(a). This mode is a surface mode: the displacement is exponentially confined at the surface, meaning that its amplitude decays along z with the analytic dependence $u_x(z) \propto e^{-\gamma_u |z|}$. The decay length is approximate equal to the wavelength: $1/\gamma_u \approx \Lambda$. Solving Eq.1.6 for RSAW, the details of the associated displacement field are obtained. Both u_x and u_z are simultaneously oscillating, leading to a mixed polarization state, partially longitudinal and partially transverse along z. The two components are $\pi/2$ out of phase: the resulting motion is elliptical, confined in the sagittal plane [Fig.1.2(a-b)]. In terms of strain, the only non-zero components are ϵ_{xx}, ϵ_{zz}, and ϵ_{zx}. The leading component is ϵ_{xx}, at least close to the surface [Fig.1.2(c)]: this is of large relevance for the modeling of magneto-elastic coupling involving RSAW. The approximate phase velocity is $v_{\text{RSAW}} \approx (1-1/24)v_T$, thus lower of any bulk acoustic velocity; typical velocities for metals and oxides are in the range $2-4$ km/s [18]. The RSAW is linearly dispersing in the low-wavevector range, as for other acoustic excitations; at the boundary of the Brillouin zone deviation from the linear trend is observed [20]. Finally, the presented characteristics hold for a cubic crystal or isotropic solid. For other anisotropic crystals, three displacements are in general mixed, so that the motion is not restricted to the sagittal plane; moreover, the velocity depends on the propagation direction, and the amplitude decay in the bulk of the sample does not follow a simple exponential trend.

Supported and unsupported films

When a suspended membrane or a thin film on a substrate are considered, the topic of acoustic dynamics becomes increasingly complex. Specialized literature is available [16, 21]: here some general characteristics are reported, that help in understanding the experiments reported in the following chapters.

- Instead of only the RSAW, in a film a whole spectrum of surface acoustic modes exists, differing in frequency and spatial distribution of the displacements; if they have similar polarization to RSAW, they are named pseudo-RSAW, or Sezawa modes.

- A new class of waves appears, dubbed Love waves; they are in-plane shear waves, with strain confined in the surface plane. An infinite spectrum of Love waves
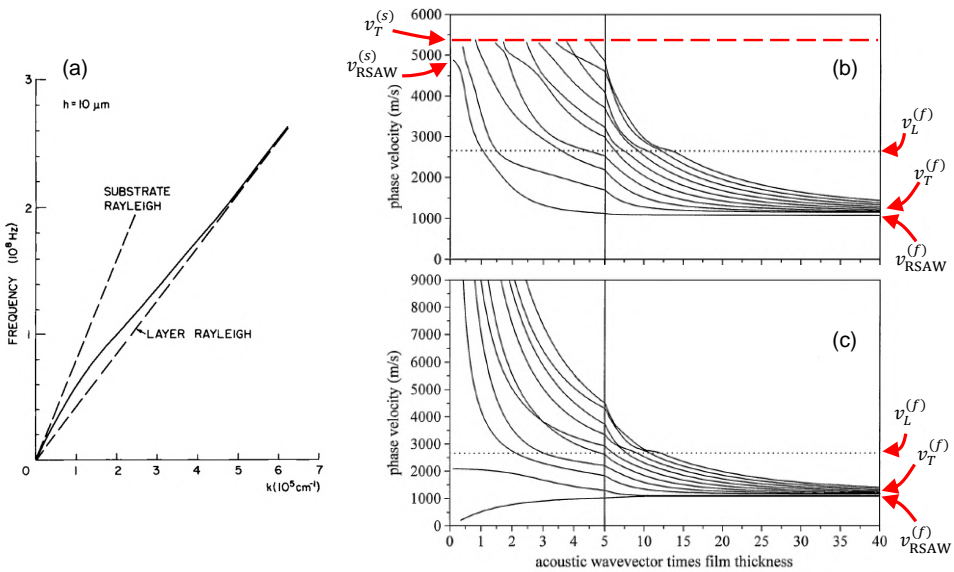
Figure 1.3: (a) Dispersion relation for RSAW for 10 μm of ZnO on Si: the dispersion is approximately linear in the small- and large-wavevector limits. From [21]. (b-c) Phase velocity of the first 10 modes in a polymeric thin film as a function of the product hk; the film is deposited on Si [panel (b)] or free-standing [panel (c)]. The phase velocities of the bare substrate or film determine the limit values of the modes. The red dashed line in panel (b) indicates the threshold of leaky modes. Adapted from [16].

only is supported if transverse velocity of the film $v_T^{(f)}$ is smaller than that of the substrate $v_T^{(s)}$ [21]. [3]

- The velocity v_{SAW} of SAWs (and thus also the frequency) only depends on the product hk, where h is the film thickness and $k = 2\pi/\Lambda$ is the acoustic wavevector.

- The dispersion relation of these modes is no more linear, featuring variations as a function of the wavevector as shown in Fig.1.3(a).

- A residual stress $\sigma_{ij}^{(r)}$ is often present, especially for film produced via epitaxy on crystalline substrate; this affects the low-wavevector spectrum [16].

In Fig.1.3(b-c) the dependence of v_{SAW} on the product hk is reported for the first ten acoustic modes. The addressed system is an isotropic polymer, but the observed phenomenology can be extended to different materials. In panel (b) the results when the polymer is deposited on Si substrate are shown: the lowest mode is the RSAW, the others are Sezawa modes. For small hk (Λ large compared to the film thickness) the lowest mode approaches the RSAW of the unloaded substrate $v_{\text{RSAW}}^{(s)}$: strictly speaking, only this mode is surface-bounded in this limit. The other modes become leaky (see below) if their velocity approaches the substrate transverse velocity $v_T^{(s)}$: in this configuration they couple to bulk modes and start radiating away from the surface [21]. In this limit

---

[3]In isotropic overlayer/substrate systems RSAW and Love waves are completely decoupled; in the general anisotropic case surface excitations with mixed polarization are present.

the thin film basically does not affect the elastic properties of the substrate. For large hk (Λ small compared to the film thickness) the lowest mode converge to the RSAW of the bare film material $v_{\text{RSAW}}^{(f)}$, while the Sezawa modes converge to the transverse velocity of the film $v_T^{(f)}$. In this limit the substrate has a negligible effect: the acoustic dynamics entirely takes place in a region far away from the buried interface. The dependence for intermediate values depends on the details of the elastic properties of substrate and film materials; generally a knee is observed when crossing the longitudinal film velocity $v_L^{(f)}$. Note that in the discussed case $v_T^{(f)} < v_T^{(s)}$: this is known as substrate loading condition. In the opposite case $v_T^{(f)} > v_T^{(s)}$, known as substrate stiffening condition, the RSAW exists only for low hk, while Sezawa modes are not present. The RSAW velocity is equal to $v_{\text{RSAW}}^{(s)}$ at $hk = 0$, increases with hk until it reaches $v_T^{(s)}$: in this condition the wave becomes leaky and is no more a confined surface wave at larger hk.

In panel (c) the case of a free-standing film is shown. In this case all the modes are strictly guided, since no energy is radiated away; in this configuration the modes are known as Lamb waves. For large hk again the lowest mode converges to the RSAW of a thick slab of the material; the higher modes converge to the transverse velocity $v_T^{(f)}$. In this limit, the system can be seen again as a semi-infinite medium. For small hk the lowest mode approaches the value $\sqrt{\sigma_{ij}^{(r)}/\rho}$. This corresponds to the sound velocity for a tensioned drumhead, as expected (while if no residual stress is present, this mode approaches zero velocity). [4]

As mentioned above, in some configurations a mode can become *leaky*, meaning that it is only approximately bounded to the surface (or interface). Leakage to the bulk takes place for specific combinations of wavelength, frequency, polarization, and propagation direction that match a bulk acoustic mode, while not allowing a genuine solution to Eq.1.6 with the surface boundary conditions. The coupling can be enhanced at specific leakage angles with respect to the surface [24]: for this reason, the leaky modes are known also as *surface skimming* modes. Surface leaky modes and the respective bulk modes are basically indistinguishable, as they share the same characteristics (polarization, frequency, dispersion). A leaky wave decades exponentially upon propagation, not only as a consequence of ordinary losses, but also as due to penetration into the bulk.

For what concerns the experiments in the following chapters, the thickness of the films investigated is much smaller than the acoustic wavelength: $hk < 0.05$ in all cases. Thus the observed acoustic dynamics is solely determined by the elastic properties of the substrates employed. Moreover, simple configurations are studied, namely isotropic systems (both for film and substrate) or cubic crystals with acoustic excitation along a $\langle 1\,0\,0\rangle$ direction: thus only the fundamental RSAW wave is expected, out of the rich zoology of SAWs here presented. Also a surface skimming wave was observed (see Ch.3), degenerate to a bulk longitudinal wave.

A special discussion is required for nanostructured systems. Considering an array of nanostructures deposited on a substrate, the acoustic properties are largely hybridized between localized modes within each nanostructure and extended modes involving the substrate. The boundary between these two cases is not sharp; this will be discussed in more detail in Ch.4 and 5, in connection to surface phononic crystals.

---

[4]This discussion naturally extends to buried interfaces: localized interface acoustic modes are supported, whose displacement is exponentially confined in both the adjacent half spaces. These waves are dubbed Stoneley waves at solid-solid interface and Scholte waves at liquid-solid interface. Peculiar dispersion, amplitude decay and polarization are exhibited [21].

1.2 Magnetic excitations in solids

In magnetic excitations the quantization of the modes is likewise superseeded by a continuum approximation that is appropriate when addressing small wavevector dynamics; the excitations will be dubbed interchangeably as SWs or magnons. Throughout this thesis, SI units are used; note that large part of the scientific community working on ferromagnets and resonance phenomena elaborates in cgs units. [5] To make clear the starting point, the constitutive equation linking the magnetic fields and the magnetization is $\mathbf{B} = \mu_0 \left(\mathbf{H} + \mathbf{M} \right)$, where μ_0 is the vacuum permeability, $\mathbf{M}$ is the magnetic moment per unit volume and $\mathbf{H}$ is the magnetic field; also the field $\mathbf{B}$ will be dubbed as the magnetic field, even though it is strictly the magnetic flux density. [6] Below the Curie temperature T_C, a ferromagnetic material exhibits spontaneous ordering of the elementary magnetic moments, resulting in a finite value for $\mathbf{M}$ even in absence of any external field. In $3d$ ferromagnets, which are considered in this work, the elementary magnetic moment $\mathbf{m}$ is primarily due to the spin angular momentum via $\mathbf{m}_s = -g_s \mu_B \mathbf{s}$, where $\mu_B = q_e \hbar / (2m_e) \approx 9.3 \cdot 10^{-24} \ \mathrm{Am^2}$ is the Bohr magneton, $g_s \approx 2$ is the Landé factor for electron spin and $\mathbf{s}$ is the spin angular momentum (adimensional as it is assumed as measured in units of $\hbar$). For the orbital motion (largely quenched in $3d$ ferromagnets [2]), a similar expression holds: $\mathbf{m}_l = -g_l \mu_B \mathbf{l}$, with $g_l = 1$ and $\mathbf{l}$ the orbital angular momentum.

For both spin and orbital magnetic moment, angular momentum is at the very core of magnetic properties of materials: for this reason the fundamental dynamical process for a magnetic moment is precession. The magnetization $\mathbf{M}$ in a magnetic field $\mathbf{H}$ is subject to a torque $\boldsymbol{\tau} = \mu_0 \mathbf{M} \times \mathbf{H}$ which determines precession around the field axis following the mechanical equation

$$\frac{d\mathbf{M}}{dt} = -\gamma \mu_0 \mathbf{M} \times \mathbf{H} \, , \qquad (1.7)$$

where $\gamma = g_s \mu_B / \hbar = q_e g_s / (2m_e)$ is the magnetomechanical ratio for an electron spin ($\gamma / 2\pi \approx 28 \ \mathrm{GHz/T}$). The precession frequency, known as the Larmor frequency, is $\omega_L = \gamma \mu_0 H$; to give an order of magnitude, a Bohr magneton in a 1 T field completes a full precession in 36 ps.

Eq.1.7 implicitly assumes a macrospin approximation: the elementary magnetic moments are averaged in a volume much larger than the unit cell, and the resulting dynamics is assumed as due to the cumulative magnetic moment. This approximation also holds for non-uniform and time-dependent magnetization dynamics, as long as (i) small enough portions of the sample can be identified, where the magnetization can be assumed as homogeneous, and (ii) the addressed timescale is much longer than the spin-spin exchange interaction, which is typically in the tens of femtoseconds range; in other words, the magnetic moments feature collective dynamics described with a classical averaged magnetic moment *if* each spin site has enough time to feel any variation of the neighbour, and to adequate its direction accordingly [1, 25]. Throughout this thesis, these conditions are largely met. The macrospin approximation is at the basis of the calculations of magnetization dynamics via micromagnetic models [26].

A summary of the energy terms relevant to magnetization dynamics is now given; further details can be found in literature [1, 2, 27].

---

[5]The book from Stöhr and Siegmann [1] employs SI units but with a different definition of the magnetic moment $\mathbf{m} = \mu_0 I A \hat{\mathbf{n}}$, with I, A, and $\hat{\mathbf{n}}$ indicating current, loop area, and surface normal, respectively; in SI units usually the factor μ_0 is omitted, thus some discrepancies in the displayed equations can be found.

[6]They are all axial vectors likewise angular momentum $\mathbf{L}$, and are parity even and time-reversal odd.

- **Exchange interaction**. It is the interaction at the basis of the formation of spontaneous magnetic order below T_C in metallic $3d$ ferromagnets. The resulting Heisenberg Hamiltonian can be written as $\mathcal{H}_{\text{exc}} = -\sum_{ij} J_{ij}\mathbf{s}_i \cdot \mathbf{s}_j$. In ferromagnets it couples neighbouring spins $\mathbf{s}_i$ via a coupling $J_{ij} > 0$: collinear configuration is favoured. This interaction is isotropic, as the only variable is the relative angle between the spins. In a macrospin framework it results in a free energy density contribution [26] $F_{\text{exc}} = A/M_s \left[(\nabla M_x)^2 + (\nabla M_y)^2 + (\nabla M_z)^2 \right]$, where M_s is the saturation magnetization and A is the exchange stiffness, measured in energy per length (relations between A, J_{ij} and the spin wave stiffness D_{sw} are given in [28]). A typical value is $A = 10$ pJ/m, resulting in energy density $10^3 - 10^5$ kJ/m^3, or equivalently $0.1 - 10$ meV/atom.

- **Magneto-Crystalline Anisotropy (MCA)**. This term sets a preferential axis for **M** given the crystal structure of the material. Ultimately it stems from the Spin-Orbit Coupling (SOC), which gives a preferential direction to the magnetic moments depending on the anisotropy of the orbitals. Typically the free energy density is indicated as $F_{\text{MCA}} = -K_u/M_s \left(\mathbf{M} \cdot \hat{\mathbf{u}} \right)^2$ in the case of a magnetization Easy Axis (EA) identified by the unit vector $\hat{\mathbf{u}}$; K_u is the uniaxial MCA constant. More involved expressions containing combinations of the director cosines are required to generally describe MCA in crystals; in polycrystalline samples, it can be usually neglected as the energy contribution averages to zero for random orientation of the grains. Note that the anisotropy constants strongly depend on temperature. Hard permanent magnets like SmCo alloys have strong MCA around 10^4 kJ/m^3, *i.e.* about 1 meV/atom; typical values for $3d$ metals are much lower, around 5 kJ/m^3 (0.5 μeV/atom) for Ni, somewhat larger (400 kJ/m^3, 40 μeV/atom) for Co along the c axis [28, 29].

- **Shape anisotropy**. At the boundary of a medium, the field **H** is discontinuous: this sets the magnetization at the boundary as sources of a demagnetizing field $\mathbf{H}_d$ acting inside the solid and antiparallel to **M** [1, 2]. Basically this is a self-interaction of **M** with dipolar origin, generally complicated to be solved (a special case is discussed in Ch.4). The result is that an anisotropy builds up, strongly dependent on the shape of the sample: in thin films an easy magnetization plane in the film surface results, while in prolate cylindrical systems an EA along the cylinder axis results. The involved energy depends on the dimension of the object, becoming more and more relevant as the size lowers. Generally speaking the shape anisotropy gives an energy term $F_{\text{sh}} = -\mu_0 \mathbf{M} \cdot \mathbf{H}_d$; the detailed expression depends on the explicit form (if it exists!) for $\mathbf{H}_d$.

- **Zeeman energy**. This is the usual energy term arising from magnetostatic interaction with an external magnetic field: $F_Z = -\mu_0 \mathbf{M} \cdot \mathbf{H}_{\text{ext}}$. The equilibrium condition corresponds to alignment of the magnetization to the field. For an order of magnitude, Zeeman energy for a Bohr magneton in a 1 T field is about 50 μeV.

- **Dipolar interaction**. Besides the demagnetizing field, if **M** is not uniform long range dipole-dipole interactions come at play, which decay with the cube of the distance. This interaction only is present if $\nabla \cdot \mathbf{M} \neq 0$, namely when there is a spatial modulation in the magnetization.

- **Magneto-Elastic Coupling (MEC)**. Interaction between the magnetic and elastic

degrees of freedom adds a further energy term. This is the main subject of this thesis, and it will be discussed in details in the next section.

- **Other terms**. In specific materials, other contributions can intervene. For example, the Dzialoshinskii-Moriya interaction is an antisymmetric exchange favouring orthogonal alignment of adjacent spins: in competition with the other interactions, it possibly stabilizes complicated spin structures like spin helices and skyrmions. In some crystal classes, a sizeable magneto-electric coupling arises, whereas an electric field acts on the magnetization state [18]. In magnetic oxides superexchange and double exchange contributions can be the relevant coupling mechanism, while in metallic ultrathin heterostructures Ruderman–Kittel–Kasuya–Yoshida (RKKY) interaction can play a relevant role [1]. All these terms are absent in the experiments discussed in this thesis.

Each of these terms can contribute to the overall free energy density F. The ground magnetic state is obtained by minimizing F. It is useful to condense all the contributions into a single *effective* magnetic field, obtained from F with a thermodynamical approach:

$$\mathbf{H}_{\text{eff}} = -\frac{1}{\mu_0}\frac{\delta F}{\delta \mathbf{M}} \ . \tag{1.8}$$

Precession dynamics in the case of different coexisting interactions is described inserting this field into Eq.1.7.

It is common experience that a magnetized body tends to align to a magnetic field: a compass needle oriented along x changes orientation if a magnetic field along z is switched on. This requires the introduction of dissipation. In the alignment of the compass needle there is variation of energy (it lowers for proper alignment) and of angular momentum, recalling that the magnetization is always accompanied by a coaxial angular momentum. These dissipations are phenomenologically accounted for in the Landau-Lifshitz-Gilbert (LLG) equation:

$$\frac{d\mathbf{M}}{dt} = -\gamma\mu_0\left(\mathbf{M}\times\mathbf{H}_{\text{eff}}\right) + \frac{\alpha}{M_s}\left(\mathbf{M}\times\frac{d\mathbf{M}}{dt}\right) \ , \tag{1.9}$$

where α (adimensional) is the so-called Gilbert damping. [7] Few comments follow.

- Dissipation is modeled via adding a *frictional* torque (second term at right-hand side of Eq.1.9). While the Larmor torque points towards the precession plane, the frictional torque at any instant points towards the equilibrium axis [see Fig.1.4(a-b)]: thus it effectively describes the tendency of the magnetization to align to $\mathbf{H}_{\text{eff}}$. The frictional torque is proportional to the precession velocity, just like a frictional force in dynamics is proportional to the linear velocity; this means that the quantity α is a proper material-dependent quantity, while the actual decay time τ for a precessing motion depends on the Larmor frequency. In a thin film with out-of-plane (OOP) magnetization (so that demagnetizing field plays no role), the relation is $\tau = 1/\alpha\omega_L$. More complicated relations hold in other cases [30].

---

[7]An almost equivalent form is

$$\frac{d\mathbf{M}}{dt} = -\gamma\mu_0(\mathbf{M}\times\mathbf{H}_{\text{eff}}) - \frac{\lambda_G}{M_s^2}\mathbf{M}\times(\mathbf{M}\times\mathbf{H}_{\text{eff}}) \ , \tag{1.10}$$

where λ_G is a Gilbert relaxation frequency. This formulation is much easier to implement numerically as it appears already in normal form. The simulated behaviour shown in Fig.1.4 has been calculated with this form.
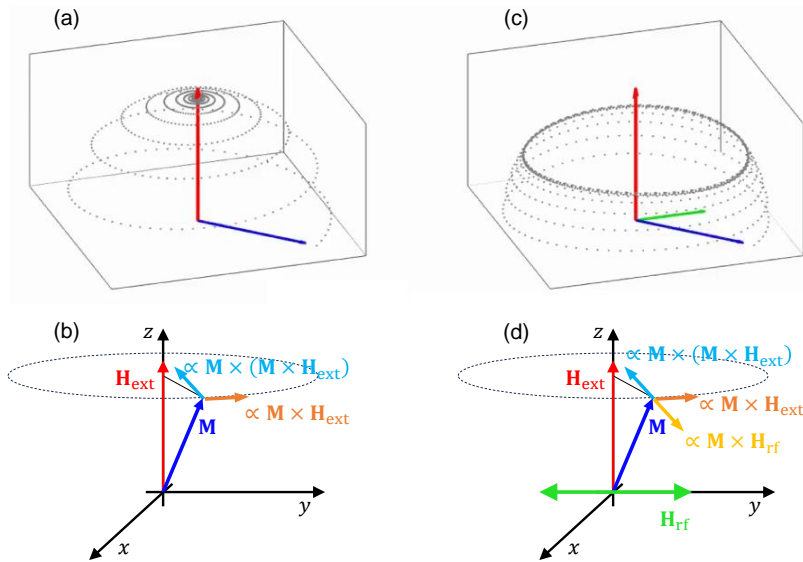
Figure 1.4: (a-b) Dynamics of the magnetization according to the LLG equation (Eq.1.9). The magnetization **M** (blue arrow) precesses around an external magnetic field $\mathbf{H}_{\text{ext}}$ (red arrow) under the action of the Larmor torque ($\propto \mathbf{M} \times \mathbf{H}_{\text{ext}}$, orange arrow). Because of dissipation, a frictional torque [$\propto \mathbf{M} \times (\mathbf{M} \times \mathbf{H}_{\text{ext}})$, light blue arrow] forces **M** to describe a spiralling trajectory [dotted line in panel (a)] until it aligns to the field. (c-d) Dynamics of the magnetization adding a radio-frequency oscillating term $\mathbf{H}_{\text{rf}}$ (green arrow) orthogonal to the static field. The additional torque ($\propto \mathbf{M} \times \mathbf{H}_{\text{rf}}$, yellow arrow) balances the frictional torque and, after an initial transient, **M** keeps precessing on a stationary orbit. This is the principle of magnetic resonance spectroscopy with the width (in frequency) of the resonance peak representing the dissipative terms.

- In the phenomenological coefficient α, all the interactions responsible for dissipation of energy and angular momentum are included: scattering with defects, emission of finite-wavevector modes, magnetic-dipole radiation in free space etc.

- $\mathbf{H}_{\text{eff}}$ depends on **M** (see Eq.1.8): this means that during the precession $\mathbf{H}_{\text{eff}}$ changes as well. Thus the LLG equation is only meaningful if it is within a thermodynamical limit, as discussed in connection with the macrospin approximation. Seen from a computational point of view, it must be meaningful to compute at any instant $\mathbf{H}_{\text{eff}}$ in a given configuration, then apply Eq.1.9 to make **M** evolve, then compute again the new $\mathbf{H}_{\text{eff}}$ etc.

Ferromagnetic resonance

If the external field $\mathbf{H}_{\text{ext}}$ is not static but also contains a time-dependent component, the framework does not change: $\mathbf{H}_{\text{eff}}$ is computed via Eq.1.8 and the dynamics is obtained solving Eq.1.9. A special condition occurs when the time-dependent contribution is a harmonic field $\mathbf{H}_{\text{rf}}$ at angular frequency ω_L, typically in the radio-frequency (rf) range. In this case a resonance phenomenon takes place, as the additional torque supplied by $\mathbf{H}_{\text{rf}}$ points away from the z axis [see Fig.1.4(c-d)]: the magnetization can be set into stable

precession, with perfect balance of the frictional Gilbert torque and the externally supplied torque. The torque is maximized if the rf field is orthogonal to the static component of $\mathbf{H}_{\text{eff}}$. This is the condition of Ferromagnetic Resonance (FMR), a technique largely applied to investigate the magnetostatic properties of ferromagnetic materials and nanostructures [31, 32]. Extensions of FMR exist, such as electron paramagnetic resonance (EPR) appropriate for non-ferromagnetic systems and capable of precise quantification of impurities and investigation of local field environment; Spin Wave Resonance (SWR), which is basically FMR extended to standing SW modes across the thickness of a ferromagnetic slab; nuclear magnetic resonance (NMR), where all this started from, which employs sometimes different concepts (and of course probes different interactions) but it basically shares the same conceptual framework.

Experimentally, two approaches are employed. In the first case, a rf electromagnetic cavity is employed; via a waveguide, a rf wave providing $\mathbf{H}_{\text{rf}}$ is injected and resonates with narrow bandwidth at a single cavity mode. The sample is placed in a cavity antinode, and $\mathbf{H}_{\text{ext}}$ is tuned in strength until the sample is observed to strongly absorb the rf intensity, meaning that ω_L has been swept to the same frequency of the cavity mode. In the second case, $\mathbf{H}_{\text{ext}}$ is fixed, and the sample is mounted on a rf chip that allows generations of tunable rf magnetic fields: typically it is a stripline, where AC current is injected, thus generating an AC field. The frequency of the injected current is tuned until strong absorption is observed, meaning that the rf field has reached ω_L. In the former case only one resonance point can be obtained per cavity (unless higher cavity modes are employed); in the latter case, the resonance condition can be observed in a continuous band of frequencies: this technique is sometimes dubbed Broadband FMR (B-FMR).

In both cases the wavelength of the rf field is much larger than the sample dimensions: this means that only uniform precession throughout the sample can be probed, or at most odd-order Perpendicular Standing SWs (PSSWs) to which the rf field has a finite coupling along the film thickness. A special case of FMR analytical dependence is elaborated in Ch.4; all these and much more details on the potentialities of FMR techniques can be found in literature [31]. As a final note, it is worth stressing that in the conventional FMR approaches the additional time-dependent torque is provided by a an electromagnetic wave, *i.e.* by photons. The discussed physical process, though, is not restricted to photon-driven FMR, but can be extended to other effective rf fields. This is the approach discussed in Sect.1.3, where an effective rf magnetic field results from MEC for time-dependent strain provided by SAWs.

Magnon spectrum in ferromagnets

Of the vast topic of SW spectrum in ferromagnets, only two highlights are here presented, relevant for the experiments discussed in the rest of this thesis: the case of the bulk isotropic ferromagnet, and the case of the ferromagnetic slab, appropriate for thin films.

The bulk isotropic ferromagnet. To get a glimpse of the general trends of SW spectra, we start considering an infinite isotropic ferromagnet where only exchange, Zeeman and dipolar interactions are at play. The SW spectrum reads [33]

$$\omega_{\mathbf{k}} = \gamma\mu_0 \sqrt{\left(H_{\text{ext}} + \frac{2A}{\mu_0 M_s}k^2\right)\left(H_{\text{ext}} + \frac{2A}{\mu_0 M_s}k^2 + M_s \sin^2\theta_{\mathbf{k}}\right)}, \qquad (1.11)$$

where $k = |\mathbf{k}|$ is the absolute value of the SW wavevector and $\theta_{\mathbf{k}}$ is the angle between
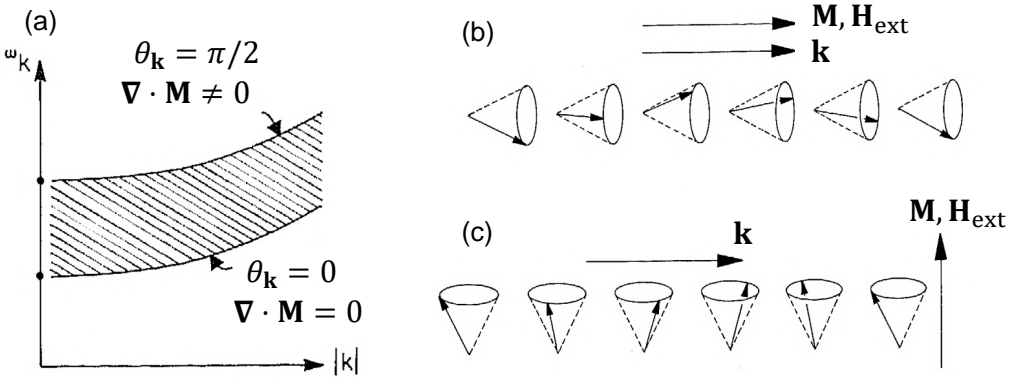
Figure 1.5: (a) Schematic dispersion relation for exchange SWs. The general trend is parabolic, as dictated by the exchange coupling. The modes cover a manifold of possible state, identified by the angle $\theta_{\mathbf{k}}$ between the wavevector $\mathbf{k}$ and the external field $\mathbf{H}_{\text{ext}}$. (b-c) Sketch of SWs propagating along $\mathbf{H}_{\text{ext}}$ [*i.e.* $\theta_{\mathbf{k}} = 0$, panel (b)], and propagating orthogonal to $\mathbf{H}_{\text{ext}}$ [*i.e.* $\theta_{\mathbf{k}} = \pi/2$, panel (c)]. The two configurations have different dipolar energy, as quantified by $\boldsymbol{\nabla} \cdot \mathbf{M}$. Adapted from [33].

$\mathbf{H}_{\text{eff}}$ and $\mathbf{k}$.

The dispersion is approximately parabolic in the large-k limit, where the SWs are called *exchange* waves since the leading term is proportional to the exchange stiffness A. This is schematically shown in Fig.1.5. The lowest band corresponds to $\theta_{\mathbf{k}} = 0°$, and its analytical dependence is $\omega_{\theta_{\mathbf{k}}=0} = \omega_L + \gamma 2Ak^2/M_s$: the external field shifts rigidly upwards the band. For this band the static component of $\mathbf{M}$ is along $\mathbf{k}$: thus $\boldsymbol{\nabla} \cdot \mathbf{M} = 0$ and no dipolar interactions are at play [Fig.1.5(b)]. The precession cone is circular and the dispersion is exactly parabolic at any k. The highest band corresponds to $\theta_{\mathbf{k}} = \pi/2$. In this case for $k \neq 0$ dipolar interactions are present, as $\boldsymbol{\nabla} \cdot \mathbf{M} \neq 0$ [Fig.1.5(c)]. As a result (i) the SW has larger energy (upward shift of the branch given by the term $M_s \sin^2 \theta_{\mathbf{k}}$), and (ii) the precession cone distorts from circular to elliptical (with the major axis perpendicular to $\mathbf{k}$). In the extreme limit of large wavevector, all contributions are negligible as compared to the exchange term, and the SW spectrum is isotropic and parabolic.

The isotropic ferromagnetic slab. In the opposite limit of small wavevector, the finite extension of the ferromagnetic sample must be taken into account via shape anisotropy effects. In this case the SWs are known as *magnetostatic* modes: despite the name they are not static modes, but real waves, mostly with propagating character. The name stems from the fact that their dynamics is largely determined by the magnetostatic parameters of the sample (namely shape and aspect ratios of the ferromagnet and possible MCA); since oftentimes the largest effect is given by the dipolar interactions as due to demagnetizing fields, they are also known as *dipolar* waves. This is the appropriate model for the SWs investigated in this thesis, as the typical wavevectors addressed are in the few inverse micron range.

Consider a model of an isotropic slab of thickness h, free at both surfaces. The geometry of the system is depicted in Fig.1.6(a): the normal to the upper surface is along z, the magnetic field is applied in plane (IP) along the x axis. To start with, the exchange stiffness is neglected. If the slab is thin (namely if $h \ll 1/k$), it is convenient to treat separately the dispersion for out of plane (OOP) and IP wavevector. The OOP wavevector
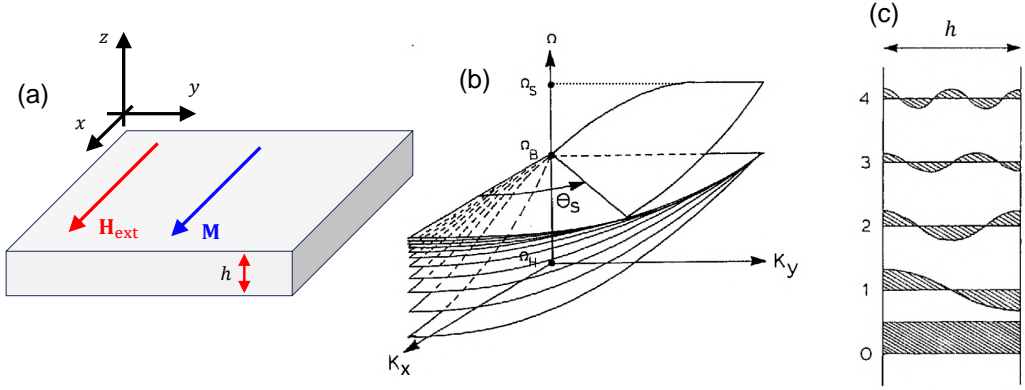
Figure 1.6: (a) Scheme of the configuration discussed for the isotropic slab. A ferromagnet of thickness h lies in the (x, y) plane; it is magnetically saturated along the x direction by an external field $\mathbf{H}_{\text{ext}}$. (b) Normalized IP dispersion relation for dipolar SWs. Each sheet represents the dispersion for a specific value of OOP k_z. All the modes are degenerate at $k = 0$, where the dynamics corresponds to the uniform precession probed by FMR. Along k_x the modes exhibit negative dispersion, while they are all degenerate and non-dispersive along k_y. For $\theta_S < \theta_{\mathbf{k}} < \pi/2$ the surface Damon-Eshbach mode arises, with frequency higher than all the other modes. The normalized frequencies Ω_H, Ω_B, and Ω_S are defined in the text. (c) Distribution along the slab thickness of the first five OOP modes in case of unpinned surface magnetization. Adapted from [33].

component k_z is no longer a continuous variable but takes on discrete values, as appropriate for quantized waves in a confined system [Fig.1.6(c)]. The boundary conditions for $\mathbf{M}$ (namely pinned or unpinned magnetization at the surfaces, depending mostly on the morphological quality of the surface) lead to different sets of solutions: for example, for unpinned magnetization, the lowest mode is truly uniform across the depth of the slab, while for pinned surfaces it features two nodes at the boundary; similar discussion holds for the higher modes. However, the core of the following discussion is unaffected by the boundary conditions.

The IP dispersion is a set of two-dimensional surfaces, whose frequency in Fig.1.6(b) is plotted as a function of the IP wavevector. The slab is assumed as magnetically saturated, *i.e.* $\mathbf{M} \parallel \mathbf{H}_{\text{eff}} \parallel \hat{\mathbf{x}}$. The normalized units used in the reported figure are appropriate to model the general trend of the dispersion: $\Omega_H = H_{\text{eff}}/M$, $\Omega_B = \sqrt{\Omega_H(\Omega_H + 1)}$, $\Omega_S = \Omega_H + 1/2$. Each sheet in Fig.1.6(b) corresponds to a different value of k_z, namely a different spatial distribution of the SW amplitude across the slab thickness. Together, the sheets correspond to the manifold depicted in Fig.1.5(a), in the low-k region. For $\mathbf{k} \parallel \mathbf{H}_{\text{eff}}$ the modes are non-degenerate and show negative dispersion, *i.e.* they decrease in frequency for increasing wavevector. For $\mathbf{k} \perp \mathbf{H}$ all the modes are degenerate and the frequency does not depend on the wavevector. In all cases, the value Ω_B for $\mathbf{k} = 0$ corresponds to the uniform mode as probed in FMR experiments.

An additional sheet exists for $\theta > \theta_S$: it is known as the Damon-Eshbach (DE) surface mode. This mode is observed most easily for $\mathbf{k} \perp \mathbf{H}_{\text{eff}}$, where it reaches the highest frequency Ω_S at large enough wavevector. Notably, DE mode exhibits non-reciprocal character: the propagation direction is given by $\mathbf{H}_{\text{eff}} \times \hat{\mathbf{n}}$, where $\hat{\mathbf{n}}$ is the external normal unit vector. Thus for the geometry of Fig.1.6(a) the upper surface supports a DE mode propagating to the left while the lower surface supports a DE mode propagating to the
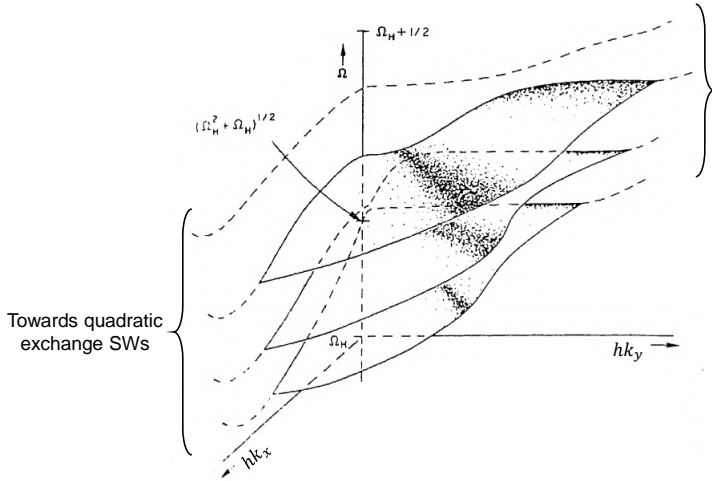
Figure 1.7: Dispersion relation for exchange-dipolar SWs. The exchange interaction modifies the spectrum of the dipolar SWs: the sheets are not degenerate at $k = 0$, nor for $\theta_\mathbf{k} = \pi/2$. Moreover, at large k the sheets start swinging up quadratically, as required for exchange-dominated SWs. The DE mode now is not distinguishable as it crosses all the subsequent sheets (the change of gradient in the knees highlighted by the black dots is the hybridization with the DE mode). Adapted from [33].

right. The mode is localized to the surface: its precession amplitude decay in the bulk with a decay constant proportional to k_y for pure transverse propagation; if θ is reduced from $\pi/2$, the decay constant increases until diverges for $\theta = \theta_S$. In the experiment discussed in Ch.3, SWs at small θ are addressed: thus the DE mode was not observed. The case of OOP magnetized slab is reported in literature [33, 34] and is not relevant for the experiments discussed in this thesis.

   If now the exchange interaction is switched on again, the so-called *exchange-dipolar* waves are obtained (see Fig.1.7): the name suggests that they are SWs with partial exchange and partial dipolar character. The most apparent effect is that at large enough k each frequency surface swings up parabolically, following in the limit of large k the trend of bulk SWs in an infinite medium [Fig.1.5(a)]. Moreover, if the exchange coupling is present, the quantized modes along z are no longer degenerate since an extra exchange term is added: this separates vertically the various sheets. This means that (i) at $k_{IP} = 0$ the degeneracy is lifted, *i.e.* sheets for different k_z start from different frequencies: this is the physical origin of the signals observed in SWR (see above); (ii) the degeneracy for $\mathbf{k} \perp \mathbf{H}$ is lifted as well; (iii) the DE mode is somehow shared between different sheets and it is not possible anymore to isolate it. In the limit of large h, the eigenvalue sheets become a continuum of modes and the variable k_z a continuous variable as for the infinite isotropic ferromagnet. In the dipolar-exchange regime, a key characteristic is that after the decrease in frequency at small k, there is a bending upwards due to exchange that dominates at large k. This means that in the low-k region the dispersion relation has a negative slope, so a negative group velocity: they propagate backward with respect to the wavevector. For this reason the dipolar-exchange waves in the low-k region (before the vertex of the parabola) are known as Magnetostatic Backward Volume Waves. A summary of the observed SWs in the different geometries is given in Fig.1.8.
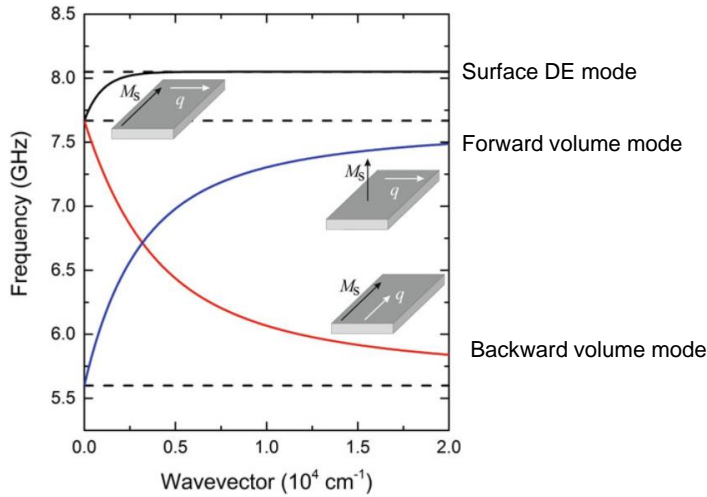
Figure 1.8: Schematic summary of SWs observed in different configurations. The surface DE mode can be observed for $\mathbf{k} \perp \mathbf{M}$; the backward volume SWs are observed for $\mathbf{k} \parallel \mathbf{M}$; when $\mathbf{M}$ is OOP, forward volume SWs are observed (not discussed here). Adapted from [27].

The present summary is only valid for an isotropic ferromagnet; in case MCA is present, the SW spectrum is accordingly modified. The details are not relevant for the present thesis; they can be found in selected literature [33–35].

1.3   Magneto-elastic coupling

Having introduced the two main characters at play, namely low-wavevector acoustic and magnonic excitations, now their coupling is discussed. The topic falls within the broad subject of MEC, encompassing both static and dynamical effects. The general framework will be briefly described; then the focus will shift to dynamics, as this is the interest of this thesis. The flow of the discussion will be: (i) definition of the free energy density contribution due to MEC, (ii) derivation of the effective magnetic field, (iii) application of this field to the case of space- and time-varying elastic strain, as relevant for modeling SAW-driven magnetization dynamics in the framework of the LLG equation.

MEC is traditionally distinguished from MCA, even though microscopically they both arise from the same mechanisms, namely (i) anisotropy in the atomic structure, which affects the energy of electronic levels in crystal field environment, and (ii) SOC, which allows this anisotropy to influence the magnetic subsystem. The basic experimental observation is that the length of a ferromagnet changes by some parts per million when it is magnetized, as the solid can lower its magnetic anisotropy energy upon straining: this spontaneously takes place if the magnetic energy saving is larger than the cost in elastic energy. This effect is generally known as *magnetostriction*. Typical energies are in the sub-millielectronvolt per atom range [see Fig.1.9(a)]: for Ni it is about 100 μeV/atom [37], comparable to MCA energy, and can rarely be neglected. Insights into the microscopic origin are obtained by tight-binding calculations. In Fig.1.9(b) results of calculations for bulk Fe upon uniaxial strain are reported: the density of states for some d bands at the Fermi level is modified, resulting in modification of SOC and of MCA.
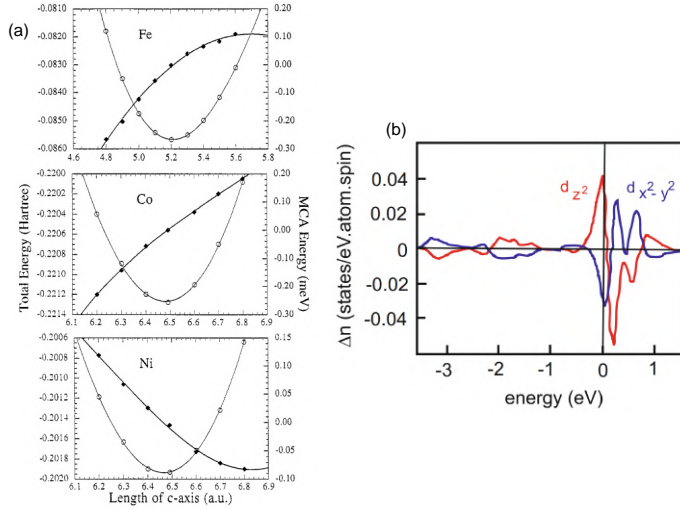
Figure 1.9: (a) Variation of MCA upon uniaxial strain along the c axis for Fe, Co, and Ni (filled diamonds, right scale) as obtained via DFT calculations; the overall energy is also reported (empty circles, left scale), showing a parabolic minimum corresponding to the equilibrium configuration. (b) Calculated change of density of states upon uniaxial compression of bulk Fe, from tight-binding calculations. A shift to lower (higher) energy of bands with d_{z^2} (red) [$d_{x^2-y^2}$ (blue)] symmetry is observed. This changes SOC interaction, and consequently affects the magnetic anisotropy of the system. Adapted from [36].

Joule magnetostriction and its free energy density

In a ferromagnet solid below T_C, Joule (or linear) magnetostriction models the interplay between strain and magnetization, namely what are the constitutive relations between ϵ_{ij} and **M** if (i) the system is magnetically saturated via an external field (magnetostriction), or if (ii) a strain is externally imposed (inverse magnetostriction). Other effects exist, again related to MEC: for an overview see Ref.[37] and references therein.

Magnetostriction involves strain and the square of the magnetization [18]: $\epsilon_{ij} = N_{ijkl}M_kM_l$. Despite being a second-order effect it is usually predominant on piezomagnetism (linear in the magnetization). Here below only the case of a cubic crystal is discussed; for other crystallographic classes see [18, 37].

The free energy density contribution due to magnetostriction in a cubic lattice is [38]

$$F_{\text{MEC}} = B_1 \left[\epsilon_{xx} \left(\alpha_x^2 - \frac{1}{3} \right) + \epsilon_{yy} \left(\alpha_y^2 - \frac{1}{3} \right) + \epsilon_{zz} \left(\alpha_z^2 - \frac{1}{3} \right) \right] + \\ + B_2 \left[\epsilon_{yz} \alpha_y \alpha_z + \epsilon_{zx} \alpha_z \alpha_x + \epsilon_{xy} \alpha_x \alpha_y \right] , \tag{1.12}$$

where α_i are the director cosines quantifying the angle between axis i and the direction of **M**, and B_i are the magneto-elastic coefficients (measured in energy per volume: typical values for $3d$ ferromagnets are in the ± 10 MJ/m^3 [37]); note that this is an approximate expression as higher order terms can be present. [8] From the definition of director cosine,

---

[8]In literature sometimes there is a factor 2 in front of B_2: this amounts to a renormalization of that quantity, but has no relevance for the following discussion. Note also that the quantity $B_i\alpha_j\alpha_k$ are in relation to the original tensor coefficients N_{ijkl}, as can be obtained from [18].

$\alpha_i = M_i/M_s$: thus Eq.1.12 is recast as [13]

$$F_{\text{MEC}} = \frac{B_1}{M_s^2} \sum_i \epsilon_{ii} \left(M_i^2 - \frac{1}{3} \right) + \frac{B_2}{M_s^2} \sum_j \sum_{i \neq j} M_i M_j \epsilon_{ij} \; : \tag{1.13}$$

here the fact that magnetostriction is quadratic in M_i is more apparent.

In Eq.1.13 F_{MEC} is linear in ϵ_{ij}. This is unphysical as would lead to arbitrary energy saving upon strain: the balance with the elastic free energy density, which is quadratic in ϵ_{ij}, leads to an energy minimum for any **M**. Note that since the magnetization saturates at large field, the same holds for the magnetostrictive strain. [9] For further details see [37, 38]. Experiments usually give access not to B_i but to the related parameters

$$\lambda_{[100]} = -\frac{2}{3} \frac{B_1}{C_{11} - C_{12}} \qquad \lambda_{[111]} = -\frac{1}{3} \frac{B_2}{C_{44}} \; , \tag{1.14}$$

where the Voigt notation (see Sect.1.1) has been used for the stiffness coefficients. In a cubic lattice $\lambda_{[100]}$ and $\lambda_{[111]}$ completely describe the magnetostriction. They are adimensional and typical values for Ni (Fe) are $\lambda_{[100]} = -65(24) \cdot 10^{-6}$ and $\lambda_{[111]} = -28(-23) \cdot 10^{-6}$ [37]. In the case of an isotropic ferromagnet, a single parameter λ_s is sufficient; for a polycrystalline average of a cubic lattice it amounts to

$$\lambda_s = \frac{2}{5} \lambda_{[100]} + \frac{3}{5} \lambda_{[111]} \; . \tag{1.15}$$

Magnetostriction results in the definition of a magnetic uniaxial anisotropy. The nature of the anisotropy axis (being it an easy or hard axis) depends on the sign of the magnetostriction parameters; for details see Ref.[38]. In the static limit, this can be exploited to toggle bistable magnetic (bit) state in magnetic nanostructures [39, 40].

Effective field

The effective MEC field is computed via Eq.1.8. We consider a thin film geometry, appropriate for the samples investigated in this thesis; the surface normal is along the z axis. Following Ref.[41], a new Cartesian frame (α, β, γ) is introduced: the γ axis is aligned with the static magnetization, and the β axis lies IP. The relation between the two Cartesian frames is sketched in Fig.1.10. In the new frame, the dynamical components of **M** lie in the (α, β) plane. This is also the plane where the effective MEC field is to be evaluated: according to Eq.1.8 and 1.13 it reads for a cubic lattice [41]

$$\begin{aligned}
\mu_0 M_s H_{\text{MEC},\alpha} =& - 2B_1 \sin\theta \cos\theta \left[\epsilon_{xx} \cos^2\varphi + \epsilon_{yy} \sin^2\varphi - \epsilon_{zz} \right] + \\
& - 2B_2 \left[(\epsilon_{xz} \cos\varphi + \epsilon_{yz} \sin\varphi) \cos(2\theta) + 2\epsilon_{xy} \sin\theta \cos\theta \sin\varphi \cos\varphi \right] \\
\mu_0 M_s H_{\text{MEC},\beta} =& \, 2B_1 \sin\theta \sin\varphi \cos\varphi \left[\epsilon_{xx} - \epsilon_{yy} \right] + \\
& - 2B_2 \left[\cos\theta (\epsilon_{yz} \cos\varphi - \epsilon_{xz} \sin\varphi) + \epsilon_{xy} \sin\theta \cos(2\varphi) \right]
\end{aligned}$$
.
$$\tag{1.16}$$

---

[9]Joule magnetostriction is also at play in the ferromagnetic core of transformers, whereas a soft ferromagnet is saturated by an ac field. During the (very narrow) hysteresis curve, the magnetization does not change smoothly but presents finite jumps as due to pinning of domain walls at defects (Barkhausen effect). The sudden jumps of the magnetization generate small strain pulses that can be heard with a broadband acoustic receiver; in some old transformers, it can also be heard by bare ear as a hum.
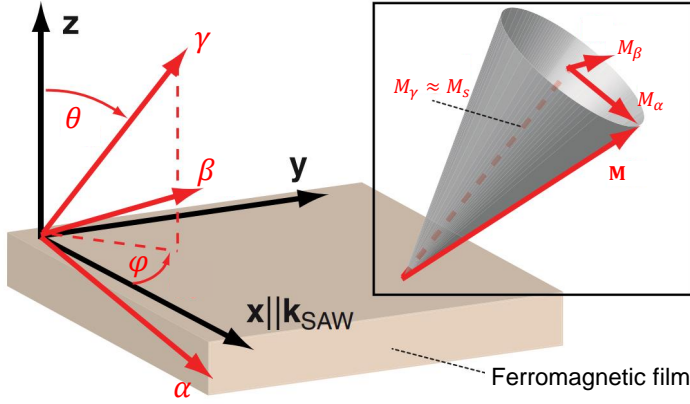
Figure 1.10: Scheme of the sample (cubic ferromagnetic slab) with the two Cartesian frames required for the evaluation of $\mathbf{H}_{\text{MEC}}$. The film lies in the (x, y) plane, with the x oriented along the wavevector of the SAW (see below). In the auxiliary Cartesian frame the γ axis points in the direction of the saturated magnetization, the β axis lies IP, and the α axis is consequently defined to have a right-handed triplet. The tilt θ and azimuth φ angles are indicated. In the inset, the precession cone for $\mathbf{M}$ is shown: the dynamical components (and so the precession plane) are in the (α, β) plane. Adapted from [41].

Now the discussion specifies on the experimental situation discussed in the next chapters. First, when the leading strain field is ϵ_{xx} Eq.1.16 reduces to

$$
\begin{aligned}
\mu_0 M_s H_{\text{MEC},\alpha} &= -2B_1 \epsilon_{xx} \sin\theta \cos\theta \cos^2\varphi \\
\mu_0 M_s H_{\text{MEC},\beta} &= 2B_1 \epsilon_{xx} \sin\theta \sin\varphi \cos\varphi \, .
\end{aligned}
\tag{1.17}
$$

Second, when the equilibrium axis for $\mathbf{M}$ lies IP, as forced by the external field, then $\theta = \pi/2$: only one component is non-vanishing

$$
\mu_0 M_s H_{\text{MEC},\beta} = 2B_1 \epsilon_{xx} \sin\phi \cos\phi = B_1 \epsilon_{xx} \sin(2\varphi) \, .
\tag{1.18}
$$

Note that along the γ axis there is a time-dependent effective MEC field: however it is collinear to the equilibrium magnetization and does not contribute to modify its orientation.

The torque acting on $\mathbf{M}$ is computed moving back to the original Cartesian frame, where in the (x, y) plane it holds

$$
\begin{aligned}
\mathbf{M} &= M_s \begin{pmatrix} \cos\varphi \\ \sin\varphi \end{pmatrix} \\
\mu_0 \mathbf{H}_{\text{MEC}} &= \frac{B_1}{M_s} \epsilon_{xx} \sin(2\varphi) \begin{pmatrix} -\sin\varphi \\ \cos\varphi \end{pmatrix} \, ,
\end{aligned}
\tag{1.19}
$$

such that the resulting MEC torque is

$$
\boldsymbol{\tau}_{\text{MEC}} = \mathbf{M} \times \mu_0 \mathbf{H}_{\text{MEC}} = \hat{\mathbf{z}} B_1 \epsilon_{xx} \sin(2\varphi) \, .
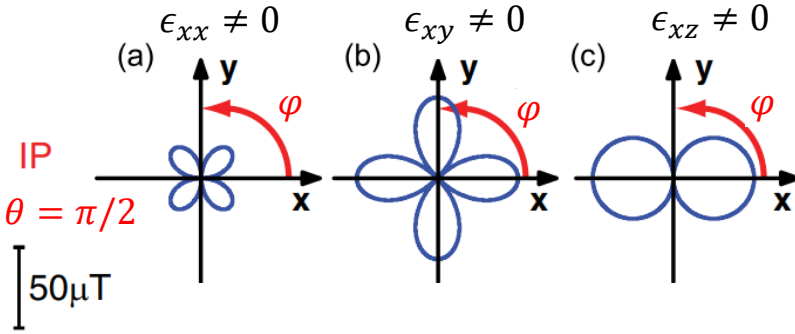\tag{1.20}
$$

Figure 1.11: The amplitude of $\mathbf{H}_{\text{MEC}}$ (see Eq.1.16) as a function of the IP angle φ is reported as polar plot. The case $\theta = \pi/2$ is considered. Each panel considers a single component of the strain. Adapted from [41].

The effective MEC torque points OOP and is in phase to the strain. The same results can be obtained keeping all the calculation in the original Cartesian frame (the notation is more lengthy) [42].

From Eq.1.20 it can be seen that the sign of the torque does not depend on the saturation direction of $\mathbf{M}$: the dynamics is the same if the sample is saturated along $\pm\hat{\gamma}$. This is ultimately a consequence of the magnetostriction being a quadratic interaction in the magnetization. On the other hand, the sign and amplitude of $\mathbf{H}_{\text{MEC}}$ (and thus also of $\boldsymbol{\tau}_{\text{MEC}}$) feature fourfold symmetry in the azimuth angle φ. In particular, as shown in Fig.1.11(a) the MEC field vanishes if $\mathbf{M}$ is either collinear or orthogonal to the strain field, while it is maximum for $\varphi = 45°$ $(+n\pi/2)$ [41, 43, 44]. An important note: if $\mathbf{M}$ is set at a different IP azimuth φ, also $\mathbf{H}_{\text{MEC}}$ rotates jointly. This suggests that it is not appropriate to simply think of a strain-induced MEC field, whose torque is maximized for some value of φ. Rather, $\mathbf{H}_{\text{MEC}}$ is *defined* by $\mathbf{M}$, both in direction and in strength (see Eq.1.8). It is better to think of it in general as a kind of self-interaction of the system; for this reason no general explicit formula exists that simply gives the MEC field for a given strain field.

MEC in the dynamical case

If $\epsilon_{ij}(t)$ is a time-dependent harmonic strain, a time-dependent harmonic field $\mathbf{H}_{\text{MEC}}(t)$ results. It can be added with the other contributions to the overall effective field $\mathbf{H}_{\text{eff}}$ and then inserted into the LLG equation. In analogy to photon-driven FMR experiments, the time-dependent acoustic strain can supply a torque to balance the Gilbert damping: stable precession can result. Moreover, the strain can feature harmonic space dependence, as resulting from an acoustic wave with $\epsilon_{ij}(\mathbf{r}, t)$. Similarly, the field $\mathbf{H}_{\text{MEC}}(\mathbf{r}, t)$ is harmonic in space and can sustain $\mathbf{M}$ precession with a phase modulation, namely a SW. This is the conceptual background behind SAW-driven FMR (SAW-FMR).

As a general rule of thumb, to have large coupling between SAW and SW (and between two dynamical modes in general), the overlap of the corresponding waves has to be maximized. This requires matching of both the wavelengths and of the frequencies. Thus in general the best condition is obtained when there is matching of the dispersion relation of the two modes. This typically happens for SWs and SAWs in the few
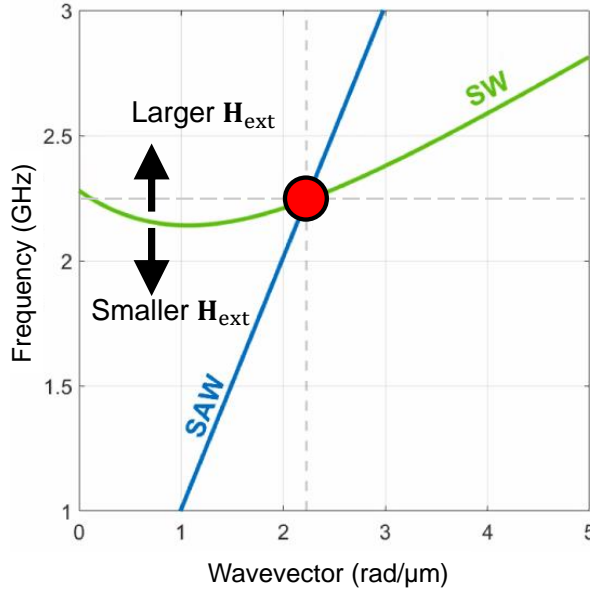
Figure 1.12: Schematic dispersion relations for a SAW (blue) and for an exchange-dipolar SW (green). The dashed gray lines indicate frequency and wavevector of the experimentally excited SAW. Upon tuning $\mathbf{H}_{\text{ext}}$ the SW dispersion can be shifted vertically until a matching to the excited SAW is obtained (red circle).

inverse micron and few gigahertz range, if moderate magnetic fields are applied (see Fig.1.12). The typical experimental approach is to fix wavevector and frequency of the SAW (which are proportional via the sound velocity), and the strength of H_{ext} is tuned until a magnon band is swept vertically and matches the excited acoustic mode; this approach is conceptually similar to the electromagnetic-cavity in photon-driven FMR. Note, however, that the dispersion matching is not strictly mandatory: it is observed that a high-amplitude acoustic wave drives the magnetization into precession even if no natural magnetic mode exists at the probed wavevector and frequency [45].

An important note: the discussed approach considers the strain field $\epsilon_{ij}(\mathbf{r}, t)$ as an external condition that acts on $\mathbf{M}$, while the back-action of $\mathbf{M}$ on the strain is neglected. This back-action is in general expected, as the underlying thermodynamics connecting the acoustic and magnetic reservoirs gives *two-ways* relations. Neglecting the back-action is a good approximation whenever the SAW amplitude is much larger than the SW amplitude, so that the energy flow is basically one-way. The experiment discussed in Ch.3 (and in most of the referred literature as well) falls in this category. I will refer to this as the case of phonon-driven magnons, or SAW-FMR as above. On the other hand, this approach is not appropriate to describe strong magnon-phonon coupling, whereas the two subsystems act one to each other. In this case a different formalism has to be developed: in Ref.[41, 46] the back-action is explicitly calculated and the coupled motion of magnetization and acoustic field is computed. The approach I will follow in Ch.5 is different, and the details will be described later.

SAW-driven SWs have been largely investigated in the past decade employing lithographically patterned devices. An array of metallic Inter-Digitated Transducers (IDTs) is

evaporated with a specific spatial periodicity on a piezoeletric substrate. A rf voltage is applied to the IDTs, resulting in alternating poling of the piezoelectric: an acoustic wave is launched if a mode exists at the frequency of the rf voltage *and* at the wavelength of the IDT pattern. After propagation across the device, the SAW is sensed by a second array of IDTs located at the opposite side: in the piezoelectric the SAW strain generates a rf voltage transient which is recorded via a Virtual Network Analyser. If a ferromagnetic thin film is deposited between the exciting and sensing IDTs, the SAW can excite magnetization precession: this happens if the resonance condition is met. The observable is the reduced amplitude at the sensing IDT when FMR is driven [20, 47, 48]. In a series of publications starting from 2012, Weiler *et al.* investigated the details of MEC coupling in the dynamical regime, with special focus on Ni thin films [41, 43, 44]. These experiments also allowed to elucidate more intriguing aspects, like the non-reciprocal MEC in ferromagnetic multilayers [49] and in Dzyaloshinskii-Moriya compounds [50].

Transient-Grating spectroscopy

Ultrafast laser pulses can impulsively trigger acoustic and magnetic dynamics in a sample. This is the topic of this chapter, with emphasis on the role of a spatially non-uniform pump in fixing the wavevector spectrum of the excitations. Having an experimental technique to perform finite-wavevector spectroscopy is of relevance in solid-state physics, as in many systems the phase diagram is determined by the energy competition of low-frequency excitations: this calls for characterization tools for the dispersion relations of the involved modes. Moreover, some excitations exhibit mode crossing (*i.e.* energy and wavevector degeneracy) at finite wavevector: again, the details of the mode coupling could be addressed with a wavevector-selective technique. An all-optical (contact-less, as it is sometimes qualified) tool to selectively excite finite-wavevector dynamical modes is of large experimental relevance: a variety of samples can be addressed in this way, with minor requirements as compared to lithographically patterned devices. Finally, low-energy propagating modes have been proposed as basic elements for new-generation information technology, and their possible energy-efficient excitation via light pulses can be of interest for technical fallouts.

The subject of optical excitation of wavevector-selected transients is tackled starting from some generalities on the pump-probe scheme and the specificities of optically-triggered acoustic and magnetic dynamics (Sect.2.1); then the details of TG spectroscopy are presented (Sect.2.2); some relevant examples of material transient gratings are reported in Sect.2.3, with special emphasis on opportunities from magnetization-sensitive experiments; finally, in Sect.2.4 the setup implemented and used for the experiments discussed in this thesis is reported. The approach will be mainly phenomenological: for further details the interested reader can refer to classical textbooks [51–54] and publications [16, 55–62] on the subject.

2.1 All-optical excitation and detection of acoustic and magnetic transients

The experiments discussed in this thesis aim at probing acoustic and magnetic excitations, and their mutual interaction. The main experimental technique is time-resolved (tr) optical spectroscopy, namely photon-in/photon-out spectroscopy on out-of-equilibrium samples.

The employed approach is known as *pump-probe*. In a pump-probe experiment, a pump optical pulse with duration Δt excites the sample into a largely non-thermal state. The primary excitation process is usually very fast as compared to the investigated phenomena, and can be assumed as a single instant, dubbed time zero (t_0). The pump event
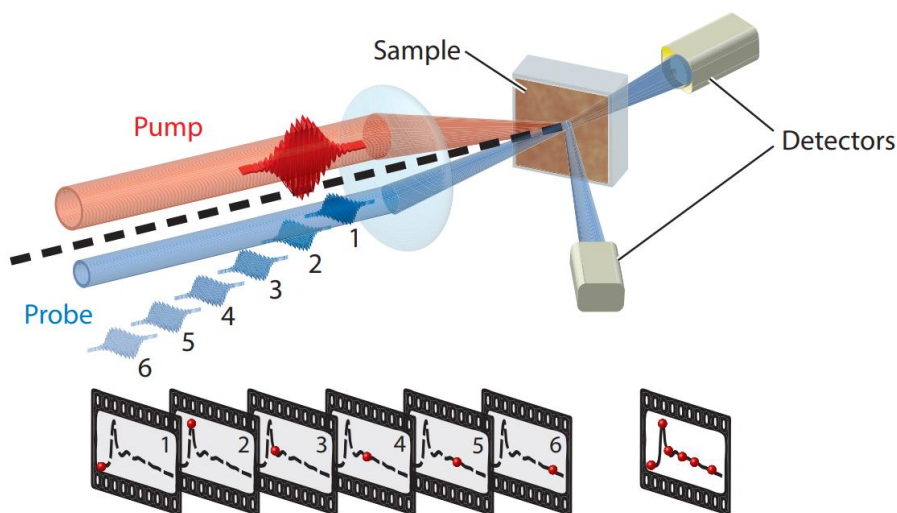
Figure 2.1: Scheme of an optical pump-probe experiment. The pump pulse excites the sample; the probe pulse, at variable delay, probes the instantaneous state occupied by the system. The transient signal, acquired in transmission or reflection geometry, gives information on the overall transient dynamics triggered by the pump. From Ref.[3].

can also consist of a configuration more complicated than a single pulse, as it happens in TG spectroscopy. The non-equilibrium state is characterized by non-thermal population of particles and quasi-particles, whose detail depends on the characteristics of the pump beam (duration, wavelength...). The sample then relaxes towards the free energy minimum: along the de-excitation path successive cascading events can take place, ultimately degrading the input pump energy into thermal energy. The probe beam monitors the sample during the relaxation, resulting in a time-resolved signal informative of the sample states transiently occupied.

To observe slow dynamics, the probe beam can be a CW laser, whose modification upon interaction with the sample (in terms of intensity, polarization...) is continuously monitored via fast detection. If fast dynamics is addressed (say, in the picosecond scale or faster), no continuous acquisition scheme is available: the only possibility is to employ a stroboscopic approach, whereas also the probe beam is pulsed. It is mechanically delayed with respect to the pump, usually employing retroflector mirrors on a mechanical delay-line. [1] The signal at a fixed delay is acquired, usually averaging some hundreds of thousands of pump-probe events to improve statistics; then the delay line is moved, and the signal at a different delay is acquired. This process allows to reconstruct the full dynamics of the signal after the pump event, as schematically shown in Fig.2.1. In the pulsed configuration the fastest dynamics that can be probed is given by the finite duration of the employed pulses, which can be routinely in the 100 fs scale or lower; technical advancement to employ sub-femtosecond pulses is now mature to start investigation at that extreme timescale [63].

---

[1]A mechanical movement of 10 μm of a retroflector mirror corresponds to a delay variation of 60 fs: thus the sub-picosecond scale is largely within routine technical possibilities.

The pump-probe scheme is meaningful if the sample has enough time from a pump event to the next to recover the original ground state; this typically takes place in the microsecond scale, thus a laser repetition rate as high as 1 MHz can be employed. The pump fluence is usually high (typically in the millijoule per centimeter square range), to ensure large excitation of the sample; on the other hand, the probe fluence is much lower, so that the signal can be interpreted in the framework of perturbation theory. In other words, the probe must be faint enough to only *sense* the state of the sample, without inducing further non-equilibrium dynamics.

A final note is of relevance for the experiments discussed in this thesis. As stated above, the duration of the pulses sets the ultimate time resolution of the observable dynamics (possibly further limited by the precision of the delay line, by jitter of the two pulses, and other instrumental issues). There is also a more fundamental aspect, if the experiment addresses oscillatory modes (like SAWs and SWs). The temporal envelope of the pump is approximately Gaussian, with Full Width at Half Maximum (FWHM) Δt; thus the Fourier Transform (FT) of the envelope is again a Gaussian, whose FWHM is approximately $1/\Delta t$. It turns out that the pump can efficiently excite only those oscillatory modes whose frequency is well within the bandwidth of the pump: $f_{\max} \approx 1/(2\Delta t)$. This regime is also known as *impulsive* excitation regime.

In the following, some basic mechanisms for excitation and detection of acoustic and magnetic transients via light pulses are briefly discussed. For a broader overview see Ref.[18].

Excitation: Inverse acousto-optics

Acoustic transients can be optically generated by pump pulses in absorbing sample. The pump energy is absorbed by the electronic reservoir, and via complex relaxation pathways it ultimately degrades into thermal energy: this couples to the elastic degree of freedom via thermo-elastic expansion. In the impulsive regime, acoustic waves can be triggered.

This approach has been extensively used in the context of picoacoustics to generate acoustic pulses at the surface of metallic samples [64]: time- and space-resolved probing of these transients allows to evaluate the sound velocity and surface acoustic anisotropies (from the deformation of the wavefronts, expected circular for an isotropic surface). This approach is also at the basis of the generation of wavevector-selected SAWs via TG spectroscopy. In anisotropic solids the thermal expansion can also lead to thermally-excited shear waves [65].

Other effects can be at play: for example, if free carriers are optically injected in the conduction band of a poled ferroelectric, they locally screen the elementary electric dipoles, resulting in elastic strain as due to piezoelectricity (recall that all ferroelectrics are also piezoelectrics). This effect is known as photostriction; it has been observed *e.g.* in the static regime via the deformation on a magnetostrictive overlayer [66].

Excitation: Inverse magneto-optics

Light can be used to manipulate magnetic order. From the simplest application of heat-assisted magnetic recording to recent experiments on non-thermal excitation of precession and all-optical switching, this field proceeded at the same pace with the development of ultrafast laser technology. Moreover, fundamental questions related to the intrinsic timescale for dissipation of angular momentum in strongly out-of-equilibrium

transient states are addressed in such investigations, as discussed in the introduction. Literature is available on the topic: I suggest in particular Ref.[8, 25].

The field can be broadly divided in two categories: thermal and non-thermal effects. Experimentally, the former do not depend on the light polarization, while the latter do. In thermal effects, the pump light is absorbed and leads to local heating. This modifies the magnetization, which is reduced following the $M_s(T)$ curve. Moreover, heating largely affects the anisotropy constants. As a result, shape anisotropy and MCA are reduced upon laser irradiation, and this can be exploited to perform magnetization switching at lower coercivity, or to trigger magnetization precession. Details on this aspect will be presented in Ch.4 in connection with experimental results.

Non-thermal effects are dominated by the pump electric field, rather than its intensity. For example, in some magnetic oxides the anisotropy is largely affected by impurities; exciting such impurities with a properly-polarized laser allows to impulsively modify the anisotropy landscape of the material, thus exciting magnetization dynamics [67]. Note that, despite the laser photons are absorbed, the triggering mechanism of the magnetization is not thermal, in the sense that it takes place before the input energy has degraded to heat.

Another class on phenomena, not involving photon absorption, have to be considered. In this case the laser field drives a non-resonant process involving virtual levels, with close reminiscence to stimulated Raman scattering. During the duration Δt of the pulse, the system is driven from the ground state into a non-equilibrium superposition of higher electronic states where the effective SOC is enhanced: the spin state of the involved electron feels a different effective magnetic field, and it is kicked out from its pointing. When the light pulse is over, the electron falls back to the ground state manifold, but since the spin points in a different direction the final state is slightly higher in energy: the difference equals the energy of a magnon wavepacket. From a qualitative point of view, everything goes as if the laser optical field acted as an effective impulsive magnetic field directed along the propagation direction and with a sign given by the helicity of the pump photons: no magnetization dynamics is excited for linearly polarized light, and coherent precession is triggered for circularly polarized light.

In the experiments discussed in this thesis, only thermal effects were exploited for the generation of both acoustic and magnetic transients; the presented overview may serve as a suggestion for future developments.

Detection: Acousto-optics

The acousto-optic effect relates variation in the dielectric tensor ε_{ij} (or its inverse) to elastic strain: $\Delta \left(\frac{1}{\varepsilon_{ij}} \right) = p_{ijkl}\epsilon_{kl}$, where p_{ijkl} is the acousto-optic (or photo-elastic) tensor [18]. To gain the basic idea, consider an isotropic solid subject to hydrostatic pressure: the atoms or molecules pack more closely, and the refractive index increases. Upon pressure, also the electronic polarizability changes: in a compressed solid the electrons are bonded more tightly, and their polarizability reduces. This again affects the refractive index. Enhanced packing and reduced polarizability compete and can result in finite acousto-optic effect. In case of a generic strain field, local compression or tilt of the electronic orbitals are still at the basis of a variation of the dielectric tensor. The general result is the introduction of birefringence and dichroism in the optical spectra; if the sample is anisotropic, the optical axes can also rotate.

Acousto-optic effect is largely used in manufacturing and testing of plastic objects:
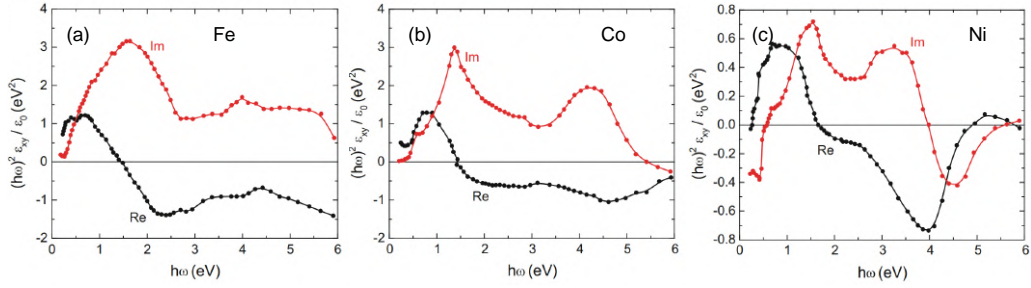
Figure 2.2: Experimental values of the real and imaginary parts of ε_{xy} in the optical range for Fe, Co, and Ni. Adapted from [8].

polarization of the light is modified by induced strain, which thus becomes visible at crossed polarizer detection. These measurements provide a rapid way to locate regions of stress concentration. Another application of acousto-optic effect is routinely employed in high-power laser technology: in Acousto-Optic Modulators (AOMs) the laser beam is deflected via Bragg diffraction off a piezoelectrically excited acoustic wave inside an acousto-optic crystal. The same physical principle is at the basis of TG detection of SAWs, and in general of time-resolved optical detection of acoustic transients [68, 69]. Also Photo-Elastic Modulators (PEMs) are based on the same principle.

Detection: Magneto-optics

The dielectric tensor is modified by the magnetic state of matter: thus via light-matter interaction it is possible to probe magnetism. The key notion is that polarized light changes its polarization state and/or intensity when interacting with a magnetically ordered sample. The effect can be observed in transmission or in reflection, depending on the experimental geometry and on the requirements of the sample (*e.g.* a thick opaque sample can only be probed in reflection), resulting in the techniques known as Faraday Rotation (FR) and Magneto-Optical Kerr Effect (MOKE).

Consider a cubic sample and a Cartesian frame oriented along its principal axes. In the paramagnetic or unmagnetized state ε_{ij} is diagonal. If the sample is magnetized along z, off-diagonal terms $\varepsilon_{xy} = -\varepsilon_{yx}$ appear:

$$\begin{pmatrix} \varepsilon_{xx} & \varepsilon_{xy} & 0 \\ -\varepsilon_{xy} & \varepsilon_{yy} & 0 \\ 0 & 0 & \varepsilon_{zz} \end{pmatrix} . \tag{2.1}$$

This expression summarizes the observation that circularly polarized waves propagating along z experience a different dielectric coefficient: the real part of ε_{xy} gives magnetic circular birefringence (different phase velocity) and the imaginary part gives magnetic circular dichroism (different absorption cross section). The result is that an input beam linearly polarized leaves the sample with rotated polarization and non-zero ellipticity. The measurements of one or both of these quantities is the goal of magneto-optical spectroscopy: information on the underlying magnetization state of the material can be obtained.

Magneto-optics mainly probes the orbital magnetic moment, not the spin one: the latter can be derived assuming a fixed relation between the two [8]. This is the gross
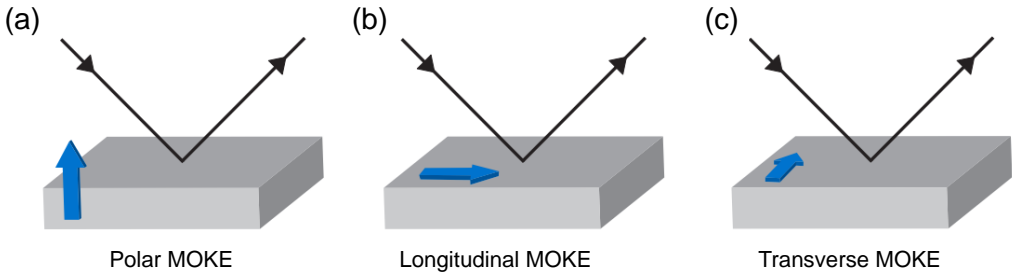
Figure 2.3: Possible geometries for MOKE, defined by the orientation of **M** (blue arrow) with respect to the sample surface and to the reflection plane. Adapted from [71].

reason why transition metal ferromagnets (whose orbital angular momentum is largely quenched [1]) feature smaller magneto-optical effects with respect to rare-earth; a common experimental trick is to dope a system with some heavy element such as Bi or a rare earth, resulting in effective enhancement of magneto-optical signal [70]. Note that as electronic transitions are involved in the definition and evaluation of ε_{ij}, the magneto-optical effects are typically strongly wavelength-dependent, as can be seen in Fig.2.2.

In FR geometry, often the effect of the dielectric tensor (Eq.2.1) is condensed in the expression $\theta_{\text{FR}} = VhM_z$, where the quantities are the rotation angle of the polarization, the Verdet constant, the sample thickness, and the z component of the magnetization, respectively. In MOKE geometries (see Fig.2.3), the following phenomenological approach is often useful (full calculations can be found in literature [8, 18]). In Eq.2.1 information on **M** is encoded in the off-diagonal coefficients; alternatively [8, 20] one explicitates the **M** dependence, employing a magnetization-independent (but material-dependent) coefficient α. For an isotropic sample, the induced dielectric polarization is $\mathbf{P} = \alpha\mathbf{E} \times \mathbf{M}$, where **E** is the optical field of the probing beam. Assuming magnetization along z, and incident light propagating parallel to **M** with $\mathbf{E} \parallel \hat{\mathbf{x}}$, a component P_y is generated: this radiates an electromagnetic wave coherent with the incoming field, but with orthogonal polarization. Superposition of this wave with the reflected wave results in rotation of the polarization direction, as observed in polar MOKE configuration. In other MOKE configurations, the required experimental geometry can be understood employing the same concepts. For example in longitudinal MOKE configuration, no effect is observed for a normally impinging beam; the effect is maximized at large off-normal angle.

2.2 Transient-Grating spectroscopy

TG spectroscopy is an experimental technique that by design addresses finite-wavevector excitations. It involves three input optical beams (two pumps with different wavevector, and the probe) and an output beam obtained via diffraction of the probe; this can be defined as a type of Four Wave Mixing (FWM) spectroscopy. In a TG experiment, two frequency-degenerate coherent pump pulses simultaneously impinge on the sample at angle $\pm\theta$ from the surface normal, as shown in Fig.2.4. Their interference generates a periodic modulation of the optical field at the sample position, with a wavevector selected by the experimental geometry. Via light-matter interaction, the optical grating translates into a periodic modulation of some material excitation: for example, excited electronic states can be populated in correspondence to intensity fringes of the optical grating. In
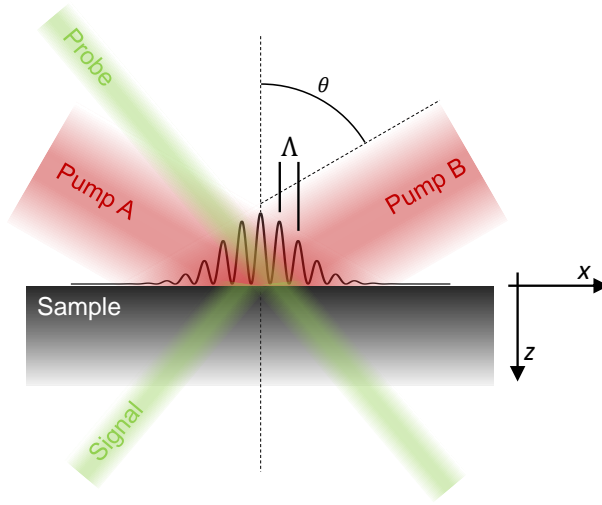
Figure 2.4: Sketch of the TG working principle with cross-sectional view at the (x, z) scattering plane. Two degenerate pump beams (Pump A and Pump B) impinge on the sample at angle $\pm\theta$ from the sample normal; their interference generates an optical grating with spatial period Λ. Modulated excitation in the sample diffracts the probe beam (diffraction in reflection is also possible, not depicted here).

the sample, deviation from thermal equilibrium couples to the optical properties, namely the refractive index and/or the extinction coefficient: thus the sample behaves as a physical grating to the probe beam, that can be diffracted. Since the diffraction efficiency depends on the amount of deviation of the optical properties from equilibrium (what is dubbed the grating *depth*), the intensity of the signal beam is a proxy for the material excitation: the time pattern of the sample response corresponds to time pattern of the signal. This is the meaning of the expression *transient grating*: upon pump-induced excitation, the sample exhibits spatially modulated optical properties, capable of diffracting the probe beam; diffraction then ceases as soon as the material excitation dissipates, by local relaxation or by diffusion. The time scale of the induced transients is extremely variable: from tens of femtoseconds (electronic transients), to picoseconds (optical phonons, spin diffusion), to nanoseconds (acoustic phonons and low-energy magnons) and more (thermal diffusion, space-charge accumulation, chemical reactions and mixing).

Generally speaking, the entire process can be thought as a single step convolution of the three input beams with an appropriate sample response function. The result is the dielectric polarization responsible for the emission of the outgoing beam:

$$
\begin{aligned}
P_i(\mathbf{r}, t) = \int d\mathbf{r}_1 d\mathbf{r}_2 d\mathbf{r}_3 \int dt_1 dt_2 dt_3 \; E_j(\mathbf{r}_1, t_1) E_k(\mathbf{r}_2, t_2) E_l(\mathbf{r}_3, t_3) \cdot \\
\cdot \mathcal{R}_{ijkl}^{(3)}(\mathbf{r} - \mathbf{r}_1, \mathbf{r} - \mathbf{r}_2, \mathbf{r} - \mathbf{r}_3, t - t_1, t - t_2, t - t_3) \,,
\end{aligned}
\tag{2.2}
$$

where E_i ($i = x, y, z$) is the i-th component of an input electric field, the space and time indexes 1 to 3 refer to the three input beams, and $\mathcal{R}_{ijkl}^{(3)}$ is the third-order response function; repeated indices are summed. The expression in Eq.2.2 is very general, allowing for space and time non-locality; it is basically the definition of $\mathcal{R}_{ijkl}^{(3)}$, and as such is not
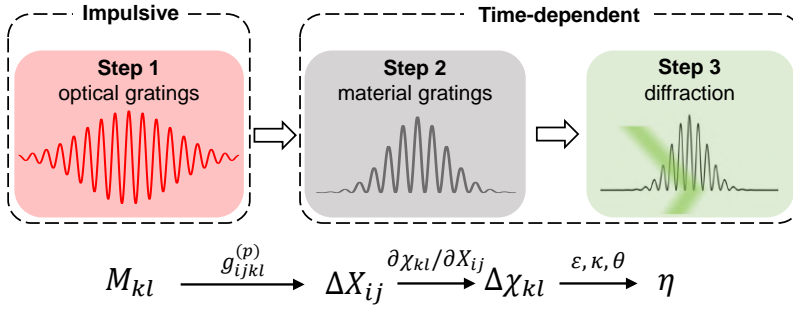
Figure 2.5: Block diagram for the experimental chain for TG spectroscopy. The impulsive optical grating modeled by a modulation tensor M_{kl} (Step 1) triggers an excitation in the sample ΔX_{ij} (Step 2), which couples to the optical properties resulting in a modulation of the optical susceptibility $\Delta \chi_{kl}$; the probe is diffracted by the time-dependent material grating with a correspondingly time-dependent efficiency η (Step 3). The meaning of the quantities displayed at the bottom is explained in the main text.

much insightful. Elaboration of this equation with proper assumptions leads to simplification and eventually to direct addressing of some of the entries of $\mathcal{R}^{(3)}_{ijkl}$ upon selected TG experimental geometries [52, 72]. The following discussion will be more practical: following Ref.[54] three steps are conceptually separated and described, namely (i) formation of an optical grating by the two pump pulses; (ii) interaction of the optical grating with the sample and formation of a spatially-modulated transient variation of the dielectric properties; (iii) diffraction of the probe beam by the induced transients; the detection of the transient diffracted intensity presents some subtleties and is discussed as a further fourth step. Of course this separation is an approximation to the one-step model; still, it proves rather useful to understand experiments and to envision further applications. In Fig.2.5 the conceptual flow of the experiment is represented. An alternative approach, involving concepts from nonlinear optics, is briefly outlined in Appendix B.

Step 1: Optical gratings

The first step of the model only involves the two pump beams, which are identified with the subscripts A and B. The sample lies in the (x, y) plane and the optical axis is along z. The two pumps are assumed as coherent pulses, with complex amplitude $\mathbf{A}_i$ ($i = A, B$) and same optical angular frequency ω_p and wavelength λ_p. They are identified by the different propagation direction, defined by the angle $\pm \theta$ from the sample normal, namely $\mathbf{k}_A = k_x \hat{\mathbf{x}} + k_z \hat{\mathbf{z}}$ and $\mathbf{k}_B = -k_x \hat{\mathbf{x}} + k_z \hat{\mathbf{z}}$:

$$\mathbf{E}_A(\mathbf{r}, t) = \frac{\mathbf{A}_A}{2} e^{i(k_x x + k_z z - \omega_p t)}$$

$$\mathbf{E}_B(\mathbf{r}, t) = \frac{\mathbf{A}_B}{2} e^{i(-k_x x + k_z z - \omega_p t + \phi)} \ . \tag{2.3}$$

By geometry $k_x = \pm |\mathbf{k}| \sin \theta$ and $k_z = |\mathbf{k}| \cos \theta$, where $|\mathbf{k}| = 2\pi / \lambda_p$. A possible difference in the optical phase ϕ is explicitly added; the factor two at the denominator accounts for the complex conjugate that should be added to have real fields. The finite pulse duration Δt is encoded in the amplitude, together with the polarization state; moreover, the pulses are assumed to impinge on the sample at the same instant t_0.
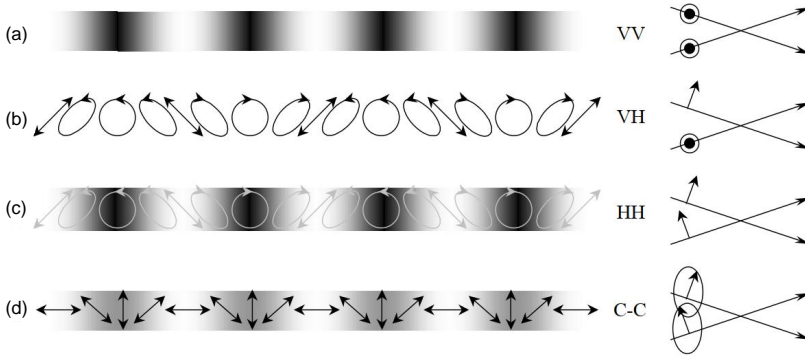
Figure 2.6: Four possibilities of optical grating for different polarization of the input beams; on the right the beams polarization is sketched (in top view), on the left the results at the interference region are shown (in front view), with black-white scale indicating the intensity modulation and the arrows indicating the polarization of the resulting field. (a) Both beams *s*-polarized: pure intensity grating. (b) One beam *s*- and one beam *p*-polarized: pure polarization grating. (c) Both beams *p*-polarized: mixed intensity and polarization grating. (d) Both beams circularly polarized (opposite helicity): mixed intensity and linear polarization grating. From Ref.[73].

The optical intensity in the interference region is

$$I \propto |\mathbf{E}_A + \mathbf{E}_B|^2 = |\mathbf{E}_A|^2 + |\mathbf{E}_B|^2 + 2\mathbf{E}_A \cdot \mathbf{E}_B^* =$$
$$= \frac{|\mathbf{A}_A|^2}{4} + \frac{|\mathbf{A}_B|^2}{4} + \frac{\mathbf{A}_A \cdot \mathbf{A}_B^*}{2} e^{i(2k_x x - \phi)} , \quad (2.4)$$

where the complex conjugate is denoted with the apex star. Assuming that the two beams have the same amplitude and are both *s*-polarized (*i.e.* $\mathbf{A}_A = \mathbf{A}_B \equiv \mathbf{A} \propto \hat{\mathbf{y}}$), Eq.2.4 becomes

$$I \propto \frac{|\mathbf{A}|^2}{2} \left[1 + e^{i(2k_x x - \phi)} \right] , \quad (2.5)$$

whose real part is

$$I \propto \frac{|\mathbf{A}|^2}{2} \left[1 + \cos\left(2k_x x - \phi\right) \right] . \quad (2.6)$$

Thus the intensity has a cosine modulation along the x axis; the phase difference ϕ only amounts to a lateral shift of the optical grating. The spatial period Λ of the optical grating and its wavevector q are given by

$$q = \frac{2\pi}{\Lambda} = 2k_x = \frac{4\pi \sin\theta}{\lambda_p} , \quad (2.7)$$

recalling that $k_x = (2\pi/\lambda_p)\sin\theta$. The induced wavevector, which lies IP by design, can be tuned either by changing the impinging angle θ, or changing the optical wavelength λ_p. Note that the latter is a motivation driving research for the extension of TG spectroscopy to FEL-based experiments, where EUV or X-ray photons are employed in order to achieve reduced grating pitch, possibly down to few nanometers; this, of course, in addition to the specific physics that can be addressed at those photon wavelengths.

Having both beams s-polarized in not the only possibility. A generalization of Eq.2.4 is given by defining a modulation tensor M_{ij} as

$$M_{ij} = A_{A,i} A_{B,j}^* \,, \tag{2.8}$$

where as above $A_{X,i}$ is the i-th component of the electric field amplitude of beam X. The amplitude of the intensity modulation in this case is given by $\Delta I = |\mathrm{Tr}\,(M_{ij})|$. In the case of two s-polarized beams $M_{ij} = \mathrm{diag}(0, |\mathbf{A}|^2, 0)$ and $\Delta I = |\mathbf{A}|^2$ as expected. With the definition 2.8 generalized polarization gratings, induced *e.g.* for $\mathbf{A}_A \perp \mathbf{A}_B$, can be treated on equal footing: this approach is relevant to model dichroism-sensitive dynamics. Some cases are shown in Fig.2.6, and are addressed at length in Ref.[54]. Two concluding notes:

- the optical grating is stationary if the two pumps have the same frequency: for non-degenerate beams (generalized FWM condition), traveling grating structures are obtained;

- the FT of the pump grating on the sample is peaked at finite wavevector $\pm q$:

$$I(\mathbf{k}) \propto e^{-\frac{(k_x \mp q)^2}{2\sigma^2}} \,, \tag{2.9}$$

  where σ is a broadening in wavevector space due to finite size of the optical grating and to non-unity fringe visibility; here k_x is the x component of the independent variable $\mathbf{k}$. The excitation triggered in the sample has to be compatible with this wavevector spectrum.

Step 2: Transient gratings in materials

The optical grating is transferred to the sample via light-matter interaction. A huge phenomenology can be addressed: I refer to the next section for some examples. To first order, the optical grating identified by the modulation tensor M_{ij} linearly couples with the variation ΔX_{ij} of a material property X:

$$\Delta X_{ij} = g_{ijkl}^{(p)} M_{kl} \,, \tag{2.10}$$

where the coupling strength $g_{ijkl}^{(p)}$ is a rank-four tensor which depends also on the pump frequency (thus the p superscript). Depending on the nature of excitation, ΔX can be a scalar (*e.g.* temperature, density), vectorial (*e.g.* electric field, drift velocity, magnetization) or tensorial (*e.g.* stress, strain) quantity: Eq.2.10 should be modified accordingly case by case.

The modulated variation of property X couples to the optical properties of the sample, inducing a corresponding modulation of refractive index and/or extinction coefficient. Since in general the optical properties of a solid are anisotropic, it is useful to keep on with tensorial expressions using the optical susceptibility χ_{ij}; this also allows to treat dichroism and birefringence. [2] To first order one can write

$$\Delta \chi_{ij} = \left(\frac{\partial \chi_{ij}}{\partial X_{kl}} \right) \Delta X_{kl} \,. \tag{2.11}$$

---

[2]Optical (or dielectric) susceptibility is related to the dielectric function via $\chi_{ij} = \varepsilon_{ij} - 1$; the complex refractive index $\tilde{n} = n + i\kappa$ can then be obtained since $\varepsilon = \tilde{n}^2$, whenever the magnetic permittivity can be set to one (which is usually the case in the optical regime). Note that the tensorial nature of the optical properties is lost with the last identity.

This shows that the anisotropy of $\Delta\chi_{ij}$ may be either due to the sample medium itself (*e.g.* crystalline structure, external fields, order parameters...) or be induced by the grating: for instance, even in an isotropic solid, pump-induced thermal expansion creates anisotropy, in the form of strain along x. Combining Eqs.2.10 and 2.11, the variation of the susceptibility can be related directly to the optical modulation tensor.

A wide class of light-induced gratings is quasi-stationary, *e.g.* temperature gratings. In these cases the grating amplitude experiences monotonous decay as due to diffusion processes (heat diffusion in the case of temperature gratings). Other mechanisms involve amplitude oscillations in connection to wave propagation: for example density variations create sound waves, *i.e.* acoustic phonons. Often the two mechanisms coexist, resulting in coherent amplitude oscillations superimposed to an incoherent monotonous background.

Adopting thermodynamical concepts like temperature, density etc. is valid only if the absorbed energy is locally thermalized: in this approximation, the triggered dynamics gives information on the *equilibrium* properties of the sample, like the frequency of acoustic phonons, or the thermal diffusion constant. This simplified discussion thus requires previous knowledge (or at least a careful handling) of the timescale of the involved excitations coupling the various degrees of freedom in the sample. Real equilibrium is obtained in the sample as a whole only when the pump-induced spatial inhomogeneity is washed out. Importantly, Eq.2.10 and 2.11 linearly couple the material response to the input optical trigger: in other words, such equations implicitly assume linear response theory. With this assumption equilibrium statistics can be used to compute the material evolution, which translates in the possibility to extract *equilibrium* parameters from the observed TG-induced dynamics: for instance, the frequency of TG-triggered acoustic oscillations relates to the equilibrium phonon spectrum of the sample under study, or the decay time of quasi-stationary thermal grating is given by the equilibrium thermal properties. This is a strong assumption, whose validity can be explored via systematic variation of the pump fluence. Indeed, at large pump fluence, the system is thrown in a largely perturbed state, where the material properties (*e.g.* phonon frequency, thermal diffusion coefficient...) deviate from the equilibrium values. An example of this is discussed in chapter 4.

Four further comments:

- The quantity $\partial\chi_{ij}/\partial X_{kl}$ can be obtained from very different measurements: for instance, the influence of strain on the optical susceptibility can be derived from static elasto-optic experiments (see *e.g.* Ref.[18]). This demonstrates the utility of the conceptual separation between pump-induced excitation (Eq.2.10) and subsequent modification of the optical properties (Eq.2.11).

- In the presented scheme, the excitation triggered by the pump is also the one responsible for the variation in optical susceptibility: this is not always the case. Indeed, the primary excitation is oftentimes electronic: during its decay, different lower-energy states (*e.g.* electronic or vibrational) can be populated and thus form secondary gratings; finally, local thermalization produces a temperature grating, with corresponding stresses and density modulations. All these deviations from equilibrium can couple to the optical properties of the sample, so that they result in transient material gratings. The flow of energy from the optical grating to all these cascading excitations is basically encoded in $g_{ijkl}^{(p)}$. A possible scheme of the de-excitation path is sketched in Fig.2.7, involving electronic population ΔN,
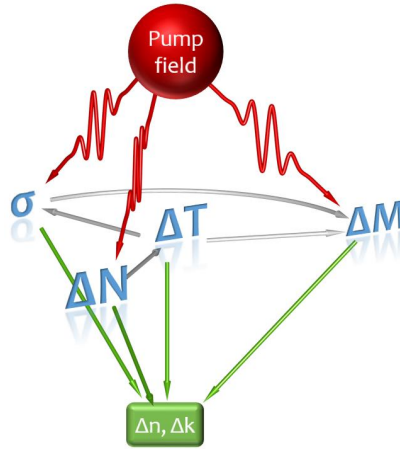
Figure 2.7: Scheme of possible de-excitation paths for a TG experiment. The field of the optical grating can couple to a primary population grating ΔN, to strain σ, to a magnetization grating ΔM; successive relaxation can lead to secondary gratings, like temperature gratings ΔT. In all cases, the transient material gratings couple to the optical constants Δn and $\Delta \kappa$.

strain σ, magnetization ΔM and temperature ΔT: these are the relevant cases for the experiments discussed in this thesis.

- The optical susceptibility is in general complex: the modulation of the optical properties of the sample can involve the refractive index (real part) or the extinction coefficient (imaginary part) as well, resulting in the formation of so-called phase or amplitude gratings, respectively, in analogy with standard grating nomenclature. The specificity of these two kinds can be addressed via phase-sensitive detection techniques [74].

- In single-pump experiments, the relaxation of the excitation either takes place locally (*e.g.* electron-hole recombination) or by OOP diffusion; with TG spectroscopy also the IP diffusion (*i.e.* lateral transport phenomena) can be addressed, as schematically shown in Fig.2.8. Comparison of TG and single-pump experiments allows to quantify anisotropic diffusion processes.

Step 3: Diffraction from transient gratings

The detection of the transient excitation in the sample proceeds with standard diffraction of the probe from the induced modulation of the optical susceptibility. The amplitude of the diffracted intensity is a measure of the amplitude of deviation $\Delta \chi_{ij}$ from equilibrium, namely the grating depth.

For the probe and scattered beams (denoted from now on with letters C and D, respectively), the usual law of diffraction applies [75]:

$$\Lambda \left[\sin \theta_C + \sin \theta_D\right] = m\lambda_C , \quad m = 0, \pm 1, \pm 2 \ldots \tag{2.12}$$

where m is the diffraction order; the angles θ_C and θ_D are measured from the sample normal, with the convention that an angle is positive if measured counter-clockwise (other
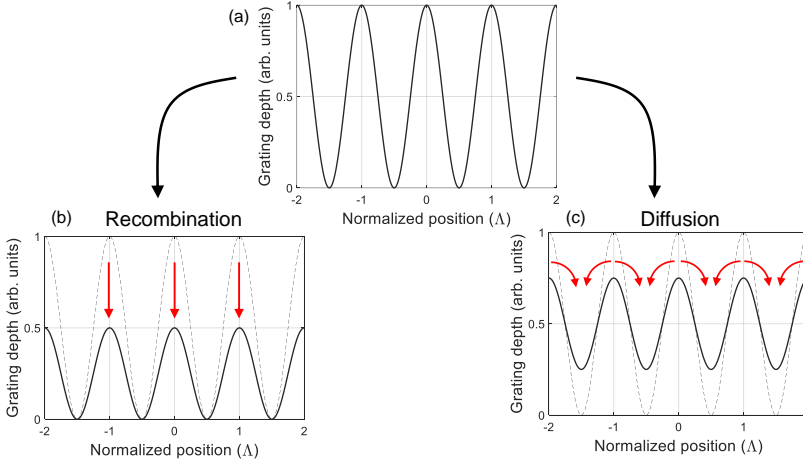
Figure 2.8: A material grating with unitary amplitude [panel (a)] relaxes via local recombination effects [panel (b)] or by diffusion [panel (c)]. In the former case, the maxima of grating depth reduce in amplitude; in the latter case the reduction of the maxima is accompanied by a rise of the minima. In both cases the overall contrast decreases.

conventions exist, with proper modification of Eq.2.12). The vectorial meaning is that the probe beam acquires, upon diffraction from the grating, an extra wavevector component equal to an integer multiple of the grating wavevector, namely

$$\mathbf{k}_D = \mathbf{k}_C + m\mathbf{q}, \quad m = \pm 1, \pm 2 \ldots \tag{2.13}$$

where $\mathbf{k}_D$ is the wavevector of the m-th order diffracted beam. Since the grating is not moving, the probe and scattered beams have the same frequency and absolute value of the wavevector.

If the grating thickness d is larger than its pitch Λ (case of *thick* grating), the grating wavevector is strictly on the reciprocal x axis. With the experimental geometry of Fig.2.9, Eq.2.13 becomes

$$\begin{aligned} k_{D,x} &= k_{C,x} + mq \\ k_{D,z} &= k_{C,z} . \end{aligned} \tag{2.14}$$

This set of equations can be solved, with the constraint of same frequency for the two beams, only if

$$2k_{C,x} = mq, \tag{2.15}$$

which is the Bragg condition. An equivalent restatement is

$$\sin \theta_C = \frac{m\lambda_C}{2\Lambda} ; \tag{2.16}$$

or again: [3]

$$|\theta_C| = |\theta_D| . \tag{2.17}$$

---

[3]Sometimes the angle of the diffracted beam is measured from the incoming beam, rather than from the grating normal. In this alternative case, Eq.2.17 is modified into $|\theta_C| = |\theta_D/2|$; Eq.2.12 must be modified, too.
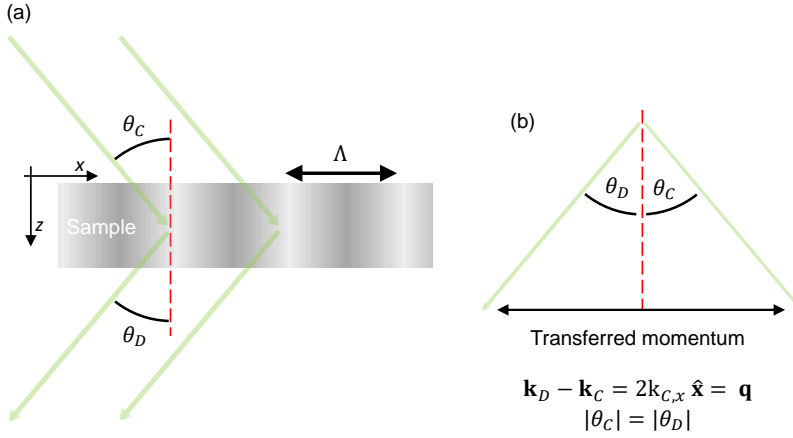
Figure 2.9: Sketch of Bragg diffraction in the case of a thick grating. (a) Diffraction in the Bragg condition occurs when constructive interference corresponds to specular reflection at the grating fringes: $|\theta_C| = |\theta_D|$. (b) In Bragg condition the transferred momentum is entirely along x and amounts at the grating wavevector **q**.

Restated again, in the Bragg configuration the angle for constructive interference also corresponds to specular reflection from the grating fringes. The physical meaning is that only in this reflection-diffraction configuration the waves diffracted at arbitrary depth along the z direction all add in phase (see Fig.2.9). In the opposite limit of $\Lambda \ll d$ (condition of *thin* grating), the grating wavevector exhibits smearing in the reciprocal z direction of order d^{-1} caused by the finite thickness of the grating. The constraints are relaxed in this case, and diffraction can take place also if the incidence angle is not matching the Bragg condition.

There is no clear boundary between these two limiting cases: this brings the discussion to the diffraction efficiency, which employing for brevity the complex refractive index $\tilde{n} = k + i\kappa$ reads

$$\eta = \left(\frac{\pi d}{\lambda_C}\right)^2 \left[(\Delta n)^2 + (\Delta\kappa)^2\right]\ \eta_g\ . \tag{2.18}$$

The efficiency depends of course on the grating depth (terms Δn and $\Delta\kappa$). Following Ref.[62], η contains also a geometrical term η_g accounting for the possibility of off-Bragg diffraction (namely, that the probe beam impinges at an angle different from the Bragg angle):

$$\eta_g = \left[\frac{\sin\left(\frac{\Delta q_z d}{2}\right)}{\frac{\Delta q_z d}{2}}\right]^2 , \tag{2.19}$$

where $\Delta q_z = |\cos\theta_C - \cos\theta_D|n_C k_C$ is the wavevector mismatch in the forward direction between probe and signal beams, and n_C is the refractive index at the probe wavelength. From Eq.2.19 η_g equals unity if:

- $d \to 0$, namely if the grating is thin or if the diffraction is due to surface morphological modulations: in these cases the geometrical coefficient is unimportant;
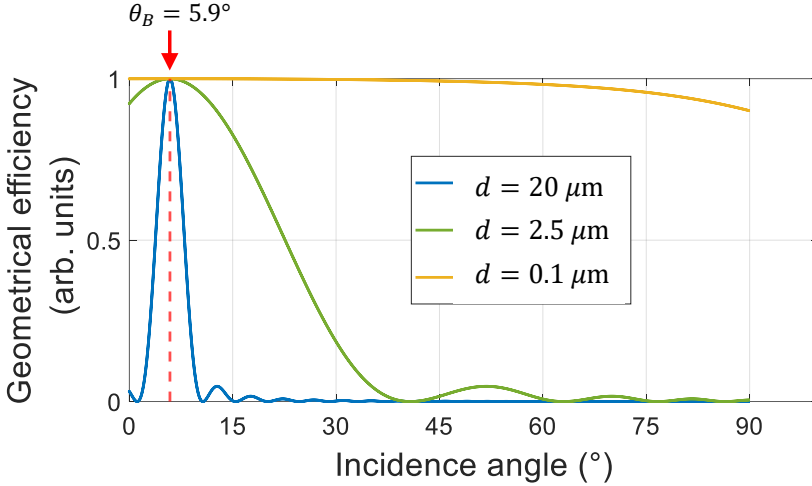
Figure 2.10: Geometrical efficiency η_g as a function of the probe input angle θ_C for three values of grating thickness d. The calculation, based on Eq.2.19, assumes values for probe wavelength, grating pitch and refractive index corresponding to the conditions for the experiments discussed in the following chapter, namely $\lambda_C = 0.514$ μm, $\Lambda = 2$ μm, $n_C = 1.5$. The peak of efficiency corresponds to proper Bragg configuration, and it is approximately $\theta_B = 5.9°$. The diffraction efficiency is symmetrical with respect to $\theta_C = 0°$.

- $\Delta q_z \to 0$, which happens if $|\theta_C| = |\theta_D| = \theta_B$, *i.e.* for proper Bragg incidence.

These aspects are shown in Fig.2.10, where the dependence of η_g on the input probe angle θ_C is shown for the case $\lambda_C = 0.514$ μm, $\Lambda = 2$ μm, $n_C = 1.5$ (relevant for the experiment discussed in the next chapter). Three values of grating thickness are assumed, namely $d = 20$ μm (thick grating, blue line), $d = 2.5$ μm (intermediate thickness, green line), $d = 0.1$ μm (thin grating, yellow line). The peak of efficiency is always at the same input angle, corresponding to proper Bragg configuration: $\theta_C = 5.9°$ for the considered parameters. What changes with the thickness is the width of the central lobe. For diffraction from thin gratings or from surface gratings η_g can be safely neglected; if the thickness is comparable with the pitch, as it is the case for SAWs, the tolerance in the input angle is still quite relaxed (FWHM $\approx 15°$); for thick gratings the requirement becomes more stringent (FWHM $\approx 2°$).

The diffracted intensity is proportional to η: for quasi-stationary grating η decays monotonously, while for a coherent mode it exhibits a time modulation at the mode frequency. Note that measuring the diffracted intensity is a standard experimental task, which does not require complex instrumentation: diffraction efficiency of 10^{-6} can be routinely detected, which corresponds to variation in the optical path $d\Delta n < \lambda_C/1000$ (assuming Bragg configuration: $\eta_g = 1$) [54].

Step 4: Detecting transient diffraction

If the probe beam is pulsed, the diffracted intensity is acquired in a stroboscopic fashion, setting the delay between pump and probe via a mechanical stage; if the probe is a CW beam, the diffracted intensity is continuously acquired via a fast photoreceiver and digitizer. In both cases, the signal beam propagates in a direction where no other beam
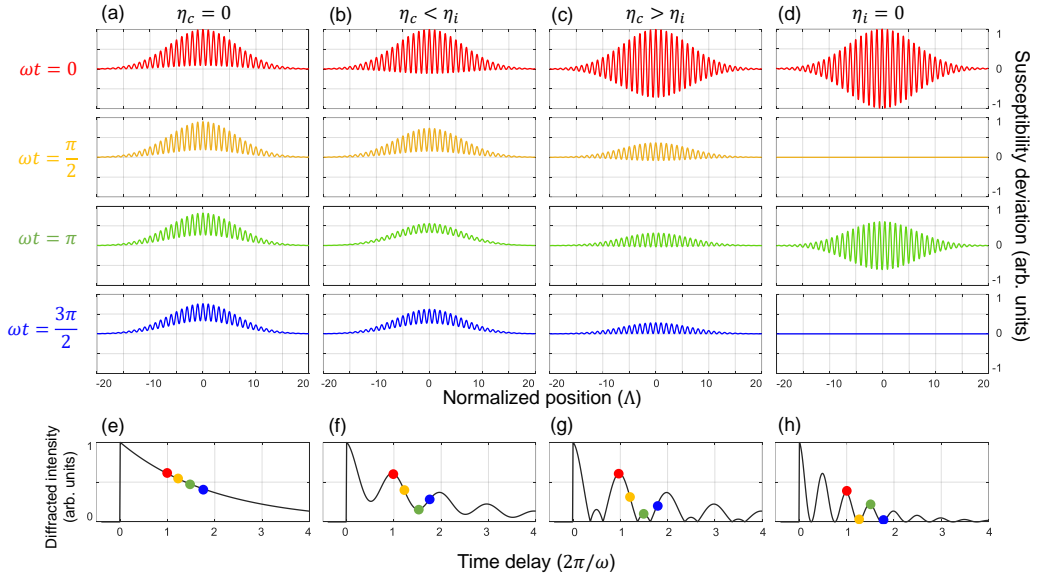
Figure 2.11: Simplicistic simulation of the induced material grating [panels (a-d)] and resulting diffracted intensity [panels (e-h)]. Four situations are considered, namely only quasi-stationary grating [$\eta_c = 0$, panels (a) and (e)]; coherent contribution smaller than the incoherent contribution [$\eta_c < \eta_i$, panels (b) and (f)]; coherent contribution larger than the incoherent contribution [$\eta_c > \eta_i$, panels (c) and (g)]; only coherent grating [$\eta_i = 0$, panels (d) and (h)]. For each case the deviation of the optical susceptibility $\Delta\chi$ is plotted as a function of the position along the sample surface normalized to the grating pitch Λ; a Gaussian spatial envelope was modeled. The amplitude of the material grating is plotted at four delays, covering a full period of the coherent contribution. The diffracted intensity, reported as a function of the normalized time delay (in units of $2\pi/\omega$), was obtained by squaring the material grating profile (see Eq.2.18), performing spatial Fast Fourier Transform (FFT) and acquiring the magnitude of the peak located at the grating spatial frequency. The coloured dots on the intensity traces relate to the four delays plotted in panels (a-d). If $\eta_c > \eta_i$ a spurious second harmonic appears in the intensity traces, that does not relate to any physical oscillation in the material: it simply originates from the π flip in the spatial phase of the grating (the green curves in panels (c-d) have opposite phase with respect to all the others).

is present: in this sense, TG spectroscopy is a background-free technique, in contrast to *e.g.* time-resolved reflectivity (tr-R) where the signal is a tiny modulation of a strong reflectivity background. Of course, this is true in theory: stray light is always present even in the direction of the signal, as due to ambient light and to diffuse scattering of the probe from the sample, and proper care must be taken to spatially and spectrally filter spurious beams.

   The diffracted intensity contains information on both the incoherent quasi-stationary grating and on the coherent modes (whenever present); let us assume that the two contributes are independent, so that the diffracted intensity is proportional to the sum of the incoherent efficiency η_i and the coherent efficiency η_c. [4] Four possibilities are schematically reported in Fig.2.11, where the instantaneous spatial configuration of the material grating is plotted at four successive time delays [panels (a-d)]; the diffracted intensity is

---

[4]Qualifying a contribution as *incoherent* automatically justifies this assumption; it is also basically always assumed in experiments.

computed as the magnitude of the spatial FFT peak at the grating wavevector. If only the incoherent contribution is present [panels (a) and (e)], the grating depth decreases monotonously, and the diffracted intensity as well. If $\eta_i > \eta_c$ at any time [panels (b) and (f)], the material grating keeps the same spatial phase during the entire dynamics, while the overall depth is modulated in time following η_c: the diffracted intensity is modulated accordingly. If $\eta_i < \eta_c$ [panels (c) and (g)], the spatial grating flips phase by π (or equivalently it shifts laterally by $\Lambda/2$) at every half period of the coherent mode [see the green curve in panel (c)]: since the scattered intensity is not sensitive to a spatial shift of the grating, this results in a modulation of the recorded signal at a frequency double of the real frequency of the coherent mode. In the limiting case of absent incoherent contribution [panels (d) and (h)], the diffracted intensity completely appears as an oscillation at double frequency. The situation can move from $\eta_c < \eta_i$ to $\eta_c > \eta_i$ during the grating evolution, if the incoherent contribution relaxes faster than the decay time of the coherent mode: for example in Ref.[76] the observed signal exhibits a decay of the component at frequency ω_c and the simultaneous rise of signal at frequency $2\omega_c$ (ω_c is the angular frequency of the coherent mode).

The analysis of the time traces must take care of this issue. In general, the acquired signal is analysed via time-domain fit of the *square* of the combination of the incoherent and coherent contributions: $I \propto (\eta_i + \eta_c)^2$. If the observed dynamics falls into the $\eta_c < \eta_i$ depicted scenario, and if only the coherent part is of interest, it is possible to fit the traces without squaring; alternatively, it is possible to fit the incoherent contribution and then analyse the residual oscillating contribution via FFT. Note that in this case the frequency is a reliable observable, while the decay constants are not: the advantage of this approach is that it is computationally cheap. This discussion is not required if phase-sensitive detection is performed: the recorded intensity is proportional to the scattered field, which encodes a possible spatial phase reversal of the material grating [74].

To conclude this section, it is interesting to compare TG spectroscopy to spontaneous light scattering, whereas radiation is diffracted by a Fourier component of the fluctuation of some material property; the process is spontaneous in the sense that the fluctuation is of statistical (thermal) origin. For instance in Brillouin Light Scattering (BLS) light is diffracted upon interaction with a low-energy excitation of the sample (acoustic phonons, magnons…), with energy compatible with the Bose-Einstein distribution at the experimental temperature. The transient grating basically is just a single Fourier component, but with an artificially enhanced amplitude, forced by the pump trigger. This analogy sets some common nomenclature for specific TG configurations: Impulsive Stimulated Brillouin Scattering (ISBS), or Raman Scattering (ISRS), corresponding to TG configurations addressing the same excitation range of Brillouin and Raman, respectively; when acoustic wave excitation is based on thermo-elastic effects ISBS is also known as Impulsive Stimulated Thermal Scattering (ISTS). A one-to-one correspondence between frequency- and time-domain techniques can be proven. Note, however, that TG spectroscopy also addresses excited states with energy far above $k_B T$ that are not thermally occupied: in this case there is no correspondence to spontaneous light scattering spectroscopy [54].

2.3   Some examples

Here some examples of the variegate phenomenology that can be probed with TG spectroscopy is given. The list is obviously non exhaustive: it mostly serves as an anthology

of some of the possibilities. Special attention is paid to magnetization-sensitive TGs. The examples given below mostly relate to a specific triggered dynamics; this is of course an approximation, as several mechanisms can coexist with the same pump trigger, and furthermore they can interact with each other, possibly resulting in complicated non-linearities. This is indeed the focus of the present thesis: acoustic and magnetization waves can be excited simultaneously and, under proper boundary conditions like external magnetic fields and anisotropies, they can interact with each other leading to novel dynamical situations.

Population gratings

Optical and Near Infrared (NIR) lasers mostly couple to electronic excitations in solid materials. Thus, the first effect of the optical grating on the sample is the promotion of electrons to some unoccupied higher-energy level [77]. A large non-thermal population of electronic levels affects the optical properties: this is clear for a two-level system, where population depletion in the ground state lowers the absorption cross-section (photoinduced transparency). This model, appropriate for semiconducting materials, predicts a modulation of the extinction coefficient $\Delta\kappa$, *i.e.* an amplitude grating. Apart from the Kramers-Krönig relations, effects of bandgap renormalization can also result in a modulation of the refractive index Δn: the general result is a mixed grating.

If the pump photon energy is resonant to an excitonic peak, excitons are nucleated in correspondence to the optical grating fringes. The same also happens if the pump has larger photon energy, after relaxation of non-thermal electrons and holes: this is an example of the formation of a time-delayed secondary grating. Large exciton density modifies the optical properties, thus monitoring the diffraction efficiency gives information on the exciton relaxation [78–80]. Two effects competes, namely recombination and diffusion (Fig.2.8). The former is a local effect: the efficiency lowers because the grating depth reduces. The latter is a non-local effect: excitons diffuse laterally from the nucleation regions to the unpopulated regions, resulting in homogeneous exciton population and thus in reduced diffraction efficiency. If the time constants for the two processes are different, they can be isolated. Moreover, for diffusion processes the time constant is quadratic in the wavevector and can be evaluated via TG experiments at different q; deviations from the quadratic trend mark the onset of super-diffusive or ballistic processes [81, 82].

Some semiconductors host spin-selective electronic transitions, which can be excited only by photon with appropriate circular polarization [83, 84]. Employing a polarization grating [*e.g.* orthogonal linear polarization for the two pumps, Fig.2.6(b)], the excited states display a population in the spin state rather than in the population density: the diffraction efficiency in crossed polarization detection is informative of both spin-flip or spin decoherence (local effect) and of spin diffusion (non-local effect), in analogy with exciton dynamics.

More exotic situations can be encountered in complex materials: for instance the population of quasi-particles in a cuprate superconductor gives information on the diffusion coefficient and on the scattering rates in the superconducting phase [85]. In general, a population grating g evolves via diffusion and recombination following a generalized diffusion equation [61]:

$$\frac{\partial g}{\partial t} = D\nabla^2 g - \frac{g}{\tau_r} \, , \tag{2.20}$$

where D is the diffusion coefficient and τ_r is the recombination time. The time constant τ_g for the decay of the population grating then is given as

$$\frac{1}{\tau_g} = Dq^2 + \frac{1}{\tau_r} \quad : \tag{2.21}$$

by changing the grating wavevector q the diffusive and recombination contributions can be disentangled.

Some chemical reactions are catalyzed by radiative energy, especially in the UV range. Thus, a solution of reactants under TG pumping at proper wavelength can end up in spatial modulation of reaction results, with possible different optical properties. Having a liquid solution is not mandatory: surface catalysis can be as well tackled in this way. For example, in Ref.[86] the entire dynamics of a reaction is observed via TG spectroscopy. This is an awesome example of multiple cascading material gratings: a population grating of the primary electronic state, excitation of acoustic phonons, population of a secondary metastable electronic state with successive formation of the reaction products, thermal diffusion away from the excited regions and finally volume change in the new product solution. All these processes take place at different timescales and can be singled out.

Thermal and phononic gratings

If fast de-excitation of the primary electronic grating takes place, a temperature grating can set in. Via thermo-optical coupling, a variation in the optical constants results; moreover, in the high-temperature fringes the material expands, leading to a density grating and to a surface displacement grating [16, 87–89]. All these effects are quasi-stationary, as they monotonously decay by heat diffusion; indirect measurement of anisotropic thermal diffusion coefficients can be obtained. The compresence of thermo-optical and displacement gratings results in a mixed phase and amplitude grating, which can be disentangled via phase-sensitive detection [74, 90].

Associated to the thermal grating, impulsive thermo-elastic expansion leads to counter-propagating acoustic fronts, namely to acoustic phonons [76, 91–93]. The wavevector selectivity of the thermal trigger acts as a filter on the broadband acoustic fronts: only those modes matching the grating wavevector q interfere constructively and build up a standing acoustic wave. In the acoustic wave, stress, density and temperature gradients all contribute to a time-dependent variation of the grating depth: thus the diffracted intensity is modulated with the same period of the wave. Note that the TG scheme only fixes the wavevector of the wave, while the frequency is dictated by the dispersion relation of the sample: thus several modes can be simultaneously excited if they have the same wavevector [94].

If the pump photon energy is below the fundamental energy gap, no excited electronic states are populated, and no thermal grating forms. Standing acoustic waves can still be triggered via electrostriction, which is a non-resonant second-order coupling between the external electric field (the optical field) and the sample mechanical degrees of freedom [72]. Basically the electric field induces in the sample an electric dipole which feels an attracting force towards the regions of high field amplitude: the pump pulse acts as an impulsive force setting a modulation in the density of the sample, *i.e.* a standing longitudinal acoustic wave. The effect is strong for large polarizability of the elementary unity (molecule in liquids or the unit cell in a solid). Note that in this case only a coherent
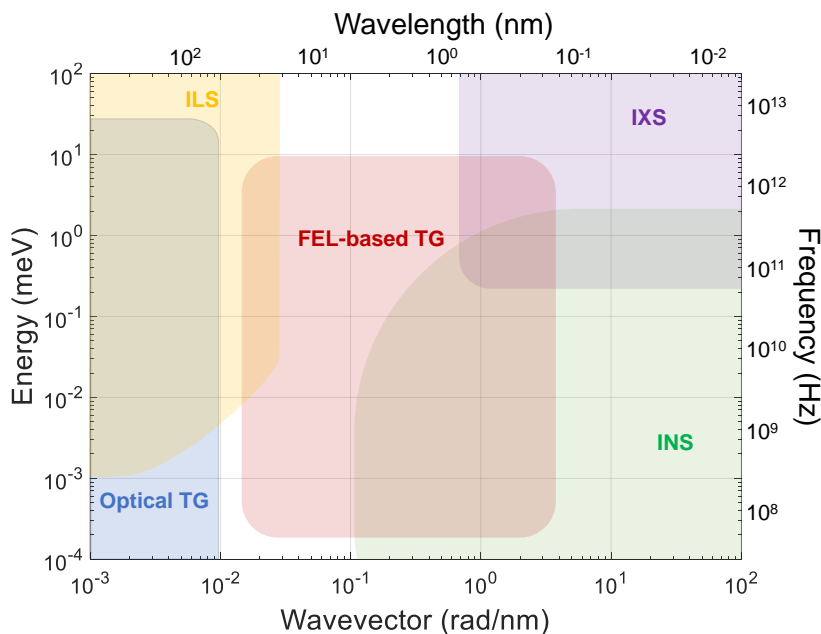
Figure 2.12: Range of typical accessible frequency and wavevector for different inelastic-scattering techniques, all capable also of magnetization-sensitive detection. ILS: Inelastic Light Scattering (Brillouin and Raman); IXS: Inelastic X-ray Scattering; INS: Inelastic Neutron Scattering.

contribution is triggered, without any incoherent quasi-stationary grating, as modeled in Fig.2.11(d) and (h).

Also optical phonons can be impulsively excited via TG. As discussed, the pump duration has to be shorter than the excited phononic mode. Thus the excitation of optical phonons (usually well within the terahertz range) requires pump pulses lasting less than 100 fs. The microscopic excitation mechanisms for optical phonons are peculiar: a broad categorization distinguishes between non-resonant stimulated Raman processes and resonant displacive mechanisms based on the Franck-Condon principle. In Ref.[95] the interested reader can find details. Note that the linear dispersion of acoustic phonons allows to evaluate the sound velocity from TG measurements at different q. On the contrary the dispersion for optical phonons is almost flat in the few inverse micron range: TG spectroscopy can prove valuable if the optical modes hybridize with other dispersive quasi-particles (see Ref.[96] for an example on optical phonon-polaritons).

Opportunities from magnetization-sensitive transient gratings

TG spectroscopy has not been applied intensively, so far, to investigate magnetization dynamics; recently this field is experiencing a boost [97–99], also motivated by the existence of setups for optical and EUV TG spectroscopy purposely dedicated to magnetization-sensitive TGs [62, 100].

Let us start with metallic ferromagnets, *e.g.* the 3*d* ferromagnets Fe, Co, Ni. These materials feature interband electronic transitions at optical frequencies, thus the pump

mechanism mostly involves photon absorption. [5] Employing two *s*-polarized beams, the intensity optical grating induces electronic excitation; on comparable timescale, magnetization quenching takes place with the same spatial period. Since the magnetization affects the off-diagonal components of the dielectric tensor, this dynamics is observable in polarization-analysed TG. On the tens of picoseconds timescale, the magnetization partially recovers, with corresponding fading of the diffracted intensity. This dynamics has been explored in thin films of ferrimagnetic alloys with perpendicular magnetic anisotropy employing EUV light gratings [100].

The magnetization quenching and the thermally-induced softening of MCA allows excitation of coherent magnon precession at the sub-nanosecond scale. This process requires specific geometry of external field and magnetic anisotropies, as will be detailed in Ch.4. The seminal experiment demonstrating this approach [101] employed a single pump, thus only non-propagating modes were observed (plus possibly PSSWs). Extension to TG pumping geometry would allow to excite finite-wavevector magnons, as recently demonstrated for ferrimagnetic alloys in an experiment led by Dr. A.A. Maznev at NFFA-SPRINT setup (results still unpublished).

On this timescale, acoustic waves with the same wavevector are also generated; frequency degeneracy can be obtained by tuning an external magnetic field. For this reason, this approach is well suited for the investigation of MEC, and this is the framework in which the experiments discussed in the next chapters were developed. Nanometric spatial resolution can be added if a TG pumping scheme is coupled to a pulsed Transmission Electron Microscopy (TEM) column, possibly with spin-polarization analysis (Lorentz Ultrafast TEM). This was demonstrated for a Permalloy film in Ref.[98], where the time- and space-dependence of the precessing magnetization was observed. Note that this seminal experiment suggested a fruitful exchange between the TG and TEM communities, aiming at advancing TEM technology to customize cartridges with on-demand sample environment and impulsive optical excitations [102].

In magnetic oxides, differently, non-thermal mechanisms for the excitation of the magnetization can be exploited, basically in a stimulated-Raman conceptual framework. If the pump photon energy is below the fundamental band-gap, electrons are promoted to a virtual in-gap state from which relaxation takes place as soon as the pump field is over. In the virtual state the different mixing of orbitals and crystal field can result in different SOC which exerts a torque on **M** for the duration of the pump pulse: when the system is back to the ground manifold, the magnetization is slightly tilted, and precession is triggered. This has been dubbed Inverse Faraday Effect, and has been demonstrated via single-pump excitation [103]: to the best of my knowledge, extension to TG spectroscopy has not been already demonstrated.

Finally, at the interface between a ferromagnetic insulator and a non-magnetic heavy metal a temperature gradient can generate a pure spin current via the spin Seebeck effect, in close analogy to thermo-electric effects [104]. The spin current can rely both on coherent magnon propagation or on incoherent diffusion: thus a time-resolved experiment based on TG excitation could be beneficial to investigate these different regimes. Moreover, the advanced modeling developed for anisotropic thermal diffusion could be extended to TG-triggered spin currents: in this context thermal TG at different wavevectors could be the technique of choice for scientific advancement in the field of spin-caloritronics.

---

[5]Any coherent electron spin precession in the conduction band is lost by electron-electron scattering with typical decoherence time of 5 fs, thus even within the pump duration [1].
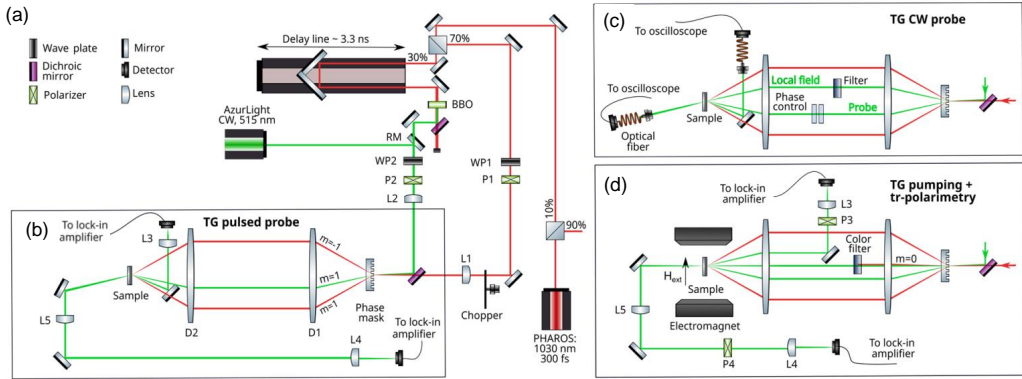
Figure 2.13: (a-b) Sketch of the optical table for TG spectroscopy at NFFA-SPRINT. The portion enclosed in panel (b) is the configuration for Mode 1 (TG spectroscopy with pulsed probe). (c) Configuration for Mode 2 (TG spectroscopy with CW probe). (d) Configuration for Mode 3 (TG-pumped optical polarimetry). Adapted from Ref.[107]

The aim of the presented literature overview and perspectives was to demonstrate the relevance of TG-based experiments for the investigation of spin and magnon dynamics, in particular in connection to the accessible frequency and wavevector range. As shown in Fig.2.12 optical TG spectroscopy covers the low-wavevector ($q < 10$ rad/μm) range; the frequency range is limited only in the upper side from the finite duration of the light pulses, while on the low-frequency side it is virtually unbound if suitable technical implementation is adopted. Note that extension of TG spectroscopy to attosecond pulses (still unexplored to my knowledge) could further extend the frequency range. This region in phase space largely overlaps to inelastic light scattering (ILS) techniques. At the large wavevector side, inelastic neutron scattering (INS) and inelastic X-ray scattering (IXS) allow to map the entire Brillouin zone of materials with good energy resolution. Technical advancements to implement TG spectroscopy at EUV and hard X-ray FEL facilities could allow to bridge the gap and to investigate the mesoscopic scale [60, 105].

2.4   TG spectroscopy at NFFA-SPRINT

At the NFFA-SPRINT (Nanoscale Foundries and Fine Analysis - Spin Polarization Resolved Instruments in the Nanoscale and Time domain) laboratory [106], a versatile setup for optical TG spectroscopy has been designed and implemented [107]. The light source is a Pharos (Light Conversion), which is a mode-locked amplified pulsed laser based on Yb:KGW gain medium; details on the Pharos source and on the other available sources (High Harmonics Generation source and Optical Parametric Amplifiers) are reported elsewhere [106, 108, 109]. An advantage of the Pharos source is its tunable repetition rate, which can be set from single burst to 1 MHz: this facilitates the optical alignment when nonlinear interactions are involved.

A sketch of the full optical setup is presented in Fig.2.13(a). It is conceived to allow for three different operational modes [panels (b-d)], which share the same upstream optical path. The three modes are described separately below; the common part is described together with Mode 1. Note that further details are given in the following chapters,

related to the specific experiment addressed case by case.

Mode 1: TG spectroscopy with pulsed probe

The setup is designed to work with the fundamental of the Pharos (1028 nm, 300 fs, transform-limited bandwidth of 5 nm). Only 10% of the Pharos intensity is delivered to the setup, while the remaining feeds other setups of the NFFA-SPRINT suite. The fundamental beam is splitted by a 70/30 beamsplitter: the larger portion is used for the pump, the remaining for generating the probe. The delay between the two portions is controlled via a corner-cube retroflector mounted on a mechanical delay stage (500 mm in length, corresponding to approximately 3.3 ns). After the delay stage, the second harmonic of the fundamental is generated in a BBO crystal (2 mm in thickness), to be employed as the probe beam (514 nm, 250 fs, 3 nm bandwidth). On both the pump and the probe paths, a half-wave plate and Glan-laser polarizer (WP1, P1, WP2, P2) allow to separately tune the energy per pulse; the polarizers are mounted on rotatable stages, allowing also for the rotation of the linear polarization of the beams.

The pump and probe beams are overlapped on a dichroic mirror and focused (lenses L1 and L2, $f = 20$ cm) on a diffractive phase mask (see details below). Several diffraction orders are obtained from the phase mask: only the $m = \pm 1$ orders for the pump and the $m = 1$ for the probe are selected, the others being mechanically blocked. These are the three input beams employed for TG spectroscopy. Note that the $m = \pm 2$ orders of the probe are collinear to the $m = \pm 1$ orders of the pump: this is not an issue as long as the probe intensity is kept significantly lower (usually a factor one hundred). The beams are collimated and focused on the sample by a couple of achromatic doublets (D1 and D2, $f = 10$ cm, 3 inches diameter) in $4f$ confocal configuration (*i.e.* from the front focus of D1 to the back focus of D2 the total distance is $4f$: the doublets are separated by $2f$). This configuration avoids a further delay stage to optimize the time overlap between the two pump beams, as they follow the same optical path. Moreover, it allows to minimize aberrations in the propagation of the Gaussian beams, and to reproduce on the sample a 1:1 image of the optical field present on the phase mask. The space available between the doublets allows also to separately control the polarization state of the pump beams.

The focused pump beams generate the transient grating in the sample, which diffracts the probe beam. Typically the footprint dimension is 50 μm (FWHM) for the pump and 30 μm (FWHM) for the probe. These quantities are not fixed, as will be explained later: actual experimental values are given explicitly in the following chapters. Large variability is present also for the fluences: typical values are in the few millijoule per square centimeter for the pump, and down to the microjoule per square centimeter range for the probe; these values are appropriate for pump-probe experiment on metallic thin films, while for insulating oxides much larger pump fluences are appropriate (some tens of millijoule per square centimeter can be reached).

The diffracted intensity is detected with a photoreceiver (Newport Femtowatt 2151) and fed into a lock-in amplifier (SR860), which is phase locked to a mechanical rotating chopper (50% duty cycle, 719 Hz) positioned along the pump path. The time resolution is limited by the cross-correlation of the pulse duration, *i.e.* about 400 fs, while the maximum delay is about 3.3 ns. This operational mode was employed for the experiment discussed in Ch.3.

Mode 2: TG spectroscopy with CW probe

If the dynamics induced by the pump event is slow enough, it can be recorded continuously with a large-bandwidth detection chain. To this purpose, a CW single-mode fiber laser (ALS Azurlight) is available. It radiates at 514 nm, right the same wavelength of the Pharos second harmonic. Via a flip mirror along the probe path [indicated as RM in Fig.2.13(a)] it can substitute the pulsed probe, and it is routed along the same path. In this operational mode the diffracted beam is recorded by a fast photoreceiver (1544-B from Newport, 12 GHz bandwidth) which is fiber-coupled to a large-bandwidth oscilloscope for digitization (Lecroy, 4 GHz bandwidth). The detection chain thus sets the largest frequency detectable to 4 GHz (corresponding to about 250 ps), while in principle no limit is set to the maximum delay observable. This operational mode is well suited to perform phase-sensitive detection [107].

Mode 3: TG-pumped optical polarimetry

In this operational mode, the same pump scheme is adopted, while for the probe the $m = 0$ order is employed; proper spectral filtering of the zero order pump is required. The polarization of the beam after interaction with the sample is selected by a Glan-laser polarizer. This mode is suitable for investigation of magnetization dynamics: a horseshoe electromagnet generating a uniform field ($\mu_0 H = \pm 100$ mT) at the sample position can be mounted. The time resolution is the same as Mode 1 if pulsed probe is employed or as Mode 2 if CW probe is employed. This mode was employed for the experiment discussed in Ch.3.

Phase masks

A phase mask is a diffraction grating where the difference in optical path is given by the real part of the refraction index (recall the distinction outlined above between phase and amplitude gratings). It is usually produced employing a transparent material (negligible extinction coefficient) and mechanically digging grooves on its surface: the accumulation of optical phase is given by the different amount of material that the rays pass through. Importantly, by proper design a phase mask can maximize the intensity diffracted at specific orders: this proves useful if only the $m = \pm 1$ orders are employed, as it is the case in the discussed setup.

The employ of phase masks for TG setups was first proposed in 1998 [110], and found large application since then [16, 52]. In Fig.2.14(a-b) a sketch is reported, illustrating the problematic that is solved with phase masks. If the pump beams are generated via a 50/50 beamsplitter, they have zero pulse-front tilt. With 300 fs duration, the longitudinal extension of the pulse is about 90 μm; if the transverse extension is about 1 mm FWHM, the propagating pulse is a very oblate ellipsoid with aspect ratio 10. One can imagine the pulse as a coin propagating with a face head-on: the optical intensity is sizeable only within the physical volume of the coin. Having zero pulse-front tilt means that the optical wavefronts are parallel to the coin face. In this condition the region of interference of the two pump pulses is limited by geometry, as can be seen in panel (a). On the contrary, upon diffraction a pulse acquires a significant pulse-front tilt: the optical wavefronts (which in air are orthogonal to the propagation direction, in the paraxial approximation) are not parallel to the faces of the coin-shape volume of sizeable intensity. In the proposed toy model, the coin is propagating with an angle between the direction
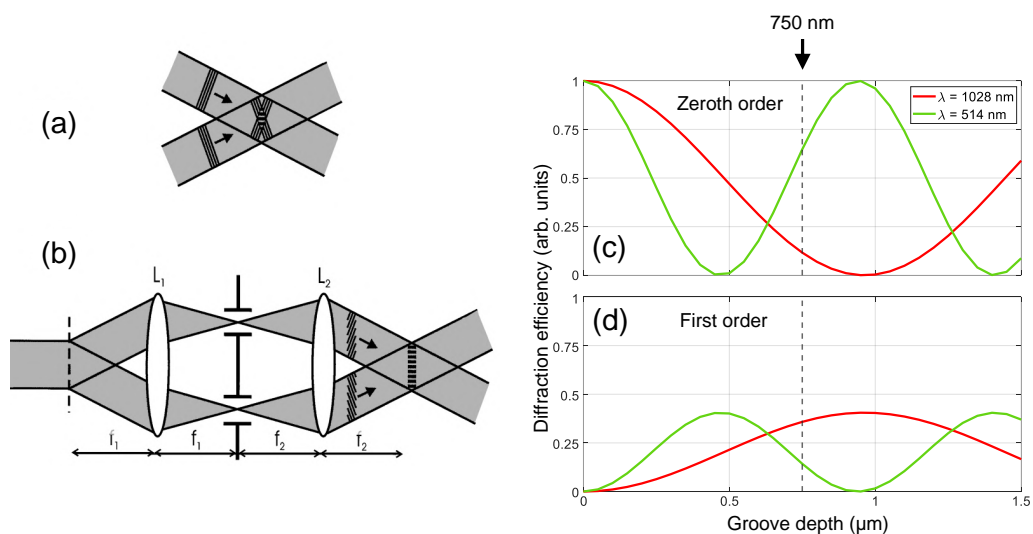
Figure 2.14: (a) If the pump pulses are obtained via a beamsplitter, no pulse-front tilt is introduced, resulting in reduced interference volume. (b) Adoption of a diffractive phase mask and confocal configuration introduces a pulse-front tilt in the propagating pulses: the interference volume is larger. From Ref.[110]. (c-d) Computed diffraction efficiency for the zeroth and first orders as a function of the groove depth; the calculation, based on Ref.[111], considers α-quartz masks and rectangular cross section of the grooves. The vertical dashed lines indicate the depth chosen for the fabrication.

of propagation and its surface normal. This condition, which is oftentimes a nuisance as deteriorates the time resolution [112], is advantageous if confocal configuration is employed: indeed, in the interaction region a larger overlap is obtained, and the resulting optical grating exhibits more fringes, as shown in panel (b). The TG experiment improves in signal-to-noise ratio. For details on the beam propagation, see Ref.[110].

The choice of diffractive phase masks for beam splitting is advantageous for other two reasons. First, if also the probe beam is obtained as a diffraction order of the same phase mask, the beam configuration at the sample position is automatically appropriate for Bragg diffraction, for any employed wavelength. This can be easily shown since the Bragg condition is the same equation giving the diffraction angles from the phase mask: if the transport optics preserve the mutual angles, both conditions are simultaneously satisfied. For this reason, in the present thesis the problematic of the geometrical efficiency of diffraction due to off-Bragg configuration was not taken into account. The second reason is related to the alignment of the detection branch: the diffracted beam is usually very weak and not detectable by eye (unless very high fluence is employed, at the risk of damaging the sample), thus accurate geometrical computation of the propagation direction is required. If a phase mask is employed, the $m = -1$ diffraction order of the probe is by design collinear to the signal beam, and it can be used for alignment.

At the TG setup presented here, phase masks were indeed employed: they are made of α-quartz (crystalline allotrope of SiO$_2$), produced via micromachining, UV lithography and dry etching at the IOM-CNR lithography facility [113]. Following literature [111], the efficiency of the phase masks can be computed as a function of pitch, groove depth, material and wavelength: as shown in the calculations reported in Fig.2.14(c-d), it is not possible to optimize the diffraction efficiency for both the pump and the probe. A compromise was adopted, setting the groove depth at 750 nm, favouring the pump efficiency (about 85% of the maximum first order efficiency) while the probe is lowered (about 40% of the maximum first order efficiency). As from Eq.2.7, the TG wavevector can be tuned by changing the incidence angle of the pump beams. To this purpose, three phase masks have been produced, with spatial period 5.05, 6.01, and 8.00 μm.

Note that the confocal configuration of the doublets reproduces at the back focal plane of D2 the same optical *field* present at the front focal plane: if an intensity grating is produced, it will have the double spatial frequency (*i.e.* the pitch Λ of the optical grating is half the pitch of the employed phase mask). Another effect of the adopted configuration relates the position of the phase mask and the spot size at the sample position. Let us assume that the front focal plane of D1 corresponds to the back focal plane for L1 and L2. In the optimal configuration the phase mask is located in the same plane: in this case the beams overlap at the back focal plane of D2 where they also exhibit the beam waist (condition of strongest focusing). If the phase mask is moved along the optical axis, the position of beam crossing after D2 does not correspond anymore to the waist of each beam, resulting in larger beam footprint on the sample.

Other reasons for versatility

The setup is conceived as a user facility within the NFFA consortium. As such it is well suited for on-demand modifications, as required by users for particular experimental needs. Here some aspects are briefly outlined.

- In all the operational modes, the signal can be acquired either in transmission or in reflection, as sketched in all the schemes of Fig.2.13. The $m = -1$ order of the probe

allows for easy optical alignment in both cases. Note that all the beams propagate parallel to the optical table: thus for reflective TG experiments (Modes 1 and 2), the sample has to be tilted in order to spatially separate the incoming probe from the outgoing signal.

- Analysis of the polarization of the signal can be performed also in diffraction experiments, as convenient to probe magnetization gratings.

- The setup can be employed for pump-probe experiments with a single pump by simply blocking one of the pump beams between the doublets. In this way, time-resolved reflectivity, transmissivity and polarimetry can be performed at the same experimental TG endstation. The tr-MOKE experiments discussed in Ch.4 and 5 have been performed in this configuration.

- Inserting wave plates between the two doublets it is possible to modify independently the polarization of the two pumps: this will prove relevant in the future to perform experiments with intensity gratings (both beam s-polarized), polarization grating (one beam s-polarized and one p-polarized), or mixed gratings (other configurations).

- The sample environment can be further specialized by usage of a UHV cell, cryogenic holder (40 K), external electric fields.

- Other operational modes can be implemented: for example, the possibility to perform heterodyne detection for polarimetry studies (the local field has to be rotated for this purpose); or the simultaneous detection of the non-rotated and rotated components of the polarization in the signal beam, which would allow for simultaneous acoustic and magnetic characterization: a quarter-wave plate and a Wollastone polarizer can be the optics of choice.

Part II

A TG approach
to magneto-acoustic waves

All-optical generation and time-resolved polarimetry of magneto-elastic resonances via TG spectroscopy

Employing the spin degree of freedom for memory storage and logic computation is one of the goals in spintronics and magnonics. Much experimental and theoretical effort is devoted to the exploitation of SWs, with improved energy efficiency of devices as charge-scattering-induced Joule dissipation is avoided; moreover, SWs well within the terahertz range have been observed, allowing to envision new generation devices at higher operational frequency [114]. Interesting reviews on the role of spintronics and magnonics for future technology can be found in literature [115–117].

Still, the generation of magnons is energetically demanding, and efficient methods to excite SWs are needed. The employ of MEC proved to be a promising pathway to overcome this issue, and also to enhance the lifetime of propagating SWs [13]: in particular, SAWs have been employed to investigate phonon-magnon coupling, as fostered by the degeneracy of SAW and SW dispersion in the few gigahertz and inverse micron ranges. Thus, SAW-driven coherent and long-living SWs can be obtained. For the investigation of magneto-elastic waves, a good starting point is a planar heterostructure composed of a ferromagnetic thin film on a semi-infinite substrate. Indeed, the quality and anisotropy properties of the ferromagnetic overlayer can be engineered via the growth recipe: based on deposition technique, chosen substrate and environmental conditions during deposition, epitaxial layers can be obtained, possibly with specific static strains as due to lattice mismatch to the substrate; or isotropic polycrystals, where the absence of IP anisotropy axes often simplifies the theoretical modeling and the comparison between experimental techniques.

IDTs on piezoelectric substrates have been employed to acoustically excite SWs in magnetic thin films [43]. The condition of SAW-FMR can be effectively reached, whereas the rf SAW elastic deformation replaces the traditionally applied rf electromagnetic field. However, this approach has some limitations, *e.g.* a limited flexibility in the explorable frequencies, due to the defined pattern of the transducers, and their in-contact operation, which requires advanced lithography facilities. Starting from 2015, Tobey and co-workers reported an all-optical approach for both the excitation of SAWs and the tr detection of the magnetization dynamics in ferromagnetic thin films, thus demonstrating a contact-less and non-invasive tool for studying magneto-acoustics and SW dynamics [118]. Their experimental approach is based on TG spectroscopy, which was proved to be efficient in generating coherent SWs in a ferromagnetic film; moreover, full tunability of SAW frequency is available by varying the grating pitch, setting this technique in the useful window for SAW-driven magnonics.

The experiment presented in this chapter expands on that approach, employing the versatile optical setup described in Ch.2. A systematic study of TG-based SAW-FMR on polycrystalline Ni thin films was performed; the wavevector-selective TG excitation scheme was combined with tr-FR, allowing for time-domain polarimetry on the triggered magnetic transients. The results presented here below confirm the observations of Tobey's group [97]. In addition, the quantitative comparison to B-FMR measurements allows (i) to estimate the effective magnetization M_{eff} and the Gilbert damping α for the investigated samples, (ii) to draw the boundaries of applicability of TG-based SAW-FMR for the investigation of magnetostatic properties of samples, and (iii) to envision specific systems that could benefit from such approach.

Three reasons can be identified for the relevance of a TG-based SAW-FMR approach. First, it is a local technique, where the volume probed is limited by the footprint of the employed laser. For comparison, standard FMR techniques are unavoidably volume-integrated;[1] also SAW-FMR with IDTs misses local resolution. Second, TG spectroscopy is wavevector-selective: information on the resonance dynamics of non-uniform modes can be addressed, with special emphasis on decay channels. Third, being TG a tr technique, the timescale for magnon-phonon coupling and the role of coherence therein can be addressed; note that this last aspect was not elaborated further, and it remains for future research.

This chapter is organized as follows: in Sect.3.1 the sample is briefly described, referring to Appendix C for further information; the details of the employed experimental techniques can be found in Sect.3.2, while the results of TG-based measurements are reported in Sect.3.3; Sect.3.4 reports comparison to B-FMR measurements, together with the discussion of the applicability limits of TG-based SAW-FMR; conclusions are drawn in Sect.3.5. The results discussed in this chapter have been published [99].

3.1   Sample growth and characterization

The experiment was conducted on three samples made of polycrystalline Ni thin films, with different thickness t and substrate. For brevity, the samples will be indicated with the letters A, B and C. For sample A, $t = (14 \pm 2)$ nm and the substrate is a (001)-oriented CaF_2 single crystal (MSE Supplies). For samples B and C, the substrate is amorphous fused silica SiO_2 (Ted Pella); the thickness is $t = (14 \pm 2)$ nm for sample B and $t = (8 \pm 2)$ nm for sample C. In all cases, the films are capped with a SiO_2 layer with thickness $t = (10 \pm 2)$ nm to prevent Ni oxidation, while ensuring high transmission of optical beams. Films and capping layers were deposited by e-beam evaporation at the CNR-IOM FNF clean room facility in Trieste, Italy.

The samples were characterized in their structure and morphology via Grazing Incidence X-Ray Diffraction (GIXRD) and X-Ray Reflectivity (XRR) in collaboration with CNR-IMM and Università degli Studi di Milano-Bicocca; morphological characterization via Atomic Force Microscopy (AFM) was also conducted at the CNR-IOM facility in Trieste; from the magnetostatic point of view, static longitudinal MOKE and FMR were performed. The details of the characterization are omitted here for brevity; the interested reader can refer to Appendix C for a thorough discussion. The relevant conclusion of this material-science side is that sample A appears as possessing the higher-quality ferromagnetic film, especially from the morphological point of view. This is attributed

---

[1]Other techniques exist, *e.g.* Nitrogen-vacancy microscopy: in this case magnetization precession can be probed with nanometer spatial resolution.

to the crystallinity of the substrate, resulting in a more ordered growth. For this reason, the following investigation has been performed on sample A; some final results on parametric magnon excitation are obtained also from sample B and C.

Choice of ferromagnetic material and substrate

Owing to its high saturation magnetostriction coefficient ($\lambda_s = -38 \cdot 10^{-6}$ for a polycrystal [119]), Ni is often the ferromagnet of choice for investigating magneto-acoustic dynamics; for comparison $\lambda_s = -7 \cdot 10^{-6}$ for Fe [28]. Ferromagnetic alloys like Galfenol or Terfenol-D exhibit record magnetostriction coefficient ($\lambda_s \approx 2000 \cdot 10^{-6}$, [27]): they can be object of future investigation. Moreover, as will become clear later, in order to observe SAW-FMR via tr-FR, it is necessary that the spatially modulated pump-induced heating results in a significant magnetization reduction: the Curie temperature of Ni ($T_C = 628$ K [28]) is sufficiently low to ensure good magneto-optical contrast.

The choice of the substrates is guided by a simple model developed on the basis of Ref.[54], where the coupling of thermal and stress-strain gratings is discussed in the framework of TG spectroscopy. For isotropic systems, or cubic ones whenever the TG wavevector q is directed along a $\langle 100 \rangle$ crystalline axis, the longitudinal strain ϵ_{xx} along q (assumed as the x axis) can be evaluated as

$$\epsilon_{xx} = \beta_{\text{eff}} \, \delta T \, , \tag{3.1}$$

where δT is the temperature rise inside the medium, and

$$\beta_{\text{eff}} = \alpha_{\text{th}} \left(1 + 2 \frac{C_{12}}{C_{11}} \right) \tag{3.2}$$

is the effective thermal expansion coefficient appropriate for plane-wave geometry; in Eq.3.2, α_{th} is the thermal expansion coefficient and C_{ij} are the elastic stiffness coefficients (in Voigt notation). The ratio C_{12}/C_{11} can be recasted using the Poisson ratio $\nu = \frac{C_{12}}{C_{11} + C_{12}}$. Thus, Eq.3.2 can be written as

$$\beta_{\text{eff}} = \alpha_{\text{th}} \frac{1 + \nu}{1 - \nu} \, . \tag{3.3}$$

On the other hand, given sample volume V, heat deposited Q and material specific heat capacity at constant pressure c_{th}, the temperature rise can be expressed as

$$\delta T = \frac{Q}{V c_{\text{th}}} \, . \tag{3.4}$$

Thus, for the seek of comparison between different substrates, a thermo-elastic efficiency η can be usefully defined as

$$\eta = \frac{\epsilon_{xx}}{Q/V} = \frac{\alpha_{\text{th}}}{c_{\text{th}}} \frac{1 + \nu}{1 - \nu} \quad : \tag{3.5}$$

it quantifies the amplitude of the acoustic excitation for given input thermal density stress. Besides the thermo-elastic efficiency, the magneto-optical contrast depends on the spatially periodic temperature gradients and on the associated magnetization modulation: thus, a higher thermal conductivity k_{th} of the substrate is detrimental for the

Table 3.1: Thermo-elastic efficiency η and figure of merit $\mathcal{F}$ as from Eq.3.6, both normalized to the CaF_2 value, together with relevant parameters for different substrates (mainly transparent). The substrates employed in the present experiment are highlighted in bold.

Substrate	α_{th} $(10^{-6}\,K^{-1})$	ν	c_{th} (J/kg·K)	k_{th} (W/m·K)	η_{norm}	$\mathcal{F}_{norm}$
CaF_2[a]	18.85	0.26	854	9.7	1	1
Al_2O_3[b]	5.8	0.21-0.33	753	41.9	0.31-0.41	0.07-0.09
$SrTiO_3$	9.4[c]	0.24[d]	518[d]	12[c]	0.79	0.64
MgO[e]	9-12	0.35-0.37	880-1030	30-60	0.48-0.79	0.08-0.26
SiO_2[f]	0.54-0.57	0.15-0.16	700-750	1.0-1.5	0.03	0.17-0.29
Si[g]	7-8	0.27	668-715	84-100	0.45-0.55	0.04-0.06

[a] Ref.[120], [b] Ref.[121], [c] Ref.[122], [d] Ref.[123], [e] Ref.[124], [f] Ref.[125], [g] Ref.[126].

experiment, as it brings faster thermalization. A cumulative figure of merit $\mathcal{F}$ can be defined via the following relation:

$$\mathcal{F} = \frac{\eta}{k_{th}} = \frac{\alpha_{th}}{k_{th}c_{th}}\frac{1+\nu}{1-\nu}\,. \tag{3.6}$$

Tab.3.1 reports results for some commonly used substrates; those employed in the present experiment are highlighted in bold font. CaF_2 was chosen as a crystalline, high-$\mathcal{F}$ substrate, and SiO_2 as an amorphous, low-$\mathcal{F}$ (about four times smaller) substrate.

The validity of the model that results in Eq.3.6 is limited by three assumptions.

- The leading stress component is longitudinal and parallel to q: this is the case in TG spectroscopy on metallic systems and for an intensity grating, as the case discussed here.

- The deposited heat Q is independent on the substrate material. This is the case in this experiment, since the absorption of radiative energy from the pump laser mostly takes place in the Ni overlayer, with almost no contribution from the transparent substrate and capping layer. Thus the thermal input stress can be assumed to be the same, at fixed Ni film thickness (while of course it will be smaller for sample C, where the Ni film is thinner);

- The substrate volume involved in the expansion is independent on the material under study. This assumption is not completely valid in the present case, since the volume involved in SAW oscillation depends on the particular acoustic mode considered, at fixed wavevector. Moreover, heat diffusion phenomena are neglected: for example, the amount of volume of substrate involved in thermal expansion depends on thermal conductivity, on thermal contact resistance and on time.

3.2 Experimentals

The magneto-acoustic dynamics was investigated via TG-based spectroscopy. As discussed in Ch.2, SAWs can be generated via the absorption of energy from the pump beams and subsequent thermo-elastic expansion; the spatial modulation of the pump
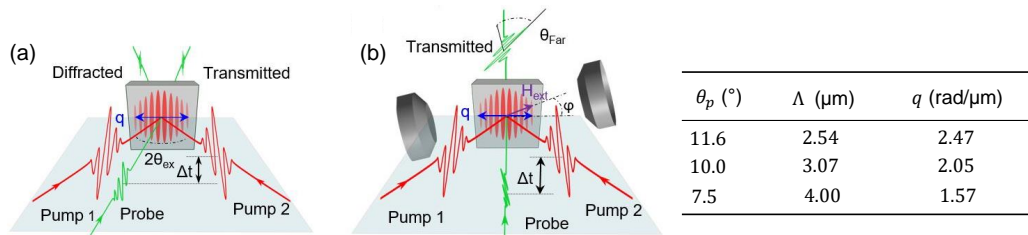
Figure 3.1: Sketch of the experimental end-stations for acoustic TG [panel (a)], and TG-pumped tr-FR [panel (b)]. The pump beams impinge on the sample with opening angle $2\theta_{ex}$ and generate a modulated excitation with wavevector q. The probe beam inquiries the sample at delay Δt after the pump trigger: in TG it is partially diffracted, while in tr-FR it is transmitted, acquiring a FR angle as a result of magneto-optical interaction with the sample magnetization. For tr-FR the external magnetic field B_{ext} is oriented IP at azimuth angle $\varphi \approx 15°$ from q. From Ref.[99]. The table reports pump off-normal angle θ_p, TG pitch Λ and wavevector q for the three experimental configurations adopted.

θ_p (°)	Λ (μm)	q (rad/μm)
11.6	2.54	2.47
10.0	3.07	2.05
7.5	4.00	1.57

intensity is inherited by the SAW pattern, whose wavelength thus matches Λ, the TG pitch. In a ferromagnetic medium, a SW of equal wavelength and frequency is generated via inverse magnetostriction [35, 127]: thus, with a magneto-optical probe it is possible to measure the dynamics of the SAW-driven SW. Recalling the relation between the TG wavevector q and the experimental parameters (Eq.2.7), the wavevector of the excited SAW and SW can be tuned by changing the impinging pump angle θ_p or the pump wavelength λ_p; here the former approach was adopted.

Optical setup

For this experiment, Mode 1 and Mode 3 detailed in Sect.2.4 were employed. In both configurations the pumping scheme is the same, only the probe and detection geometry being modified for the magneto-optical one. In Fig.3.1 sketches of the experimental end-station for these two setups are reported.

The sample is set in the vertical (x, y) plane. The pumps and the probe are s-polarized. Three geometrical configurations were used, which differ in the angle θ_p of the incoming beams; this results in three wavevectors q, whose values are summarized in Fig.3.1. Pulse energy was set to 30 nJ for each pump and 200 pJ for the probe. The laser footprint (FWHM) on the sample was about 40 μm for the pump and about 25 μm for the probe. This sets the average fluence on sample to 4.8 mJ/cm^2 for the pump (considering both beams) and 40 μJ/cm^2 for the probe. The laser repetition rate was set to 50 kHz. An external IP magnetic field B_{ext} is set with azimuth $\varphi \approx 15°$ with respect to the grating wavevector q, thus ensuring stronger MEC in the system. Note that this value for φ is at odds to MEC for uniform films, which is expected to peak at $\varphi = 45°$ [41]; however, it has been shown [128] that in a sample with modulated magnetostatic properties (as it is the case for the stripe-heated thin film) MEC peaks at about $20°$, with suppression at $45°$. The experiment reported was performed under ambient conditions at room temperature.

For the acoustic TG setup [Fig.3.1(a)], the probe beam is routed on the transient grating at the Bragg angle. The diffracted intensity, modulated by the SAW, is directly recorded by the photoreceiver. For the magneto-optical setup [Fig.3.1(b)], the probe
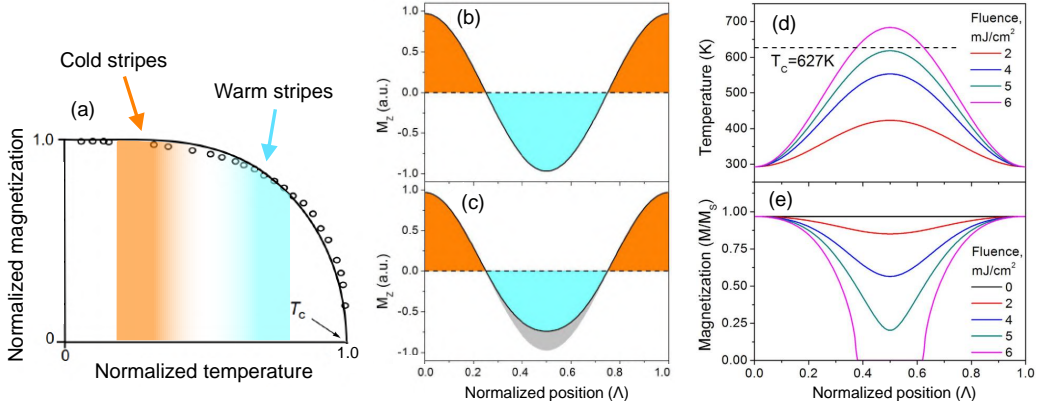
Figure 3.2: (a) Temperature dependence of M_s for Ni. The Curie temperature $T_C = 628$ K is indicated. Cold stripes (orange shaded filling) and warm striped (light blue shaded filling) exhibit different values of M_s. Adapted from Ref.[28]. (b-c) Spatial dependence of the dynamical magnetization M_z along a full SW wavelength at a fixed time; the color filling highlights regions with positive (orange filling) or negative (light blue filling) contribution to Eq.3.7. For zero temperature modulation [panel (b)], the two contributions are equivalent; for finite temperature modulation [panel (c)], the warm region (here those negatively contributing) is partially quenched. Adapted from Ref.[97]. (d-e) Spatial dependence of the local temperature $T(x)$ [panel (d)] and magnetization [panel (e)] along a full SW wavelength, as obtained from finite-element calculations. Different pump fluence conditions are reported. Adapted from Ref.[97].

beam is sent normal to the sample surface. Upon crossing the sample, the light polarization changes as a result of FR; the transmitted beam is polarization-analyzed with a Glan-laser polarizer set close to extinction [8], and the resulting intensity is recorded by the photoreceiver. In both setups, the signal is collected in transmission.

The probe footprint on the sample is much larger than Λ. This is an advantage for TG acoustic detection, since diffraction from a grating only takes place if several fringes are illuminated. [2] For what concerns the magneto-optical measurement, however, this can be an issue. Indeed, at a given time t, the dynamical component of the SW can be written as $M_z(x,t) = A\cos(qx + \phi)e^{-i\omega t}$, where A is the amplitude of wave, ϕ is an appropriate spatial phase, and ω is the angular frequency. Thus the spatial average $\langle M_z(t) \rangle_\Lambda = e^{-i\omega t} \int_0^\Lambda dx\, A\cos(qx + \phi) = 0$: the transmitted beam exhibits zero FR, at any time. Nonetheless, if the TG pumping scheme is employed, the SW and SAW amplitude distributions are entangled to a periodic temperature profile $T(x)$ along q, since the trigger mechanism is of thermal origin. [3] For this reason, the local saturation magnetization $M_s(x)$ is not uniform, but displays a reduced value in correspondence to the warm regions, to first approximation following the relation $M_s(T(x))$: the local temperature $T(x)$ determines the local value of M_s along the equilibrium magnetization curve, as schematically depicted in Fig.3.2(a).

---

[2]The resolving power R of a diffraction grating scales with the number N of illuminated grooves: $R = mN$, where m is the considered diffraction order.

[3]This is not the case in general. For example in Ref.[129] finite-wavevector SWs are excited via ultrafast electric current pulses, and the sample temperature is uniform. Detection via tr-MOKE is possible thanks to ultra-tight focusing of the probe (below 1 μm): for SWs with wavelength larger than the probed region, the spatial integral of M_z does not sum up to zero.

For a SW in such thermally-modulated landscape, the relation $M_z(x) = \tilde{A}\cos(qx + \phi)$ is a good approximation, where $\tilde{A} = A\frac{M_s(T(x))}{M_s(0)}$: the SW amplitude is modulated by a factor determined by the local temperature at position x. In this case a finite magnetization is obtained after spatial integration:

$$\langle M_z(t) \rangle_\Lambda = e^{-i\omega t} \int_0^\Lambda dx\, A \frac{M_s\left(T(x)\right)}{M_s(0)} \cos(qx + \phi) \neq 0 \,. \tag{3.7}$$

The FR of the transmitted beam is proportional to this integral. Detailed investigation and modeling of this aspect are reported in Ref.[97]. With the aid of finite-elements calculations (COMSOL Multiphysics) the authors computed for different pump fluences the local temperature $T(x)$ and the local magnetization $\frac{M_s(T(x))}{M_s(0)}$; the results are reported in Fig.3.2(d-e). It is now clear why the Curie temperature of the magnetic thin film is a key parameter to the magneto-optical sensitivity, as anticipated earlier. Low T_C results in complete demagnetization of the film, while high T_C results in too small modulation of M_s: both cases lead to reduced magneto-optical contrast. Note that the spatial modulation of M_s depends on the time elapsed after the pump triggering, because of thermalization in the film: at the same pace magneto-optical contrast is lost (*i.e.* the integral in Eq.3.7 approaches zero). This is the reason why the thermal conductivity was considered at the denominator in the definition of the figure of merit (Eq.3.6): with a high-k_{th} substrate the system would reach thermal equilibrium before the whole SW dynamics is over, thus introducing unwanted observational artifacts.

FMR setup

The B-FMR measurements were carried out using a homemade setup available at Università degli Studi di Milano-Bicocca. The sample is positioned between the polar extensions of a Bruker ER-200 electromagnet, maintaining its surface parallel to B_{ext} in the so-called *flip-chip* configuration for IP measurements. To induce **M** precession the samples are fixed on a grounded coplanar waveguide, connected to a rf source (Anritsu). The FMR signal for a fixed frequency is acquired by measuring the derivative of the absorption power downstream of the electrical transmission line as a function of B_{ext} through a lock-in amplifier. For further details on the FMR setup see Ref.[130].

The sketch reported in Fig.3.3 helps in understanding technical similarities and differences between B-FMR and TG-pumped SAW-FMR. For both techniques, the static field B_{ext} is assumed to be uniform and, together with the magnetic shape anisotropy, determines the equilibrium axis of the magnetization. In B-FMR [panel (a)], the oscillating field is provided by a rf current in a metallic waveguide. By design the oscillating magnetic field B_{rf} is orthogonal to B_{ext}, thus maximizing the magnetic dipole torque. The magnetic moments precess in-phase across the whole sample [panel (b)]. In SAW-FMR [panel (c)],the rf field is provided by the effective MEC field resulting from the SAW strain (the acoustic wavefronts are represented as red stripes). Sizeable torque requires a finite angle between B_{ext} and q. The finite wavelength of the rf field results in magnetization precession with spatial-modulated phase, *i.e.* a SW [panel (d)].
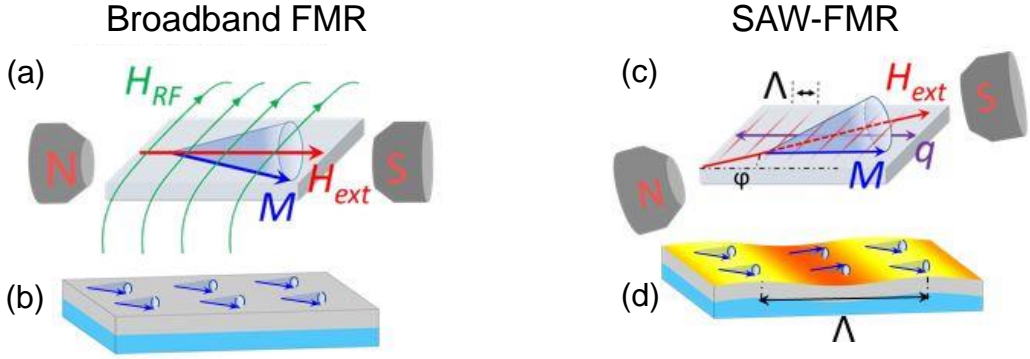
Broadband FMR

(a)

(b)

SAW-FMR

(c)

(d)

Figure 3.3: Sketch of the working principle for B-FMR and SAW-FMR. (a) The IP static magnetic field H_{ext} sets the direction of the equilibrium axis for the magnetization M; the rf excitation field H_{rf} is orthogonal to H_{ext} and can drive M into precession. (b) The magnetization precession is uniform across the entire sample. (c) In SAW-FMR an acoustic wave (the red stripes represent the wavefronts) with wavelength Λ can drive the magnetization precession via MEC effective field. The strength of the magneto-elastic torque depends on the angle φ between H_{ext} and the wavevector q. (d) The magnetization precession is not uniform, but it rather follows the spatial modulation of the acoustic driving wave: it is a SW. Adapted from Ref.[99].

3.3 TG-pumped dynamics

Acoustic dynamics

A typical measurement of TG-pumped acoustic dynamics for sample A is reported in Fig.3.4. The trace is acquired with a TG pitch $\Lambda = 2.54$ μm, corresponding to $q = 2.47$ rad/μm.

Panel (a) reports the TG raw data (blue circles). The trace oscillations lie on top of a decaying background of thermal origin, as discussed in Ch.2. The background was modeled with the functional form $I_{\text{bkg}} = Ae^{-\gamma t} + mt + q$; this can be interpreted as the incoherent sum of two heat dissipation channels, *i.e.* a sub-nanosecond decaying exponential, and a longer decaying exponential that is effectively described by a linear contribution. Another possibility is a slight misalignment of the delay line, resulting in a steady signal decrease at increasing delay. The data within 50 ps after time zero have been excluded from the analysis, as highlighted with the yellow-shaded box. Indeed, the combination of small bandwidth of the photoreceiver and of lock-in amplification results in long integration time: for this reason the fast electronic response of the material in the first picoseconds after the TG excitation is severely undersampled and distorted. A detailed investigation of the early times would require finer time steps, and it is beyond the scope of the present experiment.

The residuals after background subtraction show oscillations across zero [blue circles in Fig.3.4(b)]. As seen from the FFT magnitude of the residuals, reported in panel (c), two peaks are visible, indicating that two SAWs are excited by the TG pump. The contribution to the spectral weight at low frequency is probably a signature of incomplete background subtraction and is not further considered. A satisfactory model for the time-domain data encompasses two damped sines:

$$I = A_1 \sin\left(2\pi f_1 t + \phi_1\right)e^{-\gamma_1 t} + A_2 \sin\left(2\pi f_2 t + \phi_2\right)e^{-\gamma_2 t} + B \, . \tag{3.8}$$

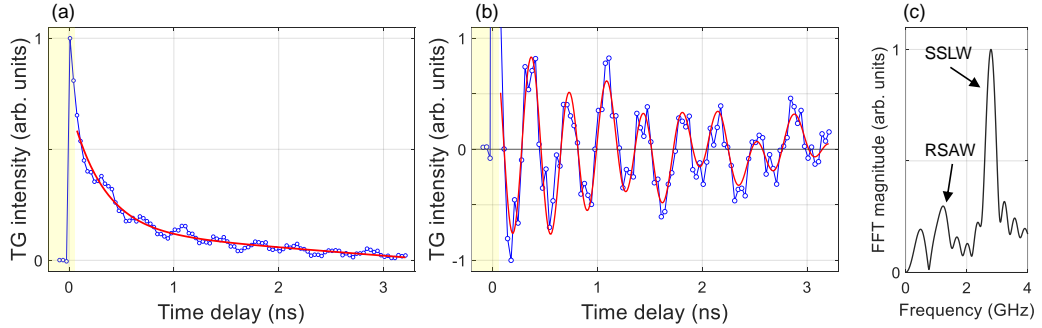**Figure 3.4:** TG acoustic investigation of sample A, for $\Lambda = 2.54\ \mu$m ($q = 2.47$ rad/μm). (a) Raw TG data (blue circles) normalized to the maximum intensity are fitted with the functional form reported in the main text (red solid line) modeling the incoherent background. (b) The residuals (blue circles) display acoustic oscillations around zero; a model encompassing two exponentially-damped sines is fitted to the data (red solid line). Data within 50 ps after time zero (highlighted with the yellow shaded region) have been excluded from the analysis. (c) FFT magnitude of the residuals. The contributions of RSAW and SSLW to the spectral weight are indicated. Adapted from Ref.[99].

Table 3.2: Best-fit parameters for the model reported in Eq.3.8, and phase velocities.

	A (arb. units)	f (GHz)	ϕ (rad)	γ (rad/ns)	c (km/s)
RSAW	0.11 ± 0.09	1.26 ± 0.06	0.0 ± 0.9	0.0 ± 0.4	3.2 ± 0.2
SSLW	1.0 ± 0.2	2.79 ± 0.02	1.3 ± 0.2	0.6 ± 0.2	7.1 ± 0.05

The best-fit parameters are reported in Tab.3.2; the phase velocity $c = \Lambda f$ of the two modes is also reported. From previous studies [97], the lower- and higher-frequency acoustic modes are attributed to the Rayleigh surface acoustic wave (RSAW) and to the Surface-Skimming Longitudinal Wave (SSLW), respectively.

Magneto-acoustic dynamics

The time-varying strain field of the observed SAWs is exploited as an effective rf magnetic field, resulting in SAW-FMR, as discussed in Ch.1.

The analytical dependence of the FMR frequency f on the resonance field $H_{\text{eff}}^{\text{res}}$ strongly depends on the magnetic anisotropies of the sample. In the case of a thin isotropic ferromagnetic film with IP H_{ext}, Kittel [131, 132] calculated

$$f = \frac{\mu_0 \gamma}{2\pi} \sqrt{H_{\text{eff}}^{\text{res}} \left(H_{\text{eff}}^{\text{res}} + \mu_0 M_{\text{eff}} \right)} . \tag{3.9}$$

The quantity M_{eff} is called effective magnetization [133, 134]. For a saturated ferromagnet it is related to M_s via

$$M_{\text{eff}} = M_s - \frac{2K_s}{\mu_0 M_s t} , \tag{3.10}$$

where K_s is the surface anisotropy constant and t is the thickness of the film. [4] Note that

---

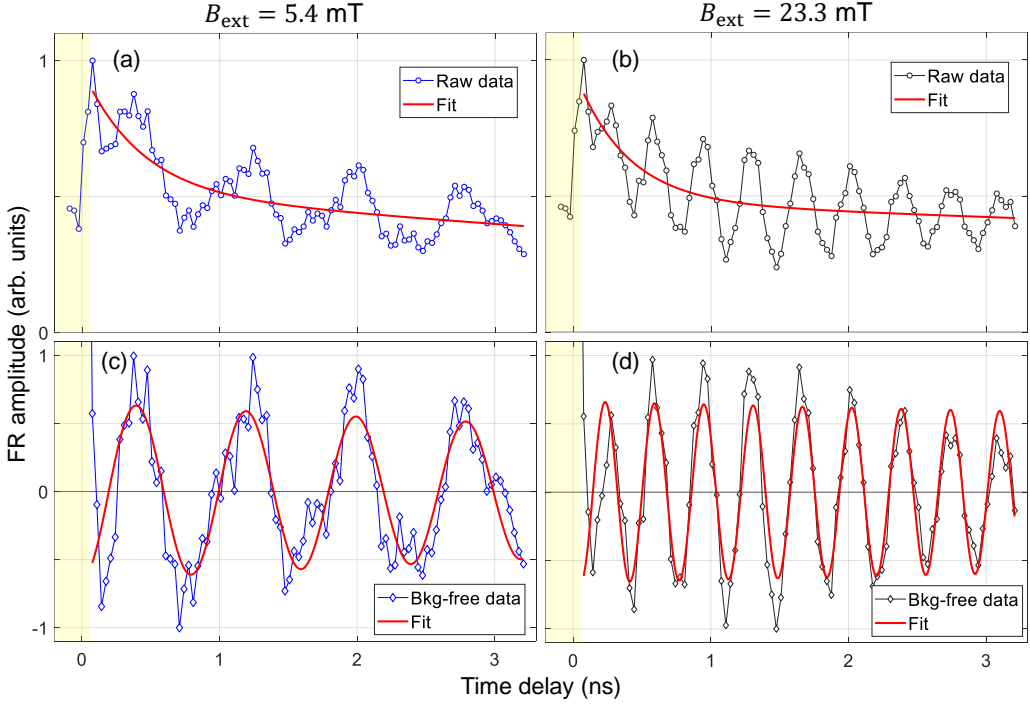[4]Basically the correction term accounts for the surface- and interface-related OOP anisotropy, mostly of

Figure 3.5: TG-pumped tr-FR for sample A and $\Lambda = 2.54\ \mu$m. The static magnetic field is set to $B_{\text{ext}} = 5.4$ mT [panels (a) and (c)] and $B_{\text{ext}} = 23.3$ mT [panels (b) and (d)]. The raw data (blue and black circles) are reported in panels (a-b), together with the fit of the background (red solid lines). The background-free data are reported in panels (c-d) (blue and black diamonds); the single-mode fits of the oscillating amplitudes are also reported (red solid lines). In all panels, the yellow box highlights the $t < 50$ ps time window, which is excluded from the analysis. Adapted from Ref.[99].

for the isotropic case here investigated, $H_{\text{eff}}^{\text{res}}$ can be substituted with $H_{\text{ext}}^{\text{res}}$; moreover, in what follows the magnetic field $B_{\text{ext}} = \mu_0 H_{\text{ext}}$ is considered.

In Fig.3.5 TG-pumped tr-FR traces are reported for sample A, again with $\Lambda = 2.54$ μm. Data for two values of B_{ext} are reported, namely $B_{\text{ext}} = 5.4$ mT [panels (a) and (c)] and $B_{\text{ext}} = 23.3$ mT [panels (b) and (d)]. As will be motivated later, these field strengths have been chosen as they correspond to SAW-FMR driven by RSAW or by SSLW, respectively. In panels (a-b) the raw data are reported (blue and black circles), together with the best-fit for background subtraction. Similarly to the acoustic data (see Fig.3.4) the first 50 ps after time zero have not been considered in the analysis, and they are masked with the yellow box. Note, with respect to Fig.3.4, that the linear background at late time delays is significantly flatter, indicating that the thermal and magnetic incoherent backgrounds are not proportional to each other, but rather have proper dynamics: this seems a hint that MEC is sensitive to the degree of coherence in the populated modes (coherent oscillations versus incoherent decays). Further investigation is required to draw any conclusion. Note also that the pre-edge data lie on a non-zero baseline, as due

---

roughness-related origin. According to Ref.[133], it is only for historical and customary reasons that this is taken into account in a renormalization of M_s, instead of being added to H_{eff} as an additional magnetic field term.

to non complete extinction of the crossed polarizer employed for the FR detection: TG spectroscopy is a background-free technique, differently from FR. [5]

The background-free traces are reported in panels (c-d) (blue and black diamonds); the fit of the oscillating traces with a single-mode exponentially-damped sine is also reported (red solid lines). From these plots it is apparent that the frequency of the tr-FR signal strongly depends on B_{ext}. Note that the amplitude of the SSLW-driven precession [panel (d)] is not properly modeled with an exponential decay, but rather displays an amplitude peak at about $t = 1.5$ ns. The shift of amplitude peak from $t = 0$ to a finite delay for SAW-driven magnetization precession is reported in literature if a misplacement is present between the source of SAWs and the probe region [45]; in the present trace probably the probe focal point was shifted from the center of the Gaussian pump footprint. Since in what follows the analysis proceeds in frequency-domain rather than in time-domain, this aspect has not been further investigated.

The frequency dependence of the tr-FR traces on B_{ext} was investigated systematically. In Fig.3.6(a) the two-dimensional map of tr-FR signal is reported versus pump-probe time delay and versus magnetic field. The field is swept from positive to negative values in 1.8 mT steps. Note that the field steps are comparable to the coercivity of the sample [see Fig.C.3(a)]: phenomena related to magnetization reversal are not observable, being entirely condensed in the trace across $B_{ext} = 0$ mT; the sample is in magnetic saturation otherwise.

To highlight the presence of a resonance behaviour, FFT was performed for each trace; the two-dimensional resulting map is reported in panel (b). The spectral weight is condensed in specific regions of frequency and magnetic field. Overlaying to the map the frequency of the TG-pumped SAWs (white dashed lines), clear matching is obtained. The interpretation, following previous literature [45, 97], is that the spectral weight enhancement indicates SAW-driven resonances, visible if $B_{eff} = B_{eff}^{res}$, such that the frequency of magnetization precession matches either the RSAW or the SSLW frequency. Note that for any value of B_{ext} both SAWs are at play, but the resonance condition can be reached only for one SAW at a specific field. Similar maps are acquired with TG pitches $\Lambda = 3.07$ μm and $\Lambda = 4.00$ μm (not shown here). A change of Λ corresponds to a change of the RSAW and SSLW frequency, along the linear dispersion relation of acoustic modes: hence, SAW-FMR resonances can be tuned at the desired frequency and magnetic field.

3.4 Comparison to FMR results

The first step to compare SAW-FMR to B-FMR results is to extract the resonance frequency and field strength for each peak in the FFT magnitude maps; also the FWHM of each peak along the field axis is extracted, as it is informative of the damping. The procedure has been carried out for the three available TG pitches ($\Lambda = 2.54$, 3.07, and 4.00 μm); in Fig.3.7(a) it is exemplified for the case $\Lambda = 2.54$ μm. The symmetry $B_{ext} \to -B_{ext}$ is exploited by folding the FFT map around the $B_{ext} = 0$ axis, in order to obtain better contrast; note that no hysteretic behavior is expected to be averaged out by this procedure, given the small coercivity $B_c < 2$ mT. From the folded map, the SAW-FMR resonance frequency is computed by integrating over a suitable range of magnetic field (approxi-

---

[5]Here with *background* we mean any detected signal that is not related to the investigated dynamics: in this sense, the pre-edge finite FR observed in Fig.3.5 is the result of an unwanted background, while the nanosecond-scale decay is an incoherent component of the triggered dynamics − even though it is then subtracted to the trace in order to highlight the coherent component, *i.e.* the oscillations.
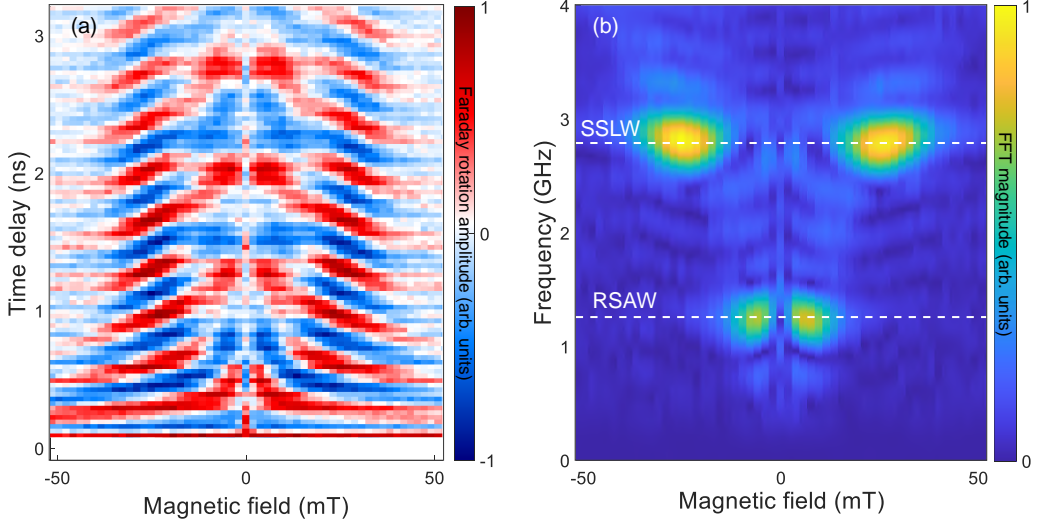
Figure 3.6: Time- [panel (a)] and frequency-domain [panel (b)] maps of tr-FR obtained on sample A for $\Lambda = 2.54\ \mu$m. The magnetic field is swept from positive to negative values. In panel (b) the horizontal dashed lines highlight the frequency of the TG-pumped acoustic waves. Adapted from Ref.[99].

mately 10 mT, but the exact range was checked to be not relevant) across the center of the FFT peak; then to the frequency-dispersed curve a Gaussian model was fitted to extract the peak frequency [panel (b)]. Similarly, by integrating over a suitable range of frequencies (approximately 500 MHz) across the center of the peak, the resonance magnetic field and its FWHM linewidth were determined via fitting again a Gaussian model [panel (c)]. Two peaks are observed for each pitch Λ, resulting in a total of six resonance points available for SAW-FMR.

Panels (d-e) Fig.3.7 compare these results to B-FMR. The resonance frequency obtained with both techniques as a function of B_{ext} is reported in panel (d). Visually, there is good matching of the two datasets; to get a quantitative estimate, the Kittel model (Eq.3.9) was fitted. For the fit to B-FMR data, both γ and M_{eff} are free parameters: the best fit is obtained for $\gamma = (2.10\pm0.06)\cdot10^{11}$ rad/s·T and $M_{\text{eff}} = (199\pm18)$ kA/m; in more common units this corresponds to $\gamma/2\pi = (32.0\pm0.9)$ GHz/T and $\mu_0 M_{\text{eff}} = (0.25\pm0.02)$ T. For the fit to SAW-FMR data, γ was kept fixed to $\gamma = 2.10\cdot10^{11}$ rad/s·T, as due to the limited number of data. The model fits the data for $M_{\text{eff}} = (195 \pm 16)$ kA/m, *i.e.* $\mu_0 M_{\text{eff}} = (0.25 \pm 0.02)$ T. Excellent agreement is observed.

Note the low M_{eff} values obtained, as compared to the saturation magnetization of Ni at room temperature ($M_s = 490$ kA/m [28]). In general, from Eq.3.10 a reduction from M_s is expected, especially in thin films, and for systems with large surface anisotropy (see Ref.[130] and the Supplemental Material therein). From Eq.3.10 the surface anisotropy can be calculated as

$$K_s = (M_s - M_{\text{eff}})\mu_0 M_s t/2\ , \tag{3.11}$$

resulting in $K_s = (1.26\pm0.07)$ mJ/m^2, which is comparable to literature values for rough thin films [135].
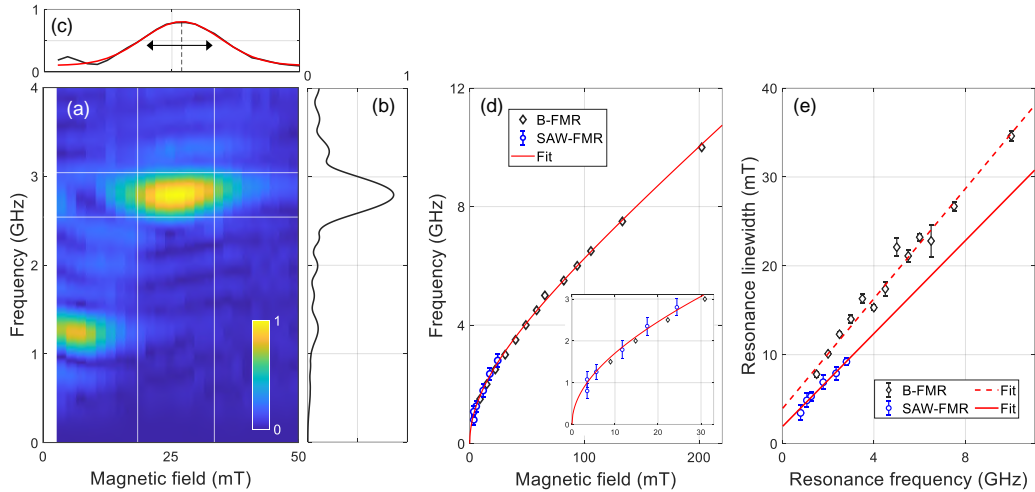
Figure 3.7: (a-c) To extract field strength, frequency and linewidth of the SAW-FMR resonances, the FFT magnitude maps have been folded [panel (a)]; the resonance frequency is obtained from Gaussian fitting of the spectrum obtained from integration in a 10-mT region across the resonance [panel (b)]; similarly, the resonance field strength and linewidth are obtained from Gaussian fitting of the lineshape obtained from integration in a 500-MHz region across the resonance [panel (c)]. The white lines in panel (a) indicate the chosen regions for the frequency and field integration. The reported map is for the case $\Lambda = 2.54\ \mu$m; the identical procedure has been carried out for the other resonance at 1.26 GHz, and for the other pitch values. (d) All the resonance frequencies from SAW-FMR are plotted as a function of the resonance field strength (blue circles), together with the results from B-FMR (black diamonds); the errorbars are the 95% confidence level of the Gaussian fit, and they are not visible in the B-FMR data. Only one fit of the Kittel model is reported (red solid line), as the best-fit curves for the two datasets are not distinguishable on the present scale. The inset reports a zoom-in on the low-frequency region. (e) Resonance linewidth as a function of the resonance frequency for SAW-FMR data (blue circles) and B-FMR (black diamonds). The linear fit of Eq.3.12 is reported as a red line, solid for SAW-FMR and dashed for B-FMR. Adapted from Ref.[99].

It is worth stressing that the magnetostatic parameters obtained via SAW-FMR and via B-FMR are in agreement. This allows to rule out two effects that could be thought to be playing a role, as itemized here below.

- Finite sample temperature, which reduces M_s and thus also M_{eff}. As the same M_{eff} is observed, both techniques are probing the sample at room temperature (or at least at *the same* temperature). This is somewhat surprising, as the triggering mechanism of the TG-based dynamics is of thermal origin: apparently, on the time-scale of the observed oscillatory dynamics (few nanoseconds), the temperature profile is closer to room temperature, and the magnetostatic parameters are not modified thereof.

- TG-induced static and dynamic rippled pattern on the sample surface, which could lead to an additional uniaxial anisotropy term of magnetic dipolar origin. From literature, this effect is known to be negligible for ripple wavelength larger than about 100 nm [61, 136, 137].

The FWHM linewidth ΔB of the resonances are reported in Fig.3.7(e). For B-FMR, the linewidth is the FWHM in a sweep of B_{ext}. For SAW-FMR, it is the FWHM of the resonance peak along the field strength axis; to be properly compared, this value has to be divided by $\sqrt{3}$. This factor is required, as can be derived from Ref.[35], since the SAW-FMR maps display the FFT magnitude rather than the imaginary part. Following standard FMR analysis [133], the Gilbert damping α is calculated by fitting the linear dependence of the linewidth on the resonance frequency:

$$\Delta B = \frac{4\pi\alpha}{\gamma} f + \Delta B_{\text{inh}} \, , \tag{3.12}$$

where ΔB_{inh} is the so-called inhomogeneous broadening term, which is a frequency-independent resonance broadening resulting in an offset. It is generally ascribed to magneto-structural disorder [133]. The best-fit parameters are $\alpha = (47 \pm 5) \cdot 10^{-3}$ and $\Delta B_{\text{inh}} = (1.8 \pm 0.5)$ mT for SAW-FMR; and $\alpha = (52 \pm 2) \cdot 10^{-3}$ and $\Delta B_{\text{inh}} = (3.9 \pm 0.4)$ mT for B-FMR. Again the agreement between the two techniques is generally good, indicating that the same physics is being probed. The Gilbert dampings from the two datasets are compatibile within the errorbars, while the inhomogeneous broadening is slightly larger in B-FMR. This can be attributed to large-scale sample inhomogeneities that give a contribution to B-FMR, as it is an area-integrated technique; the 25 μm in diameter of the probe footprint for SAW-FMR can be assumed as a lower bound for the spatial scale of such inhomogeneities.

Calculated magnon bands

As discussed in Ch.1, the SW dispersion in a ferromagnet is quadratic at large k, while it can be non-monotonous in the low-k range, as due to dipolar interactions. For this reason, it cannot be assumed *tout court* that the Kittel model can be employed to analyse the SAW-FMR data, as it is developed for the uniform precession mode. In the following, we see that for the specific case discussed in this chapter the SW dispersion is basically flat in the addressed wavevector range. This means that it is possible to directly compare SAW-FMR to B-FMR data on the basis of the Kittel model.

The approach was to numerically compute the SW dispersion, following Ref.[33, 138], where an approximate analytical relation for dipole-exchange SWs is provided. The computation employs the following parameters, suitable for sample A:
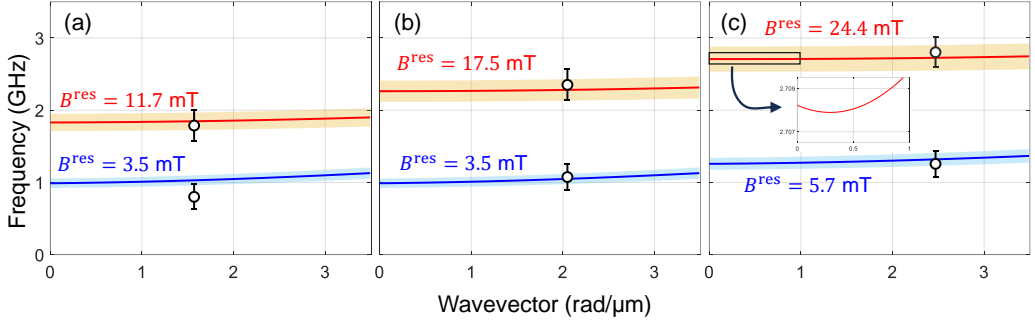
Figure 3.8: Comparison of experimental SAW-FMR results (black circles) with computed approximate SW dispersion. Panels (a-c) refer to $\Lambda = 4.00, 3.07$, and 2.54 μm, respectively. Red and blue solid lines and bands are the computed SW dispersions for the indicated values of B^{res}; the other parameters used for the calculation are reported in the main text. The inset in panel (c) shows a magnified region at low wavevector, where the dispersion non-monotonicity can be appreciated.

- Thickness of ferromagnetic layer $t = 14$ nm

- Effective magnetization $M_{\text{eff}} = (195 \pm 16)$ kA/m

- Magnetomechanical ratio $\gamma/2\pi = 32$ GHz/T

- Continuum exchange constant $\alpha_{\text{ex}} = 5 \cdot 10^{-17}$ m^2 ($\alpha_{\text{ex}} = 2A/\mu_0 M_s^2$, where $A = 8$ pJ/m is the exchange constant for Ni, see Ref.[28])

- Resonance magnetic field B^{res}: experimental values reported in Fig.3.7(d); uncertainty is $\pm 5\%$

- Angle between wavevector and magnetic field $\varphi = 15°$

In Fig.3.8 the results of the computed SW dispersion are reported. Panels (a) to (c) correspond to the resonance data for $\Lambda = 4.00, 3.07$, and 2.54 μm, respectively. The blue band indicates the RSAW-driven SWs, the red band the SSLW-driven SWs. For both, the finite width of the band corresponds to the combination of uncertainty in M_{eff} and B^{res}; the solid line is the calculation based on the most-likely parameters. As expected, the SW band vertically shifts by increasing the field strength. In the addressed wavevector range the bands are basically flat. The non-monotonicity of the bands cannot really be appreciated on the plotted scale: a zoom-in inset in panel (c) shows the presence of a global minimum at finite wavevector. Here the feature is tiny (few megahertz), but it can be non-negligible for thicker films. Superimposed to the dispersion bands, the experimental data are shown, as black circles with frequency errorbars (the wavevector errorbars are within the marker size).

Good agreement between experimental data and computed dispersions is found. This should not impress, since the dispersions are computed on the basis of the parameters obtained from the experimental data themselves. What matters here is that from these calculations it is possible to quantify the curvature of the dispersion relations. A quantitative (though rough) definition of the flatness F can be given as

$$F = \frac{f_{q_{\text{exp}}} - f_0}{f_{q_{\text{exp}}}} \, , \tag{3.13}$$

where $f_{q_{\exp}}$ is the frequency at the experimental wavevector $q = q_{\exp}$, and f_0 the zero-wavevector frequency. Basically F quantifies the percentage error if the experimental data (which are at finite wavevector) are treated as if they were at zero wavevector. For all the experimental data $F < 0.06$ is obtained, meaning that at most a 6% error is introduced in analysing the SAW-FMR data with the Kittel model. This discussion justifies *a posteriori* the validity of the proposed analysis.

Parametric excitation of high-order magnons

Having ascertained the capabilities and the reference frame of the TG-pumped SAW-FMR experiments, it is now possible to quantify the sensitivity of the technique by presenting data from the other two samples, namely sample B and sample C. Recall that these samples are characterized by a low figure of merit $\mathcal{F}$ (about four times smaller), and present severe morphological issues (see Appendix C). For sample B, B-FMR measurements resulted in very noisy signals, while no signal at all was visible for sample C; for the data presented here no comparison to B-FMR was thus possible. The field-folded FFT maps for sample B are reported in Fig.3.9(a-c) for the three values of Λ: comparing to Fig.3.7(a), additional reference lines highlight peaks at frequency different from either RSAW and SSLW. It turns out that these additional peaks lie all at frequencies given by harmonics or sub-harmonics of a driving SAW frequency, or by their linear combination. This effect has been already observed [139], and it is described as the excitation of higher-order resonances due to parametric pumping. The appearance of parametric resonances testifies that large-amplitude magnetization precession is excited via the proposed TG-pumping scheme.

Several parametric resonances are visible for sample B, while only one is observed for sample C (not shown here). Following the same analysis described above, for each peak the resonance frequency is plotted versus the resonance field [panel (d)]; the parametric resonances are included as well, and they follow the same Kittel curve. The resonance data for sample B at low frequency display a sharp cutoff at about 3.5 mT, which correlates to the opening of the hysteresis loop for this sample [see Fig.C.3(b)]: the deviation of the experimental resonances from the Kittel model can be attributed to the loss of magnetic saturation and to the formation of magnetic domains. Consistently with this hypothesis, no cutoff is observed for sample A and sample C, which exhibit smaller coercivity. Moreover, this low-frequency cutoff in sample B resembles what is observed in magneto-impedance measurements [140] when the boundary between quasistatic and resonating magnetization precession is crossed. This motivates the exclusion of the unsaturated resonance data [marked with squares in Fig.3.9(d)] from the following analysis.

For the fit of the Kittel model, γ was fixed at $1.93 \cdot 10^{11}$ rad/s·T. The best-fit values for the effective magnetization was $M_{\mathrm{eff}} = (277 \pm 16)$ kA/m for sample B and $M_{\mathrm{eff}} = (122 \pm 16)$ kA/m for sample C. The surface magnetic anisotropy calculated from these results is $K_s = (0.92 \pm 0.06)$ mJ/m^2 for sample B and $K_s = (0.91 \pm 0.05)$ mJ/cm^2 for sample C. The reduction of M_{eff} with the thickness of the ferromagnetic film is in accordance with Eq.3.10. The different M_{eff} values observed for sample A and sample B, which share the same film thickness, is understood in terms of the structural and morphological properties induced by the substrate during the Ni growth.

Fig.3.9(e) shows ΔB as a function of f for sample B and sample C; to these data the linear relation of Eq.3.12 is fitted. Consistently with above, the fit excludes data with resonance below 3.5 mT, in order to limit spurious enhancement of α due to incomplete
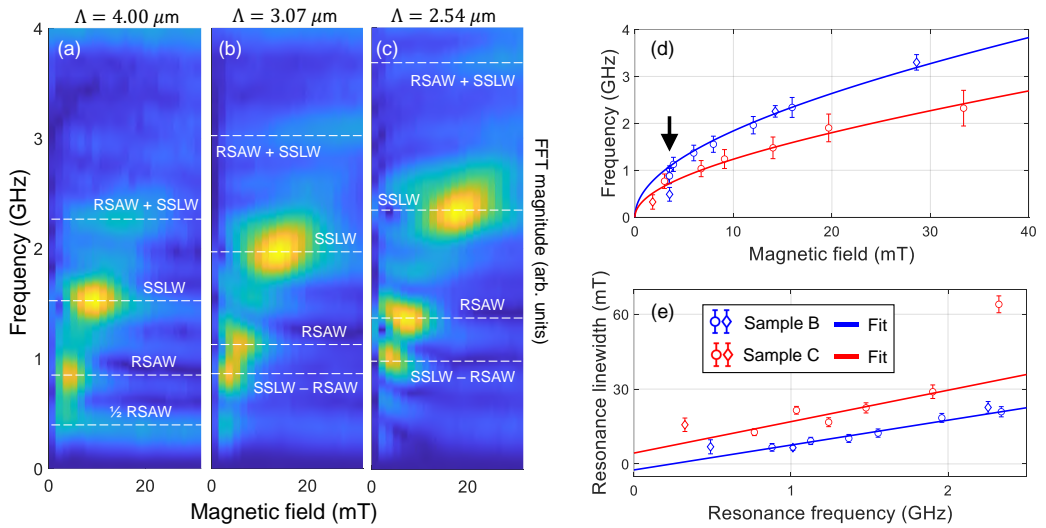
Figure 3.9: (a-c) FFT magnitude maps for sample B; the three TG pitches are indicated. The horizontal dashed lines highlight the presence of parametric excitations together with the expected SAW-driven modes. (d) Resonance frequency versus resonance field for sample B (blue) and for sample C (red). The data for the directly-driven resonances are reported as circles, the parametric resonances as diamonds. The best fits of the Kittel model (solid lines) are also reported. The arrow highlights the cutoff for the resonance of sample B at about 3.5 mT. (e) Dependence of the resonance linewidth on the resonance frequency for sample B and C. The same color and marker code as for panel (d) is adopted. The solid lines are the best fit of Eq.3.12. Adapted from Ref.[99].

magnetic saturation. The obtained Gilbert damping is $\alpha = 0.11 \pm 0.01$ for sample B and $\alpha = 0.12 \pm 0.04$ for sample C; ΔB_{inh} is compatible with zero for both samples. Such large values for α can be due to growth-induced magneto-structural disorder [130]: as reported in Ref.[141], the substrate can dramatically affect the FMR response of an ultrathin ferromagnetic overlayer, possibly washing out any FMR signal. This highlights an apparent inconsistency: despite the lower $\mathcal{F}$ and worse growth quality, sample B exhibits (i) parametric resonances, (ii) a larger M_{eff} with respect to sample A, meaning a lower surface magnetic anisotropy, and (iii) smaller inhomogeneous broadening; however, at the same time it exhibits a larger Gilbert damping (about a factor two). Further investigation, especially on the material-science side, is required to solve this puzzle.

3.5   Conclusions

A SAW-FMR experiment was performed on polycrystalline Ni thin films, combining TG-based excitation of SAWs and tr-FR polarimetry on the elastically driven magnetization precession. Via comparison to B-FMR results, SAW-FMR was validated as a method for magnetic and magneto-elastic characterization. Its space resolution is only limited by the probe laser footprint and by the SAW wavelength, thus allowing to envision sub-micron investigation if tight focusing and small Λ are employed; this results in sensitivity to *local* magnetization dynamics, a condition not achievable using area-integrated techniques like B-FMR. Material science and MEMS technology can benefit from such approach.

The limits of applicability of the presented analysis were also discussed, with emphasis on the non-flat and non-monotonous dispersion of SWs. It is worth stressing one more time that the magnetization precession is uniform in B-FMR and nonuniform in SAW-FMR: the latter could thus be thought as a SWR technique.

To conclude this chapter, a final discussion on this aspect is due. In Fig.3.10 the SAW-FMR resonance data (black spheres) are plotted in their proper three-dimensional phase space, which is spanned by the resonance frequency f, field strength B^{res}, and SAW wavevector q. The three wavevectors ($q = 1.57$, 2.05, and 2.47 rad/μm) are identified with vertical planes (orange, light blue, and purple, respectively). Two acoustic modes are at play, namely RSAW and SSLW. At fixed q, the phase velocity of each acoustic mode determines two frequencies: thus the projection onto the (f, q) plane (green dots) gives the linear acoustic dispersion for the two modes (linear fit in pink). Given the flatness of the SW dispersion in the range of interest, the projection onto the (f, B^{res}) plane (blue dots) follows the non-linear trend of the Kittel model (fit in red). For the experiment discussed here, the experimental geometry fixes q; then, by tuning the magnetic field, the SW manifold moves in the displayed phase space, while the SAW dispersions are unaffected. The acoustic and magnetic degrees of freedom couple resonantly at the experimentally selected q when the frequency of a SW matches that of a driving SAW.

Clearly the projection of the resonance data onto the (f, B^{res}) plane only makes sense if the SW dispersion is flat. This is the case for the present experiment, as discussed in reference to Fig.3.8. If this is not the case, the projected curve will be distorted, each point relating to a different SW wavevector; the analysis could not proceed on the basis of the Kittel model, but more refined models taking into account the SW dispersion would be called for. Far from being only an issue, this can prove to be a great potentiality of the SAW-FMR technique. I see two reasons for this. First, the investigation of low-energy excitations often requires wavevector selectivity, if the investigated quasiparticle are dispersive; refined models will be developed whenever required. Second,
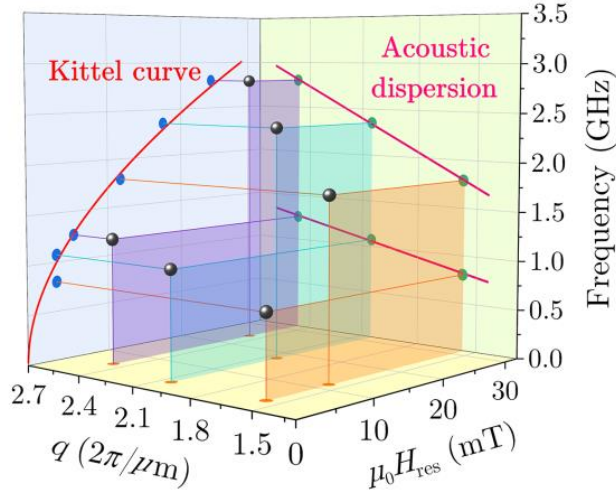
Figure 3.10: The SAW-FMR results for sample A are plotted as a function of resonance frequency, field strength and SAW wavevector (black spheres). The projection of these data onto the $q = 0$ plane results in the dataset analysed in the framework of the Kittel model for FMR. The projection onto the $B^{res} = 0$ plane results in two distinct datasets, linearly dispersed in wavevector, that correspond to the dispersion relations for RSAW and SSLW. From Ref.[99].

momentum-dependent time-resolved scattering techniques are needed to investigate complex quantum systems and devices, with special emphasis on the damping processes of low-energy excitations. This is particularly intriguing for SWs, as a dominant decay channel is Two-Magnon Scattering (TMS). This process involves the annihilation of a zero-wavevector magnon and creation of a finite-wavevector magnon with the same energy; clearly this can only take place if the SW dispersion is non-monotonous. The TMS cross section is enhanced by the presence of modulations in the magnetostatic landscape at the same wavevector as the product magnon. For this reason, this momentum-dependent damping channel could benefit from a TG-based technique; in particular, it is expected that signatures of the TMS would appear as anomalies in the Gilbert damping, as suggested in literature [142].

Part III

A model platform for magnon-phonon hybridization

One-dimensional magnonic-phononic crystals: a model platform for MEC

Artificial crystals are systems in which a material pattern is periodically reproduced by stacking different materials with the aid of advanced growth and lithography methods. Based on which material property is periodically modulated, the crystal exhibits tailored and enhanced functionalities related to light, sound, magnon propagation: this sets the usual nomenclature as photonic, phononic, magnonic crystals, respectively (and the list is not exhaustive). The base element is sometimes called an *artificial atom*, even if its characteristic length L is usually in the nano- or micrometer range; to properly speak of artificial crystals, the periodic reproduction of the artificial atom extends over a dimension much larger than L, possibly up to the macroscopic scale. The number of dimensions N over which the artificial atom is reproduced qualifies the crystal as N-dimensional: *e.g.* in one-dimensional crystals the atom replicates over a single direction. [1] In analogy to natural crystals, the base element can be composed of identifiable distinct nano-objects displaying specific geometries, just like for a polyatomic base of a crystal lattice. This allows tailoring of specific properties as due to local effects: again, the analogy to natural crystals is straightforward, just thinking to the appearance of optical phonon branches for polyatomic crystals, or to the definition of a specific magnonic Brillouin Zone (BZ) if the magnetic periodicity differs from the chemical one. Continuous progress in nanolithography and deposition techniques allows to arrange nano-objects with sub-micron periodicity, gaining access to technologically relevant frequency bands. Naturally in contact with the field of metamaterial engineering, examples of applications are stop-band crystals, unidirectional propagators (diode-like devices) and "invisibility cloacks".

In this chapter we discuss the investigation of elastic and magnetic dynamics in a sample composed of a one-dimensional array of sub-micrometer ferromagnetic Nano Wires (NWs) on a non-magnetic substrate. The regular inter-NW periodicity makes the sample at the same time a Magnonic Crystal (MC) and a Surface Phononic Crystal (SPnC), as due to the periodic modulation of both magnetostatic and surface elastic properties. The coexistence of tailored phononic and magnonic bands motivated to consider this sample as a candidate model platform for investigation of coupled magneto-mechanical modes, as discussed in Ch.5. The sample was studied with multiple techniques: static and tr-MOKE, magnetic BLS and numerical simulations with micromagnetic models were combined to gain an overview of the sample static and dynamical properties.

---

[1]Obvious extension holds for two- and three-dimensional crystals. Even four-dimensional crystals are known, with replicas along the time axis [143].
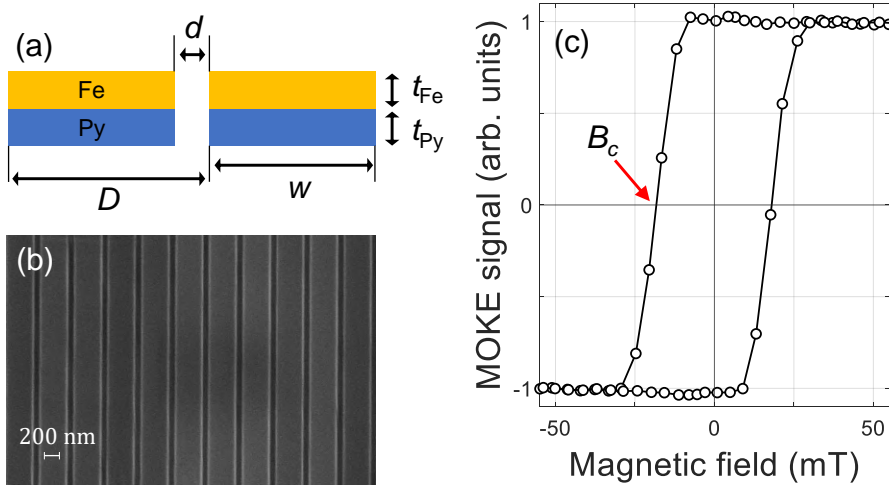
Figure 4.1: (a) Sketch of the cross section of the investigated bilayered NWs. The geometrical parameters are indicated: thickness $t_{Fe} = t_{Py} = 10$ nm, width $w = 340$ nm, inter-NW spacing $d = 70$ nm, array full periodicity $D = 410$ nm. Note the different scales for horizontal and vertical directions. (b) Top-view SEM micrograph of the investigated sample. The NWs extend in length for $l = 4$ mm. (c) Hysteresis loop obtained from longitudinal MOKE for B_{ext} parallel to the NW length. The coercive field $B_c = 18$ mT is indicated by the arrow.

This chapter is organized as follows: in Sect.4.1 an overview of the sample properties as MC and SPnC is presented, referring then to Appendix D for further details; in Sect.4.2 the tr-MOKE measurements are detailed, together with the multi-technique approach which helped in the understanding of the experimental features; in Sect.4.3 some aspects of the rich phenomenology observed via tr-MOKE are reported, as first steps of a deeper incoming investigation. I refer to Ch.5 for the detailed investigation of the coupled magneto-mechanics in this sample.

4.1 The sample

The sample is an array of bilayered NWs composed of Fe on top of Permalloy (Py, $Ni_{80}Fe_{20}$). [2] The thickness of the layers is $t_{Fe} = 10$ nm and $t_{Py} = 10$ nm. Each NW has a rectangular cross-section $w = 340$ nm in width, and it extends $l = 4$ mm in length. The NWs are deposited on Si (001) substrate, with the NW long axis aligned along the [100] direction of the substrate. The inter-NW spacing is $d = 70$ nm, giving an overall real-space periodicity $D = w + d = 410$ nm. These properties define a pseudo-BZ (pBZ) for the one-dimensional artificial crystal which extends in reciprocal space in the range $q_{pBZ} = \pm\pi/D = \pm7.7$ rad/μm. This periodicity in reciprocal space holds both for the magnonic and for the surface-phononic band structures. A sketch of the sample cross-section is reported in Fig.4.1(a).

Deep ultraviolet (DUV) exposure at $\lambda_{DUV} = 248$ nm of a photoresist followed by e-beam deposition of the ferromagnetic layers and lift-off process were employed for

---

[2]I use the convention [overlayer]/[underlayer]/[substrate], so the sample stacking is denoted as Fe/Py/Si.

the fabrication of the NWs. With this technique, highly ordered arrays of NWs can be fabricated over a large area, as can be appreciated by the top-view SEM micrograph reported in Fig.4.1(b). Further details on the fabrication method can be found in Ref.[144]. Thanks to the large area fabricated, standard magnetometry techniques can be employed for magnetostatic characterization: together with sibling systems with different geometrical and material parameters, the sample has been characterized via MOKE, Vibrating Sample Magnetometry (VSM), Superconducting Quantum Interference Device (SQUID) magnetometry, BLS, FMR and micromagnetic simulations.

Indeed, this class of samples has been extensively studied in the last 25 years, and from existing literature valuable details can be learnt for understanding the experimental observations reported in the present and following chapters. The main relevant questions are: (i) what are the acoustic and magnonic modes that can be observed in such sample? and (ii) what do we know from literature about this system, in terms of magnetic anisotropy, switching process and magnetic coupling at the Fe/Py interface? The details of the literature overview are to be found in appendix D. Here I just report the main conclusions that are drawn.

From the phononic point of view, the laser-excited modes are (i) a standing SAW with zero wavevector resulting from hybridization of RSAW with its zone-folded replicas, and (ii) the lowest-order localized breathing mode along the width of each NW. As for the magnonic counterpart, the homogeneous laser-driven excitation of the magnetic subsystem only couples to a magnon of same symmetry, *i.e.* without amplitude nodes along the thickness or the width directions. MCs fabricated as magnetic artificial atoms deposited on a non-magnetic substrate are automatically also SPnC. As such, these hybrid phononic-magnonic crystals can display strong MEC, owing to the coexistence of flat (*i.e.* with zero group velocity) phononic and magnonic bands with matching wavelength. Stationary spatial overlap of the mode anti-nodes strengthens the interaction of the coupling modes. Moreover, as will be discussed in Ch.5, for confined phononic and magnonic modes the dissipation can be engineered to obtain low-damping modes or correlated dissipation, with intriguing coupling possibilities.

To gain insights into the magnetostatic properties of such samples we referred to a series of publications starting from the late '90s, where NW arrays fabricated with the same recipe have been investigated. For what concerns the experiment I want to present, the relevant aspects are here summarized: the NWs have negligible MCA, while the shape anisotropy determines magnetic EA and Hard Axis (HA), either along or orthogonal to the NW length; the magnetization reversal process features competition of coherent rotation and magnetization curling, depending non-trivially on the specific parameters of the NWs: details on the coercivity can shed light on this; the ferromagnetic bilayer can be seen as a single effective magnetic material with inter-layer ferromagnetically coupled dynamical modes up to at least 20 GHz.

4.2   A time-resolved approach to investigate magneto-acoustic modes

To tackle the combined dynamics of the magnonic-phononic crystal we adopted a time-resolved approach. The experimental setup is obtained from slight modifications of the TG setup discussed in Ch.2: blocking one of the two pump beams and collecting the reflection of the probe from the sample, the TG setup is converted in a tr-MOKE one. The optical end-station is sketched in Fig.4.2(a).

The sample lies in the vertical (x, y) plane. Both the pump and the probe are *s-*
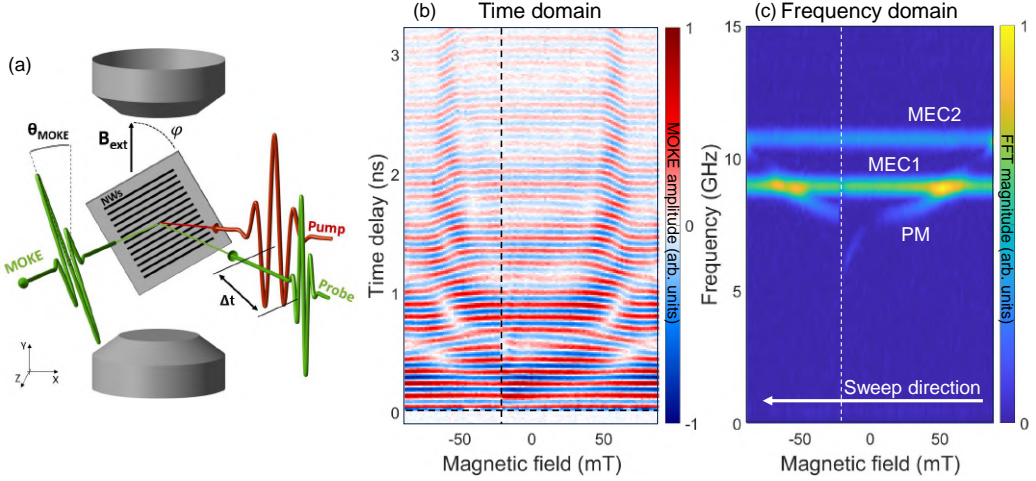
Figure 4.2: (a) Sketch of the experimental end-station for tr-MOKE. The pump and probe beams are *s*-polarized, and impinge on the sample surface with delay Δt; the reflected beam has rotated polarization as due to MOKE; the sample lies in the vertical (x, y) plane, and the external IP magnetic field B_{ext} is directed along y; φ is the azimuth angle between B_{ext} and EA. (b-c) Time- and frequency-domain maps of the tr-MOKE signal for azimuthal angle $\varphi = 60°$. The vertical dashed lines at $B_{\text{ext}} = -22$ mT highlight the magnetization reversal. The magnetic field is swept from positive to negative values.

polarized. The incidence angles from the sample normal are approximately $12°$ for the pump and $6°$ for the probe: thus the setup allows the detection mostly of the OOP component of the magnetization M_z. The laser footprint (FWHM) on the sample is about 59×49 μm^2 for the pump and 33×28 μm^2 for the probe, the slight ellipticity being due to off-normal beams. The experimental pulse energy is 80 nJ for the pump and 3.2 pJ for the probe, giving an average fluence of about 7.0 mJ/cm^2 and 0.4 μJ/cm^2, respectively. The laser repetition rate is set to 200 kHz. The external IP magnetic field B_{ext} is directed along the y axis. The azimuthal angle between B_{ext} and EA, denoted as φ, can be varied in the full 2π range: $\varphi = 0°$ corresponds to $B_{\text{ext}} \parallel$ EA, $\varphi = 90°$ corresponds to $B_{\text{ext}} \parallel$ HA. The experiment reported was performed under ambient conditions at room temperature.

As will be discussed more in detail below, the NIR pump excitation triggers acoustic modes and, via inverse magnetostriction, the phononic strain fields interact with the magnetization of the NWs, leading to coupled magneto-mechanical dynamics [145]. Moreover, it is possible to excite pure magnetization dynamics via ultrafast heat-induced magnetic anisotropy quenching upon ultrafast laser illumination. This thermal mechanism, firstly described in Ref.[101] for an easy-plane magnetic anisotropy system and then extended to different systems [146–148], requires an external magnetic field with strength comparable to the sample magnetic anisotropy. The IP field B_{ext}, whose strength is variable in the range $\pm$ 90 mT, well fits this requirement, since the sample coercive field is $B_c = 18$ mT, as extracted from static MOKE hysteresis loops [see Fig.4.1(c)].

The magnon modes excited with this mechanism rely only on the magnetostatic properties of the NWs, and can be observed via correlative static techniques (*e.g.* BLS) as well as simulated with micromagnetic models. This was done in collaboration with

IOM-CNR in Perugia (Italy).

Magnonic spectra have been measured with BLS in the back-scattering configuration, for fixed zero wavevector at variable strength of an external IP magnetic field. A 200-mW monochromatic CW solid-state laser was employed to generate the probe beam ($\lambda = 532$ nm); the beam was focused at normal incidence onto the sample surface with footprint about 30 μm in FWHM. The scattered light was analyzed in frequency by using a tandem $(3+3)$ Sandercock-type Fabry-Pérot interferometer. BLS measurements were performed at room temperature.

Micromagnetic simulations were conducted using MUMAX3, a GPU-accelerated open-source software [149]. Five NWs were simulated within a computational mesh of $512 \times 8 \times 2$, with EA oriented along the y direction. Periodic boundary conditions were applied in both IP directions. The magnetic parameters used in the simulations were: saturation magnetization for Py $M_s^{(\text{Py})} = 1 \cdot 10^7/4\pi$ A/m; saturation magnetization for Fe $M_s^{(\text{Fe})} = 2 \cdot 10^7/4\pi$ A/m; exchange stiffness for Py $A_{\text{ex}}^{(\text{Py})} = 1 \cdot 10^{-11}$ J/m; exchange stiffness for Fe $A_{\text{ex}}^{(\text{Fe})} = 2 \cdot 10^{-11}$ J/m. An external magnetic field was applied IP at an azimuthal angle φ determined from experimental data. Starting from an initial field strength of 100 mT, the external field was reduced in steps of 5 mT. At each step, SWs were excited using a sinc-shaped field pulse defined as $h(t) = h_0 \frac{\sin\left[2\pi f_0(t-t_0)\right]}{2\pi f_0(t-t_0)}$, applied in the z direction in the entire simulated area with maximum amplitude $h_0 = 50$ mT and frequency $f_0 = 30$ GHz. To obtain the power spectrum, we recorded M_z at every picosecond and then performed FFT.

In Fig.4.2(d) I report a wide-scan map of tr-MOKE results at $\varphi = 60°$, for B_{ext} swept in its full range in approximately 1.5 mT steps. For each magnetic field, the tr-MOKE signal is recorded up to 3.3 ns of delay; to each trace an exponential plus linear background is subtracted. The map in Fig.4.2(e) is obtained by taking the FFT of each trace, with Hamming windowing and zero padding. Here, three features can be identified: two flat modes featuring no frequency dispersion with B_{ext}, and a third dispersive mode. The formers are labelled as MEC modes (MEC1 and MEC2) and the latter as a pure magnonic mode (PM). By properly tuning B_{ext} a crossing of PM and MEC1 mode is observed, a condition in which coupling of magnonic and phononic modes is present. The analysis of this experimental condition is the ultimate goal of the experiment; I refer to Ch.5 for the thorough discussion. Here below I discuss the excitation mechanism of the three observed modes and discuss some phenomenological results.

MEC modes

Fe and Py feature interband electronic transitions at the NIR pump photon energy (1.2 eV), whereas the direct bandgap of Si lies above (3.5 eV [150]). This leads its optical absorption coefficient to be about four orders of magnitude smaller than for the metallic overlayers [151]. For this reason, the energy of the pump is mostly released in the magnetic NWs, that heat up and expand thermo-elastically. The periodicity of the generated strain field stabilizes standing SAWs whose wavelength matches D, the NW periodicity; the wavevector of the generated wave is $q_{\text{MEC1}} = 2\pi/D = 15.3$ rad/μm, which is the center of the second pBZ. Given the characteristic surface phonon dispersion of SPnCs, it corresponds also to a zero-wavevector mode (red arrow in Fig.D.1). Moreover, the pump-induced heating generates strain within each NW (localized breathing mode). Once the acoustic modes are set in, they can drive the NW magnetization, producing the time-modulated magnetic contrast we observe in tr-MOKE [flat modes in Fig.4.2(c)].
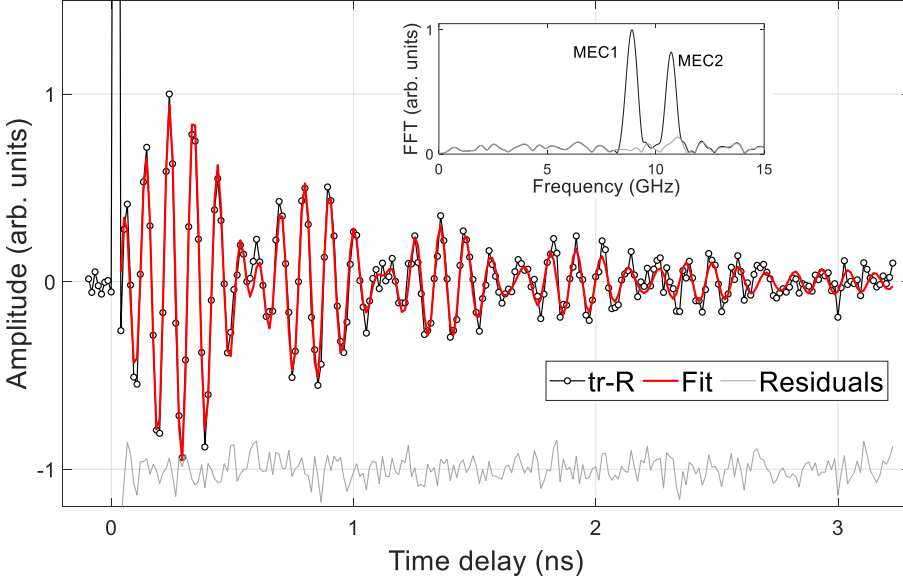
Figure 4.3: Time-domain trace (black circles) and fit (red line) of tr-R at $B_{ext} = 0$ mT. The residuals (grey line) are rigidly shifted for clarity. Inset: FFT of the original trace (black line) and of the residuals (grey line).

The attribution of such flat modes to magneto-elastic modes in similar systems is reported in literature [145, 147]. To further confirm the assignment, we performed tr-R measurements. The same laser source was employed, detecting the non-rotated component of the probe polarization. This approach has been already used for detecting acoustic modes [152]. The same laser repetition rate and fluence are employed as in tr-MOKE measurements. The time-domain trace after background removal is reported in Fig.4.3 (black circles), for $B_{ext} = 0$ mT. The fit of the function

$$y = \sum_i A_i \sin\left(\omega_i t + \phi_i\right) e^{-\gamma_i t} + B \tag{4.1}$$

is shown in red; here $i = 1, 2$ denotes the lower- and upper-frequency phononic mode, which correspond to the driving modes of MEC1 and MEC2 modes, respectively. The parameters A_i, ω_i, ϕ_i, γ_i are the amplitude, angular frequency, phase and damping parameter for i-th mode; B is a constant background. The fit does not take into account the sharp electronic peak at short time delay, for which finer sampling would be needed, and whose dynamics is beyond the interest of this work. The feature-less residuals of the fitting are shown in grey and rigidly shifted for clarity purpose. The inset of Fig.4.3 shows the FFT of the original trace (black) and of the residuals (grey): the absence of prominent spectral weight in the residual FFT further demonstrates that the fit is satisfactory.

The frequencies and dampings obtained as best-fit parameters are $f_1 = (8.89 \pm 0.05)$ GHz and $f_2 = (10.75 \pm 0.05)$ GHz, and $\gamma_1 = (0.73 \pm 0.09)$ rad/ns and $\gamma_2 = (1.4 \pm 0.1)$ rad/ns, in agreement with the parameters for the flat modes in tr-MOKE (see below). No variation of these fit frequencies with B_{ext} was appreciated; on the other hand, note that the PM mode never appears in the tr-R data. Following literature [147], we assign the lower frequency mode to RSAW of the substrate loaded with the NW array, and the

higher frequency mode to a localized (width) breathing mode of each NW. Interestingly, the expected frequency for RSAW at wavelength matching D is 35% larger than the observed f_1, assuming the phase velocity reported in [153]. Two mechanisms can be at the basis of this observed redshift: (i) at the center of pBZ the phononic bandgap opens (see Appendix D), leading to reduction in the frequency of the pumped standing wave as compared to the unloaded substrate [154–156], especially for large elastic mismatch between substrate and NWs [157]; (ii) the filling factor of the NWs being about 0.8, a Fourier decomposition of the thermal trigger gives as first non-zero component a uniform heating, which is expected to lead to softening of the elastic properties of Si [158, 159]. Note that analytical calculation of the RSAW frequency in the sample is complicated. Indeed, the effective-medium approximation (NWs + air gaps) for the overlayer cannot be applied, as it requires to be in the long-wavelength limit [160]: in this case, instead, the RSAW wavelength is comparable (actually, it is identical) to the elastic inhomogeneities length scale. Moreover, for small values of the product $q \cdot t$ (wavevector times overlayer thickness, recall Fig.1.3) the frequency of RSAW is expected to be the same as that of the substrate [16]. These considerations suggest that indeed specific acoustic dynamics related to SPnCs is at play. Acoustic BLS measurements on this sample, together with finite-elements numerical calculations involving thermoelastic models, will help clarifying this aspect.

PM mode

The polycrystalline structure of the NWs sets the shape anisotropy as the leading magnetic anisotropy term, favouring magnetization IP and along the NW long axis, which is thus the magnetic EA. If B_{ext} is non-collinear to EA and comparable in strength to the magnetic anisotropy field, the equilibrium axis for the static magnetization lies at a finite angle between these two directions (with larger spatial inhomogeneity in the magnetization as B_{ext} and EA become more orthogonal, as a consequence of demagnetizing field, see *e.g.* [161]). The pump absorption in the magnetic NWs leads to ultrafast quenching of the magnetization and concurrently to impulsive softening of the magnetic anisotropy. The modification in the energy landscape triggers precession of the magnetization around a non-equilibrium axis, which after about 100 ps [101] reverts to the equilibrium one: therefore, for later times and up to extinction, the observed dynamics reflects the equilibrium spectrum of eigenstates of the magnonic subsystem. Since the same dynamics is impulsively triggered in every NW, the precession in each NW is in phase to the others, giving a net MOKE signal (*i.e.* it is a zero-wavevector magnonic mode). Consistently, the spectral weight of the PM mode drops to zero whenever the equilibrium axis for the magnetization is collinear with EA, which happens (i) when B_{ext} approaches zero strength [see Fig.4.2(c)] or (ii) when $\varphi = 0°$ for any value of B_{ext}. This aspect will be clarified in the next section.

To confirm the assignment of the PM mode to the lowest-order magnetization precession, comparison of tr-MOKE results to BLS measurements and micromagnetic simulations is performed. In Fig.4.4 we report the frequency of the PM mode as obtained from time-domain fit of tr-MOKE traces (blue circles), and the field dependence of the lowest-order magnetic field as observed in BLS (orange circles) and in micromagnetic simulations (black line). For the time-domain fit of tr-MOKE, Eq.4.1 was employed, with the index i running over the three modes. The results for three values of φ are reported: the modification of the dispersion of PM mode by changing the azimuth will be discussed below. General agreement between the data sets and with the simulations is
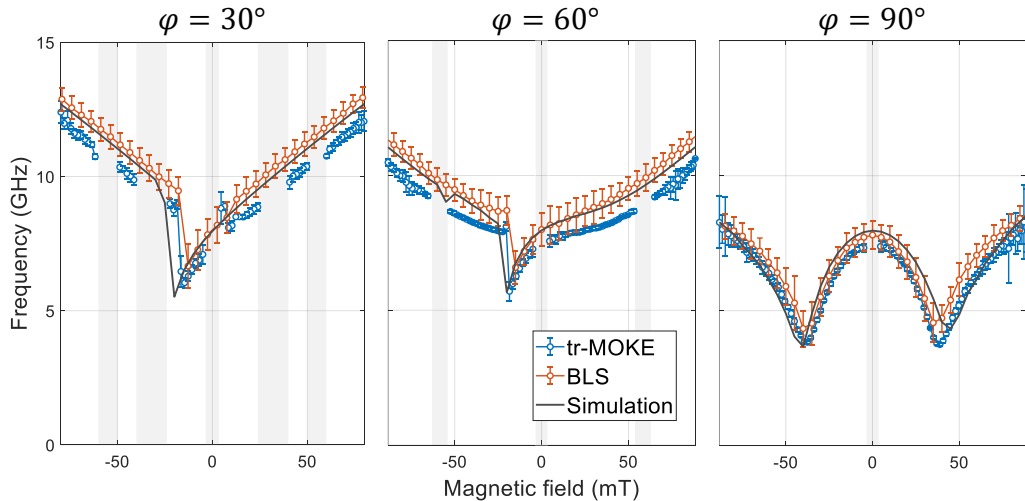
Figure 4.4: Frequency of the PM mode extracted from time-domain fit of tr-MOKE traces (blue circles), together with the frequency of the lowest-order magnon mode as obtained from BLS measurements (orange circles) and micromagnetic simulations (black line). Results for three azimuths are reported: $\varphi = 30°$, $60°$, $90°$. The vertical shaded bars indicate regions in which the extraction of frequency from tr-MOKE data is not possible.

obtained, in particular in the concavity change at positive field ($\varphi = 60°$), in the field position of the cusps ($\varphi = 90°$) and in the value of the switching field. The grey shaded bars in Fig.4.4 highlight regions in which extraction of tr-MOKE values is not possible, either because of absence of the PM mode, or because of the mixing to the MEC modes. Note the systematic redshift of the tr-MOKE data as compared to BLS and simulations: the origin of this discrepancy is temptatively discussed in the next section.

Pump selection rules for PM mode

Fig.4.4 shows that the PM mode is a natural eigenstate of the sample, and as such it can be measured via BLS. Nevertheless, close to $B_{\text{ext}} = 0$ mT it is not seen via tr-MOKE; the same happens if $\varphi = 0°$, for any value of field strength. In both these configurations, BLS shows magnonic peaks. In this section we discuss this experimental difference between tr-MOKE and BLS measurements as due to a pumping selection rule present in tr-MOKE, and not to any other probe-related issue.

First of all, we exclude a role to the probe polarization. In the employed experimental geometry [see Fig.4.2(a)], the small incidence angles from the sample normal set M_z, the OOP component of the magnetization **M**, as the leading component interacting with the probe light. Thus, we are basically in the configuration of polar MOKE (p-MOKE). In p-MOKE, the polarization of the probe beam [linear vertical (LV), or linear horizontal (LH)] has minor relevance, as can be qualitatively understood from the approach discussed in Sect.2.1. Considering only OOP magnetization and small impinging angle, the same p-MOKE occurs for LV and LH.

Next, we show that no geometric effect linked to φ is present. In the sketches in Fig.4.5, the cone of **M** precession is depicted for $\varphi = 90°$ [panel (a)] and $\varphi = 0°$ [panel
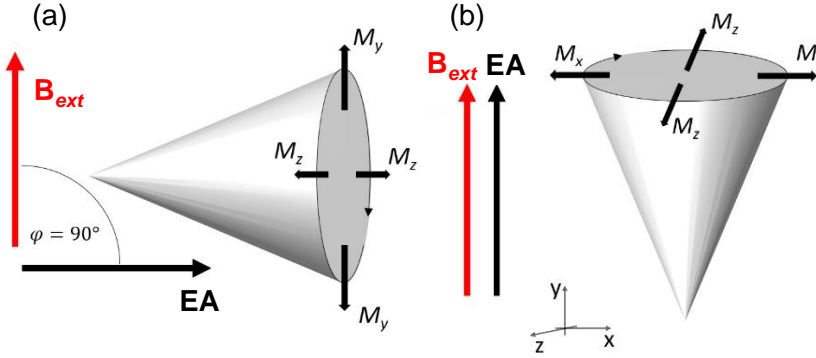
Figure 4.5: Sketch of the precession cone of the magnetization for (a) $\varphi = 90°$ and (b) $\varphi = 0°$. The external magnetic field is kept fixed along the y axis. The small dynamical components of the transverse magnetization are indicated by the arrows.

(b)]. [3] The sample lies in the (x, y) plane. Depending on the EA direction, the dynamical part of **M** lies either in the (x, z) or in the (y, z) plane. Both cases give the same result, since only M_z is probed.

The presence/absence of the PM mode, based on φ and the strength of B_{ext}, depends on the excitation mechanism (pump) rather than the detection scheme (probe). The key aspect is the pump-induced modification of the shape magnetic anisotropy. Following the work of Ref.[101], the absorption of pump photons impulsively heats the sample and causes a change of the shape magnetic anisotropy by inducing quenching of the magnetization. Two different scenarios can settle down, depicted schematically in Fig.4.6. In the first case [$\varphi = 90°$, panel (a)], at $\Delta t < 0$ (*i.e.* before pump arrives) **M** is directed along an equilibrium axis r which is determined by the vectorial sum of **B**$_{\text{ext}}$ and the shape anisotropy field; in our case the anisotropy field is directed along the EA, so r lies IP at some intermediate angle between **B**$_{\text{ext}}$ and EA. When the sample is heated by the pump ($\Delta t = 0$), the anisotropy field changes in strength, and the new equilibrium axis r' lies IP but at a different azimuth; **M** starts to precess about r'. After less than 100 ps, heat has been dissipated away (in the rest of the metallic NW or to the substrate) and the equilibrium axis goes back to r; however, **M** is out of equilibrium and keeps precessing, now about r, in a free induction decay fashion until its natural damping.

In the second case [$\varphi = 0°$, panel (b)], for $\Delta t < 0$, B_{ext} and EA are collinear, and r as well. In this scenario, the reduction of anisotropy field strength induced by the pump does not set a different direction for the equilibrium axis, so the only effect observed is magnetization quenching and recovering. Note that a very similar mechanism takes places when the leading magnetic anisotropy is of magnetocrystalline origin. The anisotropy constants routinely used to model anisotropic systems strongly depend on temperature [146, 148].

The last ingredient necessary to assess the difference of tr-MOKE and BLS measurements is related to sensitivity. The tr-MOKE setup is not able to observe thermal population of quasi-particles in the samples, since in a thermal population each quantum has an arbitrary phase to the others and so the signal averages to zero. A finite signal can be observed only when the pump impulsively triggers a dynamics which is coherent (*i.e.* with

---

[3]For panel (a), small B_{ext} is considered, meaning that the axis of the precession cone is along EA.
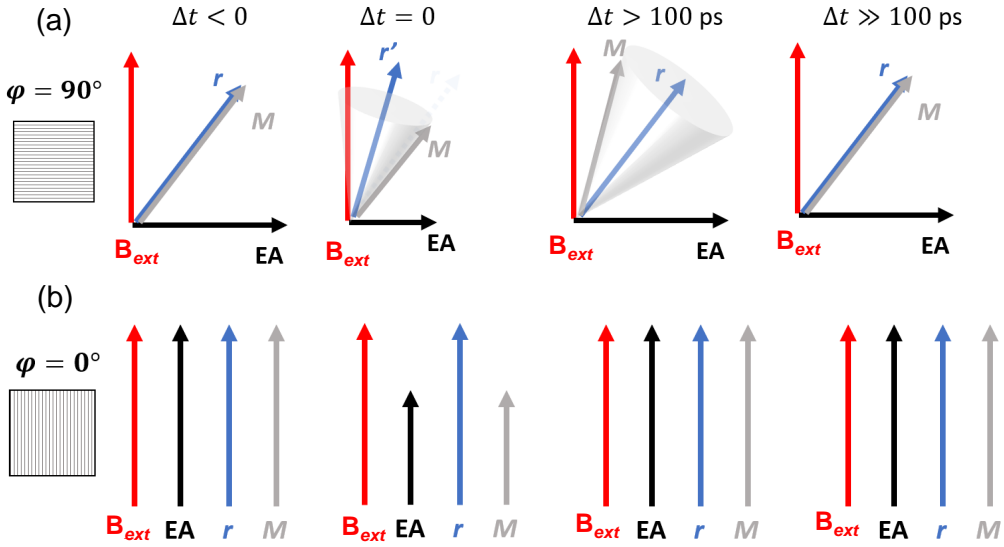
Figure 4.6: Sketch of the effect of the pump on the magnetization and the shape anisotropy EA at four different times with respect to time zero (*i.e.* the arrival of the pump). For non-collinear B_{ext} and EA [$\varphi = 90°$, panel (a)] a transient dynamical state is excited. For collinear B_{ext} and EA [$\varphi = 0°$, panel (b)] only magnetization quenching and recovery is observed.

same phase) on the entire volume probed by the probe beam, or at least when the spatial average of the signal is not zero. For example, for acoustic phonons, all the oscillators must be in phase, giving a net compression/expansion of the material; for uniform magnetization precession, **M** in the entire probed volume must precess in phase. This means that, even if the PM mode is present in certain configurations, it can only be observed via tr-MOKE if the pump is able to excite large-scale coherent dynamics: the PM mode for $\varphi = 0°$ surely exists (as observed also via BLS) and interacts with our probe beam (no selection rule is prohibiting it), but it is not observed since it is not triggered by the pump scheme used. In another language the pump induces a time-dependent reduction of symmetry of the system which enables the detection of a p-MOKE signal.

In Fig.4.7 a selection of tr-MOKE measurements is reported, supporting the picture just sketched. The angle θ denotes a vertical tilt of the magnetic field, keeping its IP component along the y axis; this angle gives a small OOP component to B_{ext}. For $\varphi = 0°$ and $\theta = 0°$ [panels (a-b)] the PM mode is absent, no matter whether the probe polarization is LV or LH. Only a faint anomaly in the intensity of MEC modes in the regions of crossing is maybe present, as highlighted by the red circles. The origin of this anomaly is unknown and it deserves further investigation. For $\varphi > 0°$ and $\theta = 0°$, the PM mode is observed, consistently with B_{ext} and EA being not collinear [panel (c)]. Finally, tilting OOP ($\theta \approx 15°$) the applied magnetic field, keeping its IP projection at $\varphi = 0°$, the PM mode pops out, again consistently with non-collinearity of B_{ext} and EA [panel (d)].
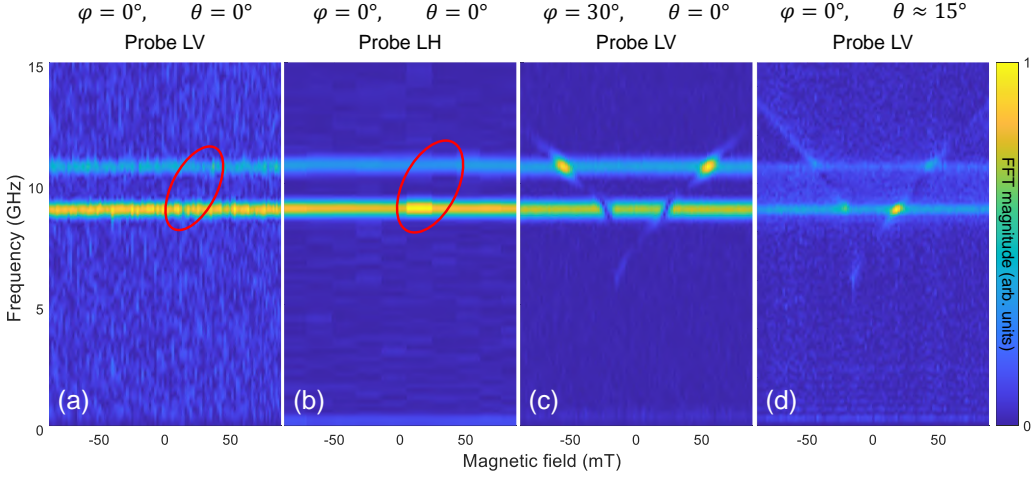
Figure 4.7: FFT magnitude maps of tr-MOKE signal for four different geometrical configurations: (a) $B_{ext} \parallel$ EA, probe polarization LV; (b) $B_{ext} \parallel$ EA, probe polarization LH; (c) B_{ext} IP with $\varphi = 30°$, probe polarization LV; (d) B_{ext} tilted OOP by $\theta \approx 15°$, while its IP component is still along EA ($\varphi = 0°$), probe polarization LV. The red ellipses in panels (a-b) highlight intensity anomalies in the MEC modes which could correlate to the interaction with the PM mode. Note the different size in magnetic field steps in panel (b).

Comparison to TG spectroscopy

The experiment described in this chapter basically consists in a modulated heating of the sample, triggering specific acoustic and magnetic dynamics. The analogy to the TG-based experiment discussed in Ch.3 is evident. Nevertheless, between the two approaches there are important differences, which are briefly discussed now.

- The large difference in absorption coefficient of the metallic NWs and the Si substrate generates a thermal contrast at time-zero which is larger than what obtained in the TG-based experiment. Given that $\alpha_{Si} = 30$ cm^{-1} and $\alpha_{Fe} = 4.7 \cdot 10^5$ cm^{-1} (same order for Py) [151], and assuming a linear optical regime in which the optical constants of the materials are not modified by the impulsive pump, a thermal contrast of about 10^4 is obtained. In similarity to the jargon used for interference patterns, this could be dubbed *fringe visibility*. A direct measurement of the same quantity in the case of TG pump is not available, but it is expected to be at most of order 10^2. So the thermal landscape is more largely modulated in the present experiment, with probably larger amplitude acoustic waves excited. This is probably the reason why an experiment employing the TG pump on the NW sample was not successful: the only signal obtained when employing the two-pumps configuration was the incoherent sum of dynamics excited by each pump singularly, with no further coherent modulation given by the TG periodicity.

- In the present experiment, access to smaller acoustic wavelength (sub-micron period) is gained, the only limitation being the miniaturization in the lithographical fabrication process; the drawback is that the sample has a fixed periodicity, and the possibility to investigate different acoustic wavelength on the same sample is lost.
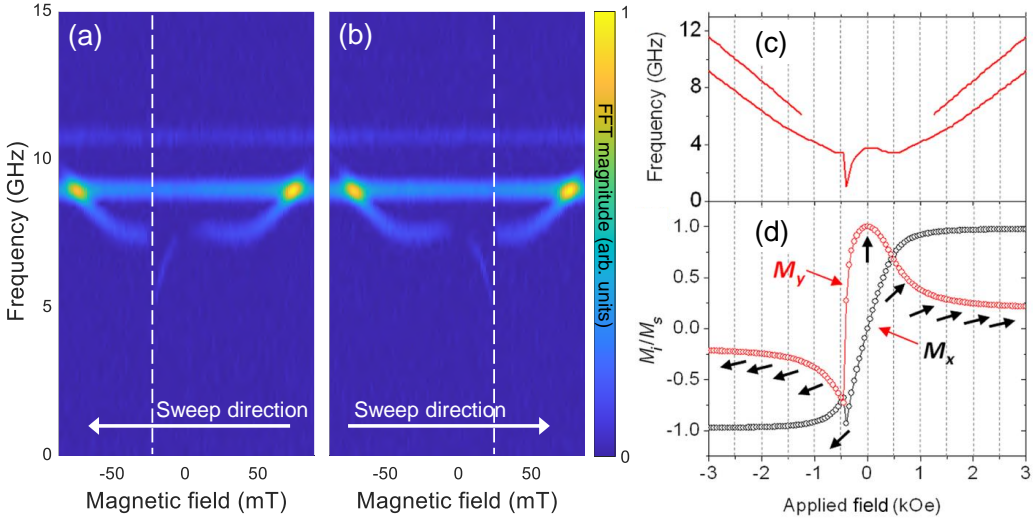
Figure 4.8: (a-b) FFT maps at $\varphi = 70°$ for opposite direction of the magnetic field sweep: the PM-mode discontinuity (highlighted by vertical dashed lines) correlates to the spin-flip. (c) Frequency of the PM mode as simulated with micromagnetic models for $\varphi = 80°$. (d) Normalized values of M_x and M_y (black and red circles, respectively) as a function of the applied field. The black arrows point in the direction of the NW average magnetization. Panels (c-d) adapted from [147].

- In TG-pumped experiment, a magneto-optical signal is observed only when the natural magnetization precession is sustained and amplified by the acoustic wave, while basically no signal is present from the pure magnetic mode (dispersive PM mode) nor from MEC modes outside the resonance region (flat modes). As motivation for this, three aspects should be noted about the TG-based experiment: (i) the amplitude of the acoustic wave is probably smaller (see comments above); (ii) the magnetic field is applied along an EA (IP, at about $15°$ from the wavevector direction) so the mechanism described in [101] is not present; (iii) the FR signal probes all the possible dynamical phases of the magnetization precession, since the magnetic material is a continuous film, and a finite signal is observed thanks to the inhomogeneous temperature profile, with obvious lowering of sensitivity; on the contrary, in the present experiment all the volume of magnetic material is precessing basically in phase (with a *caveat* regarding the lower precession amplitude for edge-localized modes) and so the signal generated adds up.

4.3   Exploring the modes

The investigated sample presents a rich phenomenology as probed via the tr-MOKE approach outlined above. Here I account for some of these aspects. The aim is to give an overview of the several facets encountered in the investigation of this sample, and to present scientific questions that will be addressed in the future.

Hysteresis from tr-MOKE measurements

The discontinuity observed in the PM-mode spectrum [see Fig.4.2(c)] at about $B_{\text{ext}} = -22$ mT is understood as the magnetization reversal (spin-flip transition), with the static magnetization flipping by $180°$. To confirm this picture, we report in Fig.4.8(a-b) two FFT maps obtained for opposite direction of the magnetic field sweep. The discontinuity takes places at opposite values of magnetic field $B_{\text{ext}} = (\pm 22 \pm 2)$ mT, as highlighted by the vertical dashed lines. Note that for values of magnetic field external to the spin-flip, the maps are symmetrical, while they are not for values within the spin-flip interval. For this reason, folding of the maps about $B_{\text{ext}} = 0$ mT cannot be performed; it is also consistent with the fact that in the current tr-MOKE configuration not the static magnetization (which actually flips in direction), but the OOP dynamical component M_z is probed. These are general differences with respect to static MOKE experiments, whereas the information on the magnetization is encoded into the anti-symmetric component of the magneto-optical signal.

Detailed investigation of the magnetization reversal in a magnetic NW array is reported in Ref.[147]. Fig.4.8(c-d) is adapted from the same reference. It reports the frequency of the NW magnonic modes simulated with micromagnetic models [panel (c)], and the values of M_x and M_y (normalized to the saturation M_s) as a function of the external field strength [panel (d)]; field sweeping from positive to negative values is assumed. The azimuthal angle is $\varphi = 80°$, almost parallel to HA. At large positive fields, the NW shows near complete saturation along the field direction. As the field strength is reduced to 500 Oe (50 mT), the mode spectrum exhibits a local minimum in frequency: this is the condition of compensation between applied field and demagnetizing field, thus minimizing the effective field around which the magnetization precesses. Thus the field position of the minimum frequency is an estimate of the anisotropy field of the sample B_a. Further reduction of the field strength results in orientation of magnetization along EA: the mode frequency increases again as the demagnetization field dominates over the applied field. As the field crosses zero, the spectrum softens and exhibits a discontinuity in correspondence of the magnetization overcoming the energy barrier exerted by shape anisotropy to its reorientation parallel to the field.

Three aspects should be highlighted. First, this description (and the micromagnetic simulations that corroborate it) approximates each NW to a single magnetic domain, for which a macrospin picture is significant. As explained in Appendix D, this approximation can fail for specific geometrical sizes of the NW: the azimuth dependence of the coercivity can give information on the details of the magnetization reversal mechanism. Still, in Ref.[147] the agreement of simulations to the experimental data is considerable, suggesting that the model indeed captures the main phenomenon at play. Second, in Fig.4.8(c) at large fields two modes are present: the lower is due to edge modes, localized close to the width boundaries of the NW, and the higher is a bulk mode, localized at the center of the NW. The formation of these two branches results from the inhomogeneity of the demagnetizing field, which is stronger close to the edges: thus the effective field (sum of the applied and the demagnetizing fields) is weaker for modes localized at the edges, giving lower precession frequency; modes localized at the center of the NW experience instead a stronger effective field, resulting in higher frequency. For lower strength of the external field, the upper mode disappears, and the lower mode expands more and more from the edge to the bulk of the NW. The second branch was not observed in the measurements I performed, consistently with the reduced range of applied magnetic field I employed. Third, all the above discussion relates to frequency-domain features.
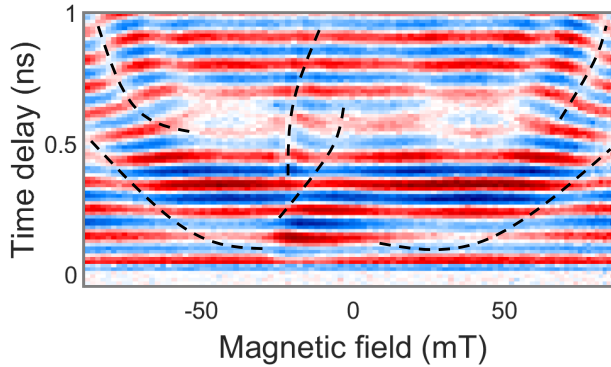
Figure 4.9: Close-up map of the time-domain map for $\varphi = 75°$ and $\Delta t < 1$ ns. The black dashed lines highlight low-amplitude paths that correlate to PM-MEC1 resonances or to magnetization reversal. In both cases, anomalies in the dynamical phase are observed.
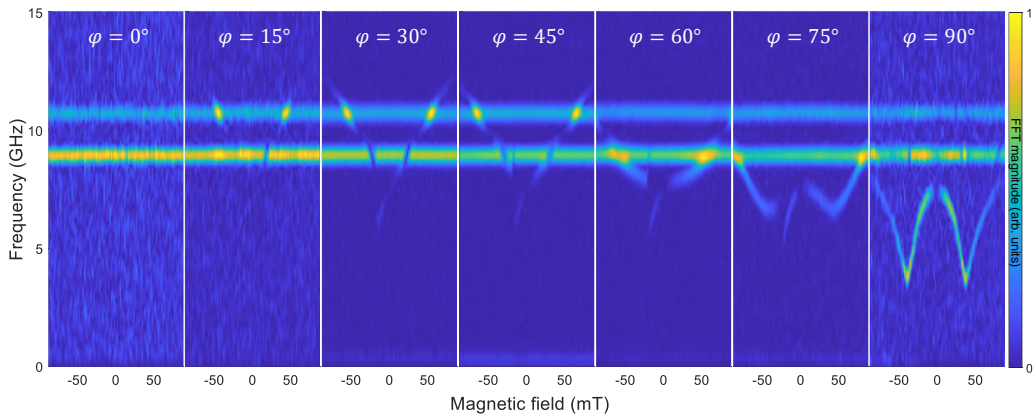

Figure 4.10: FFT maps varying the azimuthal angle from $\varphi = 0°$ (B_{ext} parallel to EA) to $\varphi = 90°$ (B_{ext} parallel to HA) in steps of $15°$.

Actually, a major strength of tr-MOKE is the possibility to observe time-dependent details, which can be particularly informative close to the magnetization switching. I just report in Fig.4.9 a close-up for short time delays ($\Delta t < 1$ ns) of the time-domain traces acquired for $\varphi = 75°$. The black dashed lines highlight paths were the trace amplitude is reduced, and which delimitate regions with anomalies in the dynamical phase. For the time being, what can be assessed with certainty is that such low-amplitude paths correlate to the mode crossings and/or to the magnetization switching. Specific time-dependent numerical models are required to deepen the understanding.

Dependence on the azimuth

The evolution of the tr-MOKE signal as a function of φ is reported in Fig.4.10. The azimuth is varied from $\varphi = 0°$ (B_{ext} parallel to EA) to $\varphi = 90°$ (B_{ext} parallel to HA) in steps of $15°$. The MEC frequencies are not affected by φ, being determined by the elastic properties of the sample. As discussed in Ch.1, for phonons whose leading strain component

is ϵ_{xx}, MEC is maximum at $45°$ between the x axis and the static magnetization. Thus, an overall increase of the MEC signal at $\varphi = 45°$ is expected. This is masked in Fig.4.10, since each map was normalized to its maximum (*i.e.* the FFT magnitude is reported in arbitrary units). This was required by the fact that for each azimuth optimization of sample alignment was performed, resulting in overall different intensity for each map; in other words, the various maps reported are not comparable in absolute amplitude of the signal. Nevertheless, a larger MEC for $\varphi = 45°$ can be traced from the map background, which is flatter for that azimuth. In striking difference, the PM mode strongly depends on φ: its field dispersion follows the expected trend for the lowest-order precession mode of the magnetization for a strongly anisotropic system dominated by demagnetizing field effects. The very apparent feature of the presence of enhancement or depletion in the spectral weight at the crossing of PM and MEC modes will be the subject of Ch.5.

For $30° < \varphi < 90°$ the PM mode dispersion was extracted via time-domain fit of the tr-MOKE traces (again Eq.4.1). Clearly, this was not possible for $\varphi = 0°$ and $15°$, as the PM mode is absent. The results are reported in Fig.4.11(a). Similarly to Fig.4.4, shaded grey bars indicate regions where the time-domain fit was not possible, as due either to the very low PM-mode intensity, or to crossing to a MEC mode. For $\varphi = 90°$ the dispersion displays a global minimum (indicated by the black arrow) which correlates to the NW anisotropy field; the obtained value is $B_a = 38$ mT. For smaller φ the dispersion modifies progressively, reducing the non-monotonicity and resembling more and more the standard Kittel precession mode which is routinely acquired *e.g.* via FMR for B_{ext} parallel to EA. For any φ the dispersion crosses the $B_{ext} = 0$ mT axis at the same frequency value $f_0 = (7.4 \pm 0.3)$ GHz. In this zero-field condition the magnetization is aligned along EA, no matter the value of φ, and the existence of a finite precession frequency results from the remanent magnetization. As a first consequence, this is evidence that the sample features isotropic remanence, which is not always the case for arrays of NWs (see *e.g.* Ref.[162]), and suggests a single-domain structure, with no relevant domain formation even when B_{ext} is applied along HA. As a second consequence, from the zero-field frequency an estimate of the magnetization remanence can be given. Kittel [131] calculated the frequency for ferromagnetic resonance in a prolate ellipsoid aligned along the z axis and subject only to shape anisotropy to be

$$f = \frac{\mu_0 \gamma}{2\pi} \sqrt{[H_z + (N_y - N_z)M_z] \cdot [H_z + (N_x - N_z)M_z]}\,, \qquad (4.2)$$

where H is the static external magnetic field, M the static magnetization and N_i the demagnetizing factors. In this expression, it is assumed that the external field is applied parallel to the prolate axis of the ellipsoid, which is the magnetic EA, and the static magnetization as well. The demagnetizing factor for a revolution ellipsoid can be calculated analytically from the aspect ratios of the axis; as explained in Appendix E, the same procedure is a good approximation also for the discussed NWs: the calculated factors for magnetization parallel to EA are $N_x = 0.06$ (width), $N_y = 0.94$ (thickness) and $N_z = 0$ (length). Setting to zero the external field in Eq.4.2, the expression for f_0 reads

$$f_0 = \frac{\mu_0 \gamma}{2\pi} M_r \sqrt{(N_y - N_z) \cdot (N_x - N_z)}\,, \qquad (4.3)$$

where M_r denotes the remanence magnetization. Since the static MOKE loops have high squareness [Fig.4.1(c)], the remanence is a good estimate of the saturation magnetization

M_s. Thus the saturation magnetization can be expressed as

$$M_s = \frac{2\pi f_0}{\mu_0 \gamma} \cdot \frac{1}{\sqrt{N_x N_y}} \ , \tag{4.4}$$

giving $M_s = (886 \pm 36)$ kA/m, or equivalently $\mu_0 M_s = (1.11 \pm 0.05)$ T. These results compare reasonably well to experimental results (VSM on Py NWs gives $\mu_0 M_s = 1$ T in Ref.[163]) and to numerical estimates ($M_s = 1054$ kA/m for the *Effective* NW (ENW) simulated in Ref.[161]).

The azimuth-dependent dispersions give also a measurement of the coercive field as a function of φ: the color-coded arrows in Fig.4.11(a) indicate the discontinuity related to the spin-flip transition. The values of the coercive field B_c as a function of φ are reported in Fig.4.11(b) (blue circles). For comparison, I report also the switching field as extracted from BLS spectra (orange circles) and form numerical simulations (black circles); the respective datasets used are those plotted in Fig.4.4. For intermediate azimuth, the three sets are consistent, at about $B_c = 20$ mT. Note that the trend in coercivity is non-monotonous: moving from $\varphi = 0°$ B_c first decreases and then increases. As discussed in Appendix D, this non-monotonicity suggests that a simple Stoner-Wohlfart model for the coherent rotation of the magnetization is not appropriate to describe the spin-flip. Further investigation is required, via static MOKE to address the coercivity or via spin-resolved SEM to directly observe the magnetization reversal.

Two final comments on the theme of the reversal are due. First, the good agreement in the coercive field values for BLS and tr-MOKE suggests that that the pump-induced heating in tr-MOKE does not have a leading role in favouring the switch transition, nor has the elastic strain. This is somehow surprising, as the coercivity is known to be a property sensitive to sample temperature [164], as happens *e.g.* in heat-assisted magnetic recording (HAMR), and to be dependent on the overall free-energy landscape of the system, which can be modified by engineered stresses in what are sometimes called straintronic devices (see *e.g.* Ref.[165]). The reason is likely to be found in the details of the time-resolved measurements: the heat pulse only triggers the magnetic precession, while the dynamics observed at the nanosecond timescale is basically that of the equilibrium configuration; further investigation is required. Second, in both tr-MOKE and BLS the spin-flip transition takes place rather abruptly as compared to static MOKE hysteresis loops reported in Fig.4.1(c). The origin of this discrepancy may be searched in the different quantities measured, the OOP component M_z for tr-MOKE and BLS or the IP component $M_{x,y}$ for static longitudinal MOKE. Performing tr-MOKE at different impinging angles could help properly assigning the different contributions.

Symmetry from tr-MOKE measurements

The possibility to perform full sweep of B_{ext} and to change at will the sample azimuth, allows to acquire experimental data in specific symmetric configurations, with interesting perspectives on the symmetry of the observed dynamics. An important premise: the raw data acquired via tr-MOKE are, needless to say, time-resolved. This means that they embody information on the phase of the dynamical observed mode. Access to this phase can be obtained via time-domain fitting; another possibility is to perform FFT of the traces, and to plot two-dimensional maps of what is called the spectral phase, *i.e.* the argument of the complex number computed via the FFT algorithm for each frequency. This second approach allows to get a full picture of the signal phase, just like FFT maps
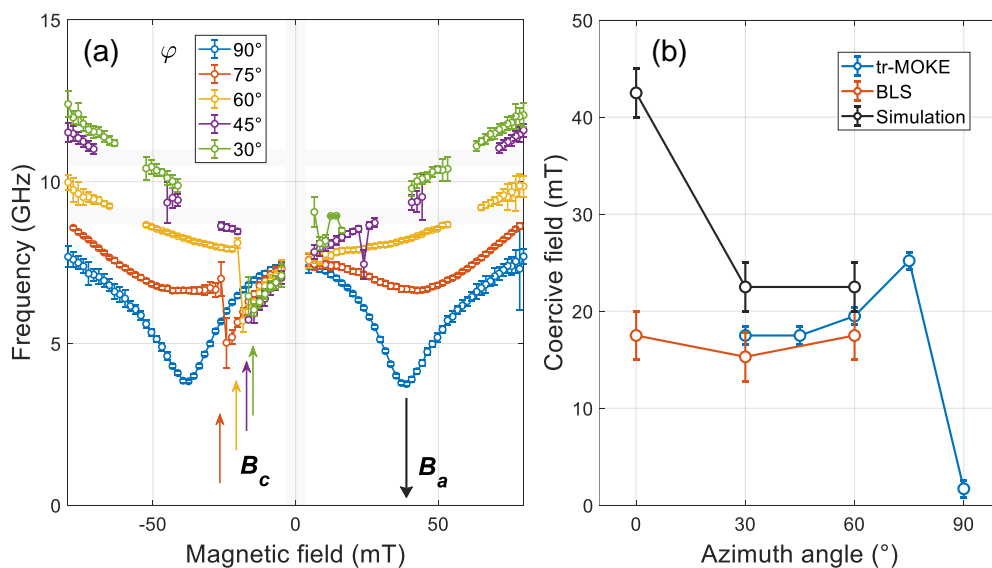
Figure 4.11: (a) Frequency of PM mode for different values of φ. The black arrow indicates the anisotropy field ($B_a = 38$ mT) as the value for the minimum frequency at $\varphi = 90°$. The coloured arrows highlight the switching fields, which are equivalent to the coercive field. (b) Azimuthal dependence of the coercive field as extracted from tr-MOKE (blue), BLS (orange) and micromagnetics simulations (black). Note that tr-MOKE does not allow extraction of B_c for low angles, while BLS and simulations do not allow extraction for $\varphi = 90°$.

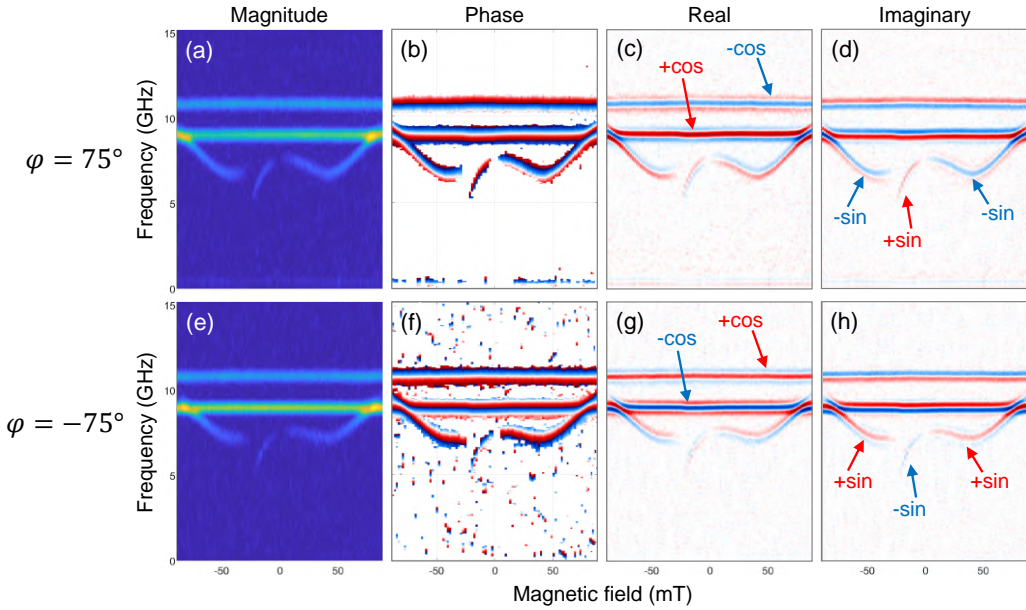**Figure 4.12:** FFT magnitude, phase, real and imaginary parts of tr-MOKE data for (a-d) $\varphi = 75°$ and (e-h) $\varphi = -75°$. The predominant phase characters are indicated for MEC modes [panels (c) and (g)] and for the PM mode [panels (d) and (h)]. A slight experimental tilt of B_{ext} is probably the reason for the different concavity of the PM mode in the two configurations.

allow to catch at a glance the dispersion of the modes. Similarly, it can be advantageous to produce two-dimensional maps of the real and imaginary parts of the FFT.

The first aspect is related to the phase of the magneto-optical signals as upon swapping $B_{ext} \leftrightarrow -B_{ext}$. Fig.4.12(a-d) shows two-dimensional maps for FFT magnitude, phase, real and imaginary parts for $\varphi = 75°$. Simplifying a bit, a mode exhibiting a positive (negative) peak in the real part behaves as a positive (negative) cosine-like mode; a mode exhibiting a positive (negative) peak in the imaginary part behaves as a positive (negative) sine-like mode. Two notes: (i) proper assignment of the modal phase requires either time-domain fit or evaluation of the spectral phase at frequency value corresponding to the magnitude peak; (ii) this two-dimensional mapping washes out any time-dependent information and assumes that the modes are stationary or at most damped. [4] With this *caveat*, taking for granted that the assignment of sine- or cosine-like character makes sufficient sense, let's focus on the MEC modes. They both have cosine-like character, with opposite sign. The easiest way to asses this is to observe that for both of them a peak symmetric along the frequency axis is present in the real part map. Another possibility is to observe the spectral phase map: MEC1 mode has white phase (= 0) in the middle, while MEC2 mode has black phase (= π). No variation is visible for opposite values of B_{ext}, indicating that the magnetization precession driven by the underlying phonon modes is unaffected by the direction of the external field, being it

---

[4]Actually, the complex Fourier Transform contains the whole amount of information contained in the time-domain datum (information gets lost when considering only the magnitude). The point is that tiny time-dependent details are encoded in equally tiny details smeared on the entire frequency axis with frequency-dependent phases. Thus, they are basically impossible to recover by eye inspection, or even by analysis of frequency-localized spectral features.

positive or negative along a fixed axis. This is consistent with the expression of the MEC torque τ_{MEC} for leading strain ϵ_{xx} (Eq.1.20). When the field changes sign, φ changes to $(\pi + \varphi)$; since $\sin\left[2\left(\pi + \varphi\right)\right] = \sin\left(2\varphi\right)$, the MEC torque is not affected thereof. Moreover, even upon spin-flip, nothing changes since the dependence on $\mathbf{M}$ is quadratic and the angle reverts to be φ.

The PM mode behaves differently: frequency-symmetric peak is present in the imaginary part map, indicating that it has sine-like character. Moreover, while the peak is negative at large positive field (negative sine-like character), it becomes positive when B_{ext} changes sign (positive sine-like character); for field larger than the coercivity (*i.e.* after the spin-flip transition), the negative sine-like character is recovered. The swap of character correlates to the change of sign for B_{ext} while the static magnetization is still pointing towards the original direction: the magnetization precesses in opposite direction (clockwise instead of counter-clockwise), as can be understood for a free magnetic moment upon simple Larmor precession.

The second aspect relates the modal phases upon swapping $\varphi \leftrightarrow -\varphi$. In Fig.4.12(e-h) the same maps are reported, for $\varphi = -75°$. Note that the PM mode concavity is a bit different from panels (a-d): this is due to a slight experimental misalignment resulting in a small tilt OOP of B_{ext}. In this configuration all the characters have the opposite sign, as compared to those for $\varphi = 75°$. For what concerns the PM mode, a cartoon involving again the Larmor precession is sufficient: given the direction of precession with the right-hand rule, the absolute phase (or equivalently the phase at time-zero) changes by π if M lies to the right or to the left of B_{ext}. For the MEC modes, it is necessary to recall Eq.1.20: if $\varphi \to -\varphi$, also the torque $\tau_{\text{MEC}} \to -\tau_{\text{MEC}}$.

Another symmetry-related aspect that can be inferred from the tr-MOKE maps relates to the leading strain components of MEC modes. As already mentioned, the efficiency of MEC strongly depends on the strain components at play and on the relative orientation between the strain field and the magnetization. In the case of RSAW, the dominant strain component is the longitudinal IP one, and MEC is maximized at $45°$ between the acoustic wavevector and the magnetization. Even though the absolute intensities of the maps in Fig.4.10 are not comparable, it is possible to compare the relative intensity $I_{\text{MEC2}}/I_{\text{MEC1}}$ of MEC2 and MEC1 modes. The back-thought is that if the two MEC modes feature different strain symmetry, then we expect the signal ratio to change as a function of φ. The result is shown in Fig.4.13, where the polar plot shows the ratio of FFT magnitudes acquired at $B_{\text{ext}} = -10$ mT, which is far enough from resonances to be unaffected thereof. There is not a clear trend in the intensity ratio of the two modes: a possible conclusion is MEC2 mode to be dominated by longitudinal IP strain, similarly MEC1. The two modes thus display the same trend in intensity as a function of φ, and the intensity ratio is basically constant. This is somehow expected if MEC2 is driven by a width-expansion breathing mode: at any azimuth this strain would be collinear to the leading ϵ_{xx} strain driving MEC1.

Fluence dependence of the PM-mode frequency

One of the main differences between tr-MOKE and BLS measurements is that in tr-MOKE there is a significant pump-induced heating of the sample, which is precisely the trigger of coherent magnetization precession. Investigation of the dependence of tr-MOKE frequency on the pump fluence is thus relevant to assess the presence of perturbative or non-perturbative regime. Here I report the analysis on the fluence dependence of the frequency of the PM mode as observed in tr-MOKE. Note that the measurements
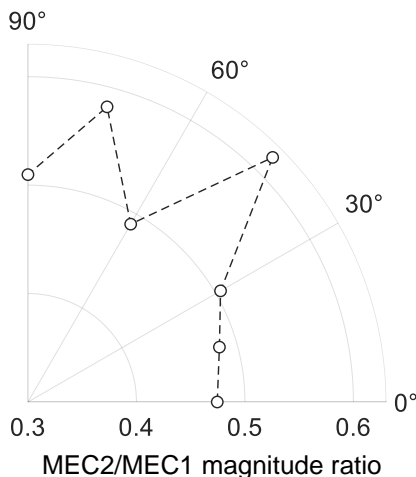
Figure 4.13: Angular (in-)dependence of the intensity ratio of MEC2 and MEC1. The radius of each point is the ratio I_{MEC2}/I_{MEC1} of the relative FFT magnitudes; the values are those at $B_{ext} = -10$ mT.
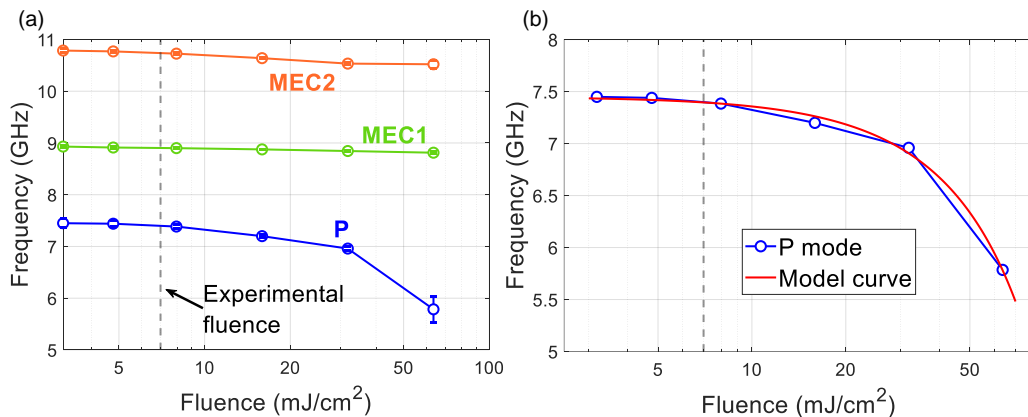
Figure 4.14: (a) Dependence on pump fluence of the frequency observed via tr-MOKE, for all the three modes. The errorbars are the 95% confidence level for the fit of the time-domain traces. The vertical dashed line indicates the fluence level set during the experiment. These measurements have been acquired at $B_{ext} = 31$ mT, $\varphi = 75°$, 100 kHz of repetition rate. (b) Comparison of the PM-mode frequency and the phenomenological model developed.

reported here below are not completely consistent with those reported in the rest of this chapter since the repetition rate is 100 kHz instead of 200 kHz. As no thermal pile-up was observed at 200 kHz, the conclusions drawn here are valid for both configurations.

Acquisition of tr-MOKE traces was performed at fixed field $B_{\text{ext}} = 31$ mT, chosen in order to have modes well-separated in frequency; the fluence was varied from 3 to 60 mJ/cm^2. Each trace, after background removal, has been fitted with three damped sines (Eq.4.1). The results for the frequency of the three modes as a function of fluence are reported in Fig.4.14(a). The frequency experiences a redshift for large fluence in all the three modes. The redshift is largely predominant for the PM mode.

To account for this fluence dependence, a simple phenomenological model was developed, that mainly ascribes the effect of fluence to a reduction in the saturation magnetization M_s as a function of the temperature T. Four steps are identified:

1. The pump energy is deposited as heat in the metallic NWs. Assuming that the experiment keeps running in the linear optical regime, the absorption coefficient is not modified by the laser absorption itself. [5] Moreover, multi-photon absorption in the Si substrate is also assumed negligible. With these approximation, the heat deposited in the NWs depends linearly on the pump fluence.

2. The deposited heat determines an increase in temperature. Also for this step, if the system remains in the linear thermal regime, the thermal and thermo-elastic coefficients (thermal expansion, specific heat, thermal conductivity) are the equilibrium ones. With these approximations, the temperature increases linearly with the deposited heat.

3. The saturation magnetization M_s depends on the temperature in a non-linear way. The relation for a three-dimensional ferromagnet is $M_s(T) \propto (1 - T/T_C)^{\beta}$, where T_C is the Curie temperature and $\beta = 0.367$ is the relevant critical exponent for a three-dimensional Heisenberg model.

4. The precession frequency depends on the magnetization via Eq.4.2. Recalling the approximate values for demagnetizing factors $N_x = 0.06$, $N_y = 0.94$, $N_z = 0$, and for the sake of simplification, N_x can be neglected and set to zero. The approximate expression for the precession frequency becomes $f(M_s) \approx \tilde{C}\sqrt{H_z^2 + H_z N_y M_z}$, where $\tilde{C}$ is an appropriate proportionality factor.

Combining all the contributions, the dependence of the PM mode frequency f on the pump fluence F is approximated as

$$f(F) \approx C_1 \sqrt{\left(1 - \frac{F}{F_C}\right)^{\beta} + C_2} \,, \qquad (4.5)$$

where F_C is the critical pump fluence, *i.e.* the fluence for which the Curie temperature is reached in the NWs, and the constants $C_{1,2}$ encompass all the remaining proportionality factors.

In Fig.4.14(b), to the results for the frequency of the PM mode a curve calculated from Eq.4.5 is overlayed. The general trend of the fluence dependence is catched. It was not possible to perform a proper fit: because of the reduced number of point the

---

[5]Strong nonlinear effects ($\Delta n/n \approx 1\%$) are expected in dielectrics and semiconductors at intensity about 10^{15} W/m^2 [18]; in our case the average intensity is 10^{12} W/m^2, so nonlinearities are indeed negligible.

fit parameters are highly correlated. Thus the red curve in Fig.4.14(b) has the value of a guide to the eye, based on the discussed phenomenological model. The conclusion is that at the experimental fluence (approximately 7 mJ/cm^2) the system is driven in the perturbative regime, significant non-linearities arising above 10 mJ/cm^2.

Note that the proposed model cannot explain the systematic redshift of the tr-MOKE frequency as compared to BLS and micromagnetic simulations observed in reference to Fig.4.4. Indeed, for negligible fluence the model approaches a flat aymptoton, thus extrapolation to zero fluence gives basically the same frequency as for the experimental fluence. The higher (approximtely 500 MHz) frequency measured with BLS cannot be simply explained by zero pump-induced heating. The observed discrepancy between tr-MOKE and BLS deserves further investigation.

A key observation on this section is due. As stated in chapter 2, the linear response approximation is oftentimes assumed in TG spectroscopy. The experimental outcome of this assumption is that the quantified observables do not depend on the pump fluence: the system is gently tickled out of equilibrium, such that its response is governed by equilibrium quantities. This is the core of the model here proposed, as well: the optical absorption and the thermo-elastic coefficients are not modified from their equilibrium values by the pump trigger. Only the saturation magnetization is assumed as substantially deviating at large pump fluence: indeed the observed magnon frequency at such large pumping deviates from the low-fluence asymptotic value. The fluence level chosen for the experiment exhibits frequencies very close to the low-fluence ones, so the experiment is run within the linear response approximation.

Coherent and dissipative coupling in a one-dimensional magneto-mechanical system

In the quest for novel electronics and information technologies, artificial crystals appear as promising candidates. As suggested from the results of Ch.4, one of the reasons is the possibility to tailor by fabrication specific anisotropies in the crystal, possibly with strong sensitivity to environmental conditions, thus obtaining efficient sensors and transductors. Moreover, the presence of collective propagating modes in selected bands can be exploited for frequency-selective signal elaboration and propagation [166].

Hybrid artificial crystals gather in a single system sensitivities to different degrees of freedom. In magnonic-phononic crystals, like the one discussed in this part, the magnonic and acoustic excitations can couple, leading to the formation of new hybrid quasi-particles called magnon-polarons. Such polarons, for which magnetic sensitivity typical of a magnonic excitation merges with low-loss propagation typical of surface acoustic waves, prove as energy-efficient information carriers, with long (up to millimeter scale) decay length [167]. Note that the magnon-phonon coupling, always present in systems with sizeable magneto-elastic constants, is boosted if frequency and wavevector degeneracy of the two quasi-particles is reached, *i.e.* when their dispersion relations intersect. The results reported in this chapter relate precisely to the condition of degeneracy for the magnonic-phononic crystal discussed in Ch.4. In this sample, wavevector matching is always met between the excited magnon and phonon (the PM and MEC modes, respectively, in the nomenclature introduced earlier), as both the modes lie at the center of pBZ. Frequency degeneracy is obtained by tuning the magnetic field B_{ext}, thus modifying the frequency of the magnon mode. Detailed tr-MOKE datasets across the region of degeneracy of the two modes allow to quantitatively assess the strength of their mutual coupling.

The chapter is organized as follows: in Sect.5.1 a literature introduction on hybrid magnonics is provided, together with insights on the different coupling mechanisms that can be at play; in Sect.5.2 the experimental procedure is outlined, and the relevance of a time-domain approach to measure the fine structure of the coupled modes is discussed; in Sect.5.3 the experimental results for a magnon-phonon crossing are analysed on the basis of a model Hamiltonian; finally in Sect.5.4 conclusions are drawn on the whole part and perspectives for future investigation are suggested.

5.1 Hybrid magnonics: an overview

The field of magnonics specifically relates to application-oriented study of magnons [168]. The basic advantage of magnonic devices with respect to standard charge-based

electronics is that magnons can propagate without experiencing Joule loss, thus possibly enabling high-rate and energy-efficient information transmission, especially in antiferromagnetic oxides where magnons in the terahertz band are hosted [169]. Moreover, such magnetic excitations naturally couple to spin-based memory and logic units, suggesting the design of all-spin-based platforms, for example leveraging magnon-driven spin-orbit torque at material interfaces [170]. The drawback is the relatively low conversion efficiency between magnons and inductive electromagnetic sources, which make energetically expensive the generation of magnons, and their short decay length, especially in ferromagnetic metals as due to scattering with free electrons.

Both aspects (generation efficiency and decay length) can be addressed by hybridizing magnons with other quasi-particles, an approach that gave birth to *hybrid magnonics*. If the new hybrid excitation inherits desired characteristics from its parent constituents, enhanced functionalities in solid-state systems and devices can be obtained. The interested reader is referred to Ref.[171–175] for useful reviews. Spectacular results in this field have been achieved in coupling magnons to microwave [176] and optical photons [177], and/or to phonons [178–180], or again to superconducting qubits [181], and optical magnons [182]. This approach has found fertile ground in the field of quantum engineering [183–185], where hybridized quasi-particles can boost transduction and sensing capabilities [186–188], perhaps down to the single-quantum detection and manipulation [189–191], or allow novel computation, simulation and storage platforms [192–194]. The contact with research on artificial crystal is evident. Engineering size, material, anisotropy results in tailored excitation; moreover, coupling between different quasi-particles is enhanced if spatial overlap in the amplitude of the involved modes is optimized, what can be sought by engineering artificial crystals. In this context, magnonic-phononic crystals are an appropriate material systems to investigate coupled magneto-mechanical excitations, as already reported in literature [145, 195].

Two fundamentally distinct coupling mechanisms are relevant in this field, namely the *coherent* and the *dissipative* coupling. The role of these two couplings in cavity magnonics is discussed at length in Ref.[196]. Coherent coupling is what usually a researcher has in mind when speaking of coupled quasi-particle. Two modes can be degenerate for a specific value of an external tuning parameter (a condition named zero-detuning); the external parameter can be a field, an angle to an anisotropy axis, some geometrical dimension etc. However, in presence of an interaction between the two modes the degeneracy is lifted and a finite energy gap opens, whose width is proportional to the coupling strength. Thus the eigenvalue spectrum of the coupled system features two hybridized modes that are not traceable to a single subsystem, but rather retain partially the character of the two original modes. The theoretical description of such avoided crossing dates back to 1929, and boasts the authorship of two giants of physics of the calibre of Wigner and von Neumann [197]: the effect is thus sometimes referred to as the von Neumann-Wigner hybridization effect. The microscopic coupling mechanism stems from mutual energy exchange between the two subsystems at a rate J [198]. The energy exchange takes places even in the mere presence of vacuum field fluctuations, with no further external perturbation [199]. If J exceeds the intrinsic damping of each subsystem to the environment, the strong coupling regime is reached. This condition is sought *e.g.* for quantum transduction [200], or to perform read-out of one subsystem via the other [201].

In dissipatively coupled systems [202, 203], the mutual exchange of energy stems from the correlation in the dissipation of the two subsystems to a common reservoir

[204, 205]. In this case, the damping of each subsystem is no more a nuisance hindering the strong coupling regime, but becomes the driving mechanism itself for the coupling. In this case the energy levels attract each other, becoming degenerate in a finite region of detuning, while the damping show non-monotonous trend with enhancement or reduction of the dissipation to the environment. This coupling mechanism requires open cavity systems and a coherent mode in the common reservoir, as can be a traveling wave [206]. Dissipative coupling is now boosting research for its close link to non-Hermitian physics (anti-$\mathcal{PT}$ symmetry [207, 208], exceptional points [209, 210]) and technological fallouts driven by engineering of the dissipation [211], with fruitful application in non-reciprocal transport [212] and synchronization [213].

Both coupling mechanisms can coexist in a single system, creating the possibility of tuning one into the other. Nonetheless, only few papers report compresence of both coherent and dissipative coupling in hybrid systems, a condition we refer to as *mixed* coupling [202, 212, 214, 215]. Experimental investigation of mixed coupling systems can be useful especially in determining under which conditions one coupling mechanism is optimized over the other, thus widening the field of engineering variables to design tailored solid-state devices.

5.2   Experimental approach

The same one-dimensional magnonic-phononic crystal discussed in Ch.4 is here investigated with specific focus on the crossing of PM and MEC modes. The aim is to assess the character (coherent or dissipative) and the strength of the coupling between the two modes. Experimentally, the condition of crossing is easily obtained by tuning the strength of the external magnetic field: recalling Fig.4.10, while the frequency of the PM mode depends on B_{ext}, the MEC modes display no dispersion. This results in the possibility to bring to degeneracy the PM mode with one or the other of the MEC modes, a condition in which coupled magneto-mechanical dynamics is observed.

The approach is to acquire tr-MOKE maps in close-up regions across the mode intersections, with small steps of B_{ext} in order to obtain detailed datasets concerning the coupled modes. For this investigation only tr-MOKE data are analyzed, for which both acoustic and magnetic dynamics are simultaneously triggered. Indeed, as detailed at the end of this chapter, the coupled magneto-mechanical dynamics is different if only the acoustic subsystem is triggered while the magnetic precession is acoustically driven, as for the SAW-FMR experiment discussed in Ch.3, or if both phonon and magnon are impulsively excited, as it is the case for this pump-probe experiment. Restated, it is the difference between exciting a mode that drives a resonance, and exciting independently two modes that can couple to each other. In the former case, energy is injected from outside (*e.g.* the pump laser) into one subsystem (the phonons) and then a different subsystem (the magnetization) absorbs partially the injected energy. In the latter case, external energy is injected into both the subsystems, and the two triggered modes can interact and further mutually exchange energy. In this picture, a pump pulse is able to excite both phononic and magnonic modes: thus tr-MOKE resides in the second scenario. Differently, magnetic BLS can only probe the magnonic modes (the PM mode plus eventually higher-order modes); also numerical simulations are unable to reproduce the coupled dynamics as long as a proper magneto-elastic field is not introduced in the model. This is the basic reason under the impossibility to study magnon-phonon coupling via BLS.
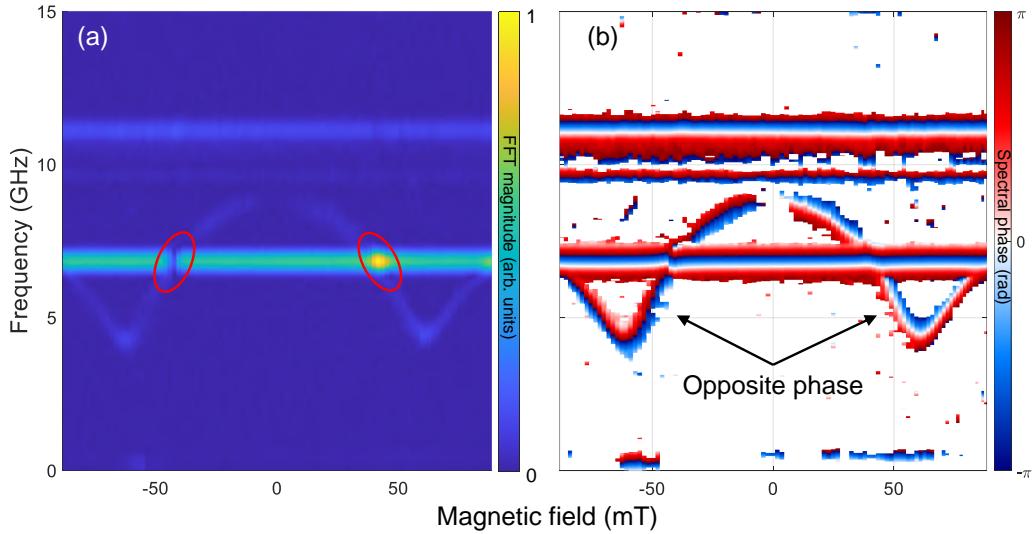
Figure 5.1: FFT maps of tr-MOKE data for the ancillary sample at $\varphi = 90°$. (a) FFT magnitude; the red ellipses indicate the presence of enhancement and depletion of the spectral weight at the PM-MEC1 crossings. (b) Spectral phase; the arrows highlight the π swap in the dynamical phase of the PM mode when B_{ext} is swept through zero strength.

The tr-MOKE data are analyzed in time-domain. The results of fitting show deviations for the frequency and the damping of the coupled modes with respect to the uncoupled ones. A model Hamiltonian encompassing both coherent and dissipative couplings is introduced in order to analyze the coupled modes. In particular, fitting the experimental results to the model eigenvalues allows to quantify the strength of the competing coupling mechanisms in the weak-coupling regime.

Coarse structure for the crossings

The maps in Fig.4.10 resulted in calculation of magnetostatic parameters (Fig.4.11) and in confirmation via correlative techniques of the nature of the PM mode (Fig.4.4). Still, the most striking feature in Fig.4.10 is the spectral weight of the FFT magnitude at the crossings of PM mode with either MEC1 or MEC2. Two cases can be observed: (i) spectral weight *enhancement* for the PM-MEC1 crossing at large azimuth ($\varphi = 60°$ and $75°$), and for any PM-MEC2; (ii) spectral weight *depletion* for the PM-MEC1 crossing at small azimuth ($\varphi = 15°$, $30°$ and $45°$). Precipitous conclusions on different nature of the mode coupling depending on the azimuth must be avoided, especially given the reduced spectral resolution of FFT maps: given a total observation window of 3.3 ns, the FFT resolution is no better than 600 MHz in FWHM.

As a demonstration that any step in the interpretation must be set carefully, I report tr-MOKE results obtained on a sibling sample. The ancillary sample was fabricated with the same DUV lithographic technique, and it is composed of the same stacking layers of ferromagnets (thickness $t_{\text{Py}} = t_{\text{Fe}} = 10$ nm), but with different geometrical parameters: width $w = 310$ nm, inter-NW spacing $d = 300$ nm and full NW periodicity $D = 610$ nm. What motivated the investigation of a new sample is that the configuration at $\varphi = 90°$ is highly symmetrical and as such can be more insightful; still, looking again at Fig.4.10

no mode crossing is visible in the full range accessible for B_{ext}. The ancillary sample, having approximately a factor $3/2$ larger periodicity D, is expected to host a factor $2/3$ lower-frequency MEC1 mode; moreover, since the layer stacking and thickness is the same, the lowest-order magnon will be basically the same, possibly featuring different magnetostatics given the different filling ratio of the NWs. Thus in the ancillary sample a PM-MEC1 crossing for $\varphi = 90°$ is expected to take place. Indeed, as shown in Fig.5.1(a) the MEC1 mode lies at $f = (6.8 \pm 0.05)$ GHz, and crosses the PM mode at opposite fields $B_{ext} = \pm 41$ mT. As expected, the anisotropy field for this sample is larger ($B_a = 61$ mT), as a consequence of the different filling ratio of the NW pattern resulting in reduced inter-NW dipolar interaction and reduced screening of the demagnetizing field; more-over, note that the reduction in the MEC1 frequency is smaller than the expected factor $3/2$: this is a further hint that specific non-linearities in the phonon spectrum are present, as due to the phononic-crystal structure, that result in the failure of linear-dispersion models for the phonons. Notably, as highlighted by the red ellipses in Fig.5.1(a), the spectral weight of the FFT magnitude is either enhanced or depleted depending on the field being positive or negative, respectively. Looking at the spectral phase in Fig.5.1(b), the only difference between the two crossings is the PM mode swapping the dynamical phase by π upon passing beyond the axis $B_{ext} = 0$ mT, consistently with the discussion on symmetries reported in the previous chapter. The conclusion of this ancillary experiment is that the enhancement/depletion feature is a *coarse structure* in the mode crossing, which mainly relates to the dynamical phases of the interacting modes: no direct information on the details of the coupling (strength and coupling mechanism) is encoded therein.

To substantiate this picture, following Ref.[196] we performed systematic computations of the frequency spectra for two quasi-degenerate modes, as a function of their frequency detuning. The spectra are computed as FFT of simulated time-domain maps, in analogy to the experimental data acquired via tr-MOKE. Three values for the coupling strength g and two values for the relative phase $\Delta\phi$ were considered; only coherent coupling was assumed for simplicity. I believe the conclusions of this reasoning are not affected by these simplification. The two-dimensional maps for the calculated FFT magnitude and spectral phase are reported in Fig.5.2; the calculated theoretical eigenvalues are shown as black solid lines in each panel. In order to allow a direct comparison to the experimental data, the simulated time-window was fixed to 3 ns, resulting in smearing of the FFT peaks along the frequency axis by about 600 MHz in FWHM as expected; the intrinsic damping of the modes was assumed negligible in order to highlight the merely instrumental contribution. For $g = 0$ rad/ns (no coupling), the FFT magnitude at the crossing strongly depends on the relative phase of the modes: mixing of signals with same or opposite dynamical phase results in enhancement or depletion of the spectral weight, respectively. In this case, no coupling at all takes place, the effect originating only from the coherent superposition of indipendent modes. For $g = 1$ rad/ns (weak coupling), the theoretical eigenvalues start to hybridize and to experience frequency repulsion (see the black solid lines), but the frequency gap is smaller than the spectral resolution. Partial spectral superposition of the modes determines again enhancement and depletion in the spectral weight, depending on the relative modal phase. For $g = 2$ rad/ns (strong coupling) the two hybridized branches are well separated and no coherent artifact appears in the FFT magnitude. Thus, inspection of only the magnitude does not allow to disentangle coupling and dynamical-phase effects in the case of zero and weak coupling. Combined analysis of the spectral phase can help in this job. For exam-
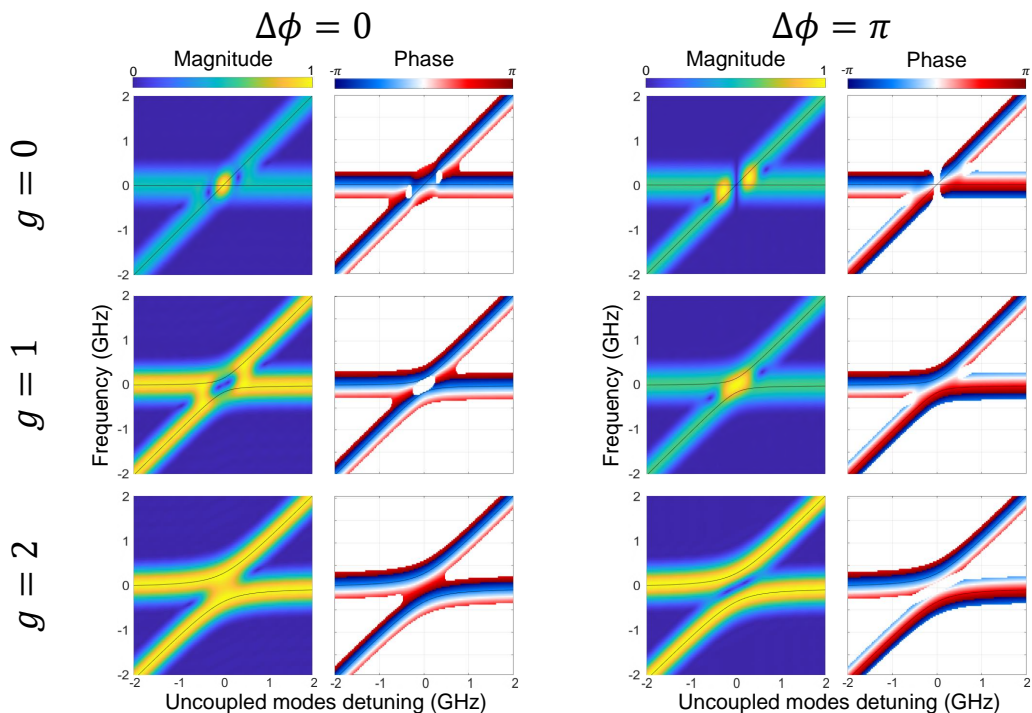
Figure 5.2: Two-dimensional maps for FFT magnitude and spectral phase calculated for the crossing of two modes. The abscissa is the relative frequency detuning of the uncoupled modes, so in each map one mode is flat and one has linear dispersion with unitary slope. For three values of coherent coupling strength ($g = 0$, 1 and 2 rad/ns) the calculation has been carried out for $\Delta\phi = 0$ and π, where $\Delta\phi$ is the phase difference of the two modes. The computed frequency for the coupled modes is reported as black solid lines. For the calculations, only coherent coupling was assumed, and the FFT resolution was assumed as limited to 600 MHz in FWHM by the finite observation time window computed.
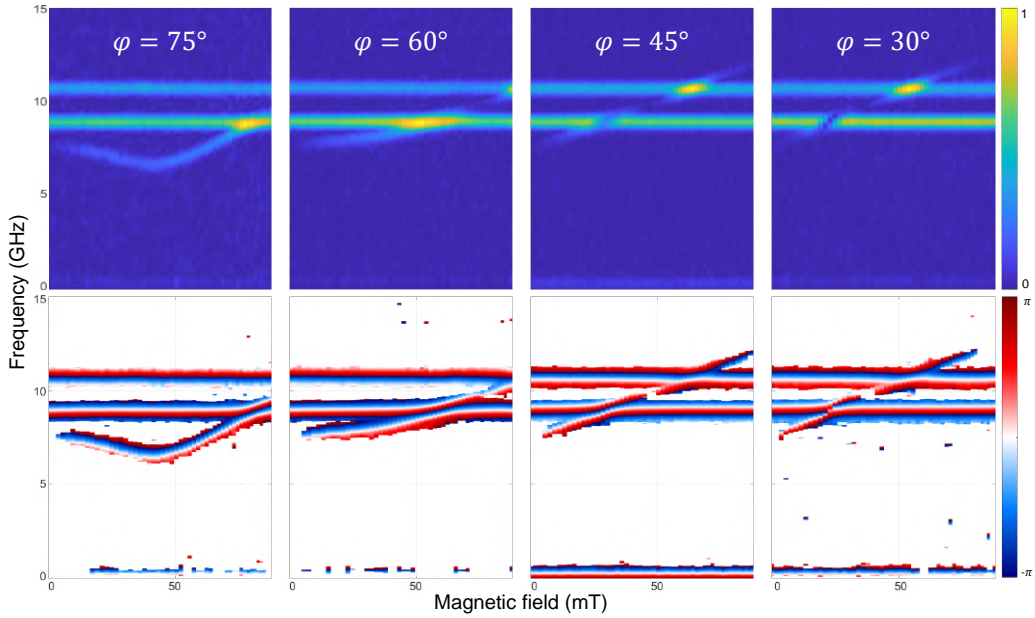
Figure 5.3: FFT magnitude (top) and spectral phase (bottom) of the experimental configurations in which crossing was observed.

ple, the magnitude maps for $g = 0$ rad/ns and $\Delta\phi = 0$ is quite similar to that for $g = 1$ rad/ns and $\Delta\phi = \pi$, showing spectral-weight enhancement in the region of the crossing; the phase maps, instead, are strikingly different and could guide the analysis. As a final comment on the aspect of the coarse structure, in Fig.5.3 an overview of the experimental results for FFT magnitude and spectral phase is reported. Four azimuth angles are shown, namely $\varphi = 75°$, $60°$, $45°$ and $30°$. The spectral phase for PM-MEC1 crossing displays qualitatively the same behaviour for the four angles, and looking at Fig.5.2 the crossing could be coarsely labeled as weakly coupled with small $\Delta\phi$; differently, the magnitude displays either enhancement or depletion. This further demonstrates that the mere spectral weight cannot be assumed as an indicator of a coupling mechanism instead of another, nor of different coupling strengths. In can be noted also that the spectral phase at the PM-MEC2 crossing is qualitatively different: this is a hint that a possible different coupling mechanism could be at play.

The conclusion of this discussion is that for poorly-resolved FFT, *i.e.* when the spectral resolution is coarser or comparable to the frequency separation of the coupled modes, the magnitude can give artifacts in the peak intensity which are not related to the physics driving the mode coupling. The spectral phase, on the other hand, seems more reliable in the assessment of the coupling: proper modeling of the spectral phase dependence could be a viable road for the investigation of weakly-coupled systems. The path I followed was different: any information in the complex FFT (magnitude and phase) is already encoded in the time-domain data. Moreover, time-dependent details of the mode dynamics (*e.g.* details of the damping and anomalies in the dynamical phase) are readily available in the time-domain data, while they are basically impossible to be recovered from the Fourier-transformed data as they are encoded in details smeared on the entire frequency axis with frequency-dependent phases. For these two reasons (pos-
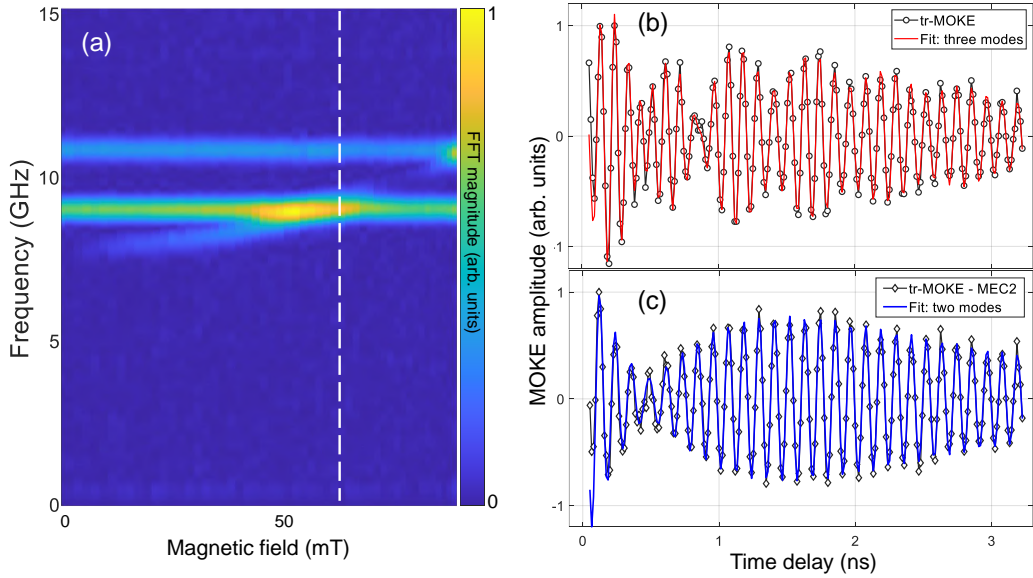
Figure 5.4: (a) FFT magnitude for $\varphi = 60°$; the vertical dashed line at $B_{ext} = 61.8$ mT highlights the field value chosen for this time-domain analysis. (b) Original time-domain trace (black circles) and fit with three modes (red line). (c) Result of the subtraction of MEC2 fit to the original trace (black diamonds) in order to highlight the residual contribution, and fit of the residual with two modes (blue line).

sible artifacts in the FFT magnitude and direct availability of details in time-domain) the following analysis was performed via time-domain fitting. Looking retrospectively to the results shown until now in this part, starting from time-domain data a deviation into frequency-resolved maps proved quite insightful as they gave in a glimpse the general dispersion of the modes, allowing also to compare with correlative frequency-domain techniques; now it is necessary to go back to time-domain for getting insights into the coupling mechanism.

5.3 Analysis of a PM-MEC1 crossing

Among all the crossings observed (see Fig.5.3), I investigated in detail only the PM-MEC1 crossing for $\varphi = 60°$. The reason for this choice is twofold: (i) at this angle the PM mode is quite intense, allowing a reliable analysis in time-domain; (ii) the field position of the crossing is entirely within the range available with the electromagnet. Note that also the PM-MEC2 crossing at $\varphi = 30°$ satisfies these requirements; it will be object of future investigations.

The coarse structure of the targeted crossing in Fig.5.3 shows enhancement character. To gain insights into the fine structure of the mode crossing, the time-domain structure of our data is exploited. The tr-MOKE traces were fitted with the function in Eq.4.1; the index i runs on all the three modes, *i.e.* the PM, MEC1 and MEC2 modes. Note that the necessity to consider three modes to fit each trace is not obvious: for example, in case of negligible coupling, at zero detuning two modes are exactly degenerate and the trace should be satisfactorily fitted with only two damped modes; this aspect gets more

dramatic if pure dissipative coupling is at play, as will appear clearer in a while. The results shown in Fig.5.4 demonstrates that three modes were indeed required. It reports analysis of tr-MOKE data at $\varphi = 60°$ for $B_{\text{ext}} = 61.8$ mT. This field value has been chosen since, as the following analysis demonstrates, it is the nominal value of degeneracy of the uncoupled modes, *i.e.* it corresponds to the zero detuning condition; the following discussion holds stronger for other field values. In Fig.5.4(a) appears, surprisingly, that $B_{\text{ext}} = 61.8$ mT does not correspond to the region of maximum enhancement, again testifying the presence of artifacts in the FFT spectral weight. In panel (b) the original trace (black circles) and the fit with three modes (red line) are reported. Panel (c) reports (black diamonds) the data obtained as the original trace to which the MEC2 fit was subtracted. The aim of this procedure is to highlight the contributions due to the two interacting modes, namely the PM and MEC1 modes. The fit with the residual two modes is also reported (blue line). Here, it is apparent that the amplitude modulation in the first nanosecond, reminiscent of Rabi oscillations for crossing-avoiding levels, requires two modes to be properly fitted.

Following this analysis, time-domain fits were performed of traces acquired in finely sampled intervals (approximately 0.3 mT) of magnetic field in a close-up of the PM-MEC1 crossing region; the original three-moded traces were employed. In Fig.5.5 the values of frequency [panel (a)] and damping [panel (b)] obtained as best-fit parameters are reported: the avoided crossing of the frequencies is a clear demonstration of the von Neumann-Wigner hybridization effect [197]. The errorbars are the 95% confidence level of the fitting algorithm. The color code for the PM and MEC1 modes interpolates between predominant phonon-character (green) and magnon-character (yellow). In panel (a) also dashed lines are reported, matching the asymptotic values of the modes at large detuning: the crossing of these lines at $B_{\text{ext}} = 61.8$ mT indicates the value of the expected zero detuning. In panel (b) the same color code is used. The damping for the two interacting modes is field-dependent; degeneracy in the dampings is observed about $B_{\text{ext}} = 67$ mT. As highlighted by the arrows, there is a mismatch between the position of zero detuning and the crossing of the dampings. This asymmetry suggests that unusual coupling of the modes is at play, and motivates a step into theoretical modeling of the coupling.

Model Hamiltonian for coherent and dissipative coupling

The Hamiltonian $\mathcal{H}$ modeling both coherent and dissipative coupling can be written [202, 204] under the rotating wave approximation as

$$\mathcal{H}/\hbar = \tilde{\omega}_A a^\dagger a + \tilde{\omega}_B b^\dagger b + g \left(a^\dagger b + e^{i\Phi} a b^\dagger \right) \ . \tag{5.1}$$

Here $a^\dagger$ and $b^\dagger$ (a and b) are the creation (annihilation) operators for mode A and B, respectively; in the present experiment the modes are the phonon and the magnon, flat and dispersive respectively. The generalized angular frequency of uncoupled mode $i = (A, B)$ is denoted as $\tilde{\omega}_i = \omega_i - i\gamma_i$, encompassing both the angular frequency ω_i and the intrinsic damping γ_i. The parameter g is the strength of the coupling, whose nature depends on the value of the phase Φ: pure coherent coupling for $\Phi = 0$, pure dissipative coupling for $\Phi = \pi$. The coupling term (the third on the right-hand side in Eq.5.1) is sometimes written as $(J + i\Gamma) \left(a^\dagger b + a b^\dagger \right)$, where J and Γ are the coherent and dissipative coupling strengths, respectively [203, 214]. The two expressions are equivalent, once the correspondence $g e^{i\Phi/2} = J - i\Gamma$ is made. This is equivalent to define a
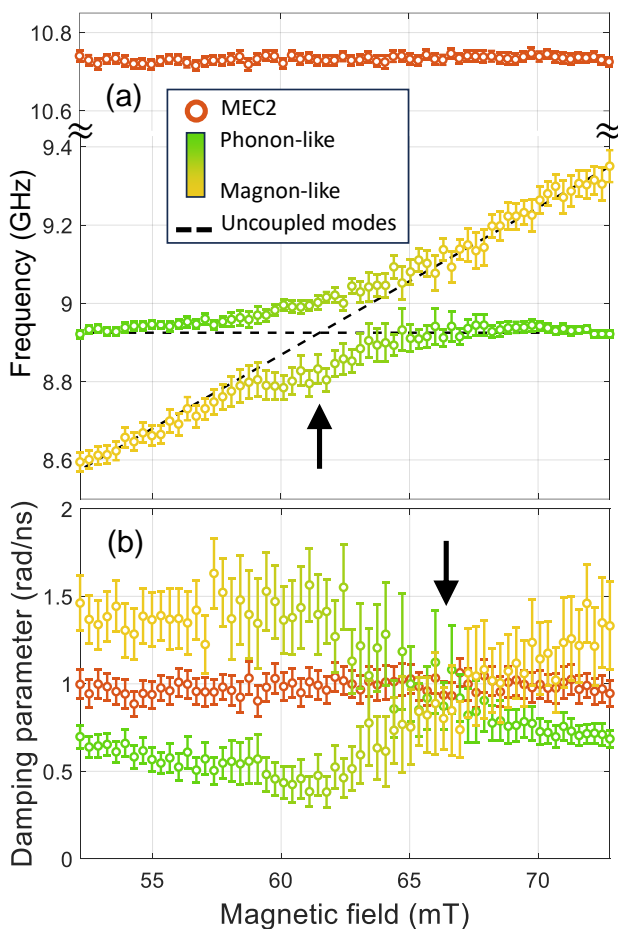
Figure 5.5: Results for frequency [panel (a)] and damping [panel (b)] obtained as best-fit parameters from time-domain traces in a close-up of the PM-MEC1 crossing for $\varphi = 60°$. The experimental data for the hybridizing modes show deviations from the uncoupled modes, mixing phonon character (green circles) and magnon character (yellow circles). The frequency values for the uncoupled modes are shown as black dashed lines. The arrows highlight the mismatch between the field values for zero-detuning [panel (a)] and for damping crossing [panel (b)]. The fit results for the non-coupling MEC2 mode are also reported (orange circles).
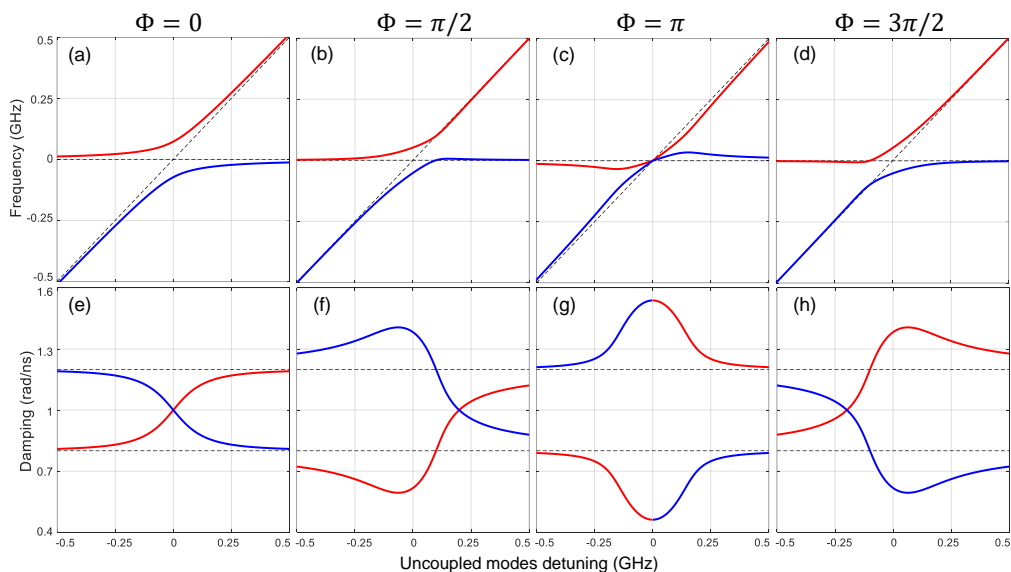
Figure 5.6: Modification of the eigenvalues of $\mathcal{H}$ upon changing the coupling phase Φ. (a-d) Frequency dispersion (real part). (e-h) Damping (imaginary part). All plots are shown as a function of the uncoupled frequency detuning. The upper branch ($\tilde{\omega}_+$) and the lower branch ($\tilde{\omega}_-$) results are shown in red and blue lines, respectively. The uncoupled values for frequency and damping are shown in each plot as black dashed lines. For comparison to the experimental results, $\gamma_A = 1.2$ rad/ns and $\gamma_B = 0.8$ rad/ns was assumed; the coupling strength was kept at $g = 0.5$ rad/ns.

complex coupling parameter $\tilde{g}$ that can be expressed either with its real and imaginary parts (J and Γ) or with its absolute value and argument (g and $\Phi/2$). The Hamiltonian in Eq.5.1 is non-Hermitian, owing both to the imaginary part of $\tilde{\omega}_i$ and to the dissipative coupling term.

To calculate the coupled eigenvalues, the Hamiltonian is rewritten as

$$\mathcal{H}/\hbar = \begin{pmatrix} a^\dagger & b^\dagger \end{pmatrix} \begin{pmatrix} \tilde{\omega}_A & g \\ ge^{i\Phi} & \tilde{\omega}_B \end{pmatrix} \begin{pmatrix} a \\ b \end{pmatrix} , \tag{5.2}$$

and the problem reduces to the diagonalization of the 2×2 matrix. Thus the coupled eigenvalues of $\mathcal{H}$ are calculated to be

$$\tilde{\omega}_\pm = \left(\frac{\tilde{\omega}_A + \tilde{\omega}_B}{2} \right) \pm \sqrt{ \left(\frac{\tilde{\omega}_A - \tilde{\omega}_B}{2} \right)^2 + g^2 e^{i\Phi} } , \tag{5.3}$$

where, in analogy with above, the real part of $\tilde{\omega}_\pm$ gives the angular frequency and the opposite imaginary part gives the damping. The subscripts $+$ and $-$ indicate the upper and lower branches, respectively. In Fig.5.6 the coupled (red and blue lines) and uncoupled (black dashed lines) eigenvalues are plotted as a function of the uncoupled modes frequency detuning. To closely compare to the experimental results, the intrinsic dampings of the uncoupled modes have been set to 0.8 rad/ns and 1.2 rad/ns for the flat and dispersive mode, respectively, and the coupling strength g has been set to 0.5 rad/ns. At $\Phi = 0$ [panels (a) and (e)], the frequency degeneracy at zero detuning is lifted and a gap opens proportional to the coupling strength [216]; this is often understood as the *smoking gun* for hybridization. The dampings, on the other hand, attract each other and become degenerate at zero detuning. At $\Phi = \pi$ [panels (c) and (g)] the deviations from the uncoupled values are opposite: the coupled frequencies experience level attraction, resulting in extension of the degeneracy to a finite region across zero detuning, while the dampings repel each other, a condition often interpreted as sub- and super-radiant modes [217, 218].

Note that the coupled eigenvalues for $\Phi = 0$ and $\Phi = \pi$ have a high degree of symmetry: $\omega_\pm$ features inversion symmetry with respect to the point of degeneracy of the uncoupled modes, while for $\gamma_\pm$ the point for inversion symmetry is the average damping of the uncoupled modes, *i.e.* $(\gamma_A + \gamma_B)/2$. This symmetry is broken if both couplings are at play, *i.e.* for mixed coupling, as shown for $\Phi = \pi/2$ [panels (b) and (f)] and $\Phi = 3\pi/2$ [panels (d) and (h)]. In these intermediate cases, the frequency repulsion is weaker than for $\Phi = 0$ and the deviation from the uncoupled frequencies is asymmetric. The dampings have an intermediate trend, displaying both repulsion and degeneracy. The most striking feature is that the condition for degenerate dampings is shifted from zero detuning: this can be assumed as an experimental indicator for mixed-coupling systems.

Analysis of the fit results

On the basis of this brief theory detour, the analysis proceeded by fitting frequency and damping data reported in Fig.5.5 with the theoretical eigenvalues of Eq.5.3. Note that the aim was to fit together both frequency and damping, *i.e.* to get a unique set of best-fit parameters that optimize the model function for both datasets; to further complicate, the model involves complex parameters. The computational solution adopted consists in appending in a single numerical vector the frequency and damping values, whose abscissa was a two-fold repeated magnetic field vector; the model function is then defined
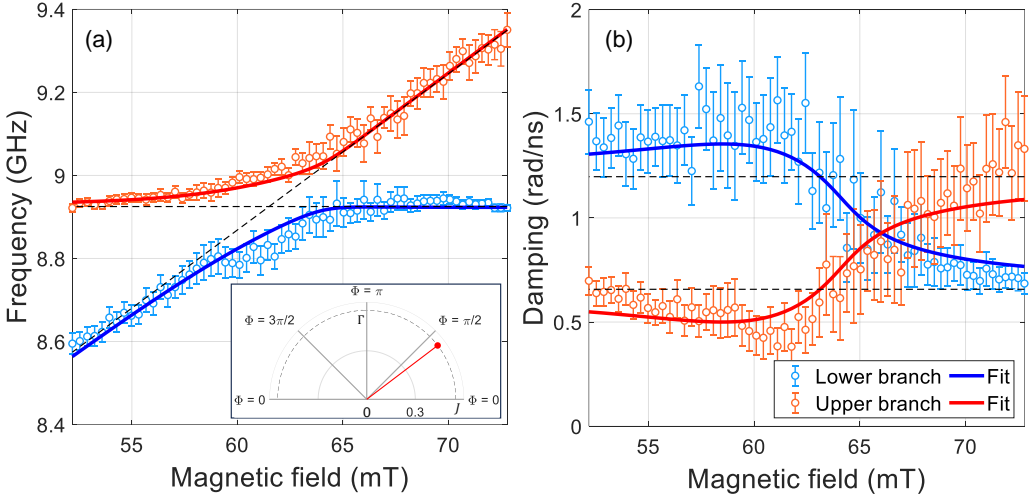
Figure 5.7: Fitting of the frequency [panel (a)] and damping [panel (b)] on the basis of the calculated eigenvalues of the model Hamiltonian. The data for the lower (upper) branch are displayed in blue (red). The best-fit curves are shown with the same color code. The uncoupled frequency and damping are reported as black dashed lines. The inset of panel (a) shows the mapping of the complex coupling parameter to a plane spanned by J ($\Phi = 0$, pure coherent coupling) and Γ ($\Phi = \pi$, pure dissipative coupling); the red dot lies in correspondence to the value of $\tilde{g}$ obtained from the fit.

as a step-wise function, which assumes the model frequency in the first half and the model damping in the second half of its field of definition. During the fit all the parameters are left free to vary. The PM mode is assumed as linear in B_{ext}: this is a reasonable approximation of the actual non-linear dispersion, given the reduced detuning window.

The results of the fit are reported in Fig.5.7, for frequency [panel (a)] and damping [panel (b)]. The data for the upper (lower) frequency branch are shown in red (blue). The same color code is adopted for the best-fit curves. The uncoupled frequencies and dampings, which are fit parameters too, are reported as black dashed lines. The fit results for the intrisic dampings are $\gamma_p = (0.66 \pm 0.02)$ rad/ns and $\gamma_m = (1.20 \pm 0.04)$ rad/ns. The model well describes the trend of the experimental data. In particular it catches the observed mismatch between the frequency zero-detuning and the crossing of the damping. The fit parameters related to the coupling result $g = (0.55 \pm 0.03)$ rad/ns and $\Phi = 1.3 \pm 0.1$, corresponding to $J = (0.44 \pm 0.04)$ rad/ns and $\Gamma = (-0.33 \pm 0.04)$ rad/ns. To discuss the coupling phase Φ, it can be instructive to map the complex coupling parameter $\tilde{g}$ to a half-plane[1] spanned by J and Γ: in this picture the radius gives the absolute value of the coupling and the argument gives the degree of mixing of coherent and dissipative mechanisms. Pure coherent coupling corresponds to a real $\tilde{g}$, pure dissipative coupling to an imaginary $\tilde{g}$, mixed-coupling to any other situation. The inset of Fig.5.7(a) reports the discussed mapping; the red dot is located in correspondence of the fit results, showing that the system is close to a 50:50 ratio of coherent and dissipative coupling. Finally, the coupling strength g obtained from the fit has to be compared to the intrinsic damping of the modes. A standard quantifier of the coupling, often en-

---

[1]Only a half-plane is sufficient since the coupling term appears as squared in the eigenvalue equation Eq.5.3: the phase translation $\Phi \to \Phi + 2\pi$ corresponds to a rotation of only π in this complex plane.

countered in studies on coherent coupling, is the cooperativity $\mathcal{C}$, which is the ratio of the coupling strength to the intrinsic dampings, namely $\mathcal{C} = g^2/\gamma_m\gamma_p$. The meaning, roughly, is that if g exceeds both the intrinsic dampings γ_m and γ_p(*i.e.* if $\mathcal{C} > 1$), then the two hybridizing modes exchange energy to one another at a rate larger than the irreversible energy loss to the environment: this is the onset of the strong coupling regime. For the present experiment, the values obtained from the fit give $\mathcal{C} = 0.38 \pm 0.05$. This low value of cooperativity sets the sample as weakly coupled. This is expected, given the discussion above on the observed artifacts in the FFT magnitude.

A final comment on the relevance of a time-domain approach. As already discussed, the FFT magnitude of the tr-MOKE traces has poor spectral resolution. This has been ascribed to the limited observation time window, which sets the minimum frequency linewidth to 600 MHz in FWHM: the gap opening approximately 200 MHz wide is thus masked, the Rayleigh criterion being largely not met. However, besides instrumental resolution, the peak linewidth is affected also by the lifetime of the observed excitation: this holds also for standard frequency-domain techniques, where the lifetime contribution to the linewidth is dominant whenever the instrumental broadening can be neglected. From the results obtained in this chapter, the lifetime contribution to the peak linewidth would be between 100 and 200 MHz: the details of the crossing would be equally masked, even assuming no instrumental broadening. In general, whenever the intrinsic damping is larger than the coupling strength, frequency-domain techniques can give fictitious results, whereas the time-domain approach presented allows for reliable quantification of the coupling, pushing forward the resolution limit. This is particularly important for weakly-coupled systems, and even more for dissipatively-coupled systems experiencing level attraction.

5.4   Conclusions and look-outs

In part III, I presented the experimental investigation of a one-dimensional magnonic-phononic crystal, expected to be an ideal system to investigate magneto-elastic coupling as due to tailored and localized modes. The employed time-resolved approach proved suitable to analyse some aspects of the sample magnetostatics and acoustic dynamics, as discussed in Ch.4. Comparison to correlative static techniques was helpful both for further confirming the observed signals, and for highlighting the specificity of the dynamical approach. What really motivated the employ of a pump-probe scheme is the possibility to impulsively trigger both phononic and magnonic dynamics in the artificial crystal, and to analyse the decay of the coupled modes on their natural timescale. The results of this investigation, reported in the present chapter, show evidence of competing coherent and dissipative coupling in the sample, as deduced from the observed asymmetry in the frequency and damping of the coupled modes. A model Hamiltonian was presented, that unifies on equal footing both coupling mechanisms with continuous tuning from one to the other via the phase Φ. Quantitative estimation of the strength and degree of mixing of the coupling was obtained via fitting the eigenvalues of the Hamiltonian to the experimental data.

Being able to quantify the degree of coherent and dissipative coupling can help in identifying the experimental parameter which tunes the coupling from one mechanism to the other. In cavity magnonics (magnon-photon hybridization), it is possible to tune from dissipative to coherent coupling *e.g.* by moving the magnetic system (oftentimes a micron-size sphere of Yttrium Iron Garnet) either in a node or in an antinode of the cavity
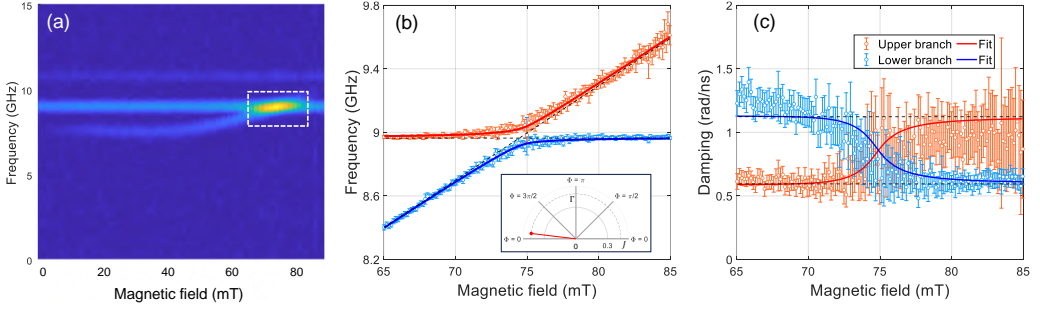
Figure 5.8: Analysis of PM-MEC1 crossing for sample azimuth $\varphi = 75°$ and magnetic field tilted OOP approximately $\theta = 15°$. (a) Wide-scan map of FFT magnitude; the white box highlights the crossing region which has been investigated with finer field steps. Frequency and damping [panels (b) and (c)] are extracted from time-domain fit. The upper (lower) branch is reported as red (blue) circles. The fit of the Hamiltonian eigenvalues to the frequency and damping data are shown as solid lines. The uncoupled values are indicated by black dashed lines. The inset of panel (b) shows the location of the complex coupling parameter $\tilde{g}$ in the (J, Γ) plane.

photon field [202, 204]. A similar effect can be speculated to be present also in magneto-mechanical systems, where displacing the magnetic resonator in positions with different standing strain field could enhance one coupling mechanism at the expense of the other. For the magnonic-phononic crystal here investigated, a possibility is to set $\varphi = 90°$ (B_{ext} parallel to HA), thus squeezing the PM mode to be an edge mode localized at the borders of the NWs [147, 219], closer to strain antinodes; or to design the NW periodicity to have hybridization with higher-order magnetic modes, whose spatial distribution along the NW width is different.

A preliminary demonstration of this possibility has been explored, as reported in Fig.5.8. The sample azimuth was set to $\varphi = 75°$, and the field B_{ext} was tilted OOP by approximately $15°$. Panel (a) shows that the PM-MEC1 crossing lies entirely within the accessible field range. This is a consequence of the increased steep in the PM mode (for comparison to the condition of field completely IP, see Fig.5.3): the presence of an OOP field component results in strong demagnetizing fields arising across the NW thickness, modifying localization and energetics of the magnon. Details on the spatial distribution of the mode in this configuration require numerical simulations. The same analysis procedure discussed in Section 5.3 has been applied. The results of the time-domain fit are impressively different: in this configuration the degeneracy of the damping lies in correspondence to the zero-detuning condition, suggesting negligible dissipative coupling. The fit of the Hamiltonian eigenvalues corroborates this, giving $g = (0.43 \pm 0.03)$ rad/ns and $\Phi = 6.0 \pm 0.1$. The system still exhibits weak coupling between the modes, but coherent coupling is largely the leading mechanism in this experimental configuration.

These results confirm the measured sample as a relevant platform to address the interplay between mechanical and magnetic dynamical modes. For such artificial systems two key advantages can be outlined. First, each artificial atom can be purposely designed. The magnetic anisotropies can be set by fabrication, resulting in tailored magnetostatics and excitation spectra, and eventually in simple models for their description to be employed. Also the choice of materials for the stacking layers and of the cross sections largely influences the magnonic modes, allowing for example tunable localization. Tailoring the cross section also sets specific localized phononic modes residing in

each artificial atom. Second, the artificial atoms are not isolated: beyond localized excitations, the system hosts collective propagating modes, an appealing theme particularly for applications. The symmetry of the artificial lattice and the spacing between each component are further degrees of freedom to take advantage from. As a final comment, I would like to stress that for one- and two-dimensional magnonic-phononic crystals, the artificial atoms are of course fabricated on top of a substrate. This, far from being a nuisance, can become a potentiality for addressing reservoir-mediated couplings, as the results reported in this chapter show. In summary, engineering of artificial atoms (localized excitations) and of the artificial lattices (delocalized excitations) can be basically decoupled, and can be the driving force to envision tailored devices with specific functionalities. Of course, *mutatis mutandis* this is to be generalized to other types of hybrid artificial crystals, the only obstacle seeming the inventiveness and imagination of researchers.

Conclusions

Objectives

In this thesis I explored the coupling of phonons and magnons in transition metal ferromagnetic samples. The focus was the investigation of the details of the intertwined magneto-acoustic dynamics resulting from impulsive excitation of finite-wavevector acoustic and magnetic transients via all-optical techniques.

Results

The addressed systems were polycrystalline Ni thin films e-beam evaporated on transparent substrates, and magnonic-phononic crystals composed of sub-micron polycrystalline ferromagnetic nanowires produced via DUV lithography on Si substrate.

On the Ni thin film samples, SAWs generated via TG at three different wavevectors were observed to drive resonant magnetization precession. The condition of SAW-FMR required tuning the strength of an external IP magnetic field. Analysis of the resonance results, in terms of resonance field and linewidth, allowed to perform close comparison to photon-driven B-FMR measurements. The drawn conclusion was that SAW-FMR probes the same physics as B-FMR, with finer spatial resolution as given by the laser footprint. Moreover, the limit of applicability of the technique was identified, on the basis of magnon bands calculated with an approximate model: as SAW-FMR is driven by finite-wavevector acoustic modes, discrepancies from B-FMR results are expected to take place if the magnon frequencies deviate substantially from the uniform precession frequency.

The magnonic-phononic crystals exhibited rich phenomenology in the transient state after pump excitation. Both acoustic and magnetic modes were triggered by the same pulse; they were identified on the basis of the dependence on the strength of the IP external magnetic field, and of correlative tr-R and BLS measurements and simulation with micromagnetic models. The pump selection rules for excitation of the purely magnetic mode were experimentally identified. At azimuthal angle $\varphi = 60°$, the magnon-phonon crossing was analysed in detail via tr-MOKE. Fitting of the time-resolved transients revealed avoided crossing of the modes, as a demonstration of the von Neumann-Wigner hybridization effect. The evident asymmetry between the damping parameter dispersion and the condition of zero-detuning prompted the development of a Hamiltonian model suitable for coexisting coherent and dissipative coupling, so far observed in photon-magnon coupling. Fitting the model to the observational data resulted in quantification of the degree of mixing of coherent and dissipative coupling.

Future directions

Specific outlooks for the experiments discussed have been already presented in the corresponding chapters. Here I would like to schematically illustrate some research directions that can be pursued with the developed instrumentation and the framework presented in this thesis.

- **Exploring non-thermally excited magnons in magnetic oxides.** In a TG setup finite-wavevector magnons could be excited exploiting the crossed-polarization configuration for the pump beams. Recalling the reservoirs model presented in the introduction, this approach would be complementary, since energy is initially injected into the spin subsystem: specific coherent flow of energy and angular momentum to the phonon bath and to other reservoirs could be traced. The systems of choice are typically complex magnetic oxides, where the phase diagram could be mapped, and possibly modified, by TG-triggered large perturbations in the magnetization.

- **Exploring quenching of ferroelectric order.** Ferroelectrics are another class of broken-symmetry phase. Here, large injection of carriers in the conduction band could lead to screening of the electric dipoles and accompanied structural modifications occurring before electron-hole recombination takes place. The timescale of such screening-driven distortions could be addressed via a TG approach.

- **Exploring the non-linear acoustic regime.** In the Impulsive Stimulated Brillouin Scattering configuration for TG (the same employed for the Ni experiment), SAWs are generated together with quasi-stationary surface ripples, which decay via incoherent thermal diffusion. Such ripple deformation assimilate the excited sample to a transient phononic crystal: at large ripple depth, modification of the spectra are expected, much in the same way as happens for real phononic crystals. Long-living acoustic waves would be observed to chirp as the quasi-stationary ripples relax. This would mark the onset of a non-linear transient state, where the properties observed via TG would be no more the equilibrium properties of the sample.

- **Exploring light-driven phase transitions.** With proper tuning of pump wavelength and properties of the TG optical grating at the sample, basically any experiment observing a light-induced phase transition could be replicated via TG. Under which conditions (in terms of TG pitch, fluence...) the locally-driven transition propagates to the whole laser footprint? What are the relevant timescale and the low-energy excitations responsible? Questions like these could be addressed, with the extension of TG spectroscopy to a photon-energy tunable source.

- **Towards extreme timescales.** The flourishing field of attosecond electronic spectroscopy could benefit from a TG approach: ultrafast (at the electron-dynamics timescale) phenomena like Optically Induced Spin TRansfer (OISTR) or light-induced electronic reactions could be tackled leveraging the space resolution of TG spectroscopy.

Appendices

Beyond uniform excitation

Here some aspects related to the relevance of spatial confinement or non-uniformity of the pump beam are reported; the focus is on single-pump experiment, with the aim at giving a further insight into the relevance of TG spectroscopy.

The maximum frequency excited by an impulsive trigger is $f_{\text{max}} \approx 1/2\tau$, where τ is the time duration of the pump pulse. This limit is set by the FT of the temporal extension of the pump Gaussian intensity, which results in a Gaussian frequency spectrum centered at zero. With the same approach, the spatial extension of the intensity sets the limit of the excited wavevector band: the more the pump is focused, the larger the wavevector bandwidth is, again accordingly to (space) FT. In this light, some relevant literature with focus on optical excitation of magnetic dynamics is briefly discussed now.

In Ref.[129], the authors employ an ultrafast NIR pump to generate a pulse of photo-excited carriers in a heterostructure composed of Fe/GaAs; the system is electrically poled, so that the photo-current flows OOP [see Fig.A.1(a)]. An Oersted field is generated IP, anti-symmetric along a diameter of the Gaussian pump footprint. The field can be written approximately as

$$B(x) \propto \frac{1}{x} \left(1 - e^{-x^2/R^2} \right) \ , \tag{A.1}$$

where $R \approx 4 \ \mu$m is the radius of the laser footprint. The leading Fourier component of $B(x)$ is at wavevector $k = 2\pi/4R$, which is thus the wavevector of the excited spin wave in the Fe overlayer.

A different approach is discussed in Ref.[220]. In antiferromagnetic DyFeO$_3$ the optical penetration depth is tuned between $\delta = 50$ nm and $\delta = 350$ nm by changing the pump photon energy: thus the pump energy is confined in a small layer of thickness approximately δ, where the spin orientation is modified by thermal effects [Fig.A.1(b)]. The exponentially-localized modulation couples to a broadband magnon wavepacket, which propagates in the OOP direction away from the surface. Upon FT of the depth profile of the deposited energy, a Lorentzian shape for the wavevector band is obtained: wavevector-selective probe allows to confirm the Lorentzian distribution in the amplitude of the modes composing the excited wavepacket.

From Ref.[221] (and Supplemental Information) another aspect can be outlined. An ultrafast pump pulse is focused to a small area (7 μm^2) on the surface of ferrimagnetic oxide Lutethium Iron Garnet [Fig.A.1(c)]. The localized impulsive trigger can couple to a broadband spectrum of magnons in wavevector domain; time-resolved magneto-optical imaging allows to acquire the amplitude of the excited modes in frequency and wavevector. In this experiment IP propagation is addressed, so the excited band is Gaussian,
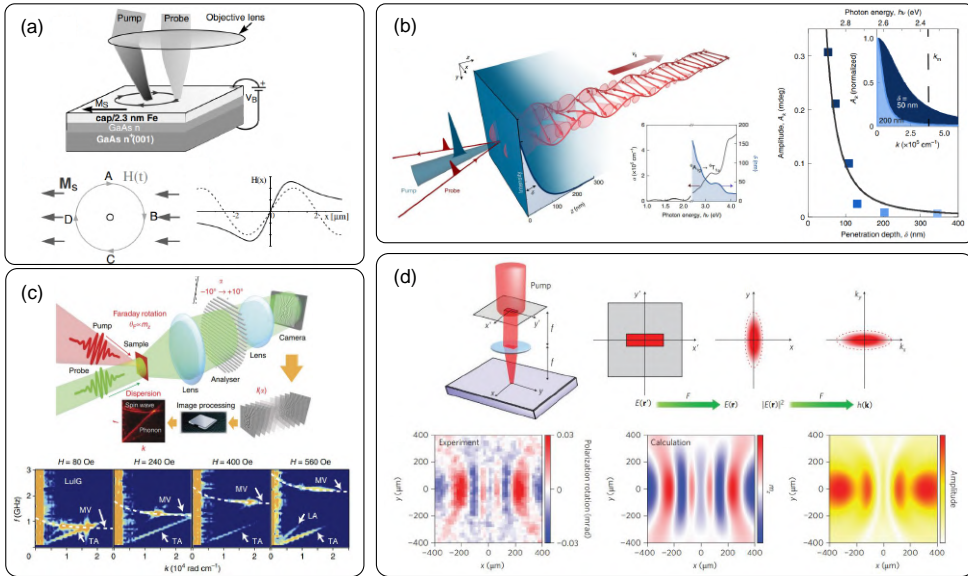
Figure A.1: Overview of some literature optical pump-probe experiments highlighting the connection of spatial localization to wavevector band of induced magnons. (a) The OOP photocurrent triggered by pump absorption generates a cylindrycally-symmetric magnetic field, whose leading spatial Fourier component is at finite wavevector. Adapted from [129]. (b) Deposition of pump energy beneath the sample surface is limited within a thickness given approximately by the optical penetration depth δ: a magnon wavepacket propagating into the bulk is triggered, whose wavevector spectrum is the Lorentzian FT of the exponential energy confinement. Adapted from [220]. (c) A tightly focused pump excites broadband (in frequency and wavevector) magnon modes, which are observed via magneto-optical imaging. The intensity of the modes depends not only on the impulsive excitation, but also on the magnetic susceptibility. Adapted from [221]. (d) Spatial shaping of the pump footprint results in selective directionality in the excited modes. Adapted from [222].

centered at zero wavevector. Despite this, the amplitude of the excited modes does not decay monotonously for increasing wavevector (*i.e.* it is not proportional to the Gaussian pulse bandwidth), rather it is enhanced for specific modes depending on external parameters like the angle of an external magnetic field **H**, or its strength, and on time delay. This is understood on the basis of the magnetostatic susceptibility $\chi_{ij}^{(m)}$, given that $M_i(\mathbf{k}, \omega) = \chi_{ij}^m(\mathbf{k}, \omega) \tilde{H}_j(\mathbf{k}, \omega)$, where the magnetization **M** and the other quantities are reported in reciprocal space for spatial and temporal frequency. Beyond technicalities, the point is that the amplitude of a magnon mode identified by ω and **k** is proportional to the susceptibility at the addressed frequency and wavevector. This is the reason why not all the modes compatible with the temporal and spatial FT of the pump are excited.

With on-purpose engineering of the pump spatial profile, the directionality of finite-wavevector modes can be selected, as discussed in Ref.[222]. In this experiment, circularly-polarized photons excite via Inverse Faraday Effect the magnetization precession in the magnetic oxide $Gd_{1.3}Yb_{0.6}BiFe_5O_{12}$: the effective impulsive magnetic field $h(\mathbf{r}, t) = h(\mathbf{r})\delta(t - t_0)$ has the same spatial FT of the pulse intensity and can couple to a proportionally broadband wavepacket of spin waves. Given a Gaussian spatial profile of the footprint, possibly with different semiaxes length a and b along the x and y directions, the spatial FT of the impulsive field is

$$h(\mathbf{k}) = h_0 e^{-\left(\frac{k_x^2 a^2}{2} + \frac{k_y^2 b^2}{2}\right)} \ , \quad h_0 = \int d\mathbf{r}\, h(\mathbf{r}) \ . \tag{A.2}$$

At loose focusing, the observed dynamics closely compares to uniform ferrimagnetic resonance data; at tight focusing, however, different frequencies and linewidths are observed, a result interpreted in terms of excitation of finite-wavevector magnons. Moreover, with spatial shaping of the pump the directionality of the magnons can be selected. For example, for an elliptical footprint with $a < b$, the effective field FT (Eq.A.2) exhibits larger bandwidth along k_x and consequently smaller-wavelength magnons are excited in the x direction; following the Huygens principle, also the propagation direction of the excited waves is predominantly along x. Other works where the discussed concepts are employed can be found in literature [198, 223].

This brief literature overview allows to draw three conclusions as rule-of-thumb guidelines: (i) for impulsive excitation as a first approximation the wavevector band is proportional to the spatial FT of the pump footprint, while the frequency band is proportional to the temporal FT of the time profile of the pulse; (ii) Fourier engineering of the spatio-temporal localization of the pump accordingly selects the excited modes; (iii) the material-dependent susceptibility accounts for further modulation in the amplitude of the excited modes; also, specific anisotropies in the sample play a role determining the final spectrum (see Ref.[224] for a very clear - theoretical - example). Finally, of course the amplitude of the *observed* modes depends on the detection efficiency, namely on the probe process.

Détour: Analogy to musical instruments

It is common experience that two different musical instruments playing the same note are distinguishable, even to the untrained hear: in the musician jargon, the two sounds (or the two instruments) are said to have different *timber*. Physically, the two sounds share the same fundamental frequency (what gives the *pitch* of the note), while they differ in the spectrum of higher harmonics: it is the different relative amplitude of these
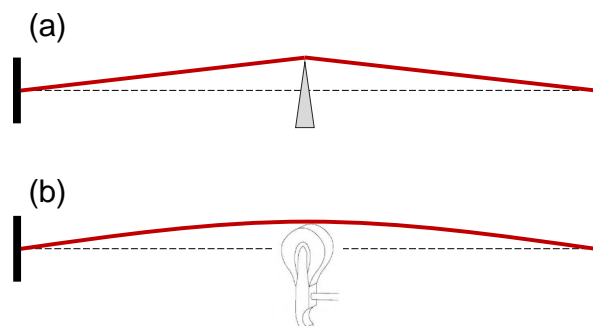
Figure A.2: (a) Sketch of the initial deformation in a harpsichord string, where a sharp plectrum deformates the string in a triangle-like shape. (b) In a piano, a rounded hammer strikes the string, giving a less sharp deformation. The difference in the excitation tool determines the different timber of the two instruments. The sketches are obviously not to scale.

higher harmonics what is perceived by our brain as a different timber. A primary role in determining the amplitude of the harmonics generated by the vibrating body is played by the excitation mechanism, in close analogy to what has been discussed above.

For simplicity, let us consider two instruments based on vibrating strings, namely harpsichord and piano. For a vibrating string with fixed ends, the fundamental frequency is $f_0 = (1/2L)\sqrt{T/\mu}$ (where L, T and μ are the string length, tension and linear mass respectively) and the wavelength is $\lambda_0 = 2L$; for higher harmonics the frequency is $f_n = nf_0$ and the wavelength $\lambda_n = 2L/n$, for n integer. In a harpsichord the excitation mechanism involves a sharp plectrum plucking the string [Fig.A.2(a)]. Right before the plectrum is released, the string is deformed in a triangular shape: as for the Fourier theorem, the spatial waveform of the string can be analysed as being composed of many higher harmonics with sizeable amplitude. Thus, when the string is left to vibrate, all these harmonics will radiate acoustic energy, synthesising a sound with rich spectrum: the timber of harpsichord is rather brilliant and sharp. In a piano the string is set into vibration by the strike of a hammer [Fig.A.2(b)]. The strike is impulsive in the sense discussed above: physical contact between the hammer and the string lasts typically about $\tau = 500$ μs, meaning that only frequencies $f < 1/2\tau = 1$ kHz can be excited. Moreover, the hammer has a radius of curvature of about 1 cm: thus the spatial deformation induced by the strike is quite rounded and fewer harmonics are required to synthesise the waveform. After the strike, less harmonics are involved in acoustic radiation, resulting in a soft and pure timber. In the spirit of the above discussion, the bandwidth of the spatial FT is smaller for the piano hammer than for the harpsichord plectrum: this results in different accessible wavevectors for the excited modes. This discussion only considered the role of the excitation tool. Specific transfer functions to the bridge, to the sounding board, to air and finally to ear can determine further modification of the harmonics amplitude: all these aspects also contribute to the perceived timber.

Nonlinear optics approach to TG

The transient grating formation and detection discussed in Ch.2 involves four light waves which do not linearly superimpose, but rather they influence each other: thus the process can be described with the tools of nonlinear optics. The following discussion only aims at presenting a useful conceptualization: the interested reader can refer to Ref.[51, 54].

In nonlinear optics the quantity of interest is the time-dependent dielectric polarization $\mathbf{P}(\mathbf{r},t)$ responsible for radiating the signal beam; in general, it is a functional of the local and time-dependent electric field $\mathbf{E}(\mathbf{r},t)$. At low field, the linear relation $P_i(\mathbf{r},t) = \varepsilon_0 \chi_{ij} A_j(\mathbf{r},t)$ is sufficient, where A_j is the j component of the electric field amplitude; at high field, expansion of the dielectric polarization into a power series in A_j is required. Moreover, since the higher-order contributions are usually small, the involved beams can be considered separately. Thus, instead of a complicated functional of the local (in time and space) field $\mathbf{E}(\mathbf{r},t)$, the polarization can be written as a power series of the amplitude of the different beams. Finally, the nonlinear-optics recipe requires that to describe a certain source term (*i.e.* the polarization at the specific frequency and wavevector of the signal), only those combinations of amplitudes are allowed for which the frequencies and wavevectors add up to the desired values.

To apply this approach to TG spectroscopy, the shorthand $\mathbf{A}(\omega_A, \mathbf{k}_A) \equiv \mathbf{A}_A$ (and similar for the other three beams: as in Ch.2 the input beams are indicated with A, B and C) is introduced for brevity; note that space and time FT has been performed. Then a power expansion in the amplitudes is written, where the resulting polarization is a function of linear combinations of the input frequencies and wavevectors:

$$P_i(\pm\omega_1 \pm \omega_2 \pm \omega_3; \pm k_1 \pm k_2 \pm k_3) = \varepsilon_0 \left[\chi_{ij}^{(1)} A_j + \chi_{ijk}^{(2)} A_j A_k + \chi_{ijkl}^{(3)} A_j A_k A_l \right] \; ; \quad \text{(B.1)}$$

here the coefficients $\chi^{(m)}$ are the higher order susceptibilities, which in general depend on the frequencies and wavevectors; negative frequencies in the combination $\pm\omega_1 \pm \omega_2 \pm \omega_3$ acquire meaning considering $A_i(-\omega_1, -\mathbf{k}_1) = A_i^*(\omega_1, \mathbf{k}_1)$ and similar. To describe TG spectroscopy, the polarization must have non-zero amplitude at the frequency and wavevector of the signal beam, *i.e.* $\mathbf{P}(\omega_D, \mathbf{k}_D) \neq 0$. For this reason, the first order term in Eq.B.1 must be driven by $\mathbf{A}_D$. The second order term involves the combination of two amplitudes: all the possibilities are $2\omega_A$, $\omega_A \pm \omega_C$, $2\omega_C$, 0 (recalling that $\omega_A = \omega_B$). Thus, this term cannot contribute at the frequency $\omega_D = \omega_C$. The third-order term provides the required combination since $\omega_D = \omega_A - \omega_B + \omega_C = \omega_C$. Higher-orders are usually unimportant as their contribution is increasingly small. Removing useless terms, Eq.B.1 becomes

$$P_i(\omega_D, \mathbf{k}_D) = \varepsilon_0 \left[\chi_{ij}^{(1)} A_{D,j} + \chi_{ijkl}^{(3)} A_{C,j} A_{A,k} A_{B,l} \right] \; . \quad \text{(B.2)}$$

All the nonlinear interactions of the grating generation and detection process are now expressed in one single quantity, the third-order susceptibility $\chi_{ijkl}^{(3)}$.

Two aspects are relevant from this approach. First, the polarization $\mathbf{P}(\omega_D, \mathbf{k}_D)$ radiates a signal wave with sizeable amplitude only if the wavevectors satisfy the same linear combination of the frequencies, namely $\mathbf{k}_D = \mathbf{k}_A - \mathbf{k}_B + \mathbf{k}_C$: this is the so-called *phase matching* condition. Note that it corresponds to the Bragg condition discussed in Ch.2, with the grating wavevector $\mathbf{q} = \mathbf{k}_A - \mathbf{k}_B$. If the phase matching condition is not met, a scattered wave can still be observed, with reduced amplitude, if the sample is sufficiently thin: this situation corresponds to diffraction at a thin grating. Second, Eq.B.2 can be rewritten as

$$P_i(\omega_D, \mathbf{k}_D) = \varepsilon_0 \left[\chi_{ij}^{(1)} A_{D,j} + \Delta\chi_{ij} A_{C,j} \right] \,, \tag{B.3}$$

with

$$\Delta\chi_{ij} = \chi_{ijkl}^{(3)} A_{A,k} A_{B,l} \,. \tag{B.4}$$

Comparison to Eqs.2.10 and 2.11 shows that the pump-induced modification of the optical susceptibility is proportional to the third-order susceptibility: quantitative TG experiments varying the polarization of the pump beams can lead to quantification of the 81 (!) entries of this tensor. Note, however, that if the separation of pump and probe is legitimate the probe *does not know* what is the origin of the modulation of the dielectric environment of the sample. For example, via TG it is possible to trigger standing acoustic waves that diffract the probe; similarly in acousto-optic modulators a rf acoustic wave is pumped in an optical crystal via piezo-electric transducers, and results in a standing acoustic wave which again diffracts a laser beam.

Characterization of Ni films

Details on sample growth

Films and capping layers for samples A, B and C discussed in chapter 3 were deposited by e-beam evaporation at the CNR-IOM FNF clean room facility in Trieste, Italy. After acetone and ethanol cleaning, the substrates were inserted into the deposition chamber, where a base pressure of 10^{-6} mbar was maintained. Thin film and capping were deposited using a Ni rod (99.995%, Alfa Aesar) and fused silica powder (99.995%, Alfa Aesar), respectively. The material targets were positioned inside a Tungsten crucible and heated up by a 10 keV electron beam. The evaporation rates r for Ni and SiO_2 were checked prior to deposition using a calibrated quartz microbalance, obtaining $r_{Ni} = 0.1$ Å/s and $r_{SiO_2} = 0.3$ Å/s, respectively; the uncertainty in the deposited thickness takes into account the uncertainty in the calibration.

Structural and morphological characterization

The samples were characterized in their structure and morphology via GIXRD and XRR in collaboration with CNR-IMM and Università degli Studi di Milano-Bicocca. A prior knowledge of the structural quality of the samples is important, as the magnetostatic properties of the Ni films are strongly influenced thereby. The reduced in-depth penetration of X-rays at grazing incidence results in enhanced surface sensitivity, relevant for investigation of thin films.

GIXRD patterns are acquired using a Cu K_α X-ray source and a position sensitive gas detector. In all the measurements, the take-off angle between the X-ray beam and the sample is fixed at $\omega = 0.5°$. In Fig.C.1(a) the GIXRD patterns for sample A (black solid line) and sample B (red solid line) are reported, for 2θ in the range $90° - 110°$. By comparing the raw data with the tabulated diffraction pattern for the Ni powder, the peaks around $93°$ and $103°$ were assigned to the (311) and (222) reflections, respectively. In powder diffraction analysis, it is customary to calculate the size D of the crystallites by using the Scherrer formula [225]:

$$D = \frac{K\lambda}{\beta \cos\theta} \, , \tag{C.1}$$

where K is the Scherrer constant fixed at 0.94 for spherical crystallites with cubic symmetry, $\lambda = 1.542$ Å is the X-ray wavelength, β the peak FWHM expressed in radians and θ the position of the peak. For polycrystalline sample the same procedure can be applied, resulting in $D = (4.4 \pm 0.5)$ nm for both samples. Note that, since the scattering plane in GIXRD geometry is basically horizontal, D mostly refers to the in-plane crystallite size;
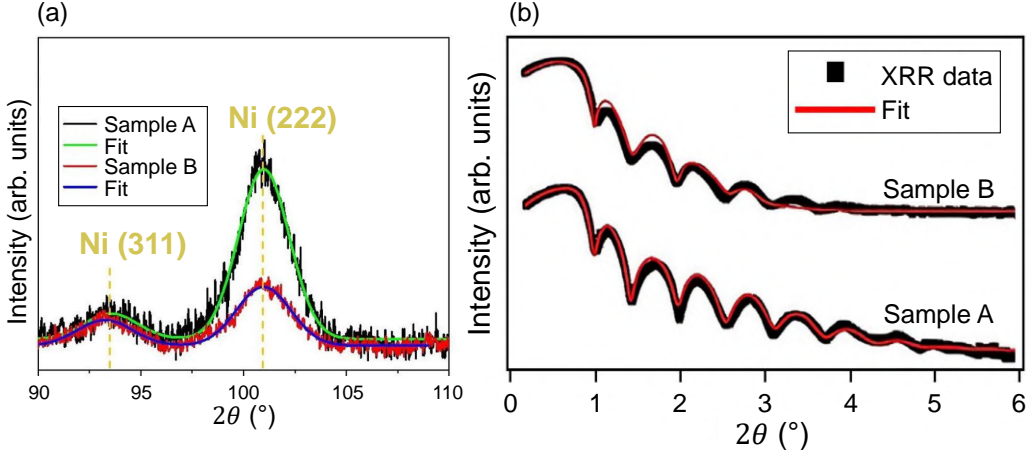
Figure C.1: (a) GIXRD patterns acquired for sample A (black solid line) and for sample B (red solid line), together with cumulative Gaussian fits (green and blue solid lines, respectively) of the two observed diffraction peaks. Based on powder diffraction database, the observed peaks are attributed to Ni (311) and Ni (222) reflections. (b) XRR data for sample A and sample B are reported as black squares. The fit to each curve is reported as red solid line.

Table C.1: Best-fit parameters to the XRR data for sample A and sample B.

	Sample A				**Sample B**		
Layer	t (nm)	r (nm)	ρ_e ($e^-/\text{Å}^3$)	Layer	t (nm)	r (nm)	ρ_e ($e^-/\text{Å}^3$)
SiO_2	8.5	1.2	0.67	SiO_2	9.6	1.3	0.67
Ni	14.4	0.4	2.30	Ni	14.4	1.3	2.38
CaF_2	Inf.	0.7	0.95 (fixed)	SiO_2	Inf.	0.9	0.67 (fixed)

nevertheless, there is no reason to suspect highly asymmetric grains, for example with columnar shape elongated along the OOP axis, especially for cubic crystals like Ni. The higher intensity of the Ni (222) diffraction peak for sample A is attributed to a different structural configuration of the ferromagnetic film, with more pronounced texturization of the crystalline grains with respect to sample B. This finding is consistent with sample A being grown on an ordered crystal, and sample B on an amorphous substrate. No GIXRD data were acquired from sample C, since the reduced Ni thickness resulted in no diffraction peaks observed; however, it is likely that also sample C hosts grains with the same size, also given that its thickness is larger than D.

From XRR measurements the thickness t, roughness r, and electronic density ρ_e for each layer composing the stack can be extracted. To this purpose, the data were simulated according to the Parrat formula [226] corrected by a Croce-Névot factor [227]; in the model, the substrate was assumed with infinite thickness, and its electron density was fixed to the nominal values. In Fig.C.1(b) the XRR collected spectra for sample A and B are reported as black squares; the red solid lines indicate the model fit to the experimental data. The best-fit parameters are summarized in Tab.C.1. The thickness of each layer is compatible with the nominal value. The same holds for ρ_e, as the expected values are 0.67, 2.29 and 0.95 $e^-/\text{Å}^3$ for SiO_2, Ni and CaF_2, respectively: this demon-

strates the reliability of the investigated systems from the chemical point of view, as severe Ni oxidation would result in altered electron density. The roughness of the Ni film is strongly influenced by the adopted substrate: for sample B (amorphous SiO_2 substrate), the roughness is more than three times larger than for sample A (crystalline CaF_2 substrate). This suggests that the Ni layer is morphologically more ordered on the latter substrate, also consistently with the results of GIXRD.

As a last step for the morphological characterization, AFM maps were acquired at CNR-IOM in Trieste: they are reported in Fig.C.2(a-c) for the three samples. The scans were obtained in standard air conditions with a Solver Pro (NT-MDT) instrument, in semi-contact mode using commercial cantilevers (NT-MDT, NSG30, nominal spring constant $k = 40$ N/m, nominal radius of curvature 10 nm). To each map, a second-order polynomial background was subtracted, and the zero-height level was set to the average plane of each map. The first observation from the color-coded height is that sample A presents a better uniformity in the surface topography; on the other hand, samples B and C display severe indented scratches, most probably due to sample wear, and structures which can be attributed to deposited dust grains. To get quantitative insight, the free software Gwyddion was employed. The structures and the scratches were masked on a height-based criterion, and displayed with blue color in the maps; this procedure ensures that only the as-deposited portions of sample surface are considered for the roughness quantitative analysis. For the selected regions highlighted in yellow boxes, the horizontal cumulative height profiles were calculated and are displayed in panels (d-f) as black solid lines. The profile waviness and roughness, computed with a built-in algorithm, are also reported, as red and green solid lines respectively. The handy meaning of waviness is that it is a low-frequency spatial filter of the profile, that reproduces the gross structures mainly due to scratches, dust and non-flatness of the substrate. For each profile the root mean square (rms) waviness W_q and roughness R_q are reported in Tab.C.2, together with the two-dimensional rms roughness S_q. For information about the standards for calculation of roughness and waviness, the interested reader is redirected to Ref.[228]. The residual roughness R_q is smaller than 1 nm, a hint that the deposition process proceeded smoothly. The cumulative roughness, taking into account both roughness and waviness, is in line within a factor two with the values obtained with XRR for the topmost layer. The last column in Tab.C.2 reports the average wavelength λ_a in the profiles. The relevance of this parameter is its correlation to enhancement of scattering between magnon states at different wavevector, with $\Delta q = 2\pi/\lambda_a$; moreover, if comparable to the TG pitch Λ it could reduce the generation efficiency of the acoustic and magnetic transients. Given the reduced concavity of the SW bands (see Sect.3.4 below) and that $\lambda_a < \Lambda$, these issues can be neglected. Note that the full image size is 30×30 μm^2, which is approximately the size of the laser spot employed in the experiment: for this reason, it is informative of the quality of the average portion of sample surface investigated during the experiment.

Magnetostatic characterization

The magnetostatic properties were investigated via static longitudinal MOKE at the NFFA facility (MBE-Cluster) in Trieste, Italy [229]. In Fig.C.3 MOKE hysteresis loops of the three samples are reported [panels (a) to (c) refer to sample A to C]. To check the expected IP magnetic isotropy of the samples, two hysteresis loops were acquired, namely at $\varphi = 0°$ and $\varphi = 90°$, where φ is the azimuthal rotation angle around the sample normal axis; for sample A $\varphi = 0°$ corresponds to having the external magnetic
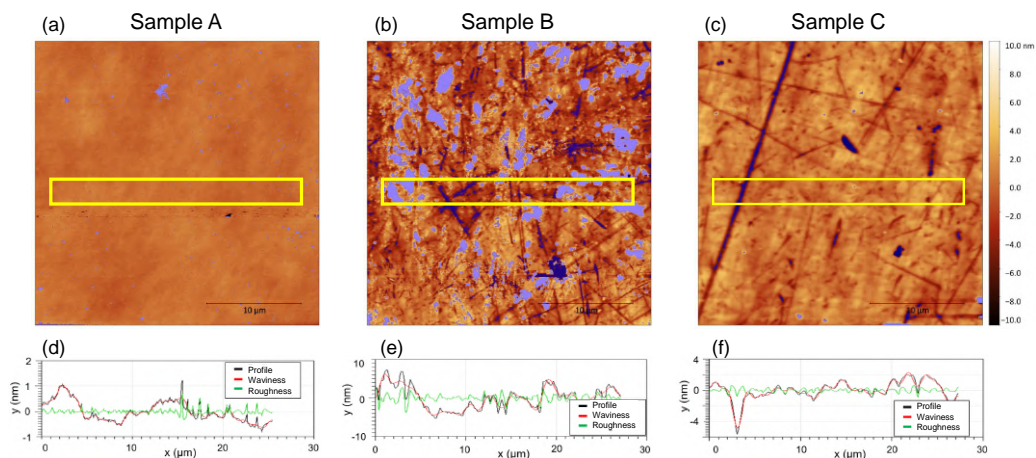
Figure C.2: (a-c) AFM maps for the three investigated samples. The masked regions are reported in blue. (d-f) Horizontal cumulative profiles (black) calculated from the regions highlighted with yellow boxes in panels (a-c); the profile waviness (red) and roughness (green) are also shown.

Table C.2: Quantitative results for roughness, waviness, and average profile wavelength for the AFM maps and profiles reported in Fig.C.2.

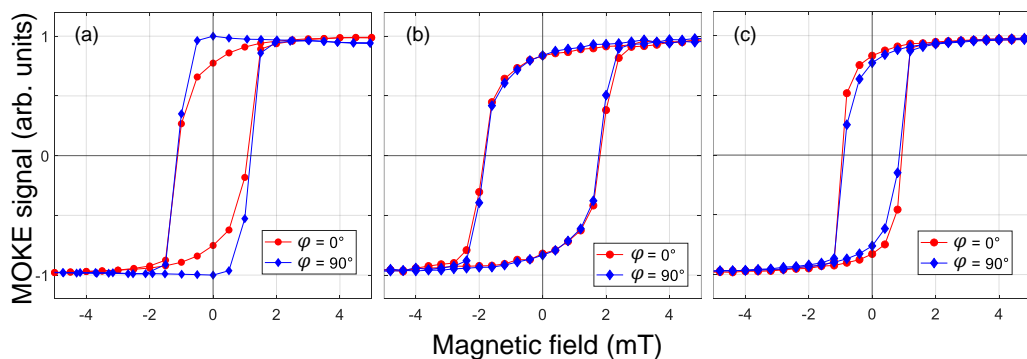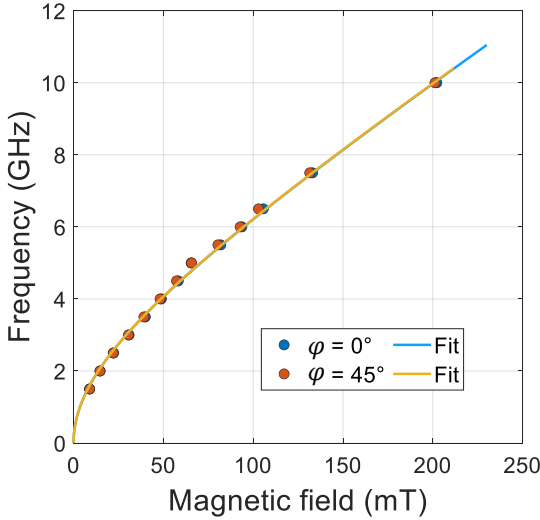|	S_q (nm)	R_q (nm)	W_q (nm)	λ_a (μm)
Sample A	0.5	0.1	0.4	0.7
Sample B	2.0	1.0	2.5	1.1
Sample C	1.5	0.3	1.1	1.4

Figure C.3: Magnetic hysteresis loops acquired via longitudinal MOKE. Panel (a-c) refer to sample A, B, and C, respectively. For each sample two loops were acquired, with $90°$ difference in the azimuth angle. Adapted from Ref.[99].

Figure C.4: B-FMR measurements for sample A at two different azimuth angles: $\varphi = 0°$ (blue circles) and $\varphi = 45°$ (orange circles), corresponding to $B_{ext} \parallel [100]$ and $B_{ext} \parallel [110]$, respectively. The best fits of the Kittel curve are reported (light blue and yellow solid lines, respectively). The table reports the best-fit values of M_{eff} and γ. Adapted from Ref.[99].

field B_{ext} parallel to the [100] axis of the substrate, while for samples B and C it corresponds to an arbitrary substrate edge since no crystallographic directions are given. All the samples show small coercivity ($B_c \leq 2$ mT) as expected for a polycrystalline Ni thin film. Samples B and C show good IP isotropy, both in the coercivity and in the remanence. On the other hand, a small uniaxial anisotropy in the remanence is observed for sample A. This could be surprising since the substrate has cubic symmetry: thus, if any anisotropy is to be observed, it should have fourfold symmetry. Nevertheless, a weak uniaxial anisotropy in ferromagnetic thin films grown via sputtering or evaporation is reported in literature [230]: what breaks the four-fold symmetry of the substrate is the off-normal axis of the effusion cone. Another source of symmetry breaking could be the magnetic field employed in e-beam evaporation. Interestingly, whatever the reason is for the anisotropy, it is not observed in the films grown on SiO_2, a hint that the crystallinity of the substrate has to be playing a role.

Since the FMR measurements reported in chapter 3 are performed at field strength much larger than 2 mT, the samples are always in magnetic saturation, and the weak magnetic anisotropy is expected not to be relevant: basically, the Zeeman energy is always much stronger than the anisotropy energy, which thus does not play a relevant role in the resonance mechanism. As a sanity check, B-FMR measurements were performed at two inequivalent azimuthal angles, namely $\varphi = 0°$ and $\varphi = 45°$, which correspond to $B_{ext} \parallel [100]$ or $B_{ext} \parallel [110]$, respectively. The FMR frequency as a function of B_{ext} is reported in Fig.C.4 for the two azimuth configurations. The data do not show any sizeable anisotropy. As will be described below in this chapter, fitting the Kittel model (Eq.3.9) to FMR data allows to calculate the effective magnetization M_{eff} and the magnetomechanical ratio γ. The best-fit results are reported in Fig.C.4 and are in complete agreement, legitimating analysis of B-FMR and SAW-FMR data on the basis of an isotropic Kittel model.

Literature overview on NW samples

Here below some literature results are reported, relevant for understanding the experimental observations reported in chapter 4 and 5. In particular, the addressed questions are: (i) what are the acoustic and magnonic modes that can be observed in our sample? and (ii) what do we know from literature about this system, in terms of magnetic anisotropy, switching process and magnetic coupling at the Fe/Py interface?

A magnonic-phononic crystal

The real-space periodicity given by magnetic NWs on a semi-infinite substrate determines the emergence of phononic and magnonic collective dynamics typical of artificial crystals. Here a quick overview of this aspect for one-dimensional magnonic-phononic crystals is reported; the modes actually observed in our experiment are highlighted.

   A phononic crystal. From the acoustic point of view, the presence of shallow (some tens of nanometers) structures loading the substrate and periodically alternating with air gaps gives rise to properties typical of a SPnC: in particular reciprocal-space periodicity in the SAW dispersion arises, together with mode hybridization and gap opening [231]. TG spectroscopy has been proved well suited for mapping the two-dimensional surface phononic band structure of SPnCs [92]: phononic hybridization at the edge and at the center[1] of pBZ is reported, as well as phononic forbidden bands [see Fig.D.1(a-b)]. Also acoustic BLS is a suitable technique to measure the phononic band structure [157]: as reported in Fig.D.1(c) quasi-flat phononic bands at the edge of pBZ with forbidden bands several gigahertz wide are observed, as due to hybridization of surface and bulk acoustic waves. With the aid of finite-elements simulations the spatial localization of the SAWs can be visualized, as reported in Fig.D.1(d) for the three bands observed via BLS. Similarly to what happens for electronic bands in solids, hybridization of modes takes place also at the center of pBZ: in a one-dimensional SPnC the first acoustic mode for zero wavevector (besides the quasi-static mode at zero frequency) is given by hybridization of RSAW with its zone-folded replicas, as highlighted by a red arrow in Fig.D.1(c).

   Each artificial atom composing the SPnC also hosts localized acoustic modes: breathing modes along the directions of strong confinement, bending and shear modes for structures with high aspect ratio cross sections, twist modes for nanopillars, are only examples of a rich phenomenology. These modes can of course be excited in their higher orders, with increasing number of nodes in the strain field in analogy to standing acoustic waves on a constrained string. For both the localized and the collective phononic

---

[1]Interestingly, it is reported that the hybridization of Rayleigh and Sezawa modes in a SPnC allows also gap opening in other position of pBZ, enabling unusual acoustic waves with zero group velocity for propagation direction oblique to the periodicity direction [92].
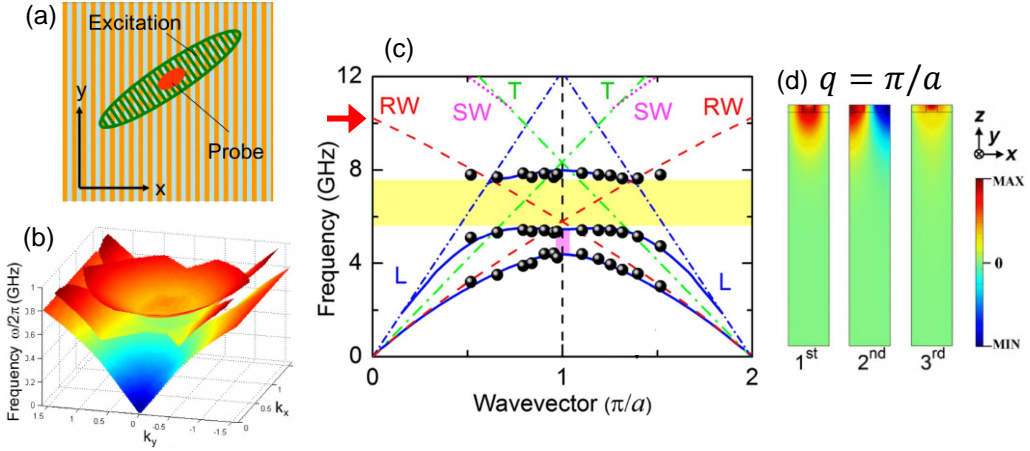
Figure D.1: (a-b) TG measurement of the surface phononic band structure in a one-dimensional NW array. The TG wavevector is varied both in magnitude and direction with respect to the NW axis [panel (a)] in order to excite SAWs from the whole first pBZ; three dispersion surfaces are observed, as a function of the two-dimensional IP wavevector [panel (b)]. Adapted from [92]. (c-d) BLS measurement of the dispersion of SAWs for wavevector along the array periodicity direction. Three small-bandwidth bands are observed [panel (c)]; the red arrow on the left highlights that the lowest-frequency mode at the center of pBZ results from hybridization of RSAW with its zone-folded replicas. Finite-elements calculations show the symmetry and thickness localization of the three observed acoustic modes at the edge of pBZ [panel (d)]. Adapted from [157].

modes, the experimental constraints and symmetries usually allow only a certain set of modes to be excited and/or probed: this is a consequence of the anisotropy both of each artificial atom and of the artificial crystal as a whole. For the experiment discussed in chapter 4 and 5, the excited modes are (i) a standing SAW with zero wavevector resulting from hybridization of RSAW with its zone-folded replicas, and (ii) the lowest-order localized breathing mode along the width of each NW.

A magnonic crystal. In close analogy to the phononic counterpart, fabrication of magnetic NWs alternating to air gaps allows formation of magnonic bands. Also for MCs mode hybridization takes place, generating flat bands and opening gaps in the band structure. One-dimensional MCs composed of NWs are relevant because of the absence of the demagnetizing field in the longitudinal configuration, owing to the strong shape anisotropy: this allows simple models to be developed for the understanding of their magnetostatics. The research in this field moved from single-layer NWs with rectangular cross-section [219, 232], to bi- [233] and trilayered [234, 235] (with a non-magnetic spacer) NWs, possibly also with asymmetric L-shaped cross-section in order to explore band-engineering and magnon localization [236]. In each of these configurations, specific modes are observed; nonetheless, a general categorization can be made for NWs whose thickness t is much smaller than the width w:

- for $t < 40$ nm the magnon amplitude is uniform along the thickness, since higher-order magnonic modes require large energy to overcome the exchange interaction with such reduced space modulation [237]. For a rule-of-thumb calculation, the difference in energy between two consecutive standing magnon modes in a film of thickness t is $\Delta E = D_{sw}(\pi/t)^2$, where D_{sw} is the spin-wave stiffness; for example
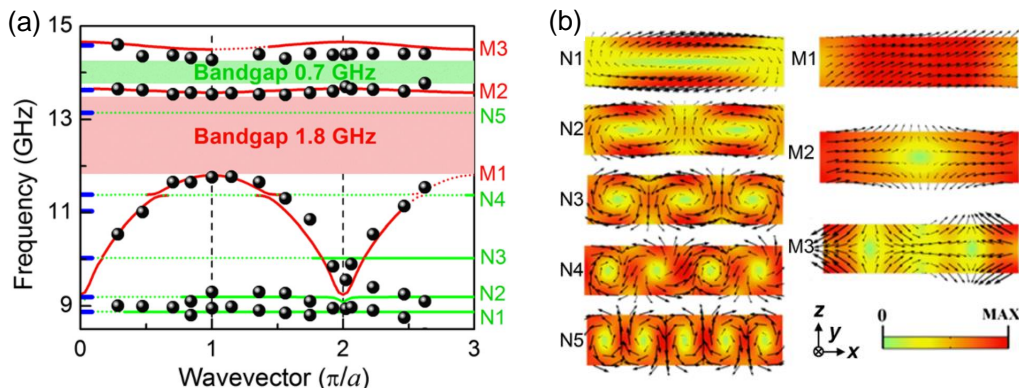
Figure D.2: (a) BLS measurements of the magnonic band structure of a Py NW array (black dots) and calculated bands (lines). (b) Localization of the dynamical magnetization along a NW cross section, as obtained from finite-elements calculations. M modes are uniform along the NW thickness, while N modes display a single node (they are first-order PSSWs). Magnetization direction is indicated by the arrows, its intensity by the color code. Adapted from [157].

this expression gives frequency separation $\Delta f = 680$ MHz or $\Delta f = 68$ GHz for $t = 100$ nm or $t = 10$ nm, respectively (I considered the case of pure Fe, for which $D_{sw} = 281$ meV Å^2 [14]; the constant varies within a factor two for Ni and Py [238]);

- along the NW width, on the other hand, higher-order quantized magnons are observed [232], in line with the argument of previous point given a width of few hundreds of nanometers;

- for bi- and trilayered NWs, both in-phase and out-of-phase precession of the magnetization in the two magnetic layers are possible, leading to acoustic and optical magnon bands. The thickness of the non-magnetic layer modulates the intra-NW coupling between the magnetic layers, allowing engineering of the frequency of the optical modes;

- for these multilayered NWs, there is the possibility to stabilize both parallel and anti-parallel magnetization in the two layers, with specific magnon bands;

- *L*-shaped cross section strengthens high-order magnonic modes mostly localized in the wide base [239].

In all of these cases, in order to have hybridization of magnonic modes and gap opening, it is required to have a sizeable inter-NW interaction, typically of dipolar origin: this is enhanced by NW spacing small as compared to the width [240], and it is always weaker for anti-parallel aligned multilayers owing to the smaller stray dipolar field.

Typically the measurement of magnonic bands in MCs is performed via magnetic BLS. In Ref.[157], the same one-dimensional magnonic-phononic crystal discussed in reference to Fig.D.1(c-d) was investigated specifically as a MC. In Fig.D.2 some results that are of interest in the context of the current experiment are reported. BLS measurements of the magnonic bands are reported, for wavevector spanning one and a half pBZ [panel (a)]. Calculated bands are drawn as solid and dashed lines, and the magnonic bandgaps
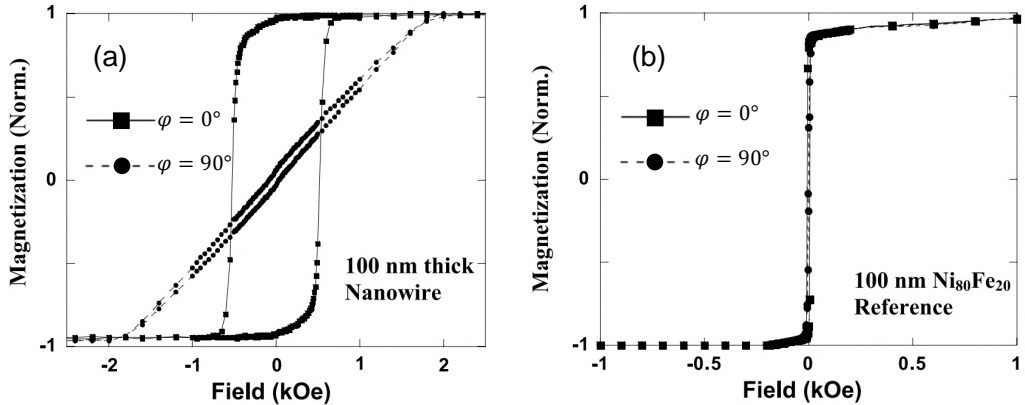
Figure D.3: VSM hysteresis loops for (a) a one-dimensional array of Py NWs ($t = 100$ nm, $w = 185$ nm, $d = 35$ nm), and for (b) an unpatterned reference film with same thickness t. The external magnetic field is applied either along the NW length ($\varphi = 0°$, squares) or orthogonal ($\varphi = 90°$, circles). Adapted from [241].

are highlighted as coloured stripes. Apart for the fundamental magnonic mode (labelled M1) which shows a prominent dispersion, the other modes are rather flat. This is understood on the basis of the finite-elements calculations [panel (b)]. The direction of the dynamical component of magnetization is indicated by the arrows, while its amplitude is indicated by the color code. The calculations refer to the modes at the edge of pBZ. Two categories of magnons are observed: those labelled as M are uniform along the NW thickness, those labelled as N display a magnetization node at the center of the thickness, *i.e.* are first-order PSSWs. Note that in this experiment the NWs are 63-nm thick: the appearance of low-frequency higher-order magnons is consistent with the above discussion on SW stiffness. As stated above, the wavevector dispersion is driven by dipolar inter-NW coupling. This is enhanced for the quasi-uniform M1 mode, while the other modes show reduced stray fields as due to the higher spatial modulation: this explains the reduced bandwidth in their dispersion. Similarly to what discussed for the phononic modes, the number and nature of the magnons excited and observed with a specific experimental protocol depend strongly on the symmetry of the experimental setup. In the experiment discussed in chapter 4, the homogeneous excitation of the magnetic subsystem only couples to a magnon of same symmetry, like the one indicated as M1 in Fig.D.2.

Anisotropy, switching process, interface coupling

In a series of publications starting from the late '90s, NW arrays fabricated with the same recipe have been investigated. For what concerns the experiment presented in chapter 4 and 5, the relevant aspects found are (i) the nature of the magnetic anisotropy, (ii) the coercivity and switching process, and (iii) the magnetic coupling at the Fe/Py interface. As will result from the following discussion (i) the sample is dominated by shape anisotropy, (ii) a competition of coherent rotation and magnetization curling is at play as for the switching process, and (iii) no specific role is played by the bilayer, *i.e.* the system behaves as a single effective magnetic materials with inter-layer ferromagnetically coupled dynamical modes.

Magnetic anisotropy. In Ref.[241] the effects of magnetic anisotropy are investigated
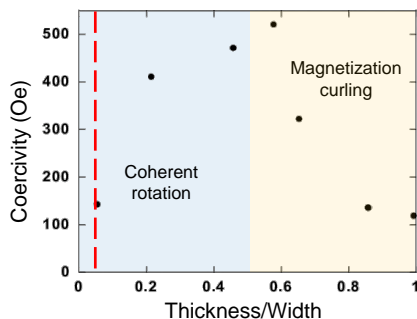
Figure D.4: Room-temperature coercivity for external magnetic field parallel to EA for different thickness-to-width ratio of the NWs. The cross-over from coherent rotation and magnetization curling is highlighted by the shaded background. The dashed red line highlights the approximate region for the sample investigated in this chapter. Adapted from [241].

measuring hysteresis loops in a one-dimensional array of Py NWs with $t = 100$ nm, $w = 185$ nm and $d = 35$ nm; comparison to an unpatterned film of the same thickness is also reported. The resulting hysteresis loops from room-temperature VSM are reported here as Fig.D.3, for the NW array [panel (a)] and for the unpatterned film [panel (b)]. The hysteresis loops for the NW array are strongly anisotropic, with clear definition of magnetic EA and HA, parallel or perpendicular, respectively, to the NW long geometrical axis: in the figure they are indicated as the angle $\varphi = 0°$ or $90°$, respectively. In the unpatterned film, the magnetization switching takes place rather abruptly, with negligible coercive field ($B_c < 5$ mT); note moreover that the hysteresis loops are identical for the two orientations of the external magnetic field, demonstrating negligible MCA. The deposited ferromagnetic layer is polycrystalline, with negligible long-range crystalline order or growth-induced texture: this is probably due to the 60-nm thick polymeric Bottom Anti Reflection Coating (BARC) employed to improve nanostructure definition in DUV-based lithography [144]. The residual magnetic anisotropy observed in the NW array can be entirely ascribed to shape anisotropy. This also allows to obtain simple approximate expression for the demagnetizing factors of the NWs (see Appendix E). This shows that the magnetic anisotropy in such systems entirely originates from shape anisotropy.

Switching process. VSM-based investigation of the coercive field for one-dimensional Py NW arrays is reported in Ref.[241, 242]. Systematic variation of NW thickness, width and spacing unveils the details of the magnetization switching process and the role of dipolar inter-NW coupling in the determination of magnetostatic properties. As shown in Fig.D.4, the coercivity as a function of the thickness-to-width (t/w) ratio displays a non monotonous trend, suggesting the presence of a cross-over in the magnetization switching mode. This is confirmed by the azimuthal dependence of the coercivity for different NW thickness, keeping constant width and spacing. Referring to Fig.D.5, for $t \leq 40$ nm the coercivity is maximum for B_{ext} parallel to EA ($\varphi = 0°$) and decreases monotonically reaching a minimum for B_{ext} parallel to HA ($\varphi = 90°$); for larger thickness, on the contrary, the coercivity increases when rotating B_{ext} away from EA, except for B_{ext} aligned along HA, for which the coercivity reaches the global minimum at every thickness. [2]

---

[2]Note that for all the investigated thicknesses, twofold symmetry ($180°$ periodicity) in the coercivity is observed: this is again consistent with negligible MCA.
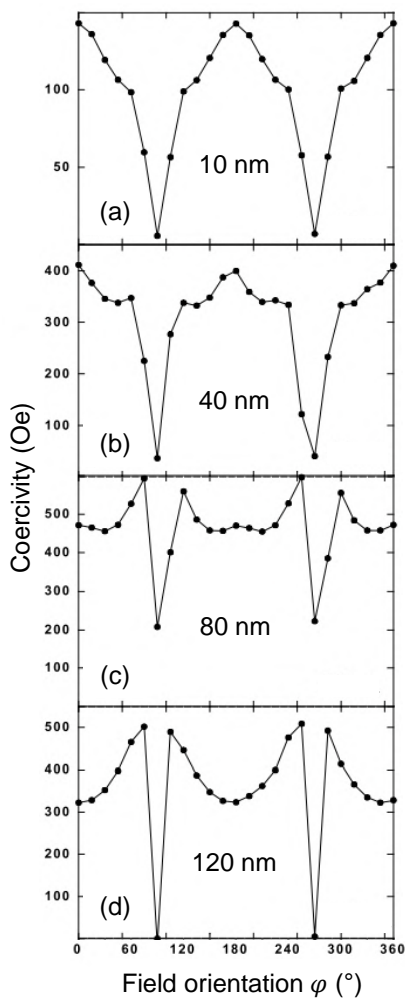
Figure D.5: Room-temperature coercivity as a function of the azimuthal angle between the external magnetic field and EA ($\varphi = 0°$: $B_{\text{ext}} \parallel$ EA; $\varphi = 90°$: $B_{\text{ext}} \parallel$ HA). Results for four thicknesses of Py NWs are reported, from 10 nm to 120 nm. Adapted from [241].
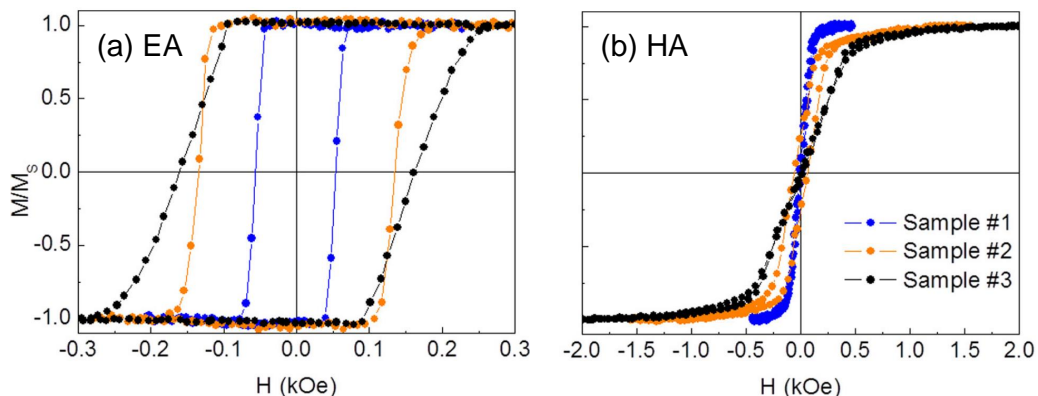
Figure D.6: Longitudinal MOKE hysteresis loops for three arrays of NWs with different composition: Py (sample #1), Fe (sample #2) and bilayer Fe/Py (sample #3). The external magnetic field is along EA [panel (a)] or along HA [panel (b)]. From [161].

The different trend in the coercivity is known as a signature of different magnetization switching modes. For thin NWs ($t \leq 40$ nm), the reduction of coercivity with increasing azimuth indicates coherent rotation as the dominant mechanism for magnetization switch, in similarity to the simple Stoner-Wohlfart model [243] for single-domain particles. Note that in Ref.[244] a modified Stoner-Wohlfart model was proposed, which shows the same qualitative trend in the coercivity: in that case, relevant for long cylindrical NWs with radius smaller than 30 nm and micron-size length, the magnetization switch involves the propagation of a single transverse domain wall. The different trend of coercivity for thicker NWs ($t > 40$ nm) is understood as the onset of magnetization curling [163, 245] as the dominant mechanism of magnetization switching. This regime is favoured by the fact that $Ni_{80}Fe_{20}$ is a soft magnetic material, and the geometrical dimensions of the NWs are larger than the exchange length (about 5.7 nm [246]), implying domain-wall propagation with low energy barriers. For the sample investigated in this chapter, t/w is about 0.06 as indicated by the vertical dashed line in Fig.D.4, so coherent rotation is expected as the dominant mechanism for magnetization switching; nevertheless, as shown later, coercivity is observed to increase with the azimuth, indicating magnetization curling to be likely compresent. Probably the presence of the Fe layer alters the phenomenology reported, shifting to lower t/w the cross-over between the two reversal mechanisms. This point deserves further investigation.

Interface coupling. The third relevant aspect is the interface magnetic coupling between Fe and Py layers. In Ref.[161] this has been studied comparing magnetostatic properties and magnonic spectra of one-dimensional NW arrays composed of Py (sample #1), Fe (sample#2) and Fe/Py (sample #3). The geometry was kept fixed for all these samples to $t = 10$ nm for each layer, $w = 340$ nm, $d = 100$ nm. Note that sample #3 is very similar, in composition and geometry, to the sample investigated in this chapter. In Fig.D.6 hysteresis loops from static longitudinal MOKE are reported for the three samples, for external field along EA [panel (a)] and along HA [panel (b)]. The coercivity increases from Py to Fe to Fe/Py sample, consistently with the general larger coercivity of Fe with respect to Py, and to larger coercivity for 20-nm thick NWs as compared to 10-nm thick. Importantly, the hysteresis of Fe/Py sample is smooth along the switching branches. The absence of intermediate jumps suggests strong ferromagnetic exchange

coupling at the interface: the two layers thus behave as a single effective ferromagnetic material. Note that MOKE is mainly sensitive to the top-most layer, as due to the optical penetration depth in metals ($\delta_{Fe} = 30$ nm, [151]); for multilayer magnetic systems a volume-integrated technique like SQUID or VSM could be beneficial. Hysteresis loops measured via SQUID (not reported here) also lack intermediate magnetization jumps, confirming interface ferromagnetic exchange coupling [235]. Agreement is also obtained in Ref.[161] via investigation of the magnonic bands and simulation with micromagnetic models. In Fig.D.7(a) magnon frequencies measured via magnetic BLS on sample #3 are reported as white circles as a function of the magnon wavevector; the image background is the intensity plot obtained from micromagnetic simulations. Good agreement between the experimental data and the simulations is obtained. Qualitatively, the same agreement [see panel (b)] can be obtained considering the NW as composed of an effective magnetic medium [ENW], where the magnetostatic parameters are the average of values for Fe and Py. The agreement to experimental data is considerable for the fundamental magnonic mode. This indicates that also the magnetization dynamics is strongly coupled in the two ferromagnetic layers, in particular for the fundamental mode. As a last aspect, results of micromagnetic simulations are reported in panel (c). The curves represent the amplitude of the dynamical component of the magnetization as a function of the position across the width of a NW; it is assumed that no dependence on the position across the thickness is present. The first five magnonic modes computed for sample #3 are reported, with the corresponding frequency at zero wavevector indicated in each subpanel. Spatially symmetric (antisymmetric) modes are shown as solid (dashed) lines. In the simulation, the contributions from Fe and Py can be isolated, and are coded in the color (yellow and blue, respectively). In the simulated modes the two magnetic layers show very similar spatial dynamics, with in-phase character. This further confirms that the strong exchange coupling at the interface sets collective magnetization dynamics, the two layers behaving as a single magnetic entity also in the dynamical regime. In-phase dynamics of the two layers is sometimes dubbed an *acoustic* magnonic mode, in similarity to the nomenclature for phonons; also *optical* magnonic modes, whereby the magnetization in the two layers precesses out-of-phase, are possible excitations of the bilayered system. It is precisely the inter-layer coupling what sets the energy (and thus the frequency) of optical magnons. Some papers report investigation of this effect, by purposely growing a Cu spacer between two ferromagnetic layers [234, 247–250]. Varying the Cu thickness in the range (5-50) nm, the coupling between the ferromagnetic layers weakens, and the magnetization state of the NW (either parallel or anti-parallel) is set by the competition between inter- and intra-NW dipolar interaction. Anti-parallel magnetization configuration of the NWs can be observed during the magnetization reversal (step-wise switch along hysteresis loops), and rich magnonic bands are observed via BLS.
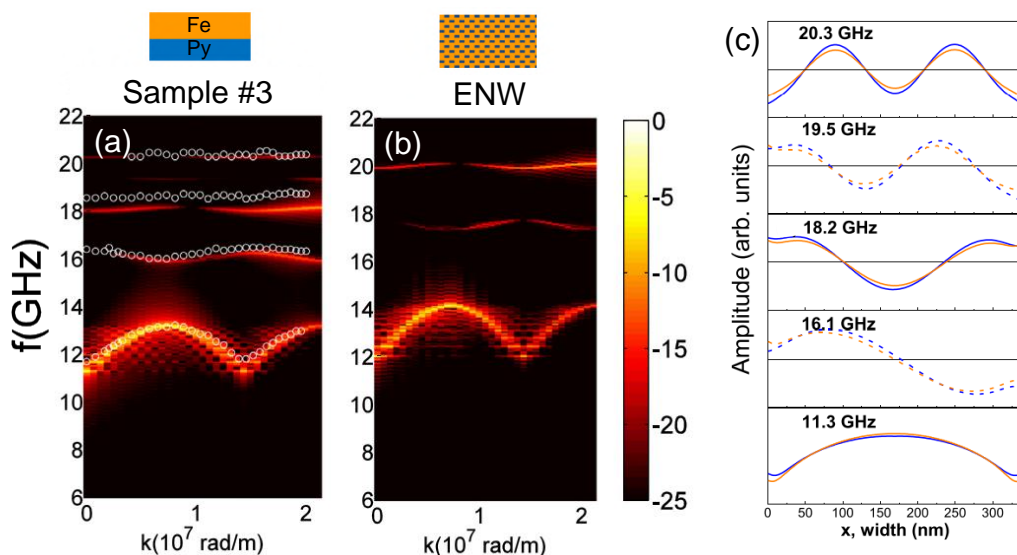
Figure D.7: (a) Magnonic frequency (white circles) measured via magnetic BLS as a function of the magnon wavevector, for sample #3 (Fe/Py bilayered NW); the background is the intensity map as obtained from micromagnetic simulations. (b) Intensity map for a fictitious effective magnetic material with properties obtained as average of Fe and Py: the lowest magnonic mode still well reproduces the experimental BLS data. (c) Amplitude of the dynamical component of the magnetization as a function of the position across the NW width, for sample #3. The first five magnonic modes are simulated, for zero wavevector; the frequency of each mode is reported in the subpanels. The contributions of Fe (yellow) and of Py (blue) are isolated. Adapted from [161].

Demagnetizing factors for orthorombic NWs

The magnetization $\mathbf{M}$ inside an ellipsoidal ferromagnet is uniform and the i-th component of the demagnetizing field can be expressed as $(H_d)_i = -\sum_j N_{ij} M_j$, where N_{ij} is the demagnetizing tensor. If $\mathbf{M}$ is aligned to one of the principal axes of the ellipsoid, N_{ij} is diagonal and its components are the demagnetizing factors. Analytical expressions for the demagnetizing factors in a generic ferromagnetic ellipsoid have been calculated in Ref.[251]. Few simple shapes can be analyzed as limiting cases of an ellipsoid (see *e.g.* Ref.[2]). Thus a ferromagnetic thin film is the limit of an oblate ellipsoid with short revolution axis: setting the OOP direction parallel to the z axis, one obtains $N_x = N_y = 0$, $N_z = 1$, meaning that no demagnetizing field arises when the film is magnetized IP. Again, a long ferromagnetic cylinder aligned along the z axis is the limit of a prolate ellipsoid: thus $N_x = N_y = 1/2$, $N_z = 0$, and demagnetizing field results from magnetization pointing orthogonal to the cylinder axis. For a ferromagnetic sphere, rotational symmetry sets $N_x = N_y = N_z = 1/3$.

In general, the demagnetizing tensor can be an extremely complicated function of the position. Luckily, a simple approximate expression for the demagnetizing factors for an orthorombic magnetic wire dominated by shape anisotropy is available, as derived extending the reasoning reported in Ref.[252]. In reference to Fig.E.1, given wire width w, the thickness is expressed as $t = r_1 w$ and the length as $l = r_2 w$, where r_1 and r_2 are the adimensional aspect ratios. The basic geometrical assumption [252] is that when the wire is magnetized along z, the demagnetizing factor N_z is proportional to the inverse geometrical dimension: $N_z = C/r_2 w$, with C some proportionality factor. Extending the
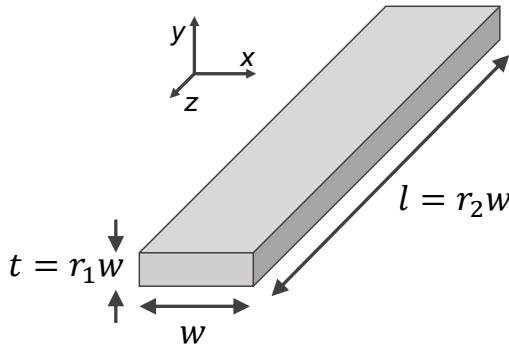
Figure E.1: Sketch of the elongated wire considered in the model. The width (w), thickness ($t = r_1 w$) and length ($l = r_2 w$) of the wire are aligned to the x, y and z axis, respectively.

reasoning, it is possible to write $N_y = C/r_1 w$ and $N_x = C/w$. Imposing the constraint $N_x + N_y + N_z = 1$ (in SI units), the proportionality factor is expressed as $C = \frac{r_1 r_2 w}{r_1 + r_2 + r_1 r_2}$. Inserting this expression for C, the demagnetizing factors are obtained as

$$N_x = \frac{r_1 r_2}{r_1 + r_2 + r_1 r_2} \, ,$$
$$N_y = \frac{r_2}{r_1 + r_2 + r_1 r_2} \, ,$$
$$N_z = \frac{r_1}{r_1 + r_2 + r_1 r_2} \, .$$

In [252], the approximated model is compared to exact solutions for the demagnetizing factors [253]: the percentage error is reported as $< 6\%$.

For the NW array investigated in part III the aspect ratios assume the large values of $r_1 = 20 \text{ nm}/340 \text{ nm} \approx 0.06$ and $r_2 = 4 \text{ mm}/340 \text{ nm} \approx 12\,000$. With these numbers, the expressions for N_i can be approximated to

$$N_x \approx \frac{r_1}{1 + r_1} \approx r_1 = 0.06 \, ,$$
$$N_y \approx \frac{1}{1 + r_1} \approx 1 - r_1 = 0.94 \, ,$$
$$N_z \approx \frac{r_1}{r_2(1 + r_1)} = \mathcal{O}\left(\frac{r_1}{r_2}\right) \, .$$

Thus, for our high aspect-ratio NWs the geometrical ratios give a reasonable estimate of the demagnetizing factors.

Acronyms

AFM Atomic Force Microscopy.

B-FMR Broadband FMR.

BLS Brillouin Light Scattering.

BZ Brillouin Zone.

DE Damon-Eshbach.

DUV deep ultraviolet.

EA Easy Axis.

ENW *Effective* NW.

EUV Extreme Ultraviolet.

FEL Free Electron Laser.

FFT Fast Fourier Transform.

FMR Ferromagnetic Resonance.

FR Faraday Rotation.

FT Fourier Transform.

FWHM Full Width at Half Maximum.

FWM Four Wave Mixing.

GIXRD Grazing Incidence X-Ray Diffraction.

HA Hard Axis.

IDT Inter-Digitated Transducer.

IP in plane.

LH linear horizontal.

LLG Landau-Lifshitz-Gilbert.

LV linear vertical.

MC Magnonic Crystal.

MCA Magneto-Crystalline Anisotropy.

MEC Magneto-Elastic Coupling.

MOKE Magneto-Optical Kerr Effect.

NIR Near Infrared.

NW Nano Wire.

OOP out of plane.

p-MOKE polar MOKE.

pBZ pseudo-BZ.

PM pure magnonic mode.

PSSW Perpendicular Standing SW.

rf radio-frequency.

rms root mean square.

RSAW Rayleigh Surface Acoustic Wave.

SAW Surface Acoustic Wave.

SAW-FMR SAW-driven FMR.

SOC Spin-Orbit Coupling.

SPnC Surface Phononic Crystal.

SQUID Superconducting Quantum Interference Device.

SSLW Surface-Skimming Longitudinal Wave.

SW Spin Wave.

SWR Spin Wave Resonance.

TEM Transmission Electron Microscopy.

TG Transient-Grating.

TMS Two-Magnon Scattering.

tr time-resolved.

tr-R time-resolved reflectivity.

VSM Vibrating Sample Magnetometry.

XRR X-Ray Reflectivity.

Bibliography

1. Stöhr, J. & Siegmann, H. C. Magnetism. *Solid-State Sciences. Springer, Berlin, Heidelberg* **5,** 236 (2006).

2. Blundell, S. *Magnetism in condensed matter* (Oxford University Press, 2001).

3. Zhang, J. & Averitt, R. D. Dynamics and control in complex transition metal oxides. *Annual Review of Materials Research* **44,** 19–43 (2014).

4. Fausti, D., Tobey, R., Dean, N., Kaiser, S., Dienst, A., Hoffmann, M. C., Pyon, S., Takayama, T., Takagi, H. & Cavalleri, A. Light-induced superconductivity in a stripe-ordered cuprate. *Science* **331,** 189–191 (2011).

5. Radu, I., Vahaplar, K., Stamm, C., Kachel, T., Pontius, N., Dürr, H., Ostler, T., Barker, J., Evans, R., Chantrell, R., *et al.* Transient ferromagnetic-like state mediating ultrafast reversal of antiferromagnetically coupled spins. *Nature* **472,** 205–208 (2011).

6. Müller, G. M., Walowski, J., Djordjevic, M., Miao, G.-X., Gupta, A., Ramos, A. V., Gehrke, K., Moshnyaga, V., Samwer, K., Schmalhorst, J., *et al.* Spin polarization in half-metals probed by femtosecond spin excitation. *Nature Materials* **8,** 56–61 (2009).

7. Beaurepaire, E., Merle, J.-C., Daunois, A. & Bigot, J.-Y. Ultrafast spin dynamics in ferromagnetic nickel. *Physical Review Letters* **76,** 4250 (1996).

8. Lalieu, M. L. & Koopmans, B. in *Handbook of Magnetism and Magnetic Materials* 477–547 (Springer, 2021).

9. Dornes, C., Acremann, Y., Savoini, M., Kubli, M., Neugebauer, M. J., Abreu, E., Huber, L., Lantz, G., Vaz, C. A., Lemke, H., *et al.* The ultrafast Einstein–de Haas effect. *Nature* **565,** 209–212 (2019).

10. Tauchert, S. R., Volkov, M., Ehberger, D., Kazenwadel, D., Evers, M., Lange, H., Donges, A., Book, A., Kreuzpaintner, W., Nowak, U., *et al.* Polarized phonons carry angular momentum in ultrafast demagnetization. *Nature* **602,** 73–77 (2022).

11. Afanasiev, D., Hortensius, J., Ivanov, B., Sasani, A., Bousquet, E., Blanter, Y., Mikhaylovskiy, R., Kimel, A. & Caviglia, A. Ultrafast control of magnetic interactions via light-driven phonons. *Nature Materials* **20,** 607–611 (2021).

12. Nova, T. F., Cartella, A., Cantaluppi, A., Först, M., Bossini, D., Mikhaylovskiy, R. V., Kimel, A. V., Merlin, R. & Cavalleri, A. An effective magnetic field from optically driven phonons. *Nature Physics* **13,** 132–136 (2017).

13. Yang, W.-G. & Schmidt, H. Acoustic control of magnetism toward energy-efficient applications. *Applied Physics Reviews* **8** (2021).

14. Kittel, C. *Introduction to solid state physics* (John Wiley & sons, inc, 2005).

15. Landau, L. D., Lifshitz, E. M., Kosevich, A. M. & Pitaevskii, L. P. *Theory of elasticity* (Elsevier, 1986).

16. Rogers, J. A., Maznev, A. A., Banet, M. J. & Nelson, K. A. Optical generation and characterization of acoustic waves in thin films: Fundamentals and applications. *Annual Review of Materials Science* **30,** 117–157 (2000).

17. Reisman, H. & Pawlik, P. *Elasticity: Theory and Applications* (John Wiley & Sons, New York, 1980).

18. Newnham, R. E. *Properties of materials: anisotropy, symmetry, structure* (Oxford University Press, 2005).

19. Auld, B. A. *Acoustic fields and waves in solids* (Wiley, New York, 1973).

20. Lüth, H. *Solid surfaces, interfaces and thin films* (Springer, 2001).

21. Farnell, G. W. & Adler, E. Elastic wave propagation in thin layers. *Physical Acoustics* **9,** 35–127 (2012).

22. Hassan, W. & Nagy, P. B. Simplified expressions for the displacements and stresses produced by the Rayleigh wave. *The Journal of the Acoustical Society of America* **104,** 3107–3110 (1998).

23. Janušonis, J. *Magneto-elastic waves in thin ferromagnetic films* PhD thesis (University of Gröningen, 2017).

24. Hashimoto, K.-Y. Bulk acoustic and surface acoustic waves. *Surface Acoustic Wave Devices in Telecommunications: Modelling and Simulation,* 1–23 (2000).

25. Kirilyuk, A., Kimel, A. V. & Rasing, T. Ultrafast optical manipulation of magnetic order. *Reviews of Modern Physics* **82,** 2731 (2010).

26. Exl, L., Suess, D. & Schrefl, T. Micromagnetism. *Handbook of Magnetism and Magnetic Materials,* 1–44 (2020).

27. Coey, J. M. & Parkin, S. S. *Handbook of magnetism and magnetic materials* (Springer Cham, 2021).

28. Coey, J. M. *Magnetism and magnetic materials* (Cambridge University Press, 2010).

29. Skomski, R., Manchanda, P. & Kashyap, A. Anisotropy and crystal field. *Handbook of Magnetism and Magnetic Materials,* 1–83 (2020).

30. Salikhov, R., Alekhin, A., Parpiiev, T., Pezeril, T., Makarov, D., Abrudan, R., Meckenstock, R., Radu, F., Farle, M., Zabel, H., *et al.* Gilbert damping in NiFeGd compounds: Ferromagnetic resonance versus time-resolved spectroscopy. *Physical Review B* **99,** 104412 (2019).

31. Farle, M. Ferromagnetic resonance of ultrathin metallic layers. *Reports on Progress in Physics* **61,** 755 (1998).

32. Menard, D. & Barklie, R. Electron Paramagnetic and Ferromagnetic Resonance. *Handbook of Magnetism and Magnetic Materials,* 1–35 (2020).

33. Patton, C. E. Magnetic excitations in solids. *Physics Reports* **103,** 251–315 (1984).

34. Prabhakar, A. & Stancil, D. *Spin waves: Theory and applications* (Springer, 2009).

35. Gurevich, A. G. & Melkov, G. A. *Magnetization oscillations and waves* (CRC press, 2020).

36. Wu, R., Chen, L., Shick, A. & Freeman, A. First-principles determinations of magneto-crystalline anisotropy and magnetostriction in bulk and thin-film transition metals. *Journal of Magnetism and Magnetic Materials* **177,** 1216–1219 (1998).

37. Sander, D. Magnetostriction and magnetoelasticity. *Handbook of Magnetism and Magnetic Materials,* 1–45 (2020).

38. Chikazumi, S. *Physics of ferromagnetism* **94** (Oxford University Press, 1997).

39. Kovalenko, O., Pezeril, T. & Temnov, V. V. New concept for magnetization switching by ultrafast acoustic pulses. *Physical Review Letters* **110,** 266602 (2013).

40. Vlasov, V. S., Lomonosov, A. M., Golov, A. V., Kotov, L. N., Besse, V., Alekhin, A., Kuzmin, D. A., Bychkov, I. V. & Temnov, V. V. Magnetization switching in bistable nanomagnets by picosecond pulses of surface acoustic waves. *Physical Review B* **101,** 024425 (2020).

41. Dreher, L., Weiler, M., Pernpeintner, M., Huebl, H., Gross, R., Brandt, M. S. & Gönnenwein, S. T. Surface acoustic wave driven ferromagnetic resonance in nickel thin films: Theory and experiment. *Physical Review B* **86,** 134415 (2012).

42. Chang, C.-L. *Opto-magnonic Crystals: Optical Manipulation of Spin Waves* PhD thesis (University of Gröningen, 2019).

43. Weiler, M., Dreher, L., Heeg, C., Huebl, H., Gross, R., Brandt, M. S. & Gönnenwein, S. T. Elastically driven ferromagnetic resonance in nickel thin films. *Physical Review Letters* **106,** 117601 (2011).

44. Gowtham, P. G., Moriyama, T., Ralph, D. C. & Buhrman, R. A. Traveling surface spin-wave resonance spectroscopy using surface acoustic waves. *Journal of Applied Physics* **118** (2015).

45. Yang, W., Jaris, M., Hibbard-Lubow, D., Berk, C. & Schmidt, H. Magnetoelastic excitation of single nanomagnets for optical measurement of intrinsic Gilbert damping. *Physical Review B* **97,** 224410 (2018).

46. Rovillain, P., Duquesne, J.-Y., Christienne, L., Eddrief, M., Pini, M. G., Rettori, A., Tacchi, S. & Marangolo, M. Impact of Spin-Wave Dispersion on Surface-Acoustic-Wave Velocity. *Physical Review Applied* **18,** 064043 (2022).

47. Polewczyk, V., Dumesnil, K., Lacour, D., Moutaouekkil, M., Mjahed, H., Tiercelin, N., Watelot, S. P., Mishra, H., Dusch, Y., Hage-Ali, S., *et al.* Unipolar and bipolar high-magnetic-field sensors based on surface acoustic wave resonators. *Physical Review Applied* **8,** 024001 (2017).

48. Polewczyk, V. *Growth of hybrid piezoelectric/magnetostrictive systems for magnetic devices based on surface acoustic wave resonators* PhD thesis (Université de Lorraine, 2018).

49. Küß, M., Heigl, M., Flacke, L., Hörner, A., Weiler, M., Wixforth, A. & Albrecht, M. Nonreciprocal magnetoacoustic waves in dipolar-coupled ferromagnetic bilayers. *Physical Review Applied* **15,** 034060 (2021).

50. Küß, M., Heigl, M., Flacke, L., Hörner, A., Weiler, M., Albrecht, M. & Wixforth, A. Nonreciprocal Dzyaloshinskii–Moriya magnetoacoustic waves. *Physical Review Letters* **125,** 217203 (2020).

51. Mukamel, S. *Principles of nonlinear optical spectroscopy* (Oxford University Press, 1995).

52. Torre, R. *Time-resolved spectroscopy in complex liquids* (Springer, 2007).

53. Lippert, E. & Macomber, J. D. *Dynamics during spectroscopic transitions: basic concepts* (Springer Science & Business Media, 2012).

54. Eichler, H. J., Günter, P. & Pohl, D. W. *Laser-induced dynamic gratings* (Springer, 2013).

55. Yan, Y.-X., Gamble Jr, E. B. & Nelson, K. A. Impulsive stimulated scattering: General importance in femtosecond laser pulse interactions with matter, and spectroscopic applications. *The Journal of Chemical Physics* **83,** 5391–5399 (1985).

56. Yan, Y.-X. & Nelson, K. A. Impulsive stimulated light scattering. I. General theory. *The Journal of Chemical Physics* **87,** 6240–6256 (1987).

57. Yan, Y.-X. & Nelson, K. A. Impulsive stimulated light scattering. II. Comparison to frequency-domain light-scattering spectroscopy. *The Journal of Chemical Physics* **87,** 6257–6265 (1987).

58. Cucini, R., Battistoni, A., Bencivenga, F., Gessini, A., Mincigrucci, R., Giangrisostomi, E., Principi, E., Capotondi, F., Pedersoli, E., Manfredda, M., *et al. Toward the Extreme Ultra Violet Four Wave Mixing Experiments: From Table Top Lasers to Fourth Generation Light Sources* in *Photonics* **2** (2015), 57–70.

59. Hofmann, F., Short, M. P. & Dennett, C. A. Transient grating spectroscopy: An ultrarapid, nondestructive materials evaluation technique. *MRS Bulletin* **44,** 392–402 (2019).

60. Svetina, C., Mankowsky, R., Knopp, G., Koch, F., Seniutinas, G., Rösner, B., Kubec, A., Lebugle, M., Mochi, I., Beck, M., *et al.* Towards X-ray transient grating spectroscopy. *Optics Letters* **44,** 574–577 (2019).

61. Choudhry, U., Kim, T., Adams, M., Ranasinghe, J., Yang, R. & Liao, B. Characterizing microscale energy transport in materials with transient grating spectroscopy. *Journal of Applied Physics* **130** (2021).

62. Foglia, L., Mincigrucci, R., Maznev, A., Baldi, G., Capotondi, F., Caporaletti, F., Comin, R., De Angelis, D., Duncan, R., Fainozzi, D., *et al.* Extreme ultraviolet transient gratings: A tool for nanoscale photoacoustics. *Photoacoustics* **29,** 100453 (2023).

63. Chang, Z., Corkum, P. B. & Leone, S. R. Attosecond optics and technology: progress to date and future prospects. *JOSA B* **33,** 1081–1097 (2016).

64. Thomsen, C., Strait, J., Vardeny, Z., Maris, H. J., Tauc, J. & Hauser, J. Coherent phonon generation and detection by picosecond light pulses. *Physical Review Letters* **53,** 989 (1984).

65. Matsuda, O., Wright, O., Hurley, D., Gusev, V. & Shimizu, K. Coherent shear phonon generation and detection with ultrashort optical pulses. *Physical Review Letters* **93,** 095501 (2004).

66. Dagur, D., Polewczyk, V., Petrov, A. Y., Carrara, P., Brioschi, M., Fiori, S., Cucini, R., Rossi, G., Panaccione, G., Torelli, P., *et al.* Visible Light Effects on Photostrictive/Magnetostrictive PMN-PT/Ni Heterostructure. *Advanced Materials Interfaces* **9,** 2201337 (2022).

67. Hansteen, F., Kimel, A., Kirilyuk, A. & Rasing, T. Nonthermal ultrafast optical control of the magnetization in garnet films. *Physical Review B* **73,** 014421 (2006).

68. Yamazaki, H., Matsuda, O. & Wright, O. B. Surface phonon imaging through the photoelastic effect. *Physica Status Solidi (C)* **1,** 2991–2994 (2004).

69. Saito, T., Matsuda, O., Tomoda, M. & Wright, O. B. Imaging gigahertz surface acoustic waves through the photoelastic effect. *JOSA B* **27,** 2632–2638 (2010).

70. Jesenska, E., Yoshida, T., Shinozaki, K., Ishibashi, T., Beran, L., Zahradnik, M., Antos, R., Kučera, M. & Veis, M. Optical and magneto-optical properties of Bi substituted yttrium iron garnets prepared by metal organic decomposition. *Optical Materials Express* **6,** 1986–1997 (2016).

71. Schellekens, A. J. Manipulating spins: Novel methods for controlling magnetization dynamics on the ultimate timescale (2014).

72. Cucini, R., Taschin, A., Bartolini, P. & Torre, R. Acoustic, thermal and flow processes in a water filled nanoporous glass by time-resolved optical spectroscopy. *Journal of the Mechanics and Physics of Solids* **58,** 1302–1317 (2010).

73. Taschin, A. *Relaxation processes on supercooled liquids by heterodyne detected transient grating experiments* PhD thesis (Università degli Studi di Firenze, 2003).

74. Johnson, J. A., Maznev, A. A., Bulsara, M. T., Fitzgerald, E. A., Harman, T., Calawa, S., Vineis, C., Turner, G. & Nelson, K. A. Phase-controlled, heterodyne laser-induced transient grating measurements of thermal transport properties in opaque material. *Journal of Applied Physics* **111** (2012).

75. Palmer, C. & Loewen, E. G. Diffraction grating handbook (2005).

76. Maznev, A., Mincigrucci, R., Bencivenga, F., Unikandanunni, V., Capotondi, F., Chen, G., Ding, Z., Duncan, R., Foglia, L., Izzo, M., *et al.* Generation and detection of 50 GHz surface acoustic waves by extreme ultraviolet pulses. *Applied Physics Letters* **119** (2021).

77. Lawson, C. M., Powell, R. C. & Zwicker, W. K. Measurement of Exciton Diffusion Lengths in $Nd_xLa_{1-x}P_5O_{14}$ by Four-Wave Mixing Techniques. *Physical Review Letters* **46,** 1020–1023. https://link.aps.org/doi/10.1103/PhysRevLett.46.1020 (15 1981).

78. Moss, S. C., Lindle, J. R., Mackey, H. & Smirl, A. L. Measurement of the diffusion coefficient and recombination effects in germanium by diffraction from optically-induced picosecond transient gratings. *Applied Physics Letters* **39,** 227–229 (1981).

79. Lawson, C. M., Powell, R. C. & Zwicker, W. K. Transient grating investigation of exciton diffusion and fluorescence quenching in Nd x Ta 1- x P 5 O 14 crystals. *Physical Review B* **26,** 4836 (1982).

80. Wang, J., Guo, Y., Huang, Y., Luo, H., Zhou, X., Gu, C. & Liu, B. Diffusion dynamics of valley excitons by transient grating spectroscopy in monolayer WSe2. *Applied Physics Letters* **115** (2019).

81. Maznev, A. A., Johnson, J. A. & Nelson, K. A. Onset of nondiffusive phonon transport in transient thermal grating decay. *Physical Review B* **84,** 195206 (2011).

82. Johnson, J. A., Eliason, J. K., Maznev, A. A., Luo, T. & Nelson, K. A. Non-diffusive thermal transport in GaAs at micron length scales. *Journal of Applied Physics* **118** (2015).

83. Cameron, A., Riblet, P. & Miller, A. Spin gratings and the measurement of electron drift mobility in multiple quantum well semiconductors. *Physical Review Letters* **76,** 4793 (1996).

84. Ishiguro, T., Toda, Y. & Adachi, S. Exciton spin relaxation in GaN observed by spin grating experiment. *Applied Physics Letters* **90** (2007).

85. Gedik, N., Orenstein, J., Liang, R., Bonn, D. & Hardy, W. Diffusion of nonequilibrium quasi-particles in a cuprate superconductor. *Science* **300,** 1410–1412 (2003).

86. Terazima, M. Revealing protein reactions using transient grating method: Photo-induced heating, volume change, and diffusion change. *Journal of Applied Physics* **131** (2022).

87. Käding, O., Skurk, H., Maznev, A. & Matthias, E. Transient thermal gratings at surfaces for thermal characterization of bulk materials and thin films. *Applied Physics A* **61,** 253–261 (1995).

88. Sander, M., Herzog, M., Pudell, J.-E., Bargheer, M., Weinkauf, N., Pedersen, M., Newby, G., Sellmann, J., Schwarzkopf, J., Besse, V., *et al.* Spatiotemporal coherent control of thermal excitations in solids. *Physical Review Letters* **119,** 075901 (2017).

89. Huberman, S., Duncan, R. A., Chen, K., Song, B., Chiloyan, V., Ding, Z., Maznev, A. A., Chen, G. & Nelson, K. A. Observation of second sound in graphite at temperatures above 100 K. *Science* **364,** 375–379 (2019).

90. Dennett, C. A. & Short, M. P. Thermal diffusivity determination using heterodyne phase insensitive transient grating spectroscopy. *Journal of Applied Physics* **123** (2018).

91. Cheng, L.-T. & Nelson, K. A. Ferroelectric phase transition in RbH 2 PO 4: Picosecond time-resolved impulsive stimulated Brillouin scattering experiments. *Physical Review B* **37,** 3603 (1988).

92. Maznev, A., Wright, O. & Matsuda, O. Mapping the band structure of a surface phononic crystal. *New Journal of Physics* **13,** 013037 (2011).

93. Krug, B., Koukourakis, N., Guck, J. & Czarske, J. Nonlinear microscopy using impulsive stimulated Brillouin scattering for high-speed elastography. *Optics Express* **30,** 4748–4758 (2022).

94. Boechler, N., Eliason, J., Kumar, A., Maznev, A., Nelson, K. & Fang, N. Interaction of a contact resonance of microspheres with surface acoustic waves. *Physical Review Letters* **111,** 036103 (2013).

95. Radu, I. E. *Ultrafast Electron, Lattice and Spin Dynamics on Rare-Earth Metal Surfaces* PhD thesis (Freie Universitaet Berlin, 2006).

96. Dougherty, T. P., Wiederrecht, G. P. & Nelson, K. A. Impulsive stimulated Raman scattering experiments in the polariton regime. *JOSA B* **9,** 2179–2189 (1992).

97. Janušonis, J., Jansma, T., Chang, C., Liu, Q., Gatilova, A., Lomonosov, A., Shalagatskyi, V., Pezeril, T., Temnov, V. & Tobey, R. Transient grating spectroscopy in magnetic thin films: simultaneous detection of elastic and magnetic dynamics. *Scientific reports* **6,** 29143 (2016).

98. Cao, G., Jiang, S., Åkerman, J. & Weissenrieder, J. Femtosecond laser driven precessing magnetic gratings. *Nanoscale* **13,** 3746–3756 (2021).

99. Carrara, P., Brioschi, M., Longo, E., Dagur, D., Polewczyk, V., Vinai, G., Mantovan, R., Fanciulli, M., Rossi, G., Panaccione, G., *et al.* All-Optical Generation and Time-Resolved Polarimetry of Magnetoacoustic Resonances via Transient Grating Spectroscopy. *Physical Review Applied* **18,** 044009 (2022).

100. Ksenzov, D., Maznev, A. A., Unikandanunni, V., Bencivenga, F., Capotondi, F., Caretta, A., Foglia, L., Malvestuto, M., Masciovecchio, C., Mincigrucci, R., *et al.* Nanoscale transient magnetization gratings created and probed by femtosecond extreme ultraviolet pulses. *Nano Letters* **21,** 2905–2911 (2021).

101. Van Kampen, M., Jozsa, C., Kohlhepp, J., LeClair, P., Lagae, L., De Jonge, W. & Koopmans, B. All-optical probe of coherent spin waves. *Physical Review Letters* **88,** 227201 (2002).

102. *IMPRESS project* https://e-impress.eu/.

103. Kimel, A., Kirilyuk, A., Usachev, P., Pisarev, R., Balbashov, A. & Rasing, T. Ultrafast non-thermal control of magnetization by instantaneous photomagnetic pulses. *Nature* **435,** 655–657 (2005).

104. Kikkawa, T. & Saitoh, E. Spin Seebeck effect: Sensitive probe for elementary excitation, spin correlation, transport, magnetic order, and domains in solids. *Annual Review of Condensed Matter Physics* **14,** 129–151 (2023).

105. Bencivenga, F. & Masciovecchio, C. FEL-based transient grating spectroscopy to investigate nanoscale dynamics. *Nuclear Instruments and Methods in Physics Research Section A: Accelerators, Spectrometers, Detectors and Associated Equipment* **606,** 785–789 (2009).

106. *NFFA-Trieste project* https://www.trieste.nffa.eu/.

107. Brioschi, M., Carrara, P., Polewczyk, V., Dagur, D., Vinai, G., Parisse, P., Dal Zilio, S., Panaccione, G., Rossi, G. & Cucini, R. Multidetection scheme for transient-grating-based spectroscopy. *Optics Letters* **48,** 167–170 (2023).

108. Cucini, R., Pincelli, T., Panaccione, G., Kopic, D., Frassetto, F., Miotti, P., Pierantozzi, G. M., Peli, S., Fondacaro, A., De Luisa, A., *et al.* Coherent narrowband light source for ultrafast photoelectron spectroscopy in the 17–31 eV photon energy range. *Structural Dynamics* **7** (2020).

109. Carrara, P. *Characterization of a High Harmonics Generation source for spectroscopic pump-probe experiments and first results on Fe(100)/MgO surface* 2020.

110. Maznev, A., Crimmins, T. & Nelson, K. How to make femtosecond pulses overlap. *Optics Letters* **23,** 1378–1380 (1998).

111. Meshalkin, A. Y., Podlipnov, V., Ustinov, A. & Achimova, E. *Analysis of diffraction efficiency of phase gratings in dependence of duty cycle and depth* in *Journal of Physics: Conference Series* **1368** (2019), 022047.

112. Frassetto, F., Fabris, N., Miotti, P. & Poletto, L. *Design study of time-preserving grating monochromators for ultrashort pulses in the extreme-ultraviolet and soft x-rays* in *Photonics* **4** (2017), 14.

113. https://www.iom.cnr.it/research-facilities/facilities-labs/synthesis-andnano-fabrication/fnf/.

114. Zakeri, K. Terahertz magnonics: Feasibility of using terahertz magnons for information processing. *Physica C: Superconductivity and its applications* **549,** 164–170 (2018).

115. Hirohata, A., Yamada, K., Nakatani, Y., Prejbeanu, I.-L., Diény, B., Pirro, P. & Hillebrands, B. Review on spintronics: Principles and device applications. *Journal of Magnetism and Magnetic Materials* **509,** 166711 (2020).

116. Dieny, B., Prejbeanu, I. L., Garello, K., Gambardella, P., Freitas, P., Lehndorff, R., Raberg, W., Ebels, U., Demokritov, S. O., Akerman, J., *et al.* Opportunities and challenges for spintronics in the microelectronics industry. *Nature Electronics* **3,** 446–459 (2020).

117. Pirro, P., Vasyuchka, V. I., Serga, A. A. & Hillebrands, B. Advances in coherent magnonics. *Nature Reviews Materials* **6,** 1114–1135 (2021).

118. Janušonis, J., Chang, C., Van Loosdrecht, P. & Tobey, R. Frequency tunable surface magneto elastic waves. *Applied Physics Letters* **106** (2015).

119. Klokholm, E. & Aboaf, J. The saturation magnetostriction of thin polycrystalline films of iron, cobalt, and nickel. *Journal of Applied Physics* **53,** 2661–2663 (1982).

120. https://www.opticalsolutions.it/en/defence-ir-components-en/caf2-en/calcium-fluoride-caf2/.

121. https://www.azom.com/article.aspx?ArticleID=52.

122. https://www.azom.com/article.aspx?ArticleID=2362.

123. Benyettou, S. First principles study of the structural, elastic and thermodynamic properties of the cubic perovskite-type SrTiO3 (2018).

124. https://www.azom.com/properties.aspx?ArticleID=54.

125. https://www.azom.com/properties.aspx?ArticleID=1387.

126. https://www.azom.com/properties.aspx?ArticleID=599.

127. Casals, B., Statuto, N., Foerster, M., Hernández-Mínguez, A., Cichelero, R., Manshausen, P., Mandziak, A., Aballe, L., Hernández, J. M. & Maciá, F. Generation and imaging of magnetoacoustic waves over millimeter distances. *Physical Review Letters* **124,** 137202 (2020).

128. Chang, C. L., Mieszczak, S., Zelent, M., Besse, V., Martens, U., Tamming, R. R., Janusonis, J., Graczyk, P., Münzenberg, M., Kłos, J. W., *et al.* Driving magnetization dynamics in an on-demand magnonic crystal via the magnetoelastic interactions. *Physical Review Applied* **10,** 064051 (2018).

129. Woltersdorf, G., Buess, M., Heinrich, B. & Back, C. Time resolved magnetization dynamics of ultrathin Fe (001) films: Spin-pumping and two-magnon scattering. *Physical Review Letters* **95,** 037401 (2005).

130. Longo, E., Belli, M., Alia, M., Rimoldi, M., Cecchini, R., Longo, M., Wiemer, C., Locatelli, L., Tsipas, P., Dimoulas, A., *et al.* Large Spin-to-Charge Conversion at Room Temperature in Extended Epitaxial Sb2Te3 Topological Insulator Chemically Grown on Silicon. *Advanced Functional Materials* **32,** 2109361 (2022).

131. Kittel, C. On the theory of ferromagnetic resonance absorption. *Physical Review* **73,** 155 (1948).

132. Kittel, C. & McEuen, P. *Introduction to solid state physics* (John Wiley & Sons, 2018).

133. Azzawi, S., Hindmarch, A. & Atkinson, D. Magnetic damping phenomena in ferromagnetic thin-films and multilayers. *Journal of Physics D: Applied Physics* **50,** 473001 (2017).

134. Longo, E., Wiemer, C., Belli, M., Cecchini, R., Longo, M., Cantoni, M., Rinaldi, C., Overbeek, M. D., Winter, C. H., Gubbiotti, G., *et al.* Ferromagnetic resonance of Co thin films grown by atomic layer deposition on the Sb2Te3 topological insulator. *Journal of Magnetism and Magnetic Materials* **509,** 166885 (2020).

135. Bruno, P. & Renard, J. .-. Magnetic surface anisotropy of transition metal ultrathin films. *Applied Physics A* **49,** 499–506 (1989).

136. Fassbender, J., Strache, T., Liedke, M., Markó, D., Wintz, S., Lenz, K., Keller, A., Facsko, S., Mönch, I. & McCord, J. Introducing artificial length scales to tailor magnetic properties. *New Journal of Physics* **11,** 125002 (2009).

137. Vayalil, S. K., Koorikkat, A., Gopi, A. K., Roth, S. V. & Kumar, P. A. Tailoring of uniaxial magnetic anisotropy in Permalloy thin films using nanorippled Si substrates. *Journal of Physics: Condensed Matter* **32,** 185804 (2020).

138. Kalinikos, B. *Excitation of propagating spin waves in ferromagnetic films* in *IEE Proceedings H (Microwaves, Optics and Antennas)* **127** (1980), 4–10.

139. Chang, C., Lomonosov, A., Janusonis, J., Vlasov, V., Temnov, V. & Tobey, R. Parametric frequency mixing in a magnetoelastically driven linear ferromagnetic-resonance oscillator. *Physical Review B* **95,** 060409 (2017).

140. De Cos, D., Garcia-Arribas, A. & Barandiaran, J. Ferromagnetic resonance in gigahertz magneto-impedance of multilayer systems. *Journal of magnetism and magnetic materials* **304,** 218–221 (2006).

141. Yoshii, S., Ohshima, R., Ando, Y., Shinjo, T. & Shiraishi, M. Detection of ferromagnetic resonance from 1 nm-thick Co. *Scientific Reports* **10,** 15764 (2020).

142. Wu, S., Smith, D. A., Nakarmi, P., Rai, A., Clavel, M., Hudait, M. K., Zhao, J., Michel, F. M., Mewes, C., Mewes, T., *et al.* Room-temperature intrinsic and extrinsic damping in polycrystalline Fe thin films. *Physical Review B* **105,** 174408 (2022).

143. Wilczek, F. Quantum time crystals. *Physical Review Letters* **109,** 160401 (2012).

144. Adeyeye, A. & Singh, N. Large area patterned magnetic nanostructures. *Journal of Physics D: Applied Physics* **41,** 153001 (2008).

145. Godejohann, F., Scherbakov, A. V., Kukhtaruk, S. M., Poddubny, A. N., Yaremkevich, D. D., Wang, M., Nadzeyka, A., Yakovlev, D. R., Rushforth, A. W., Akimov, A. V., *et al.* Magnon polaron formed by selectively coupled coherent magnon and phonon modes of a surface patterned ferromagnet. *Physical Review B* **102,** 144438 (2020).

146. Mekonnen, A., Cormier, M., Kimel, A., Kirilyuk, A., Hrabec, A., Ranno, L. & Rasing, T. Femtosecond Laser Excitation of Spin Resonances in Amorphous Ferrimagnetic Gd 1- x Co x Alloys. *Physical Review Letters* **107,** 117202 (2011).

147. Chang, C. L., Tamming, R. R., Broomhall, T. J., Janusonis, J., Fry, P. W., Tobey, R. I. & Hayward, T. J. Selective excitation of localized spin-wave modes by optically pumped surface acoustic waves. *Physical Review Applied* **10,** 034068 (2018).

148. Blank, T. G., Hermanussen, S., Lichtenberg, T., Rasing, T., Kirilyuk, A., Koopmans, B. & Kimel, A. V. Laser-Induced Transient Anisotropy and Large Amplitude Magnetization Dynamics in a Gd/FeCo Multilayer. *Advanced Materials Interfaces* **9,** 2201283 (2022).

149. Vansteenkiste, A., Leliaert, J., Dvornik, M., Helsen, M., Garcia-Sanchez, F. & Van Waeyenberge, B. The design and verification of MuMax3. *AIP advances* **4** (2014).

150. Fox, M. *Optical properties of solids* 2002.

151. *Refractive index database* https://refractiveindex.info.

152. Robillard, J.-F., Devos, A. & Roch-Jeune, I. Time-resolved vibrations of two-dimensional hypersonic phononic crystals. *Physical Review B* **76,** 092301 (2007).

153. Tarasenko, A., Čtvrtlík, R. & Kudělka, R. Theoretical and experimental revision of surface acoustic waves on the (100) plane of silicon. *Scientific Reports* **11,** 2845 (2021).

154. Nardi, D., Banfi, F., Giannetti, C., Revaz, B., Ferrini, G. & Parmigiani, F. Pseudo-surface acoustic waves in hypersonic surface phononic crystals. *Physical Review B* **80,** 104119 (2009).

155. Graczykowski, B., Mielcarek, S., Trzaskowska, A., Sarkar, J., Hakonen, P. & Mroz, B. Tuning of a hypersonic surface phononic band gap using a nanoscale two-dimensional lattice of pillars. *Physical Review B* **86,** 085426 (2012).

156. Graczykowski, B., Sledzinska, M., Kehagias, N., Alzina, F., Reparaz, J. S. & Torres, S. Hypersonic phonon propagation in one-dimensional surface phononic crystal. *Applied Physics Letters* **104** (2014).

157. Pan, H., Zhang, V. L., Di, K., Kuok, M. H., Lim, H. S., Ng, S. C., Singh, N. & Adeyeye, A. O. Phononic and magnonic dispersions of surface waves on a permalloy/BARC nanostructured array. *Nanoscale Research Letters* **8,** 1–6 (2013).

158. Ono, N., Kitamura, K., Nakajima, K. & Shimanuki, Y. Measurement of Young's modulus of silicon single crystal at high temperature and its dependency on boron concentration using the flexural vibration method. *Japanese Journal of Applied Physics* **39,** 368 (2000).

159. Shirai, K. Temperature dependence of Young's modulus of silicon. *Japanese Journal of Applied Physics* **52,** 088002 (2013).

160. Grimsditch, M. Effective elastic constants of superlattices. *Physical Review B* **31,** 6818 (1985).

161. Silvani, R., Kostylev, M., Adeyeye, A. O. & Gubbiotti, G. Spin wave filtering and guiding in Permalloy/iron nanowires. *Journal of Magnetism and Magnetic Materials* **450,** 51–59 (2018).

162. Ghaddar, A., Gloaguen, F. & Gieraltowski, J. *Magnetic properties of ferromagnetic nanowire arrays: Theory and experiment* in *Journal of Physics: Conference Series* **200** (2010), 072032.

163. Han, G., Zong, B., Luo, P. & Wu, Y. Angular dependence of the coercivity and remanence of ferromagnetic nanowire arrays. *Journal of Applied Physics* **93,** 9202–9207 (2003).

164. Osman, N. S. & Moyo, T. Temperature dependence of coercivity and magnetization of Sr 1/3 Mn 1/3 Co 1/3 Fe 2 O 4 ferrite nanoparticles. *Journal of Superconductivity and Novel Magnetism* **29,** 361–366 (2016).

165. Gopman, D. B., Dennis, C. L., Chen, P., Iunin, Y. L., Finkel, P., Staruch, M. & Shull, R. D. Strain-assisted magnetization reversal in Co/Ni multilayers with perpendicular magnetic anisotropy. *Scientific Reports* **6,** 27774 (2016).

166. Zhang, Q., Lee, D., Zheng, L., Ma, X., Meyer, S. I., He, L., Ye, H., Gong, Z., Zhen, B., Lai, K., *et al.* Gigahertz topological valley Hall effect in nanoelectromechanical phononic crystals. *Nature Electronics* **5,** 157–163 (2022).

167. Zhang, J., Chen, M., Chen, J., Yamamoto, K., Wang, H., Hamdi, M., Sun, Y., Wagner, K., He, W., Zhang, Y., *et al.* Long decay length of magnon-polarons in BiFeO3/La0. 67Sr0.33MnO3 heterostructures. *Nature Communications* **12,** 7258 (2021).

168. Chumak, A. V., Vasyuchka, V. I., Serga, A. A. & Hillebrands, B. Magnon spintronics. *Nature Physics* **11,** 453–461 (2015).

169. Rezende, S. M., Azevedo, A. & Rodríguez-Suárez, R. L. Introduction to antiferromagnetic magnons. *Journal of Applied Physics* **126** (2019).

170. Ciccarelli, C., Hals, K. M., Irvine, A., Novak, V., Tserkovnyak, Y., Kurebayashi, H., Brataas, A. & Ferguson, A. Magnonic charge pumping via spin–orbit coupling. *Nature Nanotechnology* **10,** 50–54 (2015).

171. Lenk, B., Ulrichs, H., Garbs, F. & Münzenberg, M. The building blocks of magnonics. *Physics Reports* **507,** 107–136 (2011).

172. Chumak, A., Serga, A. & Hillebrands, B. Magnonic crystals for data processing. *Journal of Physics D: Applied Physics* **50,** 244001 (2017).

173. Lachance-Quirion, D., Tabuchi, Y., Gloppe, A., Usami, K. & Nakamura, Y. Hybrid quantum systems based on magnonics. *Applied Physics Express* **12,** 070101 (2019).

174. Barman, A., Gubbiotti, G., Ladak, S., Adeyeye, A. O., Krawczyk, M., Gräfe, J., Adelmann, C., Cotofana, S., Naeemi, A., Vasyuchka, V. I., *et al.* The 2021 magnonics roadmap. *Journal of Physics: Condensed Matter* **33,** 413001 (2021).

175. Zhang, X. A Review of Common Materials for Hybrid Quantum Magnonics. *Materials Today Electronics,* 100044 (2023).

176. Zhang, X., Zou, C.-L., Jiang, L. & Tang, H. X. Strongly coupled magnons and cavity microwave photons. *Physical Review Letters* **113,** 156401 (2014).

177. Liu, T., Zhang, X., Tang, H. X. & Flatté, M. E. Optomagnonics in magnetic solids. *Physical Review B* **94,** 060405 (2016).

178. Zhang, X., Zou, C.-L., Jiang, L. & Tang, H. X. Cavity magnomechanics. *Science Advances* **2,** e1501286 (2016).

179. Berk, C., Jaris, M., Yang, W., Dhuey, S., Cabrini, S. & Schmidt, H. Strongly coupled magnon–phonon dynamics in a single nanomagnet. *Nature Communications* **10,** 2652 (2019).

180. Potts, C. A., Varga, E., Bittencourt, V. A., Kusminskiy, S. V. & Davis, J. P. Dynamical backaction magnomechanics. *Physical Review X* **11,** 031053 (2021).

181. Lachance-Quirion, D., Tabuchi, Y., Ishino, S., Noguchi, A., Ishikawa, T., Yamazaki, R. & Nakamura, Y. Resolving quanta of collective spin excitations in a millimeter-sized ferromagnet. *Science Advances* **3,** e1603150 (2017).

182. Comstock, A. H., Chou, C.-T., Wang, Z., Wang, T., Song, R., Sklenar, J., Amassian, A., Zhang, W., Lu, H., Liu, L., *et al.* Hybrid magnonics in hybrid perovskite antiferromagnets. *Nature Communications* **14,** 1834 (2023).

183. Xiang, Z.-L., Ashhab, S., You, J. & Nori, F. Hybrid quantum circuits: Superconducting circuits interacting with other quantum systems. *Reviews of Modern Physics* **85,** 623 (2013).

184. Kurizki, G., Bertet, P., Kubo, Y., Mølmer, K., Petrosyan, D., Rabl, P. & Schmiedmayer, J. Quantum technologies with hybrid systems. *Proceedings of the National Academy of Sciences* **112,** 3866–3873 (2015).

185. Clerk, A., Lehnert, K., Bertet, P., Petta, J. & Nakamura, Y. Hybrid quantum systems with circuit quantum electrodynamics. *Nature Physics* **16,** 257–267 (2020).

186. Verhagen, E., Deléglise, S., Weis, S., Schliesser, A. & Kippenberg, T. J. Quantum-coherent coupling of a mechanical oscillator to an optical cavity mode. *Nature* **482,** 63–67 (2012).

187. Wiersig, J. Enhancing the sensitivity of frequency and energy splitting detection by using exceptional points: application to microcavity sensors for single-particle detection. *Physical Review Letters* **112,** 203901 (2014).

188. Nair, J. M., Mukhopadhyay, D. & Agarwal, G. Enhanced sensing of weak anharmonicities through coherences in dissipatively coupled anti-PT symmetric systems. *Physical Review Letters* **126,** 180401 (2021).

189. Boca, A., Miller, R., Birnbaum, K., Boozer, A., McKeever, J. & Kimble, H. Observation of the vacuum Rabi spectrum for one trapped atom. *Physical Review Letters* **93,** 233603 (2004).

190. Tabuchi, Y., Ishino, S., Ishikawa, T., Yamazaki, R., Usami, K. & Nakamura, Y. Hybridizing ferromagnetic magnons and microwave photons in the quantum limit. *Physical Review Letters* **113,** 083603 (2014).

191. Tabuchi, Y., Ishino, S., Noguchi, A., Ishikawa, T., Yamazaki, R., Usami, K. & Nakamura, Y. Coherent coupling between a ferromagnetic magnon and a superconducting qubit. *Science* **349,** 405–408 (2015).

192. Braakman, F. R., Barthelemy, P., Reichl, C., Wegscheider, W. & Vandersypen, L. M. Long-distance coherent coupling in a quantum dot array. *Nature Nanotechnology* **8,** 432–437 (2013).

193. Chumak, A. V., Kabos, P., Wu, M., Abert, C., Adelmann, C., Adeyeye, A., Åkerman, J., Aliev, F. G., Anane, A., Awad, A., *et al.* Advances in magnetics roadmap on spin-wave computing. *IEEE Transactions on Magnetics* **58,** 1–72 (2022).

194. Zhang, G.-Q., Feng, W., Xiong, W., Su, Q.-P. & Yang, C.-P. Generation of long-lived W states via reservoir engineering in dissipatively coupled systems. *Physical Review A* **107,** 012410 (2023).

195. Hatanaka, D., Asano, M., Okamoto, H. & Yamaguchi, H. Phononic Crystal Cavity Magnomechanics. *Physical Review Applied* **19,** 054071 (2023).

196. Harder, M., Yao, B., Gui, Y. & Hu, C.-M. Coherent and dissipative cavity magnonics. *Journal of Applied Physics* **129** (2021).

197. Von Neumann, J. & Wigner, E. P. Über merkwürdige diskrete Eigenwerte. *The Collected Works of Eugene Paul Wigner: Part A: The Scientific Papers,* 291–293 (1993).

198. Hioki, T., Hashimoto, Y. & Saitoh, E. Coherent oscillation between phonons and magnons. *Communications Physics* **5,** 115 (2022).

199. Yoshie, T., Scherer, A., Hendrickson, J., Khitrova, G., Gibbs, H., Rupper, G., Ell, C., Shchekin, O. & Deppe, D. Vacuum Rabi splitting with a single quantum dot in a photonic crystal nanocavity. *Nature* **432,** 200–203 (2004).

200. Lauk, N., Sinclair, N., Barzanjeh, S., Covey, J. P., Saffman, M., Spiropulu, M. & Simon, C. Perspectives on quantum transduction. *Quantum Science and Technology* **5,** 020501 (2020).

201. Bagci, T., Simonsen, A., Schmid, S., Villanueva, L. G., Zeuthen, E., Appel, J., Taylor, J. M., Sørensen, A., Usami, K., Schliesser, A., *et al.* Optical detection of radio waves through a nanomechanical transducer. *Nature* **507,** 81–85 (2014).

202. Harder, M., Yang, Y., Yao, B., Yu, C., Rao, J., Gui, Y., Stamps, R. & Hu, C.-M. Level attraction due to dissipative magnon-photon coupling. *Physical Review Letters* **121,** 137203 (2018).

203. Wang, Y.-P. & Hu, C.-M. Dissipative couplings in cavity magnonics. *Journal of Applied Physics* **127** (2020).

204. Xu, P.-C., Rao, J., Gui, Y., Jin, X. & Hu, C.-M. Cavity-mediated dissipative coupling of distant magnetic moments: Theory and experiment. *Physical Review B* **100,** 094415 (2019).

205. Grigoryan, V. L. & Xia, K. Cavity-mediated dissipative spin-spin coupling. *Physical Review B* **100,** 014415 (2019).

206. Yao, B., Yu, T., Gui, Y., Rao, J., Zhao, Y., Lu, W. & Hu, C.-M. Coherent control of magnon radiative damping with local photon states. *Communications Physics* **2,** 161 (2019).

207. Zhao, J., Liu, Y., Wu, L., Duan, C.-K., Liu, Y.-x. & Du, J. Observation of anti-$\mathcal{PT}$-symmetry phase transition in the magnon-cavity-magnon coupled system. *Physical Review Applied* **13,** 014053 (2020).

208. Yang, Y., Wang, Y.-P., Rao, J., Gui, Y., Yao, B., Lu, W. & Hu, C.-M. Unconventional singularity in anti-parity-time symmetric cavity magnonics. *Physical Review Letters* **125,** 147202 (2020).

209. Li, A., Wei, H., Cotrufo, M., Chen, W., Mann, S., Ni, X., Xu, B., Chen, J., Wang, J., Fan, S., *et al.* Exceptional points and non-Hermitian photonics at the nanoscale. *Nature Nanotechnology,* 1–15 (2023).

210. Zhang, R.-Y., Cui, X., Chen, W.-J., Zhang, Z.-Q. & Chan, C. Symmetry-protected topological exceptional chains in non-Hermitian crystals. *Communications Physics* **6,** 169 (2023).

211. Zhang, Q., Yang, C., Sheng, J. & Wu, H. Dissipative coupling-induced phonon lasing. *Proceedings of the National Academy of Sciences* **119,** e2207543119 (2022).

212. Wang, Y.-P., Rao, J., Yang, Y., Xu, P.-C., Gui, Y., Yao, B., You, J. & Hu, C.-M. Nonreciprocity and unidirectional invisibility in cavity magnonics. *Physical Review Letters* **123,** 127202 (2019).

213. Toebes, C., Vretenar, M. & Klaers, J. Dispersive and dissipative coupling of photon Bose-Einstein condensates. *Communications Physics* **5,** 59 (2022).

214. Wang, W., Vasa, P., Pomraenke, R., Vogelgesang, R., De Sio, A., Sommer, E., Maiuri, M., Manzoni, C., Cerullo, G. & Lienau, C. Interplay between strong coupling and radiative damping of excitons and surface plasmon polaritons in hybrid nanostructures. *ACS Nano* **8,** 1056–1064 (2014).

215. Zhang, S., Zhang, H., Xu, T., Wang, W., Zhu, Y., Li, D., Zhang, Z., Yi, J. & Wang, W. Coherent and incoherent damping pathways mediated by strong coupling of two-dimensional atomic crystals with metallic nanogrooves. *Physical Review B* **97,** 235401 (2018).

216. Novotny, L. Strong coupling, energy splitting, and level crossings: A classical perspective. *American Journal of Physics* **78,** 1199–1202 (2010).

217. Akram, U., Ficek, Z. & Swain, S. Decoherence and coherent population transfer between two coupled systems. *Physical Review A* **62,** 013413 (2000).

218. Lu, C., Turner, B., Gui, Y., Burgess, J., Xiao, J. & Hu, C.-M. An experimental demonstration of level attraction with coupled pendulums. *American Journal of Physics* **91,** 585–594 (2023).

219. Nguyen, H. T. & Cottam, M. Microscopic dipole–exchange theory for planar nanostriped magnonic crystals. *Journal of Physics D: Applied Physics* **44,** 315001 (2011).

220. Hortensius, J., Afanasiev, D., Matthiesen, M., Leenders, R., Citro, R., Kimel, A., Mikhaylovskiy, R., Ivanov, B. & Caviglia, A. Coherent spin-wave transport in an antiferromagnet. *Nature Physics* **17,** 1001–1006 (2021).

221. Hashimoto, Y., Daimon, S., Iguchi, R., Oikawa, Y., Shen, K., Sato, K., Bossini, D., Tabuchi, Y., Satoh, T., Hillebrands, B., *et al.* All-optical observation and reconstruction of spin wave dispersion. *Nature Communications* **8,** 15859 (2017).

222. Satoh, T., Terui, Y., Moriya, R., Ivanov, B. A., Ando, K., Saitoh, E., Shimura, T. & Kuroda, K. Directional control of spin-wave emission by spatially shaped light. *Nature Photonics* **6,** 662–666 (2012).

223. Au, Y., Dvornik, M., Davison, T., Ahmad, E., Keatley, P. S., Vansteenkiste, A., Van Waeyenberge, B. & Kruglyak, V. Direct excitation of propagating spin waves by focused ultrashort optical pulses. *Physical Review Letters* **110,** 097201 (2013).

224. Khokhlov, N. E., Filatov, I. A. & Kalashnikova, A. Spatial asymmetry of optically excited spin waves in anisotropic ferromagnetic film. *Journal of Magnetism and Magnetic Materials* **589,** 171514 (2024).

225. Patterson, A. The Scherrer formula for X-ray particle size determination. *Physical Review* **56,** 978 (1939).

226. Parratt, L. G. Surface studies of solids by total reflection of X-rays. *Physical Review* **95,** 359 (1954).

227. Nevot, L. & Croce, P. Caractérisation des surfaces par réflexion rasante de rayons X. Application á l'étude du polissage de quelques verres silicates. *Revue de Physique appliquée* **15,** 761–779 (1980).

228. Eaton, P. & West, P. *Atomic force microscopy* (Oxford university press, 2010).

229. Vinai, G., Motti, F., Petrov, A. Y., Polewczyk, V., Bonanni, V., Edla, R., Gobaut, B., Fujii, J., Suran, F., Benedetti, D., *et al.* An integrated ultra-high vacuum apparatus for growth and in situ characterization of complex materials. *Review of Scientific Instruments* **91** (2020).

230. Park, Y., Fullerton, E. E. & Bader, S. Growth-induced uniaxial in-plane magnetic anisotropy for ultrathin Fe deposited on MgO (001) by oblique-incidence molecular beam epitaxy. *Applied Physics Letters* **66,** 2140–2142 (1995).

231. Ma, J. Phonon Engineering of Micro-and Nanophononic Crystals and Acoustic Metamaterials: A Review. *Small Science* **3,** 2200052 (2023).

232. Mathieu, C., Jorzick, J., Frank, A., Demokritov, S., Slavin, A., Hillebrands, B., Bartenlian, B., Chappert, C., Decanini, D., Rousseaux, F., *et al.* Lateral quantization of spin waves in micron size magnetic wires. *Physical Review Letters* **81,** 3968 (1998).

233. Gubbiotti, G., Tacchi, S., Madami, M., Carlotti, G., Yang, Z., Ding, J., Adeyeye, A. & Kostylev, M. Collective spin excitations in bicomponent magnonic crystals consisting of bilayer permalloy/Fe nanowires. *Physical Review B* **93,** 184411 (2016).

234. Gubbiotti, G., Zhou, X., Haghshenasfard, Z., Cottam, M., Adeyeye, A. & Kostylev, M. Interplay between intra-and inter-nanowires dynamic dipolar interactions in the spin wave band structure of Py/Cu/Py nanowires. *Scientific Reports* **9,** 4617 (2019).

235. Gubbiotti, G., Zhou, X., Adeyeye, A., Varvaro, G. & Kostylev, M. Effect of exchange and dipolar interlayer interactions on the magnonic band structure of dense Fe/Cu/Py nanowires with symmetric and asymmetric layer widths. *Physical Review B* **101,** 224431 (2020).

236. Gubbiotti, G., Silvani, R., Tacchi, S., Madami, M., Carlotti, G., Yang, Z., Adeyeye, A. O. & Kostylev, M. Tailoring the spin waves band structure of 1D magnonic crystals consisting of L-shaped iron/permalloy nanowires. *Journal of Physics D: Applied Physics* **50,** 105002 (2017).

237. Grimsditch, M., Malozemoff, A. & Brunsch, A. Standing spin waves observed by Brillouin scattering in amorphous metallic Fe 80 B 20 films. *Physical Review Letters* **43,** 711 (1979).

238. Kuz'Min, M., Skokov, K., Diop, L., Radulov, I. & Gutfleisch, O. Exchange stiffness of ferromagnets. *The European Physical Journal Plus* **135,** 1–8 (2020).

239. Kostylev, M., Yang, Z., Maksymov, I., Ding, J., Samarin, S. & Adeyeye, A. Microwave magnetic dynamics in ferromagnetic metallic nanostructures lacking inversion symmetry. *Journal of Applied Physics* **119** (2016).

240. Gubbiotti, G., Tacchi, S., Carlotti, G., Vavassori, P., Singh, N., Goolaup, S., Adeyeye, A., Stashkevich, A. & Kostylev, M. Magnetostatic interaction in arrays of nanometric permalloy wires: A magneto-optic Kerr effect and a Brillouin light scattering study. *Physical Review B* **72,** 224413 (2005).

241. Goolaup, S., Singh, N., Adeyeye, A., Ng, V. & Jalil, M. Transition from coherent rotation to curling mode reversal process in ferromagnetic nanowires. *The European Physical Journal B-Condensed Matter and Complex Systems* **44,** 259–264 (2005).

242. Goolaup, S., Singh, N. & Adeyeye, A. O. Coercivity Variation in Ni $_{80}$ Fe $_{20}$ Ferromagnetic Nanowires. *IEEE Transactions on Nanotechnology* **4,** 523–526 (2005).

243. Stoner, E. C. & Wohlfarth, E. A mechanism of magnetic hysteresis in heterogeneous alloys. *Philosophical Transactions of the Royal Society of London. Series A, Mathematical and Physical Sciences* **240,** 599–642 (1948).

244. Lavin, R., Denardin, J., Escrig, J., Altbir, D., Cortés, A. & Gómez, H. Angular dependence of magnetic properties in Ni nanowire arrays. *Journal of Applied Physics* **106** (2009).

245. Aharoni, A. & Shtrikman, S. Magnetization curve of the infinite cylinder. *Physical Review* **109,** 1522 (1958).

246. Ha, J. K., Hertel, R. & Kirschner, J. Micromagnetic study of magnetic configurations in submicron permalloy disks. *Physical Review B* **67,** 224432 (2003).

247. Castano, F., Hao, Y., Ross, C., Vögeli, B., Smith, H. I. & Haratani, S. Switching field trends in pseudo spin valve nanoelement arrays. *Journal of Applied Physics* **91,** 7317–7319 (2002).

248. Goolaup, S., Adeyeye, A. & Singh, N. Dipolar coupling in closely packed pseudo-spin-valve nanowire arrays. *Journal of Applied Physics* **100** (2006).

249. Gubbiotti, G., Zhou, X., Haghshenasfard, Z., Cottam, M. & Adeyeye, A. Reprogrammable magnonic band structure of layered permalloy/Cu/permalloy nanowires. *Physical Review B* **97,** 134428 (2018).

250. Gubbiotti, G., Zhou, X., Adeyeye, A., Varvaro, G. & Kostylev, M. Collective spin waves in arrays of asymmetric and symmetric width nanowires: Effect of the film layering sequence. *Journal of Physics D: Applied Physics* **53,** 135001 (2020).

251. Osborn, J. A. Demagnetizing factors of the general ellipsoid. *Physical Review* **67,** 351 (1945).

252. Sato, M. & Ishii, Y. Simple and approximate expressions of demagnetizing factors of uniformly magnetized rectangular rod and cylinder. *Journal of Applied Physics* **66,** 983–985 (1989).

253. Rhodes, P. Demagnetising energies of uniformly magnetised rectangular blocks. *Proc. Leeds Phil. Liter. Soc* **6,** 191–210 (1954).

List of publications

Refereed publications

D. Di Sante, C. Bigi, P. Eck, S. Enzner, A. Consiglio, G. Pokharel, **P. Carrara**, P. Orgiani, V. Polewczyk, J. Fujii, P.D.C. King, I. Vobornik, G. Rossi, I. Zeljkovic, S.D. Wilson, R. Thomale, G. Sangiovanni, G. Panaccione and F. Mazzola, *Flat band separation and robust spin Berry curvature in bilayer kagome metals*, Nature Physics, 19, 1135-1142 (2023).
DOI: 10.1038/s41567-023-02053-z.

F. Mazzola, S. Enzner, P. Eck, C. Bigi, M. Jugovac, I. Cojocariu, V. Feyer, Z. Shu, G.M. Pierantozzi, A. De Vita, **P. Carrara**, J. Fujii, P.D.C. King, G. Vinai, P. Orgiani, C. Cacho, M.D. Watson, G. Rossi, I. Vobornik, T. Kong, D. Di Sante, G. Sangiovanni and G. Panaccione, *Observation of termination-dependent topological connectivity in a magnetic Weyl kagome lattice*, Nano Letters, 23, 17, 8035-8042 (2023).
DOI: 10.1021/acs.nanolett.3c02022.

M. Brioschi, **P. Carrara**, V. Polewczyk, D. Dagur, G. Vinai, P. Parisse, S. Dal Zilio, G. Panaccione, G. Rossi and R. Cucini, *Multidetection scheme for transient-grating-based spectroscopy*, Optics Letters, 48, 167-170 (2023).
DOI: 10.1364/OL.476958.

D. Dagur, V. Polewczyk, A.Y. Petrov, **P. Carrara**, M. Brioschi, S. Fiori, R. Cucini, G. Rossi, G. Panaccione, P. Torelli and G. Vinai, *Visible light effects on photostrictive-magnetostrictive PMN-PT/Ni heterostructure*, Advanced Materials Interfaces, 9, 2201337 (2022).
DOI: 10.1002/admi.202201337.

P. Carrara, M. Brioschi, E. Longo, D. Dagur, V. Polewczyk, G. Vinai, R. Mantovan, M. Fanciulli, G. Rossi, G. Panaccione and R. Cucini, *All-optical generation and time-resolved polarimetry of magnetoacoustic resonances via transient grating spectroscopy*, Physical Review Applied, 18, 044009 (2022).
DOI: 10.1103/PhysRevApplied.18.044009.

M. Sygletou, S. Benedetti, M. Ferrera, G.M. Pierantozzi, R. Cucini, G. Della Valle, **P. Carrara**, A. De Vita, A. di Bona, P. Torelli, D. Catone, G. Panaccione, M. Canepa and F. Bisio, *Quantitative ultrafast electron-temperature dynamics in photo-excited Au nanoparticles*,

Small, 17, 2100050 (2021).
DOI: 10.1002/smll.202100050.

Publications in peer-review

P. Carrara,[†] M. Brioschi,[†] R. Silvani, A.O. Adeyeye, G. Panaccione, G. Gubbiotti, G. Rossi and R. Cucini, *Coherent and dissipative coupling in a magneto-mechanical system*, submitted.
[†] These authors contributed equally.

M. Tuniz, A. Consiglio, D. Puntel, C. Bigi, S. Enzner, G. Pokharel, P. Orgiani, W. Bronsch, F. Parmigiani, V. Polewczyk, P.D.C. King, J. Wells, I. Zeljkovic, **P. Carrara**, G. Rossi, J. Fujii, I. Vobornik, S. Wilson, R. Thomale, T. Wehling, G. Sangiovanni, G. Panaccione, F. Cilento, D. Di Sante and F. Mazzola, *Dynamics and resilience of the unconventional charge density wave in ScV_6Sn_6 bilayer kagome metal*, submitted.

Acknowledgments

Questa tesi chiude tre anni di ricerca scientifica, che è certo un lavoro personale, ma anche un *community effort*, impensabile senza il confronto con mentori più avanti di me, e con indispensabili compagni di strada. Insieme, questa tesi conclude per me un (primo?) periodo triestino, che mi ha formato come persona e come scienziato grazie agli incontri che ho avuto la fortuna di fare e ai rapporti che si sono costruiti. Sorprendentemente, questi due aspetti non sono stati mondi separati: la loro intersezione ha permesso che persone con cui ho condiviso il lavoro quotidiano diventassero cari amici, e amici fuori lavoro fornissero tasselli nella ricerca scientifica. Mi è insomma impossibile separare ringraziamenti formali e informali, e penso che questo sia qualcosa di cui essere grati.

Il primo ringraziamento va al prof. Rossi, supervisore di questo lavoro. Grazie per il supporto puntuale e discreto, che mi ha permesso di imparare molto provando e sbagliando in laboratorio. Nonostante i contatti a volte diradati (per colpa mia), si è sempre dimostrato disponibile alla discussione dei risultati, con interesse genuino, dall'inquadramento generale fino al dettaglio tecnico dell'esperimento. Grazie per l'entusiasmo che dimostra, che le auguro di non perdere e mi auguro di imparare sempre più. Grazie anche per come mi ha aiutato nel periodo di scrittura, e in questi mesi di transizione verso un post-doc per i suoi consigli, senza imporre alcun condizionamento, ma piuttosto dando suggerimenti e lasciando a me la libertà (e responsabilità!) di muovermi.

Ringrazio poi Riccardo, supervisore *day by day*, per la pazienza che hai dimostrato nell'insegnarmi come si sta in laboratorio dal giorno 1 del mio periodo a SPRINT, e nel sopportare la mia testardaggine (e presunzione, a volte, di cui ti chiedo scusa). Hai spesso preferito frenarti per lasciare che io mettessi le mani in pasta in prima persona, anche a costo di errori (leggi: ottiche bruciate) e di ritardi nel lavoro: grazie perché è stata una scuola impareggiabile. Grazie per la tua disponibilità al confronto e alla discussione, dai problemi tecnici (per i quali rimani insostituibile), alle questioni di fisica, dalla gestione dei rapporti umani coi collaboratori, alle corse cui ti ho costretto durante la scrittura della tesi. Non ultimo, grazie per come sai costruire un ambiente umano sul posto di lavoro, con competenza ma con anche una sana dose di leggerezza: credo che se SPRINT è il posto che è (*positivo*, per dirlo in una parola), è in gran parte merito tuo.

Ringrazio di cuore Giancarlo, che non compare formalmente in questa tesi ma che ne è stato colonna portante. Grazie per la fiducia che mi hai dimostrato. Ho avuto la fortuna di condividere con te l'ufficio in questi anni, e devo ringraziarti di come silenziosamente mi hai fatto crescere, dal buongiorno alla mattina. Grazie per la competenza con cui guidi il gruppo, per le tue mail che aprono ciascuna dieci nuove strade (e poi ne sondiamo mezza), e per la tua sensibilità nel seguire il percorso di ognuno. Grazie per la disponibilità che hai dimostrato nelle periodiche "confessioni" nel tuo ufficio a cui ricorrevo quando mi incastravo, e da cui con discrezione dirigevi il lavoro sotterra.

Un grande grazie alla Marta, con cui ho condiviso tantissimo tempo in questi anni. La costruzione del setup, e poi i primi rompimenti di testa, le mille problematiche tecniche, le collaborazioni... tutto questo è stato fatto davvero assieme, e sono sicuro che non ci sarei riuscito da solo! E grazie per aver reso tutte le ore in laboratorio molto migliori grazie alla tua lucidità, competenza e leggerezza (e i *banana breads*, e le droghe del Viaggator Goloso, e le abbreviazie *mega belle* cui la convivenza stretta ci ha costretti, etc...).

Grazie ad Andre, per la competenza tecnica e pazienza infinita con cui hai seguito il nostro lavoro e lo hai spinto oltre. Grazie anche per la sensibilità in più che dimostri oltre le necessità lavorative, che mi ha spinto a chiedermi le ragioni di quello che faccio, dentro e fuori lavoro. Grazie a tutti gli sprinterz: Gian, vero uomo di laboratorio, appassionato e inaffondabile; Ale, pozzo di scienza e di informazioni le più assurde, e al tempo stesso stupenda compagnia; Sara, che per prima mi ha incoraggiato a puntare su SPRINT per il dottorato; Michele, che quasi sei riuscito a farmi fare un corso di swing con il tuo entusiasmo (e grazie per le puntuali lezioni di triestino); Alice, per la positività che porti (eredità romana, credo) e per la determinazione che dimostri; Lorenzo, la new entry, presenza buona nel gruppo. Vi ringrazio per la compagnia a lavoro[1] e fuori lavoro (cene, bevute, Barcole...). So che questa compagnia spiccia non è scontata, ed è stato un grande regalo in questi anni, che ricorderò con affetto. Grazie al gruppo romano (esteso) dei ramanisti: Andrea, Claudia, Mattia, ogni volta che siete passati era una festa, davvero!

Grazie ai vicini di casa, i temibili T-ReX Fede, Denny, Wibke, Manuel: sapervi accanto negli atri muscosi della Experimental Hall dà una tranquillità in più per la giornata in laboratorio (anche grazie ai mille consigli che sapete dare). Grazie in particolare a Denny, grande punto di intersezione tra il dentro e il fuori lavoro, per la lucidità con cui guardi a quello che ti capita nella vita, e per lo sforzo che fai per spiegare quello che hai capito a chi della vita non capisce molto (eccomi). E grazie per avermi fatto conoscere *L'illogica alllegria*! Grazie alla Wibke (o Winke, in toscano), per la sincerità con cui vivi a partire dalle tue domande, alla ricerca di un punto di vista umano da cui abbracciare tutto.

Grazie al gruppone di APE. I thank Vincent: first of all for the growth of Ni thin films, then (perhaps above all) for your company and encouragement over the years during fundamental discussions over the warmth of a cigarette. I thank Deepak and Gio for the static MOKE measurements, and for sharing incredible experiences in the snow (the Himalayan mission on Nanos, and in Moena). Ringrazio Fede Mazzola e Chiara, per avermi coinvolto in alcuni lavori ARPES: ho solo visto la punta dell'iceberg e avrei ancora un'infinità di cose da imparare da voi.

Un grazie non solo formale ai collaboratori che hanno contribuito a questa tesi con tasselli insostituibili: Simone Dal Zilio per la fabbricazione delle maschere di fase; Pietro Parisse per le mappe AFM sui film di Ni; Emanuele Longo, Roberto Mantovan e Marco Fanciulli per le misure GIXRD, XRR, FMR e per le puntuali discussioni che hanno portato il lavoro sul Ni a conclusione; Prof. A.O. Adeyeye for the fabrication of magnonic-

---

[1] e grazie per avermi accolto al pranzo delle schiscie senza giudicare (troppo) la cucina *à la* Baba Jaga...

phononic crystals and SEM maps; Gianluca Gubbiotti e Raffaele Silvani per le misure BLS e le simulazioni MumaX3, oltre che per la disponibilità e le fondamentali precisazioni sui campioni di nanofili; Rudy Sergo per l'insostituibile competenza e supporto (e simpatia) nell'affrontare le mille questioni elettroniche. Ringrazio anche le altre persone con cui ho avuto la fortuna ed il piacere di collaborare: Dr. A.A. Maznev, Peter and Nadia from MIT; Filippo, Laura e Minci di TIMER; Nupur e prof. Bonetti; Cristian e tutta la crew del LTP a EuXFEL; Floriana, Regina e Pasquale all'interno di IMPRESS.

Grazie agli amici che mi hanno permesso di sentire Trieste come casa in questi anni. Prima di tutto i raga che per periodi più o meno lunghi mi hanno sopportato in appa: Gio C., Gio T(rivela), Albi, Luca, Teo, Bido, Bona, Gia, Edo, Richi, Trava e Mazzo. La vita in appa con voi non è stato un *vivere fuori casa*, ma lo scoprire la possibilità di sentirsi a casa pure a 400 km da Novate. Grazie in particolare ad Albi, Bido, Bona e Richi per le discussioni estemporanee che, a volte direttamente, hanno contribuito a questa tesi.

Poi ringrazio l'altra casa che ho trovato a TS: san Giacomo e la vita che ne nasce. Grazie agli amici della scuola di comunità, che insieme abbiamo visto nascere e fiorire oltre ogni calcolo e schematismo. Grazie perché con voi ho imparato quanto sia liberante condividere la vita, le domande, i passi, la fede. Grazie a Rudy per la disponibilità che mi dimostri, per la fiducia che hai avuto in me (ben più di quella che ho io!), e per la tua schiettezza. La certezza della tua amicizia mi fa guardare con fiducia a quello che avrò da fare nella vita, chissà dove nel mondo. Un grazie speciale a Giacomo, Ale (e Chiara) per il bene che mi volete immeritatamente. A Mauri, per l'onestà che hai con le tue domande. E poi a Liuk, Michi e Mariette, Cate, Vilde, Dani, Fabrizio ed Elena, Meri e Paolo, Erika, Mic, le pie donne Samantha e Valentina, Sofi, Cencio e Ale (e Antonio): la vostra compagnia è stata un aiuto concreto in questi anni. Grazie a Bona e Giulia: dopo quello che vi ho fatto passare sono grato che la verità della nostra amicizia sia emersa, più libera. Grazie a Bido, con cui ho condiviso le corse per la scrittura della tesi, oltre a traslochi, imbiancature, revisioni improvvisate del motorino: grazie per la tua amicizia trasparente. Ringrazio Edo: ancora non ho capito com'è che ci siamo incontrati, ma sono grato dell'amicizia disinteressata che è nata. Grazie a Bea, che ovunque sarai avrai un pezzo di cuore a Trieste. Grazie perché non hai paura di farmi domande cui sai che non so rispondere, perché sono anche le mie. E grazie perché so che dove sei avrò un posto dove tornare. Grazie a Carol e le suorine, per lo sguardo d'amore per tutti, a partire da me. *Grazie di tutto quello che fai per noi* a Domenico, anima della festa ovunque ti trovi: grazie per le discussioni su film d'evasione e per la musica di serie Z con cui abbiamo passato innumerevoli a/r sulla A4. Grazie soprattutto per la stima sincera che dimostri.

Grazie agli amici longobardi (ed expat), porto sicuro ogniqualvolta siamo riusciti ad incrociarci a Milano: Gino, Muso, Gulco, Marta, Cops e Giulia, Ila, Scotti (con un grazie speciale per i promemoria sulle dannate scadenze UniMI), Bianca e Albi, Samu. Grazie ai Sodali de la Pieve, e satelliti orbitanti: Giovaz, Mucho, Tommi e Agne, Landìa e Cate e Bruno, Walker e Mariachiara, Edo e Jessica, Albi, Michi, Palli e Leti. Come ormai è tradizione: *sodali (e satelliti) sì, ma soprattutto amici.*

Infine grazie alla mia famiglia, sostegno a cui continuo a guardare. Grazie alle nonne e agli zii; a Marta, Calve, Meri e Pau; a Ceci, Nico, Tommi, Michi e Betti: la vostra stima e incoraggiamento sono stati fondamentali in questi anni e mi hanno sempre fatto attendere il rientro a Novate con gioia, pur nel casino che inevitabilmente si crea. Un grazie speciale alla Nene, che non ti stanchi di mostrarmi la tua febbre di vita. Grazie ai miei genitori, che in questi anni con discrezione mi avete incoraggiato a non accontentarmi, guardandomi da lontano curiosi di sapere cosa stessi facendo della mia vita.